MPM
SCIENTIFIC
JOURNAL

ISSN 1605-2730
E-ISSN 1605-8119

MATERIALS PHYSICS AND MECHANICS

Vol. 54, N. 1, 2026

MATERIALS PHYSICS AND MECHANICS

Principal Editors:

Alexander Belyaev
Institute for Problems in Mechanical Engineering
of the Russian Academy of Science (RAS), Russia

Andrei Rudskoi
Peter the Great St. Petersburg Polytechnic University, Russia

Founder and Honorary Editor: Ilya Ovid'ko (1961-2017)
Institute for Problems in Mechanical Engineering
of the Russian Academy of Sciences (RAS), Russia

Associate Editor:

Anna Kolesnikova
Institute for Problems in Mechanical Engineering
of the Russian Academy of Sciences (RAS), Russia

Artem Semenov
Peter the Great St. Petersburg Polytechnic University, Russia

Editorial Board:

E.C. Aifantis
Aristotle University of Thessaloniki, Greece
K.E. Aifantis
University of Florida, USA
U. Balachandran
Argonne National Laboratory, USA
A. Bellosi
Research Institute for Ceramics Technology, Italy
S.V. Bobylev
Institute for Problems in Mechanical Engineering (RAS), Russia
A.I. Borovkov
Peter the Great St.Petersburg Polytechnic University, Russia
G.-M. Chow
National University of Singapore, Singapore
A.B. Freidin
Institute for Problems in Mechanical Engineering (RAS), Russia
I.G. Goryacheva
Institute of Problems of Mechanics (RAS), Russia
D. Hui
University of New Orleans, USA
G. Kiriakidis
IESL/FORTH, Greece
D.M. Klimov
Institute of Problems of Mechanics (RAS), Russia
G.E. Kodzhaspirov
Peter the Great St. Petersburg Polytechnic University, Russia
S.A. Kukushkin
Institute for Problems in Mechanical Engineering (RAS), Russia
T.G. Langdon
University of Southampton, U.K.
V.P. Matveenko
Institute of Continuous Media Mechanics (RAS), Russia
A.I. Melker
Peter the Great St. Petersburg Polytechnic University, Russia
Yu.I. Meshcheryakov
Institute for Problems in Mechanical Engineering (RAS), Russia
R.R. Mulyukov
Institute for Metals Superplasticity Problems (RAS), Russia
Yu.V. Petrov
St. Petersburg State University, Russia
N.M. Pugno
Politecnico di Torino, Italy
B.B. Rath
Naval Research Laboratory, USA
A.E. Romanov
Ioffe Institute (RAS), Russia
A.M. Sastry
University of Michigan, Ann Arbor, USA
B.A. Schrefler
University of Padua, Italy
N.V. Skiba
Institute for Problems in Mechanical Engineering (RAS), Russia
A.G. Sheinerman
Institute for Problems in Mechanical Engineering (RAS), Russia
R.Z. Valiev
Ufa State Aviation Technical University, Russia
K. Zhou
Nanyang Technological University, Singapore

"Materials Physics and Mechanics" Editorial Office:
Phone: +7(812)552 77 78, ext. 224 **E-mail:** mpmjournal@spbstu.ru **Web-site:** http://www.mpm.spbstu.ru

International scientific journal "**Materials Physics and Mechanics**" is published by Peter the Great St. Petersburg Polytechnic University in collaboration with Institute for Problems for Mechanical Engineering in the Russian Academy of Sciences in both hard copy and electronic versions. The journal provides an international medium for the publication of reviews and original research papers written in English and focused on the following topics:

- Mechanics of composite and nanostructured materials.
- Physics of strength and plasticity of composite and nanostructured materials.
- Mechanics of deformation and fracture processes in conventional materials (solids).
- Physics of strength and plasticity of conventional materials (solids).
- Physics and mechanics of defects in composite, nanostructured, and conventional materials.
- Mechanics and physics of materials in coupled fields.

Owner organizations: Peter the Great St. Petersburg Polytechnic University; Institute of Problems of Mechanical Engineering RAS.

Materials Physics and Mechanics is indexed in Chemical Abstracts, Cambridge Scientific Abstracts,
Web of Science Emerging Sources Citation Index (ESCI) and Elsevier Bibliographic Databases (in particular, SCOPUS).

© 2026, Peter the Great St. Petersburg Polytechnic University
© 2026, Institute for Problems in Mechanical Engineering RAS

МЕХАНИКА И ФИЗИКА МАТЕРИАЛОВ

Materials Physics and Mechanics

Том 54, номер 1, 2026 год

Учредители:
ФГАОУ ВО «Санкт-Петербургский политехнический университет Петра Великого»
ФГБУН «Институт проблем машиноведения Российской академии наук»

Редакционная коллегия журнала

Главный редактор
д.т.н., академик РАН **А.И. Рудской**
Санкт-Петербургский политехнический университет Петра Великого

Главный научный редактор
д.ф.-м.н., чл.-корр. РАН **А.К. Беляев**
Институт проблем машиноведения Российской академии наук (РАН)

Основатель и почетный редактор
д.ф.-м.н. **И.А. Овидько (1961-2017)**
Институт проблем машиноведения Российской академии наук (РАН)

Ответственные редакторы
д.ф.-м.н. **А.Л. Колесникова**
Институт проблем машиноведения
Российской академии наук (РАН)
д.ф.-м.н. **А.С. Семенов**
Санкт-Петербургский политехнический университет
Петра Великого

Международная редакционная коллегия:

д.ф.-м.н. **С.В. Бобылев**
Институт проблем машиноведения РАН, Россия
к.т.н., проф. **А.И. Боровков**
Санкт-Петербургский политехнический ун-т Петра Великого, Россия
д.ф.-м.н., проф. **Р.З. Валиев**
Уфимский государственный технический университет, Россия
д.ф.-м.н., академик РАН **И.Г. Горячева**
Институт проблем механики РАН, Россия
д.ф.-м.н., академик РАН **Д.М. Климов**
Институт проблем механики РАН, Россия
д.т.н., проф. **Г.Е. Коджаспиров**
Санкт-Петербургский политехнический ун-т Петра Великого, Россия
д.ф.-м.н., проф. **С.А. Кукушкин**
Институт проблем машиноведения РАН, Россия
д.ф.-м.н., академик РАН **В.П. Матвеенко**
Институт механики сплошных сред РАН, Россия
д.ф.-м.н., проф. **А.И. Мелькер**
Санкт-Петербургский политехнический ун-т Петра Великого, Россия
д.ф.-м.н., проф. **Ю.И. Мещеряков**
Институт проблем машиноведения РАН, Россия
д.ф.-м.н., чл.-корр. РАН **Р.Р. Мулюков**
Институт проблем сверхпластичности металлов РАН, Россия
д.ф.-м.н., чл.-корр. РАН **Ю.В. Петров**
Санкт-Петербургский государственный университет, Россия
д.ф.-м.н., проф. **А.Е. Романов**
Физико-технический институт им. А.Ф. Иоффе РАН, Россия
д.ф.-м.н. **Н.В. Скиба**
Институт проблем машиноведения РАН, Россия
д.ф.-м.н., проф. **А.Б. Фрейдин**
Институт проблем машиноведения РАН, Россия
д.ф.-м.н. **А.Г. Шейнерман**
Институт проблем машиноведения РАН, Россия

Prof., Dr. **E.C. Aifantis**
Aristotle University of Thessaloniki, Greece
Dr. **K.E. Aifantis**
University of Florida, USA
Dr. **U. Balachandran**
Argonne National Laboratory, USA
Dr. **A. Bellosi**
Research Institute for Ceramics Technology, Italy
Prof., Dr. **G.-M. Chow**
National University of Singapore, Singapore
Prof., Dr. **D. Hui**
University of New Orleans, USA
Prof., Dr. **G. Kiriakidis**
IESL/FORTH, Greece
Prof., Dr. **T.G. Langdon**
University of Southampton, UK
Prof., Dr. **N.M. Pugno**
Politecnico di Torino, Italy
Dr. **B.B. Rath**
Naval Research Laboratory, USA
Prof., Dr. **A.M. Sastry**
University of Michigan, Ann Arbor, USA
Prof., Dr. **B.A. Schrefler**
University of Padua, Italy
Prof., Dr. **K. Zhou**
Nanyang Technological University, Singapore

Тел.: +7(812)552 77 78, доб. 224 **E-mail:** mpmjournal@spbstu.ru **Web-site:** http://www.mpm.spbstu.ru

Тематика журнала

Международный научный журнал "Materials Physics and Mechanics" издается Санкт-Петербургским политехническим университетом Петра Великого в сотрудничестве с Институтом проблем машиноведения Российской академии наук в печатном виде и электронной форме. Журнал публикует обзорные и оригинальные научные статьи на английском языке по следующим тематикам:

- Механика композиционных и наноструктурированных материалов.
- Физика прочности и пластичности композиционных и наноструктурированных материалов.
- Механика процессов деформации и разрушения в традиционных материалах (твердых телах).
- Физика прочности и пластичности традиционных материалов (твердых тел).
- Физика и механика дефектов в композиционных, наноструктурированных и традиционных материалах.
- Механика и физика материалов в связанных полях.

Редколлегия принимает статьи, которые нигде ранее не опубликованы и не направлены для опубликования в другие научные издания. Все представляемые в редакцию журнала "Механика и физика материалов" статьи рецензируются. Статьи могут отправляться авторам на доработку. Не принятые к опубликованию статьи авторам не возвращаются.

Журнал "Механика и физика материалов" ("Materials Physics and Mechanics") включен в систему цитирования Web of Science Emerging Sources Citation Index (ESCI), SCOPUS и РИНЦ.

© 2026, Санкт-Петербургский политехнический университет Петра Великого
© 2026, Институт проблем машиноведения Российской академии наук

Contents

MATERIALS PHYSICS AND MECHANICS RESEARCH ARTICLE

Submitted: 18 July, 2025 **Revised:** 2 August, 2025 **Accepted:** 25 August, 2025

Optical detection of the quantum Hall effect in silicon nanostructures

N.T. Bagraev [1], **L.E. Klyachkin** [1]✉, **A.M. Malyarenko** [1], **N.I. Rul** [2]

[1] Ioffe Institute, St. Petersburg, Russia

[2] Peter the Great St. Petersburg Polytechnic University, St. Petersburg, Russia

✉ leonid.klyachkin@gmail.com

ABSTRACT

Electroluminescence spectra of a silicon nanostructure with edge channels covered by chains of dipole centers with negative correlation energy are demonstrated. The presence of such chains provides conditions for nondissipative transport of single charge carriers at high temperatures up to room temperature. Due to the suppression of the electron-electron interactions, the macroscopic quantum phenomena such as Shubnikov–de Haas oscillations and the quantum staircase of Hall resistance are consistent with the positions of the spectral peaks of the detected electroluminescence. The obtained results are considered in the framework of Faraday electromagnetic induction, which indicates that Landau quantization leads to the emergence of induced irradiation similar to Josephson and Andreev generation. Moreover, the detected maxima in the spectral characteristics correspond to odd fractional values of the resistance quantum staircases, while the dips in the electroluminescence spectra are observed at even fractional values of the resistance quantum ladder, which is due to the increased formation of composite bosons and fermions, respectively.

KEYWORDS

silicon nanostructure • edge channels • negative-U dipole centers • quantum Hall effect • electroluminescence electromagnetic induction

Funding. *The work was financed within the framework of the state assignment of the Federal State Unitary Enterprise Ioffe Institute No. FFUG-2024-0039 of the Ministry of Science and Higher Education of the Russian Federation.*

Citation: Bagraev NT, Klyachkin LE, Malyarenko AM, Rul' NI. Optical detection of the quantum Hall effect in silicon nanostructures. *Materials Physics and Mechanics*. 2026;54(1): 1–7. http://dx.doi.org/10.18149/MPM.5412026_1

Introduction

Currently, macroscopic quantum phenomena in semiconductor nanostructures are predominantly studied at ultra-low temperatures due to the decisive role of electron-electron interactions in suppressing nondissipative transport of single charge carriers [1,2]. Graphene is an exception, yet even in this case, the realization of nondissipative transport conditions at high temperatures requires the application of a strong magnetic field [3].

An emerging breakthrough in solving this problem is associated with advances in technology and fundamental research on topological structures [4–15]. In particular, it has been demonstrated that in ultra-narrow quantum wells with edge channels covered by chains of centers with negative correlation energy (negative U), it is possible to create conditions for nondissipative carrier transport and, consequently, observe the macroscopic quantum phenomena at high temperatures, up to room temperature [16]. The suppression of electron–electron interactions in this case is primarily related to the

Publisher: Peter the Great St. Petersburg Polytechnic University

formation of impurity dipoles due to the dissociation of neutral negative-U centers: $2D^0 \Rightarrow D^+ + D^- + U$, where U is the effective energy that accounts for the compensation of Coulomb repulsion owing to coupling with electron–vibration interactions (EVI) [17–19]. As a result of the negative correlation energy, it is feasible in many systems of impurity and structural centers to form the edge channel shells consisting of chains of negative-U dipole centers, which facilitates the segmentation of edge channels into sections (pixels) containing single charge carriers. Thus, two problems are resolved simultaneously: on one hand, the electron–electron interaction is suppressed, and on the other hand, conditions for nondissipative transport are ensured through energy exchange between a single charge carrier and the negative-U dipole centers of the edge channel shell [20].

In the presence of chains of negative-U dipole centers, nearly nondissipative transport of single charge carriers within the pixels constituting the edge channel is achieved: $h + D^- \Rightarrow D^0$, $D^+ + e \Rightarrow D^0 + h$, $D^- + D^+ + e + h \Rightarrow 2D^0 + h$. Subsequently, hole tunneling along the pixel shell is accompanied by ultrafast formation of negative-U dipole centers: $2D^0 + h \Rightarrow D^- + D^+$. Thus, the presence of negative-U centers promotes the emergence of an energy reservoir within the edge channel shells, enabling weakly nondissipative carrier transport.

In this work, boron centers embedded via diffusion into wafers of monocrystalline silicon (100) under fabrication conditions of the structure in the Hall geometry which is oriented along the [011] axis (Fig. 1) are used as negative-U dipole centers.

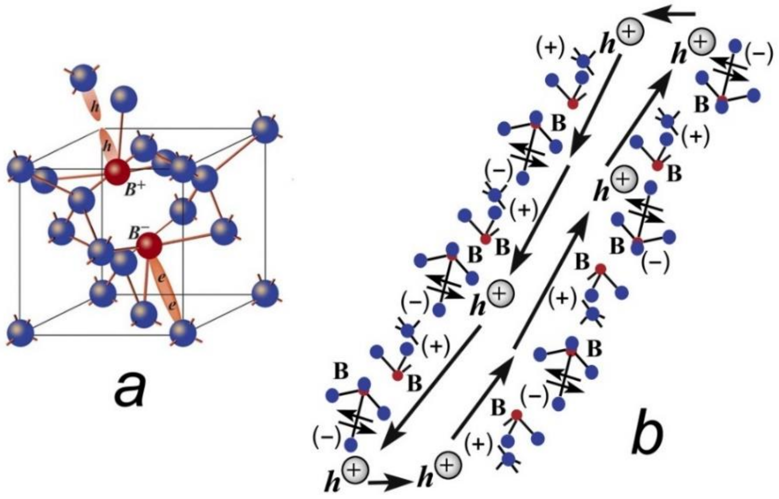

Fig. 1. Dipole trigonal boron center (B^+–B^-) with negative correlation energy (a) and the chains of the dipole boron centers in the δ-barriers confining the ultra-narrow silicon quantum well and its edge channels (b)

Negative-U shells with similar properties can be obtained not only by embedding a high concentration of impurity centers, but also by fabricating quasi-one-dimensional chains of point and extended defects [21]. For example, low-dimensional structures with similar properties within negative-U shells were realized at the interface of hybrid SiC/Si structures grown by the method of coordinated substitution of atoms [21]. In this case, the role of negative-U dipole center chains is played by crystallographically aligned chains of silicon vacancies as well as paired $C_i - V_{Si}$ centers [21].

It should be noted that the initial reduction in entropy of the semiconductor nanostructure due to the presence of negative-U shells not only allows the observation of macroscopic quantum phenomena at high temperatures but also enables the study of various processes arising from quantum interference of single charge carriers in edge channels. In this case, the pixels act as quantum boxes, and by investigating processes inside them, one can evaluate the relative contributions of equilibrium and non-equilibrium effects to quantum interference. In this work, it is demonstrated through a comparative analysis of the results obtained from studying the electrical and optical versions of the quantum Hall effect (QHE).

Materials and Method

The silicon nanostructure was fabricated using planar technology on a monocrystalline silicon (100) surface through preliminary oxidation, subsequent photolithography and gas-phase boron diffusion [22]. Careful optimization of thermal oxidation conditions to achieve an ultra-shallow diffusion profile — under a balance of vacancy and kick-out diffusion mechanisms — enabled the passivation of the boundaries of an ultra-narrow quantum well (2 nm) with boron centers. As a result, an ultra-narrow quantum well was obtained, confined by barriers composed of quasi-one-dimensional boron chains (Fig. 2), spaced 2 nm apart. Despite the high boron concentration (5×10^{21} cm^{-3} according to SIMS data [22]), the edge channels of the quantum well showed no activity in EPR measurements. However, studies of field-dependent magnetization using the Faraday method revealed a significant diamagnetic response, which is exhibited in weak magnetic fields [22]. Analysis of temperature and field dependencies of magnetization led to the proposal of a model in which boron impurity centers passivate the edge channel and are responsible for single-carrier transport. As noted above, the ground state of the impurity shells consists of chains of negative-U dipole boron centers, primarily indicated by the diamagnetic response observed when the nanostructure is placed in an external magnetic field [22].

Since the edge channel consists of pixels containing single charge carriers, conditions are established for the realization of nondissipative transport at high temperatures. In studies of this structure, the following phenomena have been observed:

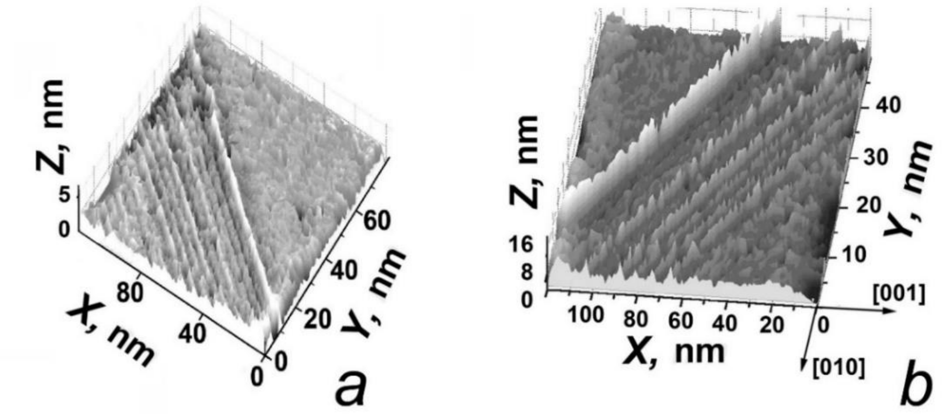

Fig. 2. STM (scanning tunneling microscope) image of the silicon nanosandwich (100) surface (a) containing chains of boron dipole centers oriented along the (011) axis (b)

Shubnikov–de Haas and de Haas – van Alphen quantum oscillations, a quantum staircase of Hall resistance, a quantum staircase of conductance [16], as well as electrical [22] and optical [20] versions of the multiple Andreev reflections. In this context, the pixels can be considered as the Andreev molecules [20].

Results and Discussion

Figure 3 presents the magnetic field dependencies of the longitudinal (R_{xx}) and lateral (R_{xy}) resistances of the silicon nanostructure, measured at a temperature of 77 K under a stabilized drain-source current I_{ds} = 10 nA. Since the presence of negative-U boron dipole center chains, which confine the edge channels of the quantum well and divide them into pixels containing individual charge carriers, creates the conditions for dissipationless transport, the characteristics of the Shubnikov–de Haas oscillations and the quantum staircase of Hall resistance are determined by the Landau quantization processes within each individual pixel and directly depend on its geometric dimensions [16,23]. In this case, the emergence of steps in the magnetic field dependence of the Hall resistance can be analyzed within the framework of Faraday's electromagnetic induction [24]:

$$\frac{dE}{d\Phi} = I_{gen}, \tag{1}$$

where dE is the change in carrier energy within the pixel upon a change in magnetic flux ($d\Phi = \Delta B \cdot S$), S is the pixel area and I_{gen} is the induced generation current.

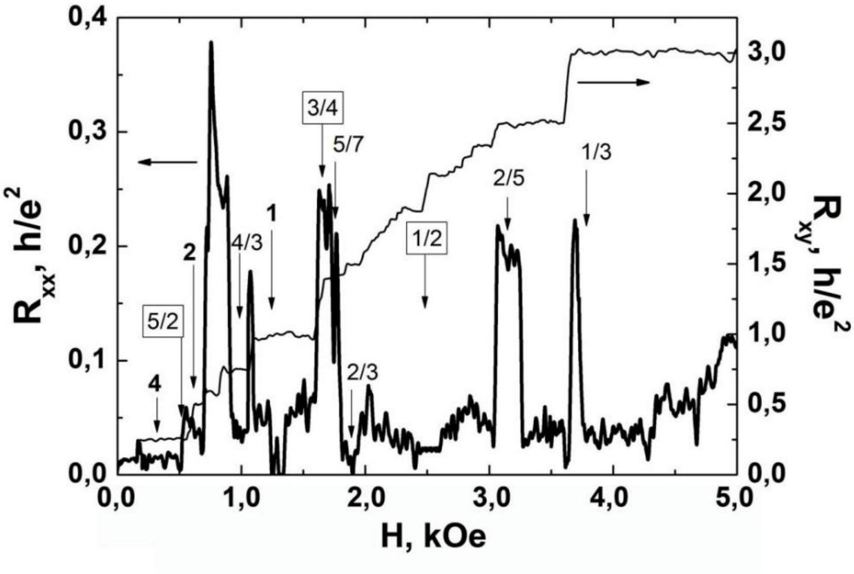

Fig. 3. Hall resistance $R_{xy}=V_{xy}/I_{ds}$ and magnetoresistance $R_{xx} = V_{xx}/I_{ds}$ of the silicon nanostructure (p_{2D}=3 × 10^{13}m^{-2}) dependencies on the external magnetic field strength. T = 77 K; I_{ds} = 10 nA

It is appropriate to express the change in magnetic flux as a change in the number of magnetic flux quanta $d\Phi = m\Phi_0$, where $\Phi_0 = h/e$. In turn, the magnitude of the energy change depends on the number of carriers (n), $dE = ne \cdot dU$ (for a pixel containing a single charge carrier, n = 1). Thus, the Faraday's relation automatically leads to the step height in the Hall dependence:

$$G = \frac{I_{gen}}{U} = \frac{n}{m} \cdot \frac{e^2}{h}, \tag{2}$$

which makes it possible to describe not only the integral QHE [23] but also the fractional QHE [16].

Approximation of the field-dependent Hall curve allows determination of the carrier density (pixel density), which, according to the dependence in Fig. 3, is 3 × 10^{13} m^{-2}. Hence, the pixel dimensions are 2 nm × 16.6 μm, and the number of pixels between the XX contacts is 124.

Since the Josephson and Andreev junctions between the negative-U dipole chains on opposite edges of the pixel stimulate the induced emission, the energy-dependent form of the Faraday's relation can be expressed as:

$$h\nu = eI_{gen}R_N\,, \tag{3}$$

where R_N is the load resistance, which in this case corresponds to the quantum resistance of the pixel ($R_N = h/e^2$). Combined with the classical form of the Faraday's relation given above:

$$\begin{gathered} h\nu = e\left(\frac{h}{e^2}\right)I_{gen} = \left(\frac{h}{e}\right)I_{gen},\ h/\Delta E = \tau, \\ e/I_{gen} = \tau,\ I_{gen} = e\Delta E/h, \\ h\nu = e\frac{\Delta E}{h}\Delta BS,\ \nu = \frac{e\Delta E\Delta BS}{h^2}. \end{gathered} \tag{4}$$

Thus, the corresponding wavelengths seem to be selected and construct a scale that aligns with the magnetic field scale in Fig. 3, thereby determining the wavelengths at which features should appear in the electroluminescence spectra corresponding to the positions of the steps in the Hall resistance staircase (Fig. 4).

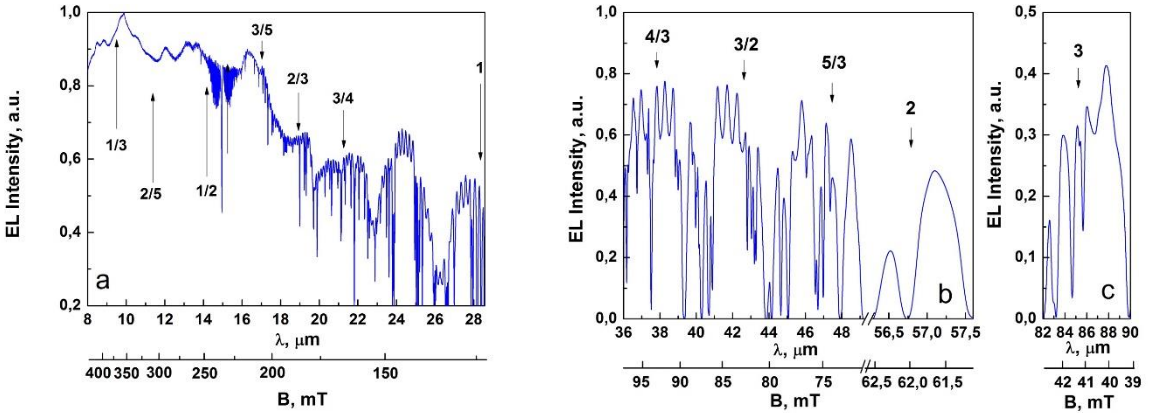

Fig. 4. Electroluminescence spectra of the silicon nanostructure in the mid- (a) and far-infrared (b,c) wavelength ranges, showing features corresponding to fractional and integer values of the quantum resistance staircase at T = 300 K

It should be noted that the frequency range of the observed electroluminescence extends into the terahertz spectral region, in accordance with the emission mechanism arising from electromagnetic induction. In this case, the proposed version of optical detection of the QHE differs from the first optical detection of the QHE achieved by monitoring changes in interband photoluminescence characteristics in an external magnetic field [25].

Figure 4 presents electroluminescence spectra obtained at T = 300 K under a stabilized drain–source current (I_{ds}), which induces a magnetic field within the edge channel pixels: $H = \Delta I_{ds}/2r_0$, where $r_0(S/\pi)^{1/2}$ is the effective pixel radius, with $r_0 = 10^{-7}$ m.

The electroluminescence spectra were recorded using the Bruker Vertex 70 infrared Fourier spectrometer. A comparison of the spectral characteristics with the quantum staircase of Hall resistance magnetic field dependencies shows good agreement between the positions of features in the electroluminescence spectra (Fig. 4) and the quantum steps (Fig. 3). It should be noted that the optical peaks corresponding to odd fractional values of the quantum resistance staircase indicate enhanced induced emission — i.e., stimulated generation of composite bosons upon the sequential capture of single magnetic flux quanta. Conversely, the observed dips in the electroluminescence spectra at wavelengths corresponding to even fractional values of the quantum resistance staircase demonstrate enhanced formation of composite fermions, which apparently leads to additional strengthening of the electron–electron interaction and the associated quenching of electroluminescence [26–30].

The consistency between the electrical and optical manifestations of the fractional QHE indicates that Landau quantization gives rise to the induced emission, similar to the Josephson and Andreev generation mechanisms, regardless of how many magnetic flux quanta are involved in the process.

Conclusion

This work presents the first experimental results demonstrating the possibility of detecting and identifying both the integral and fractional QHEs in the silicon nanostructure with the edge channels confined by the chains of dipole centers exhibiting negative correlation energy, by analysis of features in electroluminescence spectra obtained via infrared Fourier spectroscopy. It is shown that the optical detection of the QHE can be described within the framework of the Faraday electromagnetic induction. The obtained results demonstrate strong agreement between the characteristic behavior of the lateral and longitudinal resistance of the studied silicon nanostructure and the spectra of terahertz electroluminescence arising under the Landau quantization conditions.

CRediT authorship contribution statement

Nikolai T. Bagraev: writing – review & editing, conceptualization; **Leonid E. Klyachkin**: writing – original draft, investigation; **Anna M. Malyarenko**: investigation, supervision; **Nikolai I. Rul**: investigation, data curation.

Conflict of interest

The authors declare that they have no conflict of interest.

References

1. Imry Y. *Introduction to Mesoscopic Physics.* Oxford University Press; 1997.
2. Li S, Bao L, Huang S, Ning J, Shi A, Peng P, Liu J. Braiding Majorana zero modes in a two-dimensional grid structure. *Phys. Rev. A.* 2025;111: 032437.
3. Geim AK, Novoselov KS. The rise of graphene. *Nature Materials.* 2007;6: 183–191.
4. Hasan MZ, Kane CL. Colloquium: Topological insulators. *Rev. Mod. Phys.* 2010;82: 3045–3068.

5. Zhang H, Liu CX, Qi XL, Dai X, Fang Z, Zhang SC. Topological insulators in Bi_2Se_3, Bi_2Te_3 and Sb_2Te_3 with a single Dirac cone on the surface. *Nat. Phys*. 2009;5: 438–442.
6. Bauer A. x + y Floquet code: A simple example for topological quantum computation in the path-integral approach. *Physical Review A.* 2025;111: 032413.
7. Cai R, Žutić I, Han W. Superconductor/ferromagnet heterostructures: A platform for superconducting spintronics and quantum computation. *Adv. Quantum Technol.* 2023;6(1): 2200080.
8. Zhang B, Lu P, Tabrizian R, Feng PXL, Wu Y. 2D magnetic heterostructures: Spintronics and quantum future. *npj Spintronics.* 2024;2: 6.
9. Guo Y, Zhang X, Huang Z, Chen J, Luo Z, Zhang J, Li J. Quantum materials for spintronic applications. *npj Spintronics.* 2024;2: 36.
10. He QL, Hughes TL, Armitage NP, Tokura Y, Wang KL. Topological spintronics and magnetoelectronics. *Nature Materials.* 2022;21: 15–23.
11. Narang P, Garcia CAC, Felser C. The topology of electronic band structures. *Nature Materials.* 2021;20: 293–300.
12. Zhang Y, Li W, Zhang M, Qu Y, Tao R, Qi H. Topological Structure and Semantic Information Transfer Network for Cross-Scene Hyperspectral Image Classification. *IEEE Transactions on Neural Networks and Learning Systems.* 2023;34(6): 2817–2830.
13. Shevchenko AP, Shabalin AA, Karpukhin IYu, Blatov, VA. Topological representations of crystal structures: generation, analysis and implementation in the TopCryst system. *Science and Technology of Advanced Materials: Methods.* 2022;2(1): 250–265.
14. Chang H, Lu S, Zheng S, Shi P, Song B. Integrated Parameter Identification Based on a Topological Structure for Servo Resonance Suppression. *IEEE Transactions on Industrial Electronics.* 2024;71(5): 4541–4550.
15. Li S, Deng B, Grinthal A, Schneider-Yamamura A, Kang J, Martens RS, Zhang CT, Li J, Yu S, Bertoldi K, Aizenberg J. Liquid-induced topological transformations of cellular microstructures. *Nature.* 2021;592: 386–391.
16. Bagraev NT, Grigoryev VYu, Klyachkin LE, Malyarenko AM, Mashkov VA, Rul NI. High-temperature quantum kinetic effect in silicon nanosandwiches. *Low Temperature Physics.* 2017;43(1): 110–119.
17. Anderson PW. Model for the Electronic Structure of Amorphous Semiconductors. *Phys. Rev. Lett.* 1975;34(15): 953–955.
18. Watkins, GD. Negative-U properties for defects in solids. In: Grosse P. (Ed.) *Advances in Solid State Physics. Advances in Solid State Physics*. Berlin: Springer; 1984. p.163–189.
19. Bagraev NT, Mashkov VA. Tunneling negative-U centers and photo-induced reactions in solids. *Solid St. Commun.* 1984;51(7): 515–520.
20. Bagraev NT, Klyachkin LE, Malyarenko AM, Taranets KB. Express diagnostics of DNA oligonucleotides. *Technical Physics.* 2024;94(9): 1477–1482.
21. Kukushkin SA, Osipov AV. Interaction of silicon vacancies in silicon carbide. *Technical Physics Letters.* 2024;50(11): 16–20.
22. Bagraev NT, Klyachkin LE, Kudryavtsev AA, Malyarenko AM, Romanov VV. Superconductor Properties for Silicon Nanostructures. In: Luiz A. (ed.) *Superconductor.* Rijeka, Croatia: Sclyo; 2010. p.69–92.
23. Bagraev NT, Klyachkin LE, Malyarenko AM. Spin transistor effect in edge channels of silicon nanosandwiches. *Materials Physics and Mechanics.* 2023;51(4): 85–95.
24. Laughlin RB. Quantized Hall conductivity in two dimensions. *Phys. Rev. B.* 1981;23: 5632–5633.
25. Kukushkin IV, Timofeev VB. Magneto-optics of two-dimensional electrons under integer and fractional quantum Hall effects. *Usp. Fiz. Nauk.* 1988;156(1): 177–178.
26. Willett R, Eisenstein JP, Störmer HL, Tsui DC, Gossard AC, English JH. Observation of an even-denominator quantum number in the fractional quantum Hall effect. *Phys. Rev. Lett.* 1987;59: 1776.
27. Huang K, Das Sarma S, Li X. Fractional quantum anomalous Hall effect in rhombohedral multilayer graphene with a strong displacement field. *Physical Review B.* 2025;111: 075130.
28. Kousa BM, Wei N, MacDonald AH. Orbital competition in bilayer graphene's fractional quantum Hall effect. *Physical Review Letters.* 2025;134: 086502.
29. Qian Y, Zhao T, Zhang J, Xiang T, Li X, Chen J. Describing Landau Level Mixing in Fractional Quantum Hall States with Deep Learning. *Physical Review Letters.* 2025;134: 176503.
30. Zhang NJ, Nguyen RQ, Batra N, Liu X, Watanabe K, Taniguchi T, Feldman D E, Li JIA. Excitons in the fractional quantum Hall effect. *Nature.* 2025;637: 327–332.

MATERIALS PHYSICS AND MECHANICS RESEARCH ARTICLE

Submitted: July 21, 2025 **Revised: August 1, 2025** **Accepted: August 28, 2025**

Meißner–Ochsenfeld effect in semiconductor nanostructures with negative-U shells

N.T. Bagraev , N.A. Dovator, L.E. Klyachkin ✉ , A.M. Malyarenko

Ioffe Institute, St. Petersburg, Russia

✉ leonid.klyachkin@gmail.com

ABSTRACT
The Meißner–Ochsenfeld effect is demonstrated for the first time at room temperature. The diamagnetic response of a silicon nanostructure with edge channels covered by chains of negative-U dipole boron centers is studied when put in (removed from) an external magnetic field. Measurements of the diamagnetic response were carried out by recording the values of magnetization and generation currents. There is good agreement between the results of measurements of the generated internal magnetic field obtained using a ferroprobe and recording the EMF induced by the occurrence of generation currents in an external magnetic field, which determines the conditions of the mechanism of the nondissipative transport in the edge channels at room temperature, which is caused by their interactions with single carriers through negative-U dipole boron centers. The interrelation of the magnetization hysteresis and the magnitude of the EMF induced by the occurrence of generation currents indicates the possibilities of the electrical registration of the Meißner–Ochsenfeld effect in nanostructures manufactured within the framework of the Hall geometry.

KEYWORDS
silicon nanostructure • edge channels • negative-U dipole centers • electromagnetic induction • Meißner–Ochsenfeld effect

Funding. *The work was financed within the framework of the state assignment of the Federal State Unitary Enterprise Ioffe Institute No. FFUG-2024-0039 of the Ministry of Science and Higher Education of the Russian Federation.*

Citation: Bagraev NT, Dovator NA, Klyachkin LE, Malyarenko AM. Meißner-Ochsenfeld effect in semiconductor nanostructures with negative-U shells. *Materials Physics and Mechanics*. 2026;54(1): 8–16. http://dx.doi.org/10.18149/MPM.5412025_2

Introduction

For twenty years following the discovery of superconductivity, it was believed that a superconductor is a perfect conductor with zero resistance [1]. Only after the discovery of the Meißner–Ochsenfeld effect, which involved identifying an absolute diamagnetic response when a superconductor was placed in an external magnetic field, was the quantum nature of superconductivity established [2]. Subsequent studies enabled the identification of mechanisms leading to the phase state of matter that gives rise to superconductor properties and outlined pathways for realization of the high-temperature superconductors in various compounds and device structures based on them [3–15]. However, the experimental realization of nondissipative carrier transport at high temperatures remains challenging to this day. The main difficulties are associated with studies to controll the magnitude of the local negative correlation energy (negative-U), which arises from the interplay of the Coulomb repulsion and the electron–vibration interaction (EVI) [16,17]. It is precisely the compensation of the Coulomb repulsion via EVI that leads to nondissipative transport and, accordingly, to the emergence of a superconducting state. Moreover, the magnitude of the negative correlation energy

Publisher: Peter the Great St. Petersburg Polytechnic University

(negative-U) practically determines the value of the critical temperature (T_C) corresponding to the transition into the superconducting state. It should be noted that the presence of conditions giving rise to negative-U energy (i.e., possibilities for carrier pairing) is not directly linked to the realization of superconductor properties, because disorder in the system of carrier pairs tends to result in dielectric properties of the object rather than nondissipative transport [18]. Therefore, to ensure coherence in nondissipative transport, it has been proposed to use excess single charge carriers whose transfer via tunneling through formed pair centers not only promotes the emergence of the superconductor properties but also enhances them at high temperatures [19,20]. Nevertheless, these predictions have not yet been experimentally realized due to the insufficient magnitude of negative-U energy in most impurity centers and point structural defects. Furthermore, the metastability of the point defects involved in pairing, arising from the presence of the local phonon mode, also leads to decoherence of nondissipative transport and the consequent destruction of the superconductor properties [5,21]. In this case, the use of hybrid structures based on topological semiconductors and superconductors appears to be promised [22]. In particular, semiconductor nanostructures with the edge channels covered by the chains of the negative-U centers are of great interest, as they promote segmentation into regions containing single charge carriers under the compensation of the electron−electron interaction. This opens new possibilities for nondissipative transport of single charge carriers due to their interaction with the negative-U dipole boron centers. It should be noted that segment of the edge channel containing the single charge carrier can be regarded as the Andreev molecule [23,24], whose characteristics allow the study of macroscopic quantum effects [25].

The conditions described above to provide nondissipative transport via local interaction of single carriers with negative-U dipole boron centers covering the edge channels make them promising for studying quasi-one-dimensional superconductors at high temperatures, up to room temperature. In the present work, the identification of the aforementioned conditions enabling superconductivity at room temperature is demonstrated through the study of the diamagnetic response of the silicon nanostructures in shells consisting of chains of the negative-U dipole boron centers.

Method

The investigated device structure was the Hall bridge based on a silicon nanostructure (Fig. 1). An ultra-narrow silicon p-type quantum well, which forms the basis of the silicon nanostructure, was created on the surface of the n-type (100) silicon wafer. The Hall bridge was boron-doped from the gas phase with a concentration of 5×10^{21} cm^{-3}, which is measured by the secondary ion mass spectrometry (SIMS). It was found that within the ultra-shallow (8 nm) boron diffusion profile in silicon, self-ordering effects arise due to the parity of various diffusion mechanisms [26]. As a result, enhanced boron diffusion is observed along certain crystallographic directions, ultimately leading to the formation of chain-like boron-center structures via vacancy-drag effects. In particular, this results in the formation of boron chains oriented along the [011] direction and, accordingly, the alignment of the Hall bridge along this crystallographic axis. These boron chains thus

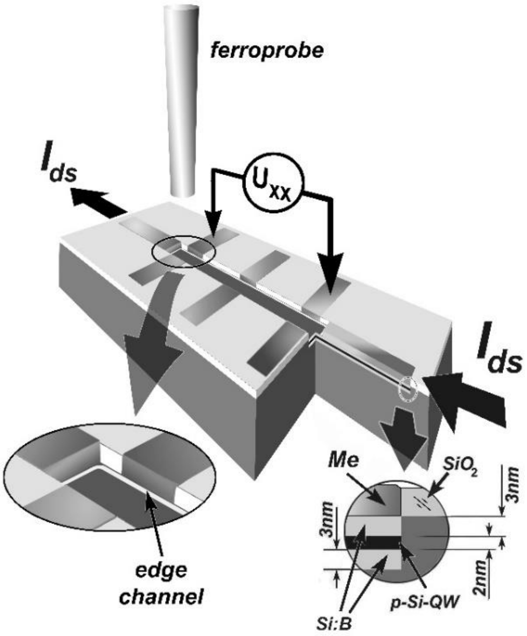

Fig. 1. A Hall bridge based on the silicon nanostructure prepared on the surface of (100) silicon wafer, which contain the topological edge channel oriented along the [011] direction with single charge carriers that occupy the separate regions, pixels, because of the compensation of electron-electron interaction. During the experiments, the ferroprobe of the magnetometer was directed perpendicular to the sample surface

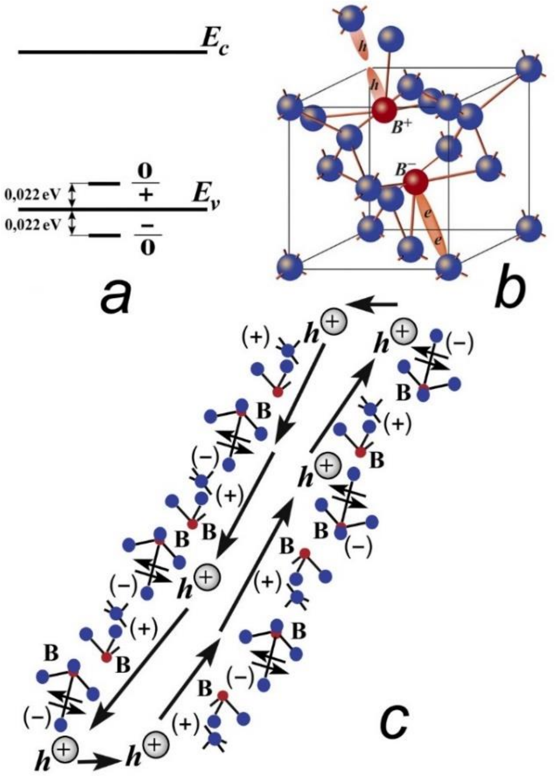

Fig. 2. Energy levels (a) of a negative-U dipole boron center (b); model of single charge carrier tunneling transport along a chain of the negative-U dipole centers (c)

confine the obtained quantum well. Given the high concentration, the distance between these chains in the near-surface layer of the nanostructures, including within the barriers that define the quantum well, corresponds to the spacing between boron centers within a single chain – 2 nm (Fig. 1). This important result is largely a consequence of the possible reconstruction of boron centers along the [111] direction upon changes in their charge/spin state (Fig. 2). In turn, the possibility of such reconstruction, as indicated above, is the reason for the formation of negative-U dipole centers due to the emergence of the local phonon mode at the extremely high concentration of boron centers [26]. Thus, the above serves as the foundation for a technology to produce the Hall bridges with a specific crystallographic orientation, which enables the confinement of the edge channels in nanostructures by the chains of the negative-U dipole centers that act as an energy reservoir for nondissipative carrier transport.

It should be noted that chains consisting of paired centers were first proposed by A.Yu. Kitaev [27,28] for exploring possibilities in quantum-computing operations (Fig. 3). However, in the absence of an internal energy reservoir within a spin loop composed of parallel chains of paired centers, the conditions for nondissipative carrier transport are not met. The reason for this is the increasing role of electron–electron interaction. This main obstacle to spin-dependent transport in an interference loop can, as it turns out, be eliminated if negative-U centers are used as the chain components.

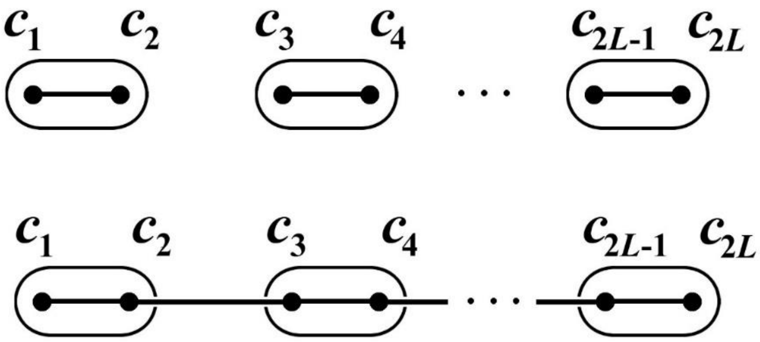

Fig. 3. Two possible types of pairing between adjacent dipole centers. Based on [27,28]

If the paired centers within the chains confining the silicon quantum well are negative-U dipole centers, then the energy reservoir for nondissipative carrier transport inside a spin loop composed of parallel chains is based on the unpairing/pairing reaction of a negative-U dipole center [29].

In this case, due to the presence of negative-U energy, singly charged centers decay into doubly charged and empty centers (Fig. 2(a)). Predominantly in tetrahedral systems, this formation of the dipole centers occurs along the [111] axis, provided that the chain is oriented along the [011] axis. Thus, the chains break down into a system of dipole centers, except for the terminal centers, which contain the single charge carrier (hole) near the contacts (Fig. 2(c)). During the passage of a longitudinal current, the single charge carrier tunnels through the dipole centers within the negative-U chain system:

$D^- + h \Rightarrow D^0$
$D^+ \Rightarrow D^0 + h$ (1)
$2D^0 \Rightarrow D^+ + D^-$

As a result of the described reactions, when a carrier tunnels, it moves to the next dipole center, having received energy from the chain. The subsequent decay of the neutral components of the dipole center is accompanied by the reverse release of energy into the chain simultaneous with its reconstruction. Thus, the exchange of energy between the carrier and the chain provides the condition for nondissipative transport during tunneling [29]. Accordingly, the tunneling processes described above are accompanied by distortions within the chain system. The criterion for realizing nondissipative transport is the evaluation of the ratio between the decay time (τ_1) of the neutral dipole states and the tunneling time (τ_2): $\tau_1 = h/\Delta E = 6.62 \times 10^{-34}/44$ meV, where 44 meV corresponds to the reduction in entropy during the decay of dipole negative-U centers; $\tau_1 = 8 \times 10^{-14}$ s; $\tau_2 = h/\Delta E = h/(I^2R) = h/(I^2h/e^2)$.

Given the values of the generation current used and the fact that the resistance of a dipole-center cell corresponds to the quantum of resistance, $\tau_1 < \tau_2$, which ensures the conditions for nondissipative transport at $T = 300$ K. It should also be noted that the two-dimensional carrier density in such edge channels, according to the Hall measurements, is 3×10^{13} m^{-2} [30].

Given the realization of nondissipative transport of single holes due to energy exchange with chains of dipole negative-U boron centers, the size of the spin-dependent transport loop is limited to a strip of dimensions 2 nm × 16 μm. It should be noted that the quantum interference regime does not depend on the loop's shape but is determined solely by its area. This area primarily defines the magnetic field value corresponding to optimal quantum interference conditions: $\Delta\Phi = \Delta BS = \Phi_0 = h/e = 4 \times 10^{-15}$ Wb, where S is the area of the interference loop; ΔB is the period of quantum oscillations as a function of the external magnetic field; Φ_0 is the magnetic flux quantum.

It should be noted that this condition is consistent with the Landau quantization conditions, which, accordingly, leads to a stepwise change in the areas of interference loops when the magnetic subband index changes. Taking into account the parameters of the edge channel region occupied by a single hole in the silicon nanostructure, the optimal magnetic field value corresponding to quantum interference is 0.124 T [30].

Thus, the characteristics of the investigated nanostructure provide the conditions for nondissipative carrier transport, which has enabled the observation of macroscopic quantum effects at high temperatures up to room temperature [30], and defines the prospects for using chains of negative-U dipole centers to observe the Meißner–Ochsenfeld effect at $T = 300$ K and, correspondingly, to identify their superconductor properties.

Results and Discussion

The Meißner–Ochsenfeld effect was observed in the study of the silicon nanostructure used, both by measuring the diamagnetic response and through measurements of the longitudinal electromotive force (EMF) induced by occurrence of generating currents when the structure was introduced into an external magnetic field.

As noted above, the transport of single charge carriers in the edge channels of nanostructures confined by the chains of the negative-U dipole centers is accompanied by the generation of a magnetic field [30]. Moreover, under an external magnetic field oriented perpendicular to the plane of the nanostructure's edge channel, a magnetic field arises inside the sample that is equal in magnitude to the external field but opposite in direction (Fig. 1) [2]. That is, the measured field response when the structure is introduced into an external magnetic field (Fig. 4) is similar to the data from studies of the Meißner–Ochsenfeld effect in superconductivity and corresponds to the manifestation of absolute diamagnetism. These results are quite understandable if one considers the similarity between the characteristics of chains of negative-U dipole centers and quasi-one-dimensional superconductors. The use of a ferroprobe magnetometer made it possible to detect a reversal in the sign of the magnetic response ΔB, thereby demonstrating that a magnetic field with the opposite sign appears within the sample. It should be noted that the sample was put in an external magnetic field of +15 nT, and accordingly, the diamagnetic response was identified by measuring the magnetic field value within the investigated structure, which was -15 nT.

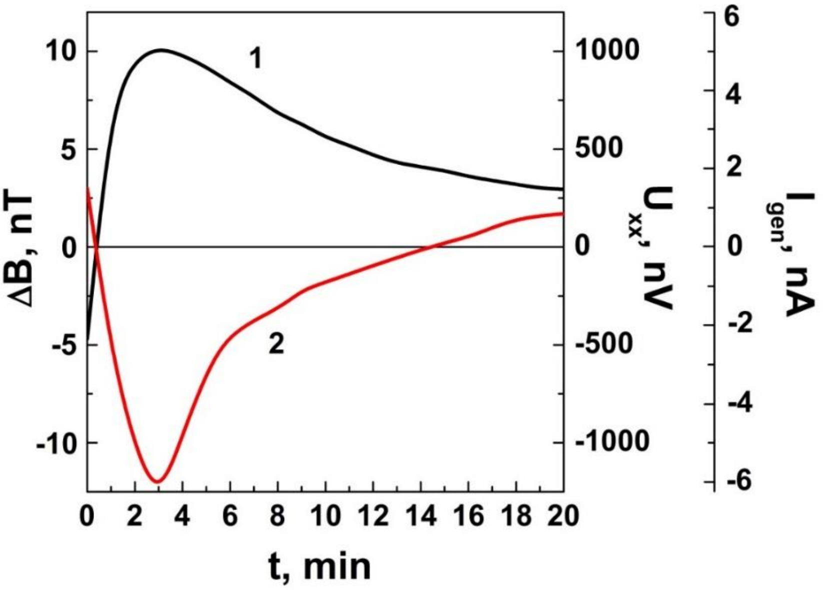

Fig. 4. EMF measured between the XX contacts of the silicon nanostructure during insertion (1) and removal (2) of the sample from an external magnetic field of 15 nT. *T* = 300 K

The experimental setup used was a five-layer magnetically shielded cylindrical chamber. All inner cylinders were made of M-79 permalloy, while the outer cylinder (with a diameter of 50 cm and length of 70 cm) was made of ARMCO steel. The cylinders are closed by lids fabricated from the same material. Inside the innermost cylinder, a Helmholtz coil system powered by a stabilized (adjustable) current source is installed. This system is used both to generate a uniform internal magnetic field and to compensate for the residual magnetic field arising from the penetration (into the shield) of the external laboratory field and the residual magnetization of the permalloy shells. The shielding factors obtained (in the frequency range 0–1 Hz) were 700 for the longitudinal (along the shield axis) and 5000 for the transverse (perpendicular to the shield axis) components of the magnetic field. During the experiments, the magnitude of magnetic induction variations inside the setup was monitored using a cesium-vapor quantum magnetometer and practically did not exceed ± 0.1 nT.

In addition to the above, monitoring the response of the magnetic moment to changes in the external magnetic field enables direct measurement of the generation currents arising within the sample. It is important to note that the EMF generated in the interference loop is directly correlated with the magnitude of the magnetic field inside the sample when it is put in an external magnetic field (Fig. 4). This allows for a significant improvement in the accuracy of the determined magnetic field, and electrical measurements also provide a convenient method for characterizing macroscopic quantum phenomena.

As mentioned above, the magnetic field magnitude inside the sample can be monitored by measuring the EMF between contacts, for example, between the XX contacts of the Hall bridge (Fig. 1). Considering the parameters of the pixels containing single carriers in the edge channel, 16.6 μm × 2 nm, their number between the XX contacts spaced 2 mm apart can be determined. Taking into account that the resistance of a single pixel R_{pix}, which represents a quantum box containing a single charge carrier, is h/e^2 = 25812 Ω, then with 125 pixels between the XX contacts, the total resistance R for their parallel connection is 200 Ω. This allows the generation current induced by the external magnetic field to be determined (Fig. 4): $I_{gen} = U_{xx}/R$.

Thus, considering that the generation of the internal magnetic field can be described within the framework of the Faraday electromagnetic induction, and taking into account the parameters of the studied structure, particularly the area of the loop between the XX contacts (Fig. 1) where the magnetic flux S = 1 μm × 2 mm [18] is localized, it can be concluded that there is good agreement between the electrical and magnetic measurements of the generated internal magnetic field.

A control experiment to study the correlation between the magnetic and electrical measurements of the external magnetic field described above involves measuring the EMF response between the XX contacts when the sample is removed from the external magnetic field (Fig. 4). The long-duration transient processes accompanying the generation of the internal magnetic field upon insertion/removal of the sample from the external magnetic field indicate the metastability of the Meißner–Ochsenfeld effect, resulting from the recharging within the system of parallel-connected quantum resistances and capacitances of pixels in the edge channels.

Conclusion

The Meißner–Ochsenfeld effect has been observed for the first time at room temperature. The diamagnetic response of a silicon nanostructure with the edge channels confined by the chains of the negative-U dipole boron centers has been studied upon insertion into (and removal from) an external magnetic field. It has been demonstrated that there is good agreement between the results of measurements of the generated internal magnetic field obtained using a ferroprobe and the EMF induced by the onset of generating currents in the external magnetic field. The observation of magnetization hysteresis due to the Meißner–Ochsenfeld effect at room temperature indicates the presence of superconductor properties induced by the interaction of the single charge carriers with the chains of the negative-U dipole centers in the shells of the nanostructure's edge channels.

CRediT authorship contribution statement

Nikolai T. Bagraev: writing – review & editing, conceptualization; **Nikolai A. Dovator**: investigation; **Leonid E. Klyachkin**: writing – original draft, investigation, data curation; **Anna M. Malyarenko**: investigation, supervision

Conflict of interest

The authors declare that they have no conflict of interest.

References

1. Abrikosov AA. The present state of the theory of superconductivity. *Sov. Phys. Usp.* 1966;8(5): 710–719.
2. Schmidt VV. *The Physics of Superconductors*. Berlin: Springer; 1997.
3. Eremets MI, Drozdov AP. High-temperature conventional superconductivity. *Sov. Phys. Usp.* 2016;59(11): 1154–1160.
4. Molodyk A, Larbalestier DC. The prospects of high-temperature superconductors. Overcoming cost barriers could make high-temperature superconductors pervasive. *Science.* 2023;380(6651): 1220–1222.
5. Godeke A. High temperature superconductors for commercial magnets. *Supercond. Sci. Technol.* 2023;36: 113001.
6. Troyan IA, Semenok DV, Ivanova AG, Kvashnin AG, Zhou D, Sadakov AV, Sobolevskiy OA, Pudalov VM, Lyubutin IS, Oganov AR. High-temperature superconductivity in hydrides. *Physics – Uspekhi*. 2022;65(7): 748–761.
7. Zhang C, Sous J, Reichman D R, Berciu M, Millis A J, Prokof'ev N V, Svistunov B V. Bipolaronic High-Temperature Superconductivity. *Phys. Rev. X.* 2023;13: 011010.
8. Eremets MI, Minkov VS, Drozdov AP, Kong PP,·Ksenofontov V, Shylin SI, Bud'ko SL,·Prozorov R, Balakirev FF, Sun D, Mozaffari S, Balicas L. High-Temperature Superconductivity in Hydrides: Experimental Evidence and Details. *J Supercond Nov Magn.* 2022;35: 965–977.
9. Lu C, Pan Zh, Yang F, Wu1 C. Interlayer-Coupling-Driven High-Temperature Superconductivity in $La_3Ni_2O_7$ under Pressure. *Phys. Rev. Lett.* 2024;132: 146002.
10. Jiang B, Luo X, Sun Y, Zhong X, Lv J, Xie Y, Ma Y, Liu H. Data-driven search for high-temperature superconductors in ternary hydrides under pressure. *Phys. Rev. B.* 2025;111: 054505.
11. Betto D, Nakata S, Pisani F, Liu Y, Hameed S, Knauft M, Lin CT, Sant R, Kummer K, Yakhou F, Brookes NB, Tacon MLe, Keimer B, Minola M. Coincident onset of charge order and pseudogap in a homogeneous high-temperature superconductor. *Nat. Commun.* 2025;16: 3579.
12. Chow SLE, Ariando A. Nickel Age of High-Temperature Superconductivity. *Advanced Materials Interfaces.* 2025;12(4): 2400717.
13. Liu P, Zhuang Q, Xu Q, Cui T, Liu Z. Mechanism of high-temperature superconductivity in compressed H2-molecular–type hydride. *Science Advances.* 2025;11(13): 9411.
14. Bacq-Labreuil B, Lacasse B, Tremblay AMS Senechal D, Haule K. Toward an Ab Initio Theory of High-Temperature Superconductors: A Study of Multilayer Cuprates. *Phys. Rev. X.* 2025;15: 021071.
15. Ma C, Zhou M, Bi J, Ma Y, Li D, Liu H, Liu G, Wang H, Ma Ya. Synthesis of medium-entropy alloy superhydride (La, Y,Ce)H_{10+x} with high-temperature superconductivity under high pressure. *Physical Review B*. 2025;11: 024505.
16. Anderson PW. Model for the Electronic Structure of Amorphous Semiconductors. *Phys. Rev. Lett.* 1975;34(15): 953–955.
17. Bagraev NT, Mashkov VA. Tunneling negative-U centers and photo-induced reactions in solids. *Solid St. Commun.* 1984;51(7): 515–520.
18. Drabkin IA, Moizhes BYa. Spontaneous dissociation of neutral into positive and negative impurity states. *Sov. Phys. Semicond.* 1981;15(4): 357–370.
19. Šimánek E. Superconductivity at disordered interfaces. *Solid State Commun.* 1979;32(9): 731–734.
20. Ting CS, Talwar DN, Ngai KL. Possible mechanism of superconductivity in metal-semiconductor eutectic alloys. *Phys. Rev. Lett.* 1980;45(14): 1213–1217.
21. Bagraev NT, Polovtsev IS. Zn-Related Center in Silicon: Negative-U Properties. *Defect and Diffusion Forum.* 1993;103-105: 367–386.
22. Hasan MZ, Kane CL. Colloquium: Topological insulators. *Rev. Mod. Phys.* 2010;82: 3045-3068.
23. Andreev AF. The Thermal Conductivity of the Intermediate State in Superconductors. *JETP.* 1964;19(5): 1228–1231.

24. Bordin A, Bennebroek Evertsz' FJ, Steffensen GO, Dvir T, Mazur GP, Van Driel D, Van Loo N, Wolff JC, Bakkers EPAM, Yeyati AL, Kouwenhoven LP. Impact of Andreev Bound States within the Leads of a Quantum Dot Josephson Junction. *Phys. Rev X.* 2025;15: 011046.
25. Bagraev NT, Klyachkin LE, Malyarenko AM, Taranets KB. Express diagnostics of DNA oligonucleotides. *Technical Physics.* 2024;94(9): 1477–1482.
26. Bagraev NT, Klyachkin LE, Malyarenko AM. Macroscopic quantum effects of electromagnetic induction in silicon nanostructures. *Materials Physics and Mechanics.* 2022;50(2): 252–265.
27. Kitaev AYu. Quantum calculations. *Phys. Usp.* 1996;39(8): 843–844.
28. Luethi M, Legg HF, Loss D, Klinovaja J. Fate of poor man's Majoranas in the long Kitaev chain limit. *Physical Review B.* 2025;111: 115419.
29. Bagraev NT, Gusarov AI, Mashkov VA. Spin-correlated electron transfer along broken bonds in semiconductors. *JETP.* 1989;68(4): 816–825.
30. Bagraev NT, Grigoryev VYu, Klyachkin LE, Malyarenko AM, Mashkov VA, Rul NI. High-temperature quantum kinetic effect in silicon nanosandwiches. *Low Temperature Physics.* 2017;43(1): 110–119.

MATERIALS PHYSICS AND MECHANICS RESEARCH ARTICLE

Submitted: October 18, 2025 **Revised: November 13, 2025** **Accepted: November 24, 2025**

Study of optical resistance of a bulk β-Ga_2O_3 crystal

D.I. Panov, N.A. Balabanov, M.M. Sergeev, V.A. Spiridonov ✉, D.A. Bauman, A.E. Romanov

ITMO University, St. Petersburg, Russia

✉ vladspiridonov@itmo.ru

ABSTRACT

The optical resistance and geometric parameters of the damaged region under the action of laser radiation on bulk β-Ga_2O_3 crystal were studied and calculated depending on the power and frequency of laser irradiation. The sample of the crystal for the study was grown by the Czochralski method and prepared by method of cleaving along the (100) plane. The optical resistance was calculated by the Liu method using the laser irradiation and ablation parameters. The experiment determined the threshold for laser damage under pulses of 1030 nm wavelength and 224 fs duration; with a beam spot size of 9.6 μm. The threshold energy density varied from 25.99 to 16.29 J/cm^2 with pulse numbers varying from 1 to 20,000. The threshold power density of incident radiation ranged from 11.6 to 7.3 GW/cm^2.

KEYWORDS

gallium oxide • laser • optical resistance • Liu's method • laser ablation • laser radiation

Funding. *This work has been supported by the grant of the Russian Science Foundation, RSF 24-12-00229.*

Citation: Panov DI, Balabanov NA, Sergeev MM, Spiridonov VA, Bauman DA, Romanov AE. Study of optical resistance of a bulk β-Ga_2O_3 crystal. *Materials Physics and Mechanics.* 2026;54(1): 17–23.
http://dx.doi.org/10.18149/MPM.5412026_3

Introduction

Beta-gallium oxide (β-Ga_2O_3) has emerged as a leading ultra-wide bandgap (UWBG) semiconductor, with a direct bandgap of ~ 4.8 eV, surpassing the performance limits of conventional materials like SiC and GaN [1–5]. Its exceptional properties including a high critical electric field (8 MV/cm^{-1}), excellent thermal stability, and the availability of high-quality substrates make it ideal for next-generation power devices, deep-ultraviolet (UV) photodetectors, and radiation-hardened applications [6–9].

Despite significant progress in understanding the electrical [10–14] and structural properties [14–20] of β-Ga_2O_3, critical challenges still remain in optimizing its performance and reliability for practical applications. One of the key issues is the material's response to various forms of radiation and environmental stress, particularly in optoelectronic applications where the material may be subjected to intense optical irradiation.

The beta phase of gallium oxide belongs to the monoclinic system, spatial group C2/m [21] with lattice parameters a = 12.214 Å, b = 3.0371 Å, c = 5.7981 Å, β = 103.83°. The unit cell of the crystal has three different oxygen positions, designated as O(1), O(2) and O(3), and two gallium positions, Ga(1) and Ga(2). Nodes O(1) and O(3) have the smallest coordination number 3, which leads to weak interplanar connections in planes (100) and (001) [22,23]. Due to the peculiarities of the crystal lattice, gallium oxide is an anisotropic material. It has been experimentally shown that a number of characteristics

Publisher: Peter the Great St. Petersburg Polytechnic University

(for example, thermal conductivity or electron mobility) have better values along the [010] direction [22–24]. However, mechanical processing is difficult due to fragility and mechanical defects of the material in the plane (010). As a result, other processing methods for β-Ga_2O_3 are being studied, including laser scribing [25–28]. Yoo J.H. et al. [29] studied the optical resistance of bulk gallium oxide, but these samples were doped with Sn, which makes its own adjustments to the optical resistance when compared with undoped samples. The paper presents the results of determining the optical resistance of β-Ga_2O_3 surface under the action of femtosecond laser pulses of the near-IR spectrum depending on the number of pulses and their repetition frequency from 10 to 201 kHz.

Materials and Methods

The sample of bulk crystal for studying the optical resistance of β-Ga_2O_3 was grown by Czochralski method using the NIKA-3 growth unit. The crystal growing process is described in detail in the paper [30]. The sample was prepared by method of chipping the bulk β-Ga_2O_3 crystal along the cleavage plane (100). The ablation of the material was performed on an experimental setup equipped with an ANTAUS-20W Yb-fiber femtosecond laser (Avesta) and a 3D coordinate moving system based on DDSM50 and MTS50M-Z8 translators (Thorlabs). For investigation the laser beam with Gaussian intensity profile, factor $M^2 < 1.1$, maximum average optical power $P_{max} = 17.5$ W at the pulse repetition frequency of 1 MHz, pulse duration of 224 fs, output beam diameter of 2.0 mm, and quasi-monochromatic wavelength 1030 nm, which transparent to β-Ga_2O_3, was used [1]. In the experiment, the laser beam was focused using a 40X, NA 0.60 objective lens into a spot with a diameter of 9.6 µm on the surface of the sample, while the latter was rigidly fixed on the coordinate table. Ablated areas were formed at the optical power in the range from 0.06 to 0.19 P_{max}, fixed exposure time of 0.1 s and different repetition pulse frequency: $201 \cdot 10^3$, $2 \cdot 10^3$, 200 and 10 Hz, respectively. As a result, the pulses number and time between its were variated as follows: 20,000 pulses every 5 µs, 200 pulses every 0.5 ms, 20 pulses every 5 ms and single pulse. Gentec Solo PE-2 M (Lake Oswego) optical power meters equipped with UP19K-110F-H9 pyroelectric power detector (Lake Oswego) used for registration of incident laser power. The uncertainty of the power meter calibration was $dP = \pm 2.5$ %.

Results and Discussion

To determine the optical resistance of the β-Ga_2O_3 sample, a series of experiments with ablated areas formation by different number pulses with a laser beam power in the range from 1.05 to 3.33 W. Figure 1 shows an optical microscope image of the sample after laser ablation. By analyzing the images obtained using a scanning electron microscope (Fig. 2), the diameters of the ablation crater were measured depending on the frequency and power of laser ablation.

It's observed from Table 1 that the value of the diameters of crater has a stepwise increase depending on a laser power. Thus, laser ablation can be quantitatively characterized by the crater diameter, which is necessary for calculating the optical resistance of the β-Ga_2O_3.

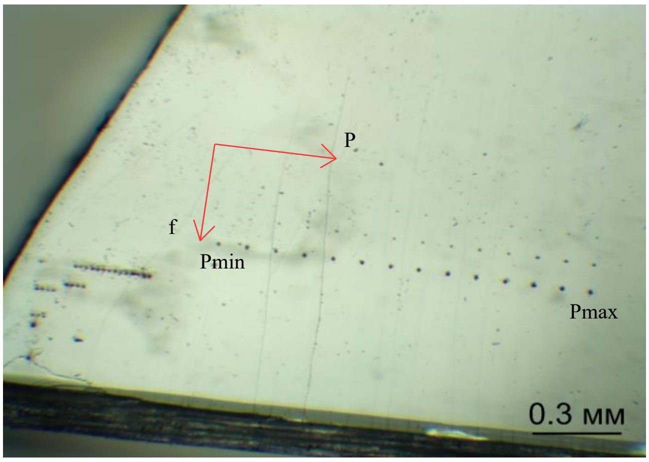

Fig. 1. An optical microscope image of β-Ga_2O_3 after laser ablation on a scale of 0.3 mm, with arrows indicating an increase in repetition rate (*f*) and optical power of laser beam (*P*)

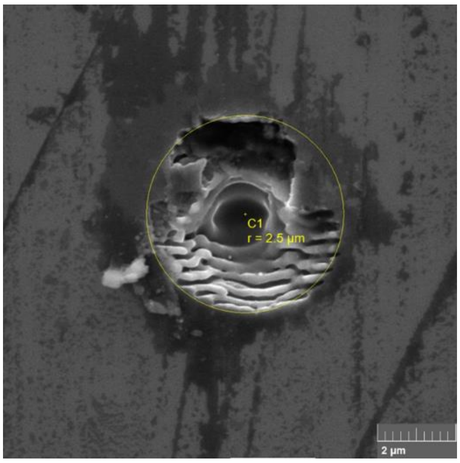

Fig. 2. An example of measuring the diameter of an ablation crater using a scanning electron microscope

Table 1. Diameter of ablated areas of sample surface in microns with error $\delta D = \pm 0.1$ um

Number of pulses	Average optical power *P*, W													
	1.05	**1.22**	**1.40**	**1.57**	**1.75**	**1.92**	**2.10**	**2.27**	**2.45**	**2.62**	**2.80**	**2.97**	**3.15**	**3.32**
20,000	5.4	5.5	5.5	5.5	5.7	5.7	6.5	8.1	8.2	8.3	8.3	8.5	8.5	9.3
200	2.5	4.2	5.0	5.3	5.5	5.5	5.7	5.9	6.0	7.5	7.6	7.7	8.0	8.1
20	2.0	2.4	2.4	2.4	4.0	4.5	4.9	5.0	5.0	5.1	5.2	5.0	5.9	6.0
1	1.5	1.5	1.6	1.7	1.8	1.6	1.5	3.5	4.2	4.3	4.5	4.5	4.5	4.4

Calculation of the optical resistance

The optical resistance of the β-Ga_2O_3 surface was determined by measuring the diameter of the craters *D* formed as a result of laser ablation at different pulse energies *E* using the Lui method [31]. Depending on the diameter of the wells squared from the energy of the impulses at which they were formed, a linear regression was given by the expression:

$$D^2(E) = 2\omega_0^2 \ln(E/E_{th}), \tag{1}$$

where ω_0 is the radius of the laser spot determined by the intensity drop on e^{-2}, which formed the crater. The energy in the pulse was calculated from the average power of incident radiation *P*, measured at the pulse repetition frequency $f = 20$ kHz, as:

$$E = P/f. \tag{2}$$

According to Eq. (1), the graphical dependence $D^2(E/E_{th})$ was plotted on a logarithmic scale along the abscissa axis. In this case, the point of intersection of the linear regression with the abscissa axis determined the pulse energy E_{th}, at which the formation of the well began, and the slope of the line corresponded to the radius of the laser spot:

$$\omega_0 = [-b/(2E_{th})\cdot N_{ph}]^{0.5}, \tag{3}$$

where N_{ph} is the value of multiphoton absorption, *b* is the linear regression constant written as a function $y = kx + b$. This function was plotted based on experimental data by least squares approximation (Fig. 3). For all points, the exposure duration was 0.1 seconds. 20,000 pulses corresponded to a frequency of 201 kHz, 200 pulses corresponded to 2.01 kHz, 20 pulses corresponded to a frequency of 201 Hz and 1 pulse at 10 Hz.

The value of N_{ph} was determined as the ratio of the energy of the bandgap of the material E_g to the photon energy E_{ph} and characterized the cross-section of multiphoton absorption, i.e. the region of the Gaussian laser beam where the energy density provided N_{ph}-photon absorption of incident radiation. In our case, at E_g = 4 eV and E_{ph} = 1.2 eV (the energy of a photon with a wavelength of 1030 nm), the value of N_{ph} = 4.

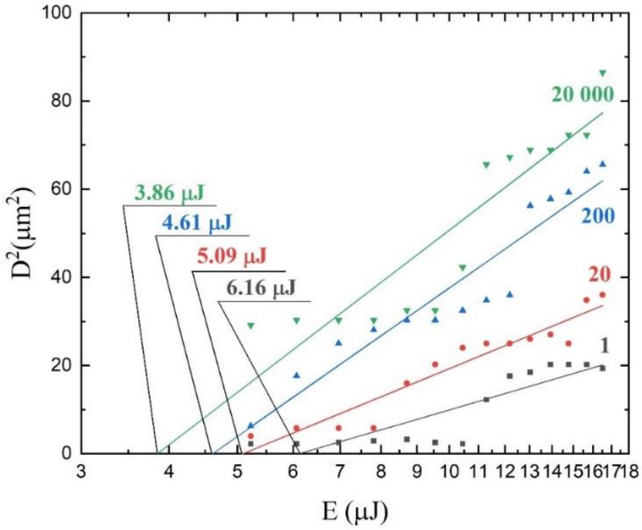

Fig. 3. Dependence of the square of the sublimation diameter on the pulse energy of the different pulses in the irradiated region: 1, 20, 200 and 20,000 pulses

Optical resistance of the sample was characterized by the energy density at which surface ablation began, and was expressed as follows:

$$F_{th} = E_{th}/(\pi\omega_0^2). \tag{3}$$

The constants of the linear regression, as well as the values of the laser spot radius and threshold energy density of the material are shown in Table 2. From the data provided, it can be seen that the threshold energy of E_{th} was maximum when exposed to a single pulse, equal to 6.16 µJ and decreased almost twice – to 3.86 µJ – with an increase in the number of pulses to 20,000. The radius of the laser spot did not depend on the number of pulses and was supposed to be 7.7 µm for all irradiation modes. An increase in the radius of the laser beam according to the computational data under the influence of 200 and 20,000 pulses indicated that the size of the ablative crater became larger than the laser spot due to spalling ablation. In this case, part of the material outside the irradiated zone was broken off and removed, thereby increasing the diameter of the ablation zone from 15.4 to 24.4 µm.

Table 2. Linear regression constants, threshold pulse energy, beam radius, threshold energy and power densities for optical resistance

Number of pulses/ repetition rate	***b***	***k***	**E_{th}, µJ**	**ω_0, µm**	**F_{th}, J/cm²**	**W_{th}, W/cm²**
1 / 10 Hz	-46.47 ± 5.96	65.76 ± 5.83	6.16	7.77	25.99 ± 4.21	$11.6 \cdot 10^9$
20 / 201 Hz	-36.81 ± 7.60	46.75 ± 7.43	5.09	7.61	21.48 ± 1.33	$9.6 \cdot 10^9$
200 / 2,01 kHz	-74.09 ± 10.64	111.68 ± 10.41	4.61	11.34	19.45 ± 3.35	$8.7 \cdot 10^9$
20,000 / 201 kHz	-71.54 ± 16.04	122.23 ± 15.69	3.86	12.18	16.29 ± 4.22	$7.3 \cdot 10^9$

The measurement error was estimated considering linear regression, the accuracy of measuring the diameter of the wells and the incident radiation power, for which an expression of the following form was used:

$$dF = F_{th}\sqrt{\left(\frac{dk}{k}\right)^2 + \left(\frac{db}{b}\right)^2 + \frac{1}{14}\sum_{i=1}^{14}\left(\frac{\delta D}{D_i}\right)^2 + \delta P^2}. \tag{4}$$

As a result, firstly, the average measurement error ranged from 16.4 % when exposed to 1 pulse to 26 % after exposure to 20,000 pulses. Measurement error can be reduced by recording not one, but several series of wells under the same laser exposure regimes. Secondly, the minimum error under the same other irradiation conditions was for the effect of a single pulse. Thirdly, ablation of the β-Ga_2O_3 surface under the influence of high-power near-infrared laser pulses occurred due to multiphoton absorption, which was random, unstable and contributed to a high measurement error. Reducing the wavelength to visible and near-UV radiation would also reduce measurement error.

From the above data of the threshold energy density F_{th}, it can be noted that its value decreased by 37 % with an increase in the number of pulses from 1 to 20,000 (Table 2). This result was typical for any materials in the transition from single-pulse to multi-pulse action. With each subsequent pulse, the fatigue of the material accumulated in the form of an increase in the concentration of local defects in the crystal lattice

Conclusions

Experiments on the effects of laser irradiation were carried out on samples of bulk crystals of gallium oxide grown using the Czochralski method and prepared by chipping along the cleavage plane. During the analysis of the laser ablation geometric parameters and calculations, the optical resistance of β-Ga_2O_3 was determined. The threshold energy density varied from 25.99 to 16.29 J/cm^2 with pulse numbers varying from 1 to 20,000 at a wavelength of 1030 nm and a pulse duration of 224 fs. The threshold power density of incident radiation ranged from 11.6 to 7.3 GW/cm^2.

CRediT authorship contribution statement

Dmitrii I. Panov: writing – review & editing, writing – original draft, conceptualization, data curation; **Nikita A. Balabanov**: writing – original draft, conceptualization, investigation; **Maxim M. Sergeev**: writing – review & editing, conceptualization, investigation; **Vladislav A. Spiridonov**: writing – review & editing, investigation ; **Dmitrii A. Bauman**: writing – review & editing; **Alexey E. Romanov**: writing – review & editing, supervision

Conflict of interest

The authors declare that they have no conflict of interest.

References

1. Spencer JA, Mock AL, Jacobs AG, Schubert M, Zhang Y, Tadjer MJ. A review of band structure and material properties of transparent conducting and semiconducting oxides: Ga_2O_3, Al_2O_3, In_2O_3, ZnO, SnO_2, CdO, NiO, CuO, and Sc_2O_3. *Applied Physics Reviews.* 2022;9(1): 011315.

2. Tsao JY, Chowdhury S, Hollis MA, Jena D, Johnson NM, Jones KA, Kaplar RJ, Rajan S, Van de Walle CG, Bellotti E, Chua CL, Collazo R, Coltrin ME, Cooper JA, Evans KR, Graham S, Grotjohn TA, Heller ER, Higashiwaki M, Islam MS, Juodawlkis PW, Khan MA, Koehler AD, Leach JH, Mishra UK, Nemanich RJ, Pilawa-Podgurski RCN, Shealy JB, Sitar Z, Tadjer MJ, Witulski AF, Wraback M, Simmons JA. Ultrawide-bandgap semiconductors: Research opportunities and challenges. *Advanced Electronic Materials.* 2018;4(1): 1600501.
3. Wong MH, Bierwagen O, Kaplar RJ, Umezawa H. Ultrawide-bandgap semiconductors: An overview. *Journal of Materials Research.* 2021;36: 4601–4615.
4. Woo K, Bian Z, Noshin M, Martinez RP, Malakoutian M, Shankar B, Chowdhury S. From wide to ultrawide bandgap semiconductors for high power and high frequency electronic devices. *Journal of Physics: Materials.* 2024;7(2): 022003.
5. Feng T, Zhou H, Cheng Z, Larkin LS, Neupane MR. A critical review of thermal boundary conductance across wide and ultrawide bandgap semiconductor interfaces. *ACS Applied Materials & Interfaces.* 2023;15(25): 29655–29673.
6. Dahiya S, Kaur D, Ghosh A, Kumar M. A strategic review on gallium oxide based power electronics: Recent progress and future prospects. *Materials Today Communications.* 2022;33: 104244.
7. Pearton SJ, Yang J, Cary PH, Ren F, Kim J, Tadjer MJ, Mastro MA. A review of Ga_2O_3 materials, processing, and devices. *Applied Physics Reviews.* 2018;5(1): 011301.
8. Petrenko AA, Kovach YaN, Bauman DA, Odnoblyudov MA, Bougrov VE, Romanov AE. Current state of Ga_2O_3-based electronic and optoelectronic devices. Brief review. *Reviews on Advanced Materials and Technologies.* 2021;3(2): 1–26.
9. Galazka Z. β-Ga_2O_3 for wide-bandgap electronics and optoelectronics. *Semiconductor Science and Technology.* 2018;33(11): 113001.
10. Singh R, Lenka TR, Panda DK, Velpula RT, Jain B, Bui HQT, Nguyen HPT. The dawn of Ga_2O_3 HEMTs for high power electronics—A review. *Materials Science in Semiconductor Processing.* 2020;119: 105216.
11. Wang X, Chang X, Wang P, Yang X, Yuan L. Research progress and prospect of the bulk single crystal growth of β-Ga_2O_3: From 1964 to 2024. *Crystal Research and Technology.* 2025;60(6): 2400255.
12. He Y, Zhao F, Huang B, Zhang T, Zhu H. A review of β-Ga_2O_3 power diodes. *Materials.* 2024;17(8): 1870.
13. Pearton SJ, Ren F, Polyakov AY, Haque A, Labed M, Rim YS. Status of Ga_2O_3 for power device and UV photodetector applications. *Applied Physics Reviews.* 2025;12(3): 031336.
14. He X, Wang M, Meng J, Hu J, Jiang Y. The effect of vacancy defects on the electronic properties of β-Ga_2O_3. *Computational Materials Science.* 2022;215: 111777.
15. Galazka Z. Growth of bulk β-Ga_2O_3 single crystals by the Czochralski method. *Journal of Applied Physics.* 2022;131(3): 031103.
16. Bauman DA, Panov DYu, Spiridonov VA, Kremleva AV, Asach AV, Tambulatova EV, Sakharov AV, Romanov AE. High quality β-Ga_2O_3 bulk crystals, grown by edge-defined film-fed growth method: Growth features, structural and thermal properties. *Journal of Vacuum Science & Technology A.* 2023;41(5): 053203.
17. Yao Y, Hirano K, Sugawara Y, Sasaki K, Kuramata A, Ishikawa Y. Observation of dislocations in thick β-Ga_2O_3 single-crystal substrates using Borrmann effect synchrotron X-ray topography. *APL Materials.* 2022;10(5): 051101.
18. Labed M, Sengouga N, Prasad CV, Henini M, Rim YS. On the nature of majority and minority traps in β-Ga_2O_3: A review. *Materials Today Physics.* 2023;36: 101155.
19. Spiridonov VA, Panov DI, Ivanov AY, Bauman DA, Romanov AE. The effect of high-temperature annealing on the properties of bulk β-Ga_2O_3 obtained in different growth atmospheres. *Materials Physics and Mechanics.* 2024;52(3): 80–85.
20. Kaminskii VV, Panov DYu, Spiridonov VA, Bauman DA, Kalganov DA, Scheglov MP, Romanov AE. Effect of high-temperature annealing on the internal friction and optical transmittance of single crystal gallium oxide. *Materials Physics and Mechanics.* 2024;52(5): 48–54.
21. Geller S. Crystal structure of β-Ga_2O_3. *The Journal of Chemical Physics.* 1960;33(3): 676–684.
22. Galeckas A, Cernescu A, Kaźmierczak-Bałata A, García-Fernández J, Bazioti C, Azarov A, Park JH, Jeon DW, Lee H, Lee WJ, Zhu R, Mei Z, Prytz O, Kuznetsov A. Optical library of Ga_2O_3 polymorphs. *arXiv.* Preprint posted online December 18, 2024;2412: 13987.
23. Víllora EG, Shimamura K, Yoshikawa Y, Aoki K, Ichinose N. Large-size β-Ga_2O_3 single crystals and wafers. *Journal of Crystal Growth.* 2004;270(3–4): 420–426.
24. Higashiwaki M. β-Ga_2O_3 material properties, growth technologies, and devices: a review. *AAPPS Bulletin.* 2022;32: 3.
25. Zhang K, Xu Z, Wang H, Zhang S, Dong B. Patterning the surface structure of transparent hard-brittle material β-Ga_2O_3 by ultrashort pulse laser. *Ceramics International.* 2022;48(19A):27650–27657.

26. Ahn M, Sarracino A, Ansari A, Torralva B, Yalisove S, Phillips J. Unique material modifications of Ga_2O_3 enabled by ultrafast laser irradiation. *Proceedings Volume 11281, Oxide-based Materials and Devices XI.* 2020;11281: 112810O.
27. Zhang K, Xu Z, Dong B, Zhang S. Process exploration of β-Ga_2O_3 blind hole processing by water-assisted femtosecond laser technology. *Journal of Alloys and Compounds.* 2023;939: 168769.
28. Panov DI, Spiridonov VA, Vasilev OS, Bogdanov PA, Bauman DA, Romanov AE. Laser processing of gallium oxide crystals in the preparation of samples for microelectronics. *Reviews on Advanced Materials and Technologies.* 2025;7(3): 198–202.
29. Yoo J, Rafique S, Lange A, Zhao H, Elhadj S. Lifetime laser damage performance of β-Ga_2O_3 for high power applications. *APL Materials.* 2018;6(3): 036105.
30. Zakgeim DA, Panov DI, Spiridonov VA, Kremleva AV, Smirnov AM, Bauman DA, Romanov AE, Odnoblyudov MA, Bougrov VE. Volume gallium oxide crystals grown from melt by the Czochralski method in an oxygen-containing atmosphere. *Technical Physics Letters.* 2020;46: 1144–1146.
31. Garcia-Lechuga M, Grojo D. Simple and robust method for determination of laser fluence thresholds for material modifications: An extension of Liu's approach to imperfect beams. *Open Research Europe.* 2021;1: 7.

MATERIALS PHYSICS AND MECHANICS RESEARCH ARTICLE

Submitted: July 14, 2025 **Revised: October 29, 2025** **Accepted: December 19, 2025**

Comprehensive study on PbO–MO (M=Mg, Zn, Cd)–As_2O_3:Tm_2O_3 glasses physical and optical properties

P.R. Rao [1], **P. Naresh** [2], **N.N. Rao** [1]✉, **BJ.R.S.N. Swamy** [1], **A.C. Babu** [3], **N.Ch.R. Babu** [4]

[1] Krishna University Dr. MRAR College of PG Studies, Nuzvid, India

[2] Velagapudi Ramakrishna Siddhartha School of Engineering, Siddhartha Academy of Higher Education (SAHE) Deemed to be University, Vijayawada, India

[3] Sir C. R. Reddy College of Engineering, Eluru, India

[4] Rajiv Gandhi University of Knowledge Technologies (AP-IIIT), Nuzvid, India

✉ nnrphy@gmail.com

ABSTRACT
Three modifier oxides, MgO, ZnO, and CdO, were mixed with 1.0 mol % of Thulium-doped lead arsenate glasses and were synthesized by the usage of melt-quenching technique. XRD patterns clearly show the evidence that samples are amorphous and had been supported with the aid of using the lack of distinct peaks. Various functional physical parameters such as molar volume, oxygen packing density (OPD), Tm^{3+} ion concentration, mean Tm^{3+} ion separation, polaron radius are evaluated by using experimentally measured densities and refractive indices. The optical absorption spectra of PbO–MO (M = Mg, Zn, Cd)–As_2O_3:Tm_2O_3 glass system have been studied. Through the application of least square fitting analysis, the J-O phenomenological parameters (Ω_2, Ω_4, Ω_6) for the three glass systems have been calculated.

KEYWORDS
optical absorption • XRD • As_2O_3 glasses • JO parameters • rare earth doped glasses

Citation: Rao PR, Naresh P, Rao NN, Swamy BJRSN, Babu AC, Babu NChR. Comprehensive study on PbO–MO (M=Mg, Zn, Cd)–As_2O_3:Tm_2O_3 glasses physical and optical properties. *Materials Physics and Mechanics.* 2026;54(1): 24–33. http://dx.doi.org/10.18149/MPM.5412026_4

Introduction

In the glass system, rare-earth ions have been thoroughly studied with respect to both their physical and chemical characteristics inside the network of glasses, which establishes the glass structure, it also incorporates optical characteristics [1,2]. Because of its exceptional prospective applications, the developments of glasses which are doped with rare-earth ions are precisely on course because of their use, including optical, semiconductors, sensors, lasers, etc. [3,4].The composition, structure and qualities of the final glass materials are directly influenced by the production technology and chemical and mineralogical makeup of the raw materials [5].

However, lead arsenic glasses are highly toxic, volatile easily at high temperature and chemical instable in moisture due to their devitrification, surface leaching along with hydrolytic attack. From the literature study [6–8], it strongly evidence that, the incorporation of suitable network modifiers/intermediate modifier like CuO, WO_3, Fe_2O_3, etc., there is change to reduce the number of non-bridging oxygens (NBOs) by forming more stable M–O–As (M = metal) linkages significantly improved the chemical durability, reducing moisture induced surface leaching and enhances long-term stability. Furthermore, the

Publisher: Peter the Great St. Petersburg Polytechnic University

presence of these oxides minimizes structural defects, enhances homogeneity, which leads the tuning of physical parameters such as density, refractive index and optical band gap. Tuning effect of the modifiers for getting stable and modified $PbO-As_2O_3$ glasses not only governed by the chemical composition nature but also their relative proportion in the glass matrix. Thus, the strategic addition of MgO/ZnO/CdO effectively mitigates the weaknesses of $PbO-As_2O_3$ glasses and enables the development of compositionally stable materials for advanced optical and photonic applications and also it nevertheless to mention that no literature available with systematic replacement of divalent modifier in the $PbO-As_2O_3$ glass host.

The RE^{3+} (Ln^{3+}) ions doped glasses are highly renowned because of their high efficient optical property and good transparency in near and mid IR region [9]. Thulium (Tm^{3+}) is recognized as one of the most potent active ions [10]. Recently, considerable attention has been given to analyzing the spectra of Tm^{3+} ions in various glass hosts, since this ion exhibits emission in the infrared region (~ 2 μm), making the glasses suitable for eye-safe LIDAR [11], gas sensors, pollution monitoring in atmosphere, biomolecule sensors, laser guided military applications etc., [12,13]. Because of the possibility of up – conversion from infrared to visible light, these ions are well-known [14–16].

Among Oxide glasses, $PbO-As_2O_3$ glasses exhibit high density and good optical transparency, which are essential for optimum efficiency for optical pumping. Metal oxides have been shown to improve the optical properties of glass, making them promising material for optical fiber amplifiers, non-linear optical systems, electronic optical switches etc. [17]. When lead arsenates glasses are modified with network altering metal ions, structural changes and local field fluctuations can be expected; these modifications may significantly influence the optical transitions of lanthanide ions and enhances the compositional stability. In this ongoing work, we report the physical, optical studies and their correlation in $PbO-MgO/ZnO/CdO-As_2O_3$ glasses doped with Tm^{3+} ions.

Materials and Methods

The present studied glass samples had been prepared by adopting the melting and quenching method. Within the area where glass is formed, the compositions selected for the current investigation is $20PbO-5MO$ (M = Mg, Zn, Cd)$-74As_2O_3$:$1.0Tm_2O_3$ all in mol % weighted by using Essce Vibra HT digital weighting balance with maximum capacity 100 gm and readability 0.1 mg. Figure 1 depicts a flow chart of the glass sample preparation process. The specific chemical composition and their codes used for present prepared samples were displayed in Table 1. All compositions were melted in platinum crucibles at 700 °C using muffle furnace. The melts were then rapidly quenched by pouring onto a preheated brass mould to avoid crystallization. The obtained glass samples were subsequently annealed at 250 °C for three hours at a cooling rate of 1 °C/min to relieve internal stresses and ensure structural stability. Figure 2 shows

Table 1. Composition of glass samples (all in mol %)

Sample Code	PbO	MO	As_2O_3	Tm_2O_3
GM	20	5.0 MgO	74	1.0
GZ	20	5.0 ZnO	74	1.0
GC	20	5.0 CdO	74	1.0

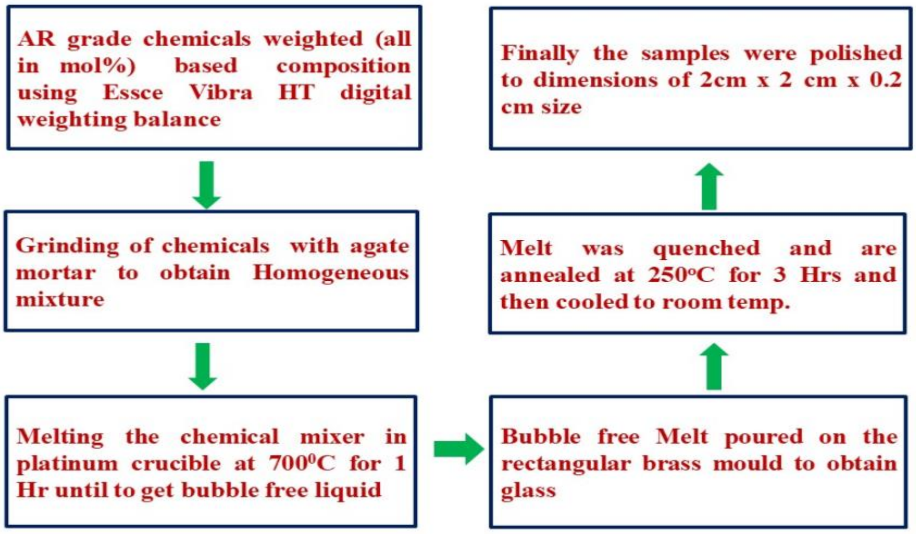

AR grade chemicals weighted (all in mol%) based composition using Essce Vibra HT digital weighting balance

Grinding of chemicals with agate mortar to obtain Homogeneous mixture

Melting the chemical mixer in platinum crucible at 700°C for 1 Hr until to get bubble free liquid

Bubble free Melt poured on the rectangular brass mould to obtain glass

Melt was quenched and are annealed at 250°C for 3 Hrs and then cooled to room temp.

Finally the samples were polished to dimensions of 2cm x 2 cm x 0.2 cm size

Fig. 1. Flow chart of various steps involved in PbO–MO (MgO/ZnO/CdO)–As_2O_3:Tm_2O_3 glass samples

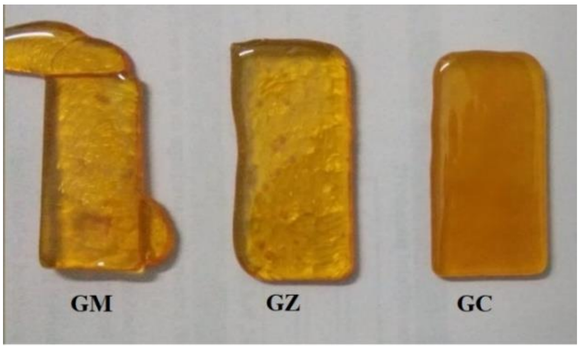

Fig.2. Photograph of prepared PbO–MO (MgO/ ZnO/CdO)–As_2O_3:Tm_2O_3 glass samples

the digital photographs of the prepared PbO–MO (M = Mg, Zn, Cd)–As_2O_3:Tm_2O_3 glasses, which clearly exhibits that the prepared samples are light yellow in colour with good transparency, and absence of visible surface defects, confirming the good quality of the synthesized glasses. Density determination was done by adopting Archimedes' principle by measuring the weights of the prepared samples in air as well in acetone by using Essce Vibra HT digital weighting balance. The refractive index of the samples was measured by using Abbe refractometer using Abbe refractometer (Model NAR-4T: Resolution ± 0.001 nD and accuracy ± 0.0002 nD) with mono bromo naphthalene as the contact layer between the glass and the refractometer prism. The amorphous nature of the prepared glasses was checked by X-ray diffraction spectra recorded on Rigaku D/Max ULTIMA III X-ray diffractometer with CuK_α (λ = 0.15406 nm) radiation. The optical absorption spectra of the glasses at ambient temperature were recorded using JASCO Model V-970 UV- vis-NIR spectrophotometer with spectral resolution of 0.1 nm.

Results and Discussion

The density of the samples was calculated using Archimedes' standard principle by measuring their weights in air (W_a) as well as in acetone (W_l) as a buoyant liquid. With the help of measured density, estimated average molecular weight of the individual samples, several important characteristic physical parameters, including molar volume, oxygen packing density (OPD), Tm^{3+} ion concentration, mean Tm^{3+} ion separation, polaron radius were calculated from standard relation and presented in Table 2 [18,19]. From the obtained and presented data from Table 2, it was noticed pragmatically among samples containing MgO, ZnO and CdO, that density is larger for GC, large for GZ and small for GM samples. In contrast molar volume shows as usual inverse behavior with densities of the glass samples. This was unexpected trend why because due to the replacement of the Mg^{2+} ions with higher molecular mass (ionic radius) ions like Zn^{2+} and Cd^{2+} we expect the reverse trend, which suggests that evidently takes place structural changes in the glass matrix. Among the present reported samples, OPD is smaller for GM, small for GZ and larger for GC. This increase in OPD suggests that the glass structure becomes compact hence leads to increase the density of the glass samples.

Table 2. Physical parameters of PbO–MO (M = Mg, Zn, Cd)–As_2O_3:Tm_2O_3 glasses

Property	Standard relation	Sample code		
		GM	**GZ**	**GC**
Average molecular weight ($\bar{M}$), g/mol	$\bar{M} = \sum X_i M_i$	197.52	199.17	201.05
Density (ρ), g/cm^3	$\rho = \left(\frac{W_a}{W_a - W_l}\right)\rho_b$	5.174	5.382	5.540
Molar volume (V_m), cm^3/mol	$V_m = \frac{\bar{M}}{\rho}$	38.176	37.006	36.290
Oxygen packing density (OPD), atoms/cm^3	$OPD = n\left(\frac{\rho}{\bar{M}}\right)1000$	63.13	65.12	66.41
Refractive index (n)	Experimental value	1.654	1.655	1.656
Molar refractivity (R_m), cm^3/mol	$R_m = \left(\frac{n^2-1}{n^2+2}\right)V_m$	13.99	13.58	13.33
Molar electronic polarizability (α_m), cm^3/mol	$\alpha_m = \frac{R_m}{2.52}$	5.552	5.389	5.291
Electronic polarizability (α_e), 10^{-25} cm^3	$\alpha_e = \frac{3(n^2-1)}{4\pi N_A(n^2+2)}$	1.454	1.455	1.457
Metallization criterion (M)	$M = 1 - \frac{R_m}{V_m}$	0.6335	0.6330	0.6326
Optical basicity (Λ)	$\Lambda = \sum x_i \Lambda_i$	1.037	1.044	1.050
Tm^{3+} ion concentration N_i, 10^{24} ions/cm^3	$N_i = \frac{N_A x_i \rho}{\bar{M}}$	1.577	1.627	1.659
Interionic distance (r_i), Å	$r_i = \left[\frac{1}{N_i}\right]^{\frac{1}{3}}$	8.590	8.502	8.447
Polaron radius r_p, Å	$r_p = \frac{1}{2}\left[\frac{\pi}{6N_i}\right]^{\frac{1}{3}}$	3.461	3.426	3.403
Field strength (F_i), 10^{15} cm^{-2}	$F_i = \frac{Z}{r_p^2}$	1.379	1.301	1.380

The refractive index (n) values were measured using monochromatic LED light of a wavelength 589.3 nm. The refractive index values for the studied samples were closely 1.65 to 1.66 following the trend $n_{GM} < n_{GZ} < n_{GC}$. Using standard relations along with the measured refractive indices, the physical parameters such as molar refractivity, molar electronic polarizability, metallization criteria and optical basicity were evaluated and the same were systematically presented in Table 2, where X_i is the mol % of the oxide compound,M_i is the molecular weight of the oxide compound, ρ_b is the density of acetone, N_A is the Avogadro number, Λ_i is the specific basicity moderating parameter of i^{th} oxide compound, Z is the thickness of the sample.

Figure 3 depicts the observed XRD patterns of the GM, GZ and GC samples. These patterns exhibit no sharp peak, confirming the amorphous nature of the prepared samples. Instead, two broad diffuse maxima are observed centered near $2\theta \approx 30°$ and ≈ 50°. In amorphous materials such as oxide glasses, these broad halos arise by diffuse scattering that originates from short range and medium range atomic correlations, rather than from long range periodicity. The high angle halo near ≈ 50° arises from short range order corresponding to the nearest neighbour cation oxygen bond distances ($d \approx 1.8$ Å) with in the basic structural units present in the glass formers such as SiO_4 tetrahedral, BO_3/BO_4 units, AsO_3 pyramids, Pb-O polyhedra and modifier oxygen linkages [20,21]. Whereas the low angle halo near ≈ 30° arises from medium range order especially in oxide glasses corresponding due to the long-range real spaces distances between inter polyhedral correlations like AsO_3 units PbO ($d \approx 3$ Å). In addition, the presence of MgO, ZnO, and CdO modifiers enhances such medium-range structural organization due to variations in bonding strength, cation size, and field strength, thereby making the ~ 30° halo more prominent.

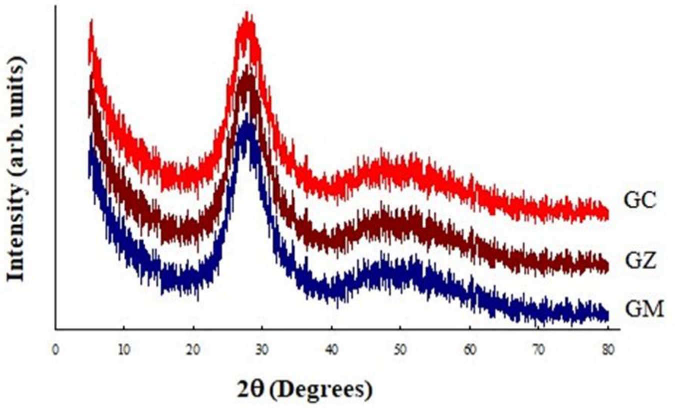

Fig. 3. X-ray diffraction pattern for PbO−MO (M=Mg, Zn,Cd) As_2O_3:Tm_2O_3 glasses

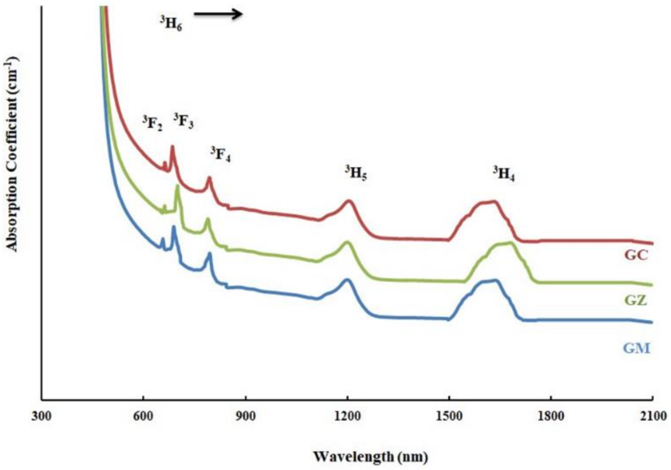

Fig.4. Optical absorption spectra of PbO−MO (M=Mg, Zn, Cd)−As_2O_3 glasses doped with Tm_2O_3

The optical absorption spectra of GM, GZ and GC glass samples within the wavelength range of 300–2100 nm were presented in Figure 4. Glass sample GM exhibits five distinct absorption peaks with peak positions at about 657, 689, 795, 1199, 1631 nm; among them, first one with less intensity appeared as a kink, whereas last one was a boarder. These identified peaks were attributed due to the transition Tm^{3+} ions from the ground state $^3H_6$ to the higher energy states $^3F_2$, $^3F_3$, $^3F_4$, $^3H_5$, $^3H_4$ respectively [22,23]. Among the three prepared samples, the other two samples also exhibit similar absorption bands with marginal blue shift in wavelengths, the corresponding energies of these transitions are presented in Table 3.

Table 3. The absorption band energies (cm^{-1}), the experimental (f_{exp}) and calculated (f_{cal}) oscillator strengths for the absorption transitions of PbO–MO (M = Mg, Zn, Cd)–As_2O_3:Tm_2O_3 glasses

Transitions	**GM**				**GZ**				**GC**			
	Energy ν, cm^{-1}	f_{exp}, 10^{-6}	f_{cal}, 10^{-6}	% diff	Energy ν, cm^{-1}	f_{exp}, 10^{-6}	f_{cal}, 10^{-6}	% diff	Energy ν, cm^{-1}	f_{exp}, 10^{-6}	f_{cal}, 10^{-6}	% diff
$^3H_6 \rightarrow {}^3F_2$	15231	2.08	2.1	0.96	15104	1.16	1.15	0.86	15092	2.89	2.35	18.68
$\rightarrow {}^3F_3$	14510	6.34	6.7	5.67	14280	5.71	6.30	10.33	14596	6.60	5.94	10.00
$\rightarrow {}^3F_4$	12584	3.92	4.08	4.08	12608	3.47	3.70	6.62	12610	3.48	3.60	3.49
$\rightarrow {}^3H_5$	8338	4.57	4.82	5.47	8314	4.51	4.63	2.66	8320	4.69	4.80	2.34
$\rightarrow {}^3H_4$	6130	3.50	3.61	3.14	5960	2.48	2.57	2.01	6131	3.72	3.68	1.08
Direct band gap, eV	2.49				2.52				2.55			
Indirect band gap, eV	2.59				2.61				2.62			
R.m.s. % deviation	4.23				5.70				9.67			

Judd-Ofelt (J–O) parameters are vital to enhancing the comprehension of optical characteristics, particularly concerning rare-earth ions such as thulium in glass matrices. They bid valuable insights into properties like, radiative transition probabilities, oscillator strengths, and branching ratios etc.

By applying J–O theory and measuring the area under the absorption curves, the experimental oscillator strengths were determined by the simplified relation [24]:

$$f_{exp} = 4.318\, X\, 10^{-9} \int \varepsilon(\vartheta)\, d\vartheta, \tag{1}$$

where $\int \varepsilon(\vartheta)\, d\vartheta$ is the area under the absorption curve, $\varepsilon(\vartheta)$ is the molar absorptivity of the respective band at ϑ:

$$\varepsilon(\vartheta) = \frac{A}{cl}, \tag{2}$$

where $\frac{A}{l}$ is the absorbance coefficient, c is the concentration of the lanthanide ion.

The calculated oscillator strengths for the electric dipole transition from the ground state (ψ) to the excited state (ψ') were obtained using the relation:

$$f_{cal} = \left(\frac{8\,\pi^2 mcv}{3h(2J+1)}\right)\left(\frac{(n^2+2)^2}{9n}\right)\sum\nolimits_{\lambda=2,4,6} \Omega_\lambda \left(\langle \psi_{J'} \rangle\right)^2, \tag{3}$$

where all the terms having their own standard meaning, which are mentioned in the literature [22,24], $\|U^\lambda\|$ are the square reduced matrix element of the unit tensor operator of the rank $\lambda = 2, 4, 6$, these standard values were acquired from [25]. The root mean square deviation values from the calculated and experimental oscillator strengths were obtained using the basic relation, which helps to understand the fitment of theoretical data with experimental data in the RE-doped glasses:

$$\mathrm{RMS}\ \% = 100\sum\frac{(f_{cal}-f_{exp})^2}{N}. \qquad (4)$$

The absorption band energies (cm^{-1}), the experimental (f_{exp}) and calculated (f_{cal}) oscillator strengths calculated for the absorption band intensities of PbO–MO (M = Mg, Zn, Cd)–As_2O_3:Tm_2O_3 glasses were presented as Table 3.

Using least squares fitting analysis, J–O parameters T_λ ($\lambda = 2,4,6$) were determined with help of values $\|U^\lambda\|^2$(taken form the literature ref), f_{exp}, f_{cal}, and ν by the relation [26]:

$$f_c = [T_2(\|U^2\|)^2 + T_4(\|U^4\|)^2 + T_6(\|U^6\|)^2]\vartheta. \qquad (5)$$

J–O Intensity parameters $\Omega_\lambda(\lambda = 2,4,6)$ are calculated from above obtained $T_\lambda(\lambda = 2,4,6)$ using the equation:

$$\Omega_\lambda = \left(\frac{3h}{8\pi^2 mc}\right)\left(\frac{9n}{(n^2+2)^2}\right)(2J+1)T_\lambda, \qquad (6)$$

where all symbols have their own significant meaning as mentioned in literature [25,26], J is taken as 13 for the ground state of Tm^{3+} ion. The obtained J–O intensity parameters $\Omega_\lambda(\lambda = 2,4,6)$ for Tm_2O_3 doped PbO–MO (M = Mg, Zn, Cd)–As_2O_3 glasses are displayed in Table 4. When the computed oscillator strengths are compared to the experimental oscillator strengths, a fair match is made. The root mean square percentage (RMS %) deviation between f_{exp} and f_{calc} is used to express the fit quality. The J–O theory's validity and suitability for the current glasses are confirmed by the comparatively low levels of these deviations [27]. In complex hosts like glass it is common that individual transition oscillator strengths differ by 10–30 % from calculated values; an RMS percentage deviation (RMS %) below ~ 20–30 % is usually considered acceptable as indicating a good correlation in rare-earth–doped glasses. For the present studied three samples, RMS % deviation is observed < 10 which represents the overall "goodness of fit" and validates whether the derived J–O parameters Ω_2, Ω_4, Ω_6 are reliable.

Table 4. J–O parameters (Ω_λ) and the bonding parameter (δ') of PbO–MO (M=Mg, Zn, Cd)–As_2O_3:Tm_2O_3 glasses and their comparison with the previous work of different glasses

Glass	**Ω_2, 10^{-20} cm^2**	**Ω_4, 10^{-20} cm^2**	**Ω_6, 10^{-20} cm^2**	**Ω_4/Ω_6**	**δ'**	**Ref.**
GM	8.35	0.863	0.336	2.56	-0.160	Present work
GZ	7.81	0.810	0.370	2.18	-0.948	Present work
GC	6.74	0.780	0.362	2.15	-1.050	Present work
PSBT	3.66	2.926	1.549	1.89	---	[22]
BBT	3.65	1.32	1.37	0.96	---	[23]
Glass B	4.15	0.80	0.40	2.00	---	[24]
Gallate	4.79	1.52	0.58	2.62	---	[28]
Germanate	4.10	0.99	0.26	3.80	---	
Aluminate	4.94	1.67	0.61	2.73	---	

Hence, the Ω_2 parameter acts like a strain for the asymmetry of the ligand field, reflecting the degree to which the local symmetry is distorted. For all the present three sets of glasses, the values of Ω_λ are projected primarily in the following sequence; $\Omega_2 > \Omega_4 > \Omega_6$ [28]. Further, it is identified that this phenomenological intensity parameter Ω_λ for $\lambda = 2, 4$ observed lower when Mg was replaced by the Zn and Cd, whereas for $\lambda = 6$, it is observed to rise with the replacement of Zn and Cd by the Mg in the glass matrices.

These results reflect among the three studied present glasses: GM has more covalent behavior than the other two. Afterward coming to the Ω_4, bids attention to the interaction of RE-ions with the atom that are away in the lattice i.e., tells about medium-range interactions that reflects the rigidity and bulk properties like density, mechanical strength and elasticity etc., Approaching to the third one, Ω_6 reveals the information about long-range interactions between the RE-ion and its environment, which plays an active role on optical and efficiency, non-radiative transitions, phonon interaction (Luminescence efficiency). Lower Ω_6 values claim less rigid, faster non- radiative relaxations due to interaction of RE-ions with lattice by producing lattice vibrations (phonons). Hence, by the obtained results, it may except that GM glass samples were rigid with lower non-radiative relaxations, same result was confirmed the higher Ω_4/Ω_6 value.

The bonding parameter (δ) which also helps to estimate the covalent character of the RE ions with the ligand bond has been calculated for each of the three glasses using the equation:

$$\delta = \frac{\Omega_2 - \Omega_2^{free-ion}}{\Omega_2^{free-ion}}. \tag{7}$$

The RE-ion Tm^{3+} in MgO mixed glass has the highest δ value, whereas CdO mixed glass exhibits the lowest δ value. The bonding parameter value might potentially be used as additional evidence for this claim. Hence, Optical data with the fitment of J–O theory imply that the Tm^{3+} environment in MgO glasses is a more covalent character with a rigid structure having higher luminescence efficiency than the other two glasses containing ZnO and CdO.

According to Davis and Mott's theory [29,30], the optical edge of non-crystallize materials can be expressed by the equation:

$$\alpha h\vartheta = A\left(h\vartheta - E_{opt}\right)^r, \tag{8}$$

where α is the absorption coefficient, A is the proportionality constant, $h\nu$ is photon energy, E_{opt} is the optical band gap energy, r = 2(allowed indirect), ½ (allowed direct) – transitions respectively. The direct and indirect optical band gaps were estimated by extrapolations of the $(\alpha h\vartheta)^r vs\ h\vartheta$ curves at $(\alpha h\vartheta)^r = 0$.

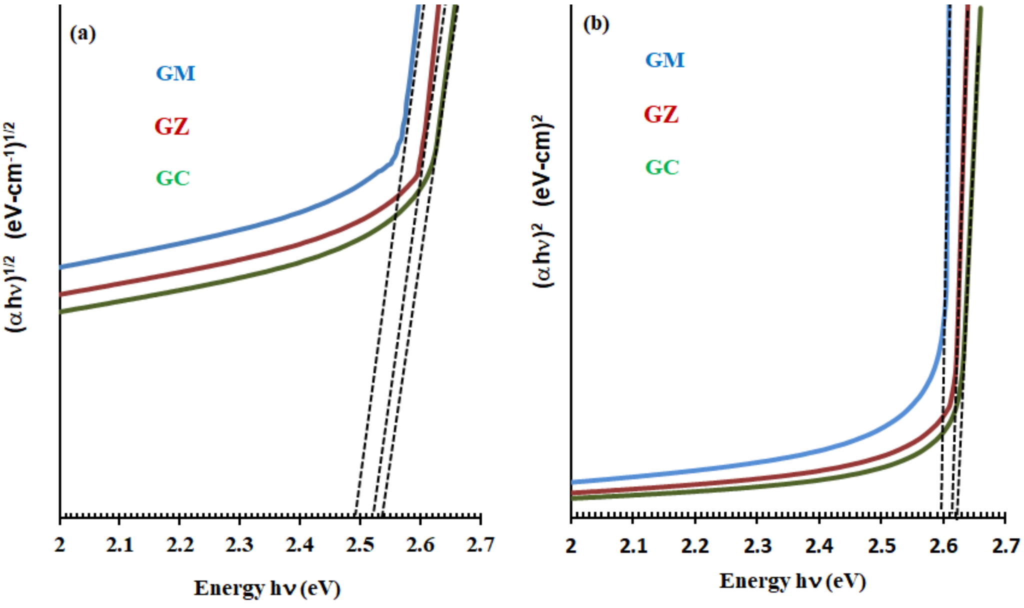

Fig. 5. Urbach plots of PbO–MO (M=Mg, Zn, Cd)–As_2O_3 glasses doped with Tm_2O_3: (a) direct; (b) indirect

Figure 5 shows $(\alpha h\vartheta)^r vs\, h\vartheta$ plots of PbO–MO–As_2O_3:Tm_2O_3 glasses. From the extrapolations, the GM glass exhibits optical direct and indirect band gaps of approximately 2.54 and 2.75 eV. Replacing ZnO or CdO with MgO produces a small but systematic increase (widening) of both direct and indirect band gaps (Table 4), reflecting reduced modified local structure from Mg^{2+} incorporation. In other way, ZnO and CdO introduce highly polarizable cations, which increase the electron donating ability of O^{2-} and cause to produce more NBOs. This increases optical basicity and raised the J–O parameter Ω_2 supports the same with causes the reduced covalency and local structural distortion around Tm^{3+} ions, leading to a more rigid matrix and higher energy optical transitions.

Conclusions

An assortment of glass systems with chemical substance 20 PbO–5 MO (M = Mg, Zn, Cd)–74 As_2O_3:1.0Tm_2O_3 was successfully prepared by conventional melt-quenching technique. The density and molar volume of the glass were found to change when MO was added to the glass system. The transitions below have been identified by glasses optical absorption spectrum $^3H_6 \rightarrow {}^3F_2$, $^3F_3$, $^3F_4$, $^3H_5$, $^3H_4$. The optical absorption spectra of these ions may be described using the J–O theory for each of the three glass systems. The J–O parameters for the three systems are calculated using least squares fitting analysis and the results indicate the following pattern: $\Omega_2 > \Omega_4 > \Omega_6$. The glasses that were combined with magnesium oxide had the highest bonding parameter δ, smaller optical band gaps all the above observations clearly indicate that the rare earth ions in this glass matrix have a larger covalent environment in glass containing MgO.

CRediT authorship contribution statement

Paritala R. Rao: investigation; **Padamati Naresh**: formal analysis, writing – original draft; **Narasimha N. Rao**: writing – review & editing; **Bhogi Jai Rama Satyanarayana N. Swamy**: conceptualization; **A. Chitti Babu**: validation & review; **N.Ch. Ramesh Babu**: investigation.

Conflict of interest

The authors declare that they have no conflict of interest.

References

1. Azman K, Azhan H, Syamsyir SYS, Mardhiah A, Nasuha MRS. Optical properties of Nd doped lead borotellurite glass. *Materials Science Forum.* 2016;846: 193–198.
2. Malge A, Sankarappa T, Sujatha T, Abdul Azeem P, Devidas GB, Kori S. Structural and DC conductivity studies of borotellurite glasses doped with ZnO, Li_2O and Dy_2O_3. *Materials Today: Proceedings.* 2020;26(2): 1960–1963.
3. Shirshnev PS, Snezhnaia ZG, Shirshneva-Vaschenko EV, Romanov AE, Bougrov VE. Relation of the optical properties of boron copper-containing glasses on the concentration of lithium. *Materials Physics and Mechanics.* 2018;40(1): 78–83.
4. Klinkov V, Archelkov VB, Semencha AV, Tsimerman EA, Sedegova TY, Rudskoy AI. Halide-containing zinc borosilicate glass as a matrix for $CsPbBr_3$ crystal. *Materials Physics and Mechanics.* 2023;51(2): 27–35.
5. Rodin AI, Ermakov AA, Erofeeva IV, Erofeev VT. Structure and properties of porous glass ceramics from siliceous rocks with the addition of $Mg(OH)_2$. *Materials Physics and Mechanics.* 2023;51(5): 127–141.

6. Kalyani B, Pujari N, Edukondalu A, Reddy MS, Vardhani CP. AC Conductivity and dielectric relaxation in $Li_2O-PbO-As_2O_3-B_2O_3$ glasses. *Chinese Journal of Physics.* 2022;79: 141–150.
7. Satyanarayana T, Nagarjuna G, Kiran KR. Spectral features of lead arsenate glasses doped with copper oxide. *Solid State Phenomena.* 2013;207: 55–67.
8. Srinivasarao G, Veeraiah N. The effect of tungsten ions on the structure of $PbO-As_2O_3$ glasses. *Physica Status Solidi A.* 2002;191(2): 370–386.
9. Jackson SD. Cross relaxation and energy transfer upconversion processes relevant to the functioning of 2 µm Tm^{3+}-doped silica fibre lasers. *Optics Communications.* 2004;230(1–3): 197–203.
10. Gebavi H, Milanese D, Liao G, Chen Q, Ferraris M, Ivanda M, Gamulin O, Taccheo S. Spectroscopic investigation and optical characterization of novel highly thulium doped tellurite glasses. *Journal of Non-Crystalline Solids.* 2009;355(9): 548–555.
11. Lakshminarayana G, Meza-Rocha AN, Soriano-Romeo O, Huerta EF, Caldiño U, Lira A, Lee D-E, Yoon J, Park T. Survey of optical and fluorescence traits of Tm^{3+}-doped alkali/mixed alkali oxides constituting $B_2O_3-BaO-ZnO-LiF$ glasses for 0.45 µm laser and 1.46 µm fiber amplifier. *Results in Physics.* 2021;26: 104343.
12. Peng B, Izumitani T. Optical properties, fluorescence mechanisms and energy transfer in Tm^{3+}, Ho^{3+} and $Tm^{3+}-Ho^{3+}$ doped near-infrared laser glasses sensitized by Yb^{3+}. *Optical Materials.* 1995;4(6): 797–810.
13. Song X, Han K, Zhou D, Xu P, Zhang P. Broadband ~1.8 µm emission characteristics of Tm^{3+}-doped bismuth germanate glass based on Ga_2O_3 modification. *Journal of Non-Crystalline Solids.* 2021;557: 120575.
14. Tanabe S, Hanada T. Effect of ligand field on branching ratio of ultraviolet and blue upconversions of Tm^{3+} ions in halide and oxide glasses. *Journal of Applied Physics.* 1994;76(6): 3730–3734.
15. Hirao K, Tamai K, Tanabe S, Soga N. Frequency upconversion and its new mechanism in Tm^{3+}-doped fluoroaluminate glasses. *Journal of Non-Crystalline Solids.* 1993;160(3): 261–267.
16. Otto AP, Brewer KS, Silversmith AJ. Red to blue upconversion in Tm-doped sol–gel silicate glasses. *Journal of Non-Crystalline Solids.* 2000;265(1–2): 176–180.
17. Muhammad Noorazlan A, Mohamed Kamari H, Zulkefly SS, Mohamad DW. Effect of erbium nanoparticles on optical properties of zinc borotellurite glass system. *Journal of Nanomaterials.* 2013;2013(1): 940917.
18. Rao NN, Naresh P, Rao PR, Swamy BJRSN, Babu AC. Influence of modifier oxide on spectroscopic features of $ZnO-CaF_2-CuO-B_2O_3:R_2O$ glasses (R = Li, Na & K). *AIP Conference Proceedings.* 2023;2368(1): 020005.
19. Biradar S, Dinkar A, Manjunatha, Bennal AS, Devidas GB, Hareesh BT, Siri MK, Nandan KN, Sayyed MI, Es-soufi H, Chandrashekara MN. Comprehensive investigation of borate-based glasses doped with BaO: An assessment of physical, structural, thermal, optical, and radiation shielding properties. *Optical Materials.* 2024;150: 115176.
20. Li J, Sun Y, Li Z, Zhang Z. Short-range and medium-range structural order in $CaO-SiO_2-TiO_2-B_2O_3$ glasses. *ISIJ International.* 2016;56(5): 752–758.
21. N'Dri K, Houphouet-Boigny D, Jumas J-C. Study of first sharp diffraction peak in As_2O_3 glasses by X-ray powder diffraction method. *Journal of Non-Oxide Glasses.* 2012;4(3): 29–37.
22. Satyanarayana T, Kityk IV, Brik MG, Ravi Kumar V, Veeraiah N. Fluorescence features of Tm^{3+} ions in $PbO-Sb_2O_3-B_2O_3$ glass ceramics. *Physica B: Condensed Matter.* 2010;405(7): 1872–1880.
23. Xu Z, Chen Y, Lin Y, Gong X, Luo Z, Huang Y. Effect of concentration on the spectral properties of Tm^{3+} ions in bismuth borate glasses. *Journal of Alloys and Compounds.* 2009;481(1–2): 411–416.
24. Ratnakaram YC, Thirupathi Naidu D, Vijaya Kumar A, Rao JL. Characterization of Tm^{3+} doped mixed alkali borate glasses—spectroscopic investigations. *Journal of Physics and Chemistry of Solids.* 2003;64(12): 2487–2495.
25. Carnall W, Crosswhite H, Crosswhite HM. *Energy level structure and transition probabilities in the spectra of the trivalent lanthanides in LaF_3.* Argonne (IL): Argonne National Laboratory; 1978.
26. Lakshman SVJ, Ratnakaram YC. Spectral studies of praseodymium(III) and thulium(III) in certain sulphate glasses. *Journal of the Less Common Metals.* 1986;126: 227–232.
27. Zhang Y, Liu J-M, Liu M-H, Zhang Z-B, Wong W-H, Zhang D-L. Error evaluation of Judd–Ofelt spectroscopic analysis. *Spectrochimica Acta Part A: Molecular and Biomolecular Spectroscopy.* 2020;239: 118536.
28. Zou X, Izumitani T. Fluorescence mechanisms and dynamics of Tm^{3+} singly doped and Yb^{3+}, Tm^{3+} doubly doped glasses. *Journal of Non-Crystalline Solids.* 1993;162(1–2): 58–67.
29. Davis EA, Mott NF. Conduction in non-crystalline systems V. Conductivity, optical absorption and photoconductivity in amorphous semiconductors. *Philosophical Magazine.* 1970;22(179): 903–922.
30. Tauc J. (Ed.) *Amorphous and liquid semiconductors.* Berlin: Springer; 2012.

MATERIALS PHYSICS AND MECHANICS RESEARCH ARTICLE

Submitted: October 29, 2025 **Revised: November 14, 2025** **Accepted: December 1, 2025**

Emission of lattice dislocations from triple junctions of grain boundaries with liquid-like inclusions near pores in high-temperature ceramics

M.Yu. Gutkin, N.V. Skiba ✉

Institute for Problems of Mechanical Engineering RAS, St. Petersburg, Russia

✉ nikolay.skiba@gmail.com

ABSTRACT

Theoretical model is suggested which describes the micromechanism of lattice dislocations emission from triple junctions of amorphous intercrystalline layers with pores and liquid-like inclusions in high-temperature ceramics. Within the model, the plastic deformation in ceramics under elevated temperatures is realized through the emission of lattice dislocations from triple junctions of grain boundaries and the subsequent glide of the emitted dislocations in the grain interior. In the exemplary case of high-temperature α-Al_2O_3 ceramics, a comparative analysis of the critical stresses for the emission of the lattice dislocations, and for their glide along the prismatic and basal slip planes in the grain interior depending on the deformation temperature was carried out in a wide temperature range from 300 to 1500 K. It is shown that the critical stress for the emission of the lattice dislocations decreases with both an increase in the length of the liquid-like inclusion and the deformation temperature, and increases with increasing the pore size.

KEYWORDS

high-temperature ceramics • pores • lattice dislocations • amorphous intercrystalline layers • deformation temperature liquid-liked inclusions

Funding. *This work has been supported by the grant of the Russian Science Foundation, RSF 23-19-00236.*

Citation: Gutkin MYu, Skiba NV. Emission of lattice dislocations from triple junctions of grain boundaries with liquid-like inclusions near pores in high-temperature ceramics. *Materials Physics and Mechanics.* 2026;54(1): 34–41.

http://dx.doi.org/10.18149/MPM.5412026_5

Introduction

High-temperature ceramics (e.g., Al_2O_3, SiC, Si_3N_4, ZrO_2) often contain amorphous intercrystalline layers (AILs) and pores that influence their mechanical properties [1–10]. The liquid-like inclusions (LLIs) are nanoscale regions where the material locally behaves in a viscous or fluid-like manner due to the stress and the temperature conditions, facilitating the plastic flow in an otherwise brittle ceramic matrix [11–13]. The pores act as stress concentrators and nucleation sites for these inclusions [14,15].

The LLIs are usually small in size (of the order of tens of nanometers) that very complicates their experimental observations [6–9]. Thus, computer modeling [16–18] and analytical models [19–23] play a significant role in this field. The results of computer modeling [17,18] have stimulated the development of theoretical works [19–23] on the study of the generation and evolution of the LLIs in ceramic materials with AILs. Within these models, the plastic deformation occurs due to the generation and the propagation of the LLIs along the grain boundaries containing pores [23] and AILs [19]. In the case when the further development of LLIs along AILs is suppressed by their triple junctions, the LLIs

Publisher: Peter the Great St. Petersburg Polytechnic University

can act as effective stress concentrators inducing the implementation of other mechanisms of stress relaxation such as the nucleation of nanocracks on the LLIs [20], the LLIs overcoming the AIL triple junctions and penetrating into a neighboring AIL [21], and the subsequent emission of lattice dislocations from the AIL triple junctions with the LLIs [22].

Recent studies have revealed the formation of LLIs near pores in the high-temperature ceramics with AILs, which significantly affect the strength, the ductility, the creep resistance, the fracture toughness, etc. [4–6] of these ceramics. So, the development of the theoretical models describing the deformation mechanisms capable to improve the mechanical properties of the high-temperature ceramic materials with pores can significantly affect the range of their practical applications.

The main aim of this work is to develop a theoretical model of a micromechanism for the enhancement of plastic deformation through the emission of lattice dislocations (LDs) from the AIL triple junctions containing LLIs near pores in high-temperature ceramics at elevated temperatures.

Model

Consider a cylindrical pore of radius R_0 placed in an equilibrium triple junction of AILs containing an LLI of length L in a ceramic sample (Fig. 1). It is assumed that the LLI occupies the entire grain boundary reaching the opposite triple junction of AILs where its further propagation is suppressed. Within the model, this LLI as a source of mechanical stresses is modeled by a dipole of edge superdislocations with the Burgers vectors $\pm\mathbf{B}$ ($\pm B$-superdislocation dipole) and the arm $R_0 + L$ (Fig. 1).

Let us consider the process of the generation of a lattice dislocation (LD) with the Burgers vector $\mathbf{b}$ (b-LD) from the AIL triple junction under the external shear stress τ (Fig. 1) with taking into account the effect of the pore on the variation in the shear stress τ. In this case, the dipole of the $\pm B$-superdislocations acts as a stress concentrator facilitating the nucleation of the LD. This process becomes energetically favorable at $\tau \geq \tau_{c1}$, where τ_{c1} is some critical value of the external shear stress τ . However, the Peierls barrier

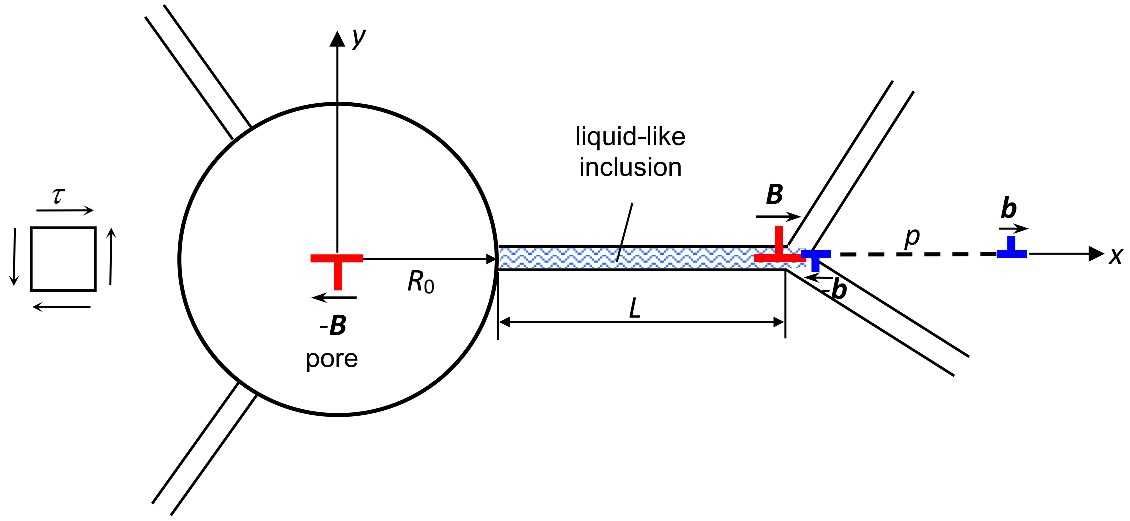

Fig. 1. Model of the LD emission from the AIL triple junction in the vicinity of a pore of radius R_0 and an LLI of length L under the external shear stress τ

hinders the movement of the emitted LD within the grain interior. Thus, the LD slip along one of the slip planes becomes possible at $\tau \geq \tau_{c2}$, where the τ_{c2} is a critical stress at which the LD can overcome the Peierls barrier.

According to the theory of defects in solids, the emission of the *b*-LD by the distance *p* from the AIL triple junction can be described as the appearance of an LD dipole with the Burgers vectors ±**b** (±*b*-LD dipole) and the arm *p* (Fig. 1). Previously, Glezer and Pozdnyakov [24] have developed a similar model although with no pore at the triple junction of grain boundaries. Thus, the LD emission can serve as an alternative mechanism of the plastic deformation enhancement in the high-temperature ceramics with LLIs in the vicinity of the pores.

Results

Consider the energy characteristics of the LD emission. The LD emission process is specified by the energy difference $\Delta W = W_2 - W_1$, where W_1 and W_2 are the total energies of the defect system before and after the LD emission (Fig. 1). The condition $\Delta W < 0$ determines the possibility of the generation of the ±*b*-LD dipole at the AIL triple junction. The energy difference ΔW is determined by the expression:

$$\mathit{\Delta} W = E_{self} + E_c + E\tau_{int}, \tag{1}$$

where E_{self} is the self-strain energy of the ±*b*-LD; $E_c \approx Gb2/[4\pi(1-\nu)]$ is the core energy of the emitted LD; *G* and *ν* are the shear modulus and the Poisson ratio, respectively; E_{int} is the energy of the elastic interaction between the ±*b*-LD dipole with the ±*B*-superdislocations, and E_τ is the effective work of the external shear stress τ spent to transfer the emitted LD over the distance *p*.

In accordance to the general approach [25], the self-strain energy E_{self} can be determined via the shear stress components of the ±*b*-LD dipole as follows:

$$E_{self} = \frac{b}{2}\int_{R_0+L+r_c}^{R_0+L+p-r_c} (\sigma_{xy}^{-b} + \sigma_{xy}^{b})dx, \tag{2}$$

where σ_{xy}^{-b} and σ_{xy}^{b} are the shear stresses of the −*b*-LD and *b*-LD located at a distance $d_1 = R_0 + L$ and $d_2 = R_0 + L + p$ from the pore center, respectively (Fig. 1).

With help of the Airy stress functions, Eq. (2) can be rewritten as follows:

$$E_{self} = \frac{b}{2}\left[\frac{\partial \mathit{\Phi}_1}{\partial y} + \frac{\partial \mathit{\Phi}_2}{\partial y}\right]_{x=R_0+L+r_c, y=0}^{x=R_0+L+p-r_c, y=0}, \tag{3}$$

where $\mathit{\Phi}_1$ and $\mathit{\Phi}_2$ are the Airy stress functions for the −*b*-LD and *b*-LD, respectively, that are given by the following well-known formulas [26]:

$$\mathit{\Phi}_1 = -\frac{bG}{2\pi(1-\nu)} y\left(\frac{1}{2}\frac{R_0^2}{r^2}\left(1-\frac{r^2 r_1^2}{d_1^2 r_2^2}\right) + ln\frac{rr_1}{r_2}\right), \mathit{\Phi}_2 = \frac{bG}{2\pi(1-\nu)} y\left(\frac{1}{2}\frac{R_0^2}{r^2}\left(1-\frac{r^2 r_1^2}{d_2^2 r_2^2}\right) + ln\frac{rr_1}{r_2}\right), \tag{4}$$

where $r = (x^2+y^2)^{1/2}$, $r_1 = (r^2 + d_1^2 + 2rd_1)^{1/2}$, $r_2 = (r^2 + d_2^2 + 2rd_2)^{1/2}$, $r_c \approx b$.

The energy E_{int} is given by a formula similar to Eq. (2):

$$E \int_{R_0+L}^{R_0+L+p} (\sigma_{xy}^{-B}{}^{B}{}_{xy\,int}, \tag{5}$$

where σ_{xy}^{-B} and σ_{xy}^{B} are the shear stresses of the −*B*-superdislocation and *B*-superdislocation located in the center of a cylindrical pore and at a distance $d = R_0 + L$ from the pore center, respectively.

By analogy with the calculation of self-energy E_{self}, the interaction energy E_{in} is written using the Airy functions as:

$$E_{int}\left[\frac{\partial\Phi_3}{\partial y}+\frac{\partial\Phi_4}{\partial y}\right]_{x=R_0+L,y=0}^{x=R_0+L+p,y=0}, \qquad (6)$$

where Φ_3 and Φ_4 are the Airy stress functions for the $-B$-superdislocation and B-superdislocation, respectively, that can be written as [26]:

$$\Phi_3=-\frac{BG}{2\pi(1-\nu)}y\left(\frac{1}{2}\frac{R_0^2}{r^2}+ln\,r\right),\ \Phi_4=\frac{BG}{2\pi(1-\nu)}y\left(\frac{1}{2}\frac{R_0^2}{r^2}\left(1-\frac{rr_3^2}{dr_4^2}\right)+ln\frac{rr_3}{r_4}\right), \qquad (7)$$

where $r_3=(r^2+d^2+2rd)^{1/2}$ and $r_4=(r^2+d^2+2rd)^{1/2}$.

The energy E_τ that specifies the work of the external shear stress τ to move the b-LD over a distance p with taking into account the effect of the pore on the variation of the shear stress τ is given by equation [27]:

$$E_\tau=-bp\tau[1+2R_0^2/(R_0+L+p)^2-3R_0^4/(R_0+L+p)^4]. \qquad (8)$$

With Eqs. (1)–(8), the energy difference ΔW can be calculated. Then the numerical calculation of the dependences $\Delta W(p)$ was carried out for different values of the external shear stress τ and the length L of the LLI in the exemplary case of high-temperature α-Al_2O_3 ceramics.

Since the material parameters (G and ν) exhibit weak dependence on the temperature, one can take $G = 169$ GPa and $\nu = 0.23$ [28]. The magnitude of the LD Burgers vector b was chosen as $b \approx 0.27$ nm [29]. According to the model [24], the magnitude of the Burgers vectors of the $\pm B$-superdislocation dipole is equal to $\approx 0.025\,L$ at the low deformation temperature $T = 300$ K and $\approx 0.075\,L$ at the high deformation temperature $T = 1500$ K. The numerical calculations of the dependences

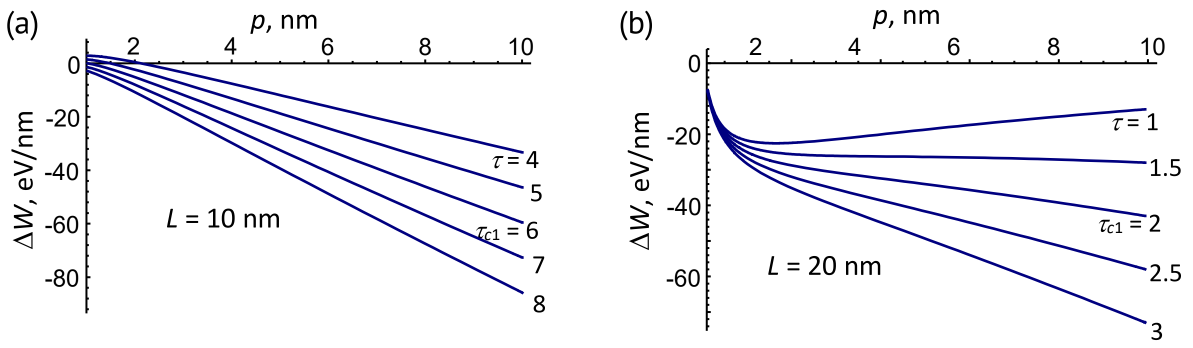

Fig. 2. The energy difference ΔW vs. the distance p at various values of the external shear stress τ, the pore radius R_0 = 10 nm, the distance L = 10 nm (a) and 20 nm (b), and the deformation temperature T = 300 K. The stress values are given in units of GPa

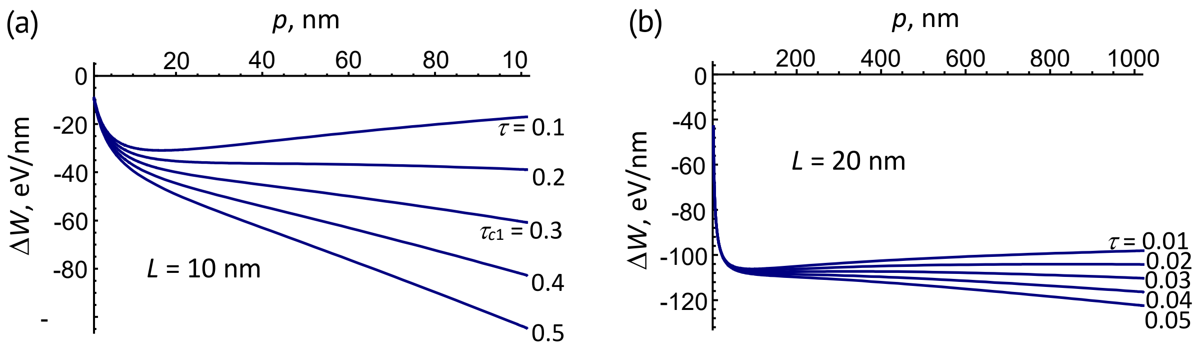

Fig. 3. The energy difference ΔW vs. the distance p at various values of the external shear stress τ, the pore radius R_0 = 10 nm, the distance L = 10 nm (a) and 20 nm (b), and the deformation temperature T = 1500 K. The stress values are given in units of GPa

$\Delta W(p)$ are illustrated in Figs. 2 and 3 for the pore radius R_0 = 10 nm, the two different values of L: L = 10 nm (Figs. 2(a) and 3(a)) and 20 nm (Figs. 2(b) and 3(b)), different values of the external shear stress τ, and the deformation temperatures T = 300 K (Fig. 2) and T = 1500 K (Fig. 3).

With the help of the conditions $\Delta W \leqslant 0$ at p = 1 nm and $\partial \Delta W/\partial p < 0$ for p > 1 nm, the critical value τ_{c1} of the external shear stress τ can be calculated. At $\tau \geq \tau_{c1}$, the LD emission is occurred in a barrier-less manner. As it can be seen from Figs. 2 and 3, the higher is the deformation temperature and the bigger is the distance L, the lower is the value of the critical stress τ_{c1} which determines the LD emission from the AIL triple junction in the vicinity of the pore. A similar calculation method can be used to determine the critical stress τ_{c1} for other deformation temperatures.

It should be noted that the implementation of the dislocation sliding along slip planes can be realized by applying an external shear stress that exceeds a certain critical value τ_{c2} at which the LD can overcome the Peierls barrier. The strong dependence of the Peierls barrier on temperature determines the temperature dependence of the critical stress τ_{c2} which (in the case of α-Al_2O_3 ceramics) is given by the following equations [30] for the LD slip along the basal (τ_{c2b}) and prismatic slip (τ_{c2p}) planes:

$$\tau_{c2b} = \tau_{0b} e^{-0.0052 \rightleftarrows T}, \qquad (9)$$

$$\tau_{c2p} = \tau_{0p} e^{-0.0026T}, \qquad (10)$$

where τ_{c0b} = 109 GPa and τ_{c0p} = 9 GPa.

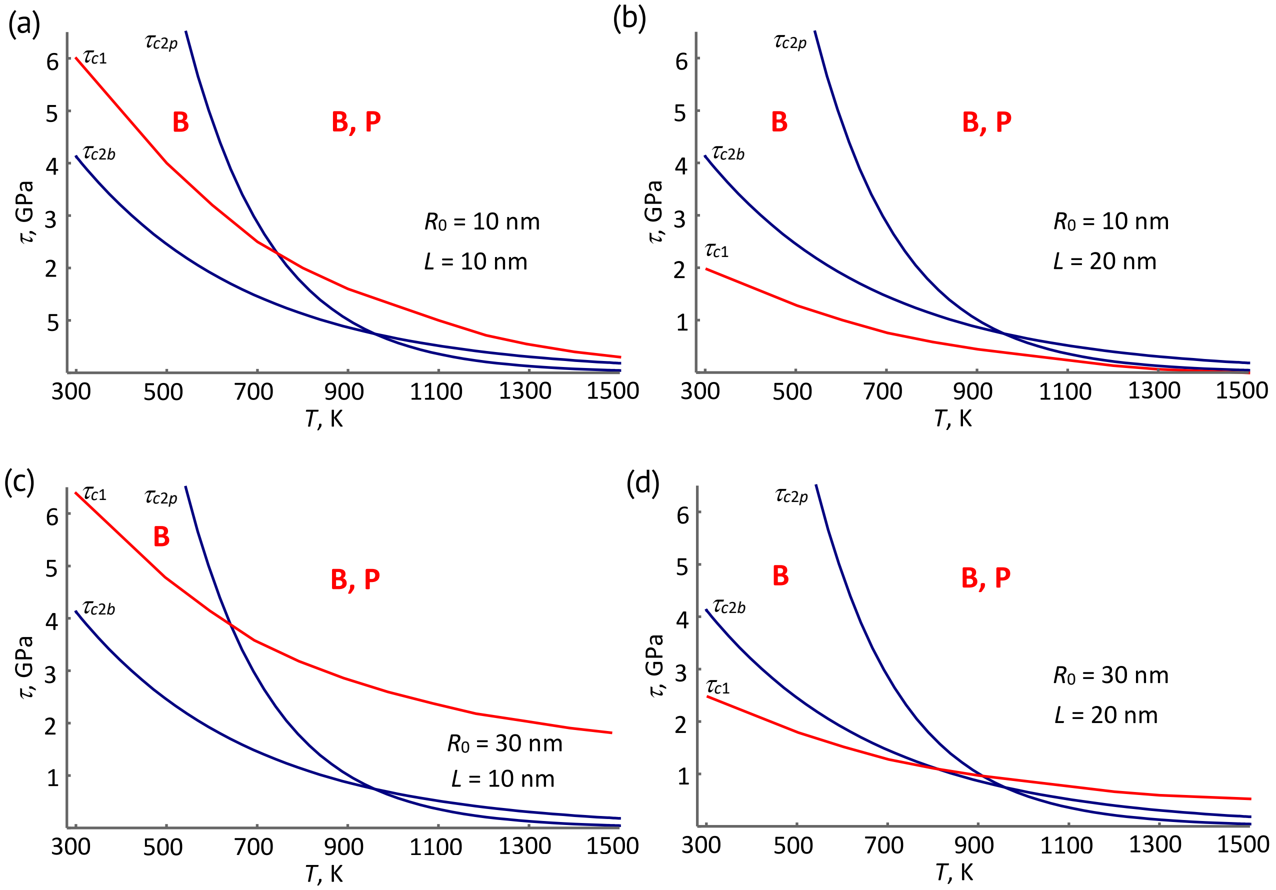

Fig. 4. The critical stresses τ_{c1} and τ_{c2} vs. the deformation temperature T at the LLI length, L = 10 nm (a,c) and (b,d) 20 nm, and the pore radius, R_0 = 10 nm (a,b) and 30 nm (c,d). Regions B and P determine the critical stresses and the deformation temperatures for the basal and prismatic slip planes, respectively

Using Eqs. (1)–(10), one can calculate the dependences $\tau_{c1}(T)$ and $\tau_{c2}(T)$ of the critical stresses τ_{c1} and τ_{c2} on the deformation temperature T in the case of the high-temperature α-Al_2O_3 ceramics with pores at the AIL triple junctions. The numerical calculation of the temperature dependences $\tau_{c1}(T)$ and $\tau_{c2}(T)$ are presented in Fig. 4 for the LLI length, L = 10 nm (Fig. 4(a,c)) and 20 nm (Fig. 4(b,d)), and the pore radius, R_0 = 10 nm (Fig. 4(a,b)) and R_0 = 30 nm (Fig. 4(c,d)). In the model, the LD emission from the AIL triple junction in the vicinity of the pore becomes energetically favorable if the condition $\tau \geq \tau_{c1}$ is satisfied. On the other side, the fulfilment of the conditions $\tau \geq \tau_{c2p}$ and/or $\tau \geq \tau_{c2b}$ determines the ability of the emitted LD to slide along one of the slip planes: the basal slip plane (region B in Fig. 4) or the prismatic slip plane (region P in Fig 4).

An increase in the LLI length L and a decrease in the pore radius R_0 contribute to the expansion of the ranges of the critical stresses and the deformation temperatures (regions B and P, Fig. 4) at which the sliding of the emitted LD in the grain interior is energetically favorable. Obviously, the effect of the LLI length L is explained by the corresponding increase in the stress of the $\pm B$-superdislocation dipole with its arm and the corresponding decrease in the image force attracting the emitted LD to the pore surface. The effect of the pore radius R_0 is also caused by the diminishing attracting image force on the LD.

Thus, the presence of pores makes it harder the emission of LDs from the neighboring AIL triple junctions. The bigger is the pore radius the higher is the critical stress for the dislocation emission.

Conclusions

A micromechanism has been suggested which describes the implementation of the plastic deformation in the high-temperature porous ceramics with liquid-like inclusions (LLIs) in amorphous intercrystalline layers (AILs). In the framework of the model, the evolution of the LLIs is suppressed by AIL triple junctions and they serve as effective stress concentrators which are capable to induce the action of alternative mechanisms of plasticity under elevated temperatures. Such an alternative mechanism of the plastic deformation enhancement can be the emission of lattice dislocation (LDs) from the triple junctions of the AILs containing the LLIs, and the subsequent glide of the emitted LDs in the grain interior along slip planes under the combined action of the external shear stress and the stress field of the LLIs. The presence of pores in AILs and their triple junctions has been expected to effect upon the emission critical conditions. Using α-Al_2O_3 nanoceramics as an example, the energy characteristics for the LD emission near a pore have been calculated. Also, a comparative analysis of the critical stresses for the emission of the LDs and for their slide along the prismatic and basal slip planes depending on the deformation temperature has been carried out in a wide temperature range from 300 to 1500 K.

It has been shown that, while the LLIs pressed to AIL triple junctions can effectively stimulate the emission of LDs from these triple junctions, the presence of pores in the neighboring AIL triple junctions makes it harder the emission of LDs. The bigger is the pore radius the higher is the critical stress for the LD emission.

It is worth mentioning that understanding the alternative mechanisms of the plastic deformation enhancement guides the engineering of the ceramic microstructures to optimize the pore distribution and the amorphous layer properties, aiming at improved the mechanical properties (the fracture toughness and the ductility) at the elevated temperatures.

CRediT authorship contribution statement

Mikhail Yu. Gutkin: writing – review & editing; **Nikolay V. Skiba**: writing – original draft.

Conflict of interest

The authors declare that they have no conflict of interest.

References

1. Maniakin P, Shalagaev SG, Archakov IYu, Konakov YaV, Kurapova OYu, Konakov VG. In-situ high-temperature bending strength measurement of YSZ ceramics manufactured using novel B2O3-based glass binder. *Materials Physics and Mechanics.* 2024;52(2): 64–75.
2. Koch CC, Ovid'ko IA, Seal S, Veprek S. *Structural nanocrystalline materials: fundamentals and applications.* Cambridge: Cambridge University Press; 2007.
3. Liu J, Huo W, Zhang X, Ren B, Li Y, Zhang Z, Yang J. Optimal design on the high-temperature mechanical properties of porous alumina ceramics based on fractal dimension analysis. *Journal of Advanced Ceramics.* 2018;7: 89–98.
4. Zhang D, Yu R, Feng X, Guo X, Yang Y, Xu X. Enhanced mechanical properties of Al2O3 nanoceramics via low temperature spark plasma sintering of amorphous powders. *Materials.* 2023;16(16): 5652.
5. Wang L, An L, Zhao J, Shimai S, Mao XJ, Zhang J, Liu J, Wang SW. High-strength porous alumina ceramics prepared from stable wet foams. *Journal of Advanced Ceramics.* 2021;10: 852–859.
6. Zhang ZL, Sigle W, Koch CT, Rühle M. Dynamic behavior of nanometer-scale amorphous intergranular film in silicon nitride by in situ high-resolution transmission electron microscopy. *Journal of the European Ceramic Society.* 2011;31(9): 1835–1840.
7. Krasnitckii SA, Sheinerman AG, Gutkin MYu. Brittle vs ductile fracture behavior in ceramic materials at elevated temperature. *Materials Physics and Mechanics.* 2024;52(2): 82–89.
8. Subramaniam A, Koch CT, Cannon RM, Rühle M. Intergranular glassy films: An overview. *Materials Science and Engineering A.* 2006;422(1–2): 3–18.
9. Kleebe HJ. Structure and chemistry of interfaces in Si3N4 ceramics studied by transmission electron microscopy. *Journal of the Ceramic Society of Japan.* 1997;105(1222): 453–475.
10. Golubev SN, Kurapova OYu, Archakov IYu, Konakov VG. Characterization of a high temperature ceramics produced via two-step additive manufacturing. *Open Ceramics.* 2021;7: 100165.
11. Hulbert DM, Jiang D, Kuntz JD, Kodera Y, Mukherjee AK. A low-temperature high-strain-rate formable nanocrystalline superplastic ceramic. *Scripta Materialia.* 2007;56(12): 1103–1106.
12. Xu X, Nishimura T, Hirosaki N, Xie R-J, Yamamoto Y, Tanaka H. Superplastic deformation of nano-sized silicon nitride ceramics. *Acta Materialia.* 2006;54(1): 255–262.
13. Chen D, Zhang XF, Ritchie RO. Effects of grain-boundary structure on the strength, toughness, and cyclic-fatigue properties of a monolithic silicon carbide. *Journal of the American Ceramic Society.* 2000;83(8): 2079–2081.
14. Rice RW. Limitations of pore-stress concentrations on the mechanical properties of porous materials. *Journal of Materials Science.* 1997;32: 4731–4736.
15. Suleiman B, Zhang H, Ding Y, Li Y. Microstructure and mechanical properties of cold sintered porous alumina ceramics. *Ceramics International.* 2022;48(10): 13531–13540.
16. Mo YF, Szlufarska I. Simultaneous enhancement of toughness, ductility, and strength of nanocrystalline ceramics at high strain-rates. *Applied Physics Letters.* 2007;90(18): 181926.
17. Demkowicz MJ, Argon AS. High-density liquidlike component facilitates plastic flow in a model amorphous silicon system. *Physical Review Letters.* 2004;93(2):025505.

18. Demkowicz MJ, Argon AS. Liquidlike atomic environments act as plasticity carriers in amorphous silicon. *Physical Review B.* 2005;72(24): 245205.
19. Gutkin MYu, Ovid'ko IA. A composite model of the plastic flow of amorphous covalent materials. *Physics of the Solid State.* 2010;52(1): 58–64.
20. Gutkin MYu, Ovid'ko IA. Plastic flow and fracture of amorphous intercrystalline layers in ceramic nanocomposites. *Physics of the Solid State.* 2010;52(4): 718–727.
21. Gutkin MYu, Mikaelyan KN. A model of strain hardening in nanoceramics with amorphous intercrystalline layers. *Physics of Complex Systems.* 2021;2(2): 51–60.
22. Gutkin MYu, Skiba NV. Emission of lattice dislocations from triple junctions of grain boundaries in high-temperature ceramics with amorphous intercrystalline layers. *Materials Physics and Mechanics.* 2024;52(1): 39–48.
23. Gutkin MYu, Krasnitckii SA, Skiba NV. Formation of liquid-like inclusions near pores in amorphous intercrystalline layers in high-temperature ceramics. *Materials Physics and Mechanics.* 2024;52(6): 8–16.
24. Glezer A, Pozdnyakov V. Structural mechanism of plastic deformation of nanomaterials with amorphous intergranular layers. *Nanostructured Materials.* 1995;6(5–8): 767–769.
25. Mura T. *Micromechanics of defects in solids.* Dordrecht: Springer Dordrecht; 1987.
26. Eshelby JD. Boundary problems. In: Nabarro FRN. (eds.) *Dislocations in solids. Vol. 1.* Amsterdam: North-Holland Publishing Company; 1979. p. 167–221.
27. Asaro RJ, Lubarda VA. *Mechanics of Solids and Materials.* Cambridge: Cambridge University Press; 2006.
28. Smithells CJ. (Ed.) *Metals reference book. 5th ed.* London: Butterworths; 1976.
29. Lagerlöf KPD, Heuer AH, Castaing J, Rivière JP, Mitchell TE. Slip and twinning in sapphire (α-Al2O3). *Journal of the American Ceramic Society.* 1994;77(2): 385–397.
30. Choi SM, Awaji H. Nanocomposites – a new material design concept. *Science and Technology of Advanced Materials.* 2005;6: 2–10.

MATERIALS PHYSICS AND MECHANICS RESEARCH ARTICLE

Submitted: November 11, 2025 **Revised: December 2, 2025** **Accepted: December 10, 2025**

The influence of microplastic deformation on the performance of a shape memory alloy vibration protection system: a modeling study

F.S. Belyaev [1] ✉, **A.E. Volkov** [2], **M.E. Evard** [2], **M.S. Starodubova** [2]

[1] Institute for Problems of Mechanical Engineering RAS, St. Petersburg, Russia

[2] St. Petersburg State University, St. Petersburg, Russia

✉ belyaev_fs@mail.ru

ABSTRACT

Shape memory alloys are promising for vibration protection systems but their long-term performance is challenged by functional fatigue due to microplastic deformation. A previously developed microstructural model that explicitly accounts for the evolution of microplastic deformation is utilized in the research to investigate the influence of this phenomenon. A one-dimensional oscillatory system with a payload isolated by two TiNi alloy springs is investigated. Numerical simulations compare the device's response in austenitic and martensitic states, with and without microplasticity, under harmonic excitation. The results confirm that microplastic deformation significantly alters the dynamic characteristics of the system, highlighting the necessity of its inclusion for accurate performance prediction. Furthermore, the analysis demonstrates the superior performance of the shape memory alloy system compared to linear elastic counterparts, showing its inherent ability to mitigate resonance across a frequency range.

KEYWORDS

shape memory alloys • vibration protection • microplastic deformation • microstructural modeling

Acknowledgements. *The research was carried out within the state assignment of Ministry of Science and Higher Education of the Russian Federation (theme No. 124041500009-8).*

Citation: Belyaev FS, Volkov AE, Evard ME, Starodubova MS. The influence of microplastic deformation on the performance of a shape memory alloy vibration protection system: a modeling study. *Materials Physics and Mechanics.* 2026;54(1): 42–56.
http://dx.doi.org/10.18149/MPM.5412026_6

Introduction

Shape memory alloys (SMAs) represent a class of functional materials that hold a key position in solving complex engineering problems due to their unique properties. These primarily include the shape memory effect (the ability to recover significant strain upon heating) and pseudoelasticity (superelasticity) – the recovery of strain upon unloading. These macroscopic phenomena are caused by a thermoelastic martensitic transformation and accompanying processes: martensite reorientation (manifested as pseudo-plasticity) and the movement of phase and twin boundaries. Thanks to this, SMAs enable the creation of mechanical devices such as dampers, isolators, and actuators, which often surpass traditional counterparts in functionality and reliability [1–5].

The relevance of SMA application in the construction industry is particularly high for tasks of seismic protection and vibration isolation. Widely used passive damping devices – rubber-metal bearings, friction dampers, and viscoelastic dampers – have a number of fundamental limitations [6,7]. Rubber isolators are characterized by issues of aging, sensitivity to temperature fluctuations, and significant residual deformations after

Publisher: Peter the Great St. Petersburg Polytechnic University

strong disturbances. Friction devices require regular maintenance and can lose reliability in the long term, while many types of metallic dampers are susceptible to low-cycle fatigue and require replacement after activation. The implementation of SMAs in damping and isolating systems allows for overcoming these drawbacks, offering a path towards creating resilient and self-centering structures [2–5,8–13].

The following SMA properties are key for application in vibration protection:

1. High damping capacity associated with hysteresis during phase transformations and martensite reorientation. Energy dissipation occurs both in the high-temperature austenitic state due to direct stress-induced martensitic transformation (requiring energy for crystal lattice rearrangement) and in the low-temperature martensitic state due to irreversible movement of twin boundaries. For TiNi-based alloys, this effect has been previously studied in detail [14] and continues to be investigated in new compositions [15,16].
2. Self-centering nature provided by the shape memory effect. This property allows a structure to return to its original position after a seismic event, minimizing residual deformations, which is critically important for maintaining the building's functionality [17–21].
3. High fatigue strength under large strains (up to 6–8 %), which is due to the predominance of reversible martensitic transformation over irreversible dislocation slip. This makes SMAs ideal candidates for cyclically loaded elements in seismic isolation [22–24].

The evolution of SMA-based device designs began with relatively simple forms. Early developments widely used wire elements, which demonstrated high fatigue strength and effective energy dissipation. Cyclic tensile experiments confirmed that such devices dissipate energy stably, and the accumulation of residual deformation slows down with an increasing number of cycles [25]. Their potential for use as hysteretic dampers in braces and column bases remains high. Subsequently, the range of configurations expanded. For example, SMA dampers in the form of rings [26], curved plates [27], helical springs [28], washers [20,28], and ring springs [29] were proposed, which demonstrated high load-bearing capacity and potential for use as passive vibration isolators in various industries. Modern research is focused on creating more complex structures, such as SMA-based composites [30–32] and porous SMA structures [33].

One of the most promising directions is the development of adaptive and tunable vibration protection systems. The ability to control the phase state (and, consequently, the stiffness and damping) of an SMA working element through thermal activation paves the way for smart systems. A classic problem of passive inertial dampers is their tuning to a fixed frequency, whereas the natural frequency of a structure can change (for example, due to changes in mass, nonlinear behavior during strong earthquakes, or traffic movement on a bridge). Research, such as that in [34,35], has confirmed the possibility of retuning the frequency of an inertial damper with SMA elements. Studies [36,37] have proposed controlled vibration damping systems based on SMA composites.

Since SMAs are characterized by a nonlinear stress-strain relationship, as well as a strong dependence of their properties on temperature and loading history, reliable means of modeling their mechanical behavior are required for the successful design of vibration protection devices. However, most works on this topic are experimental, and in those where modeling was performed, the simplest phenomenological SMA models were used, allowing only for some quantitative estimates of the device response [18,35,38,39]. Exceptions are the works [40,41], which modeled vibration protection devices with helical and slotted springs made of TiNi alloy. A microstructural model [42] capable of describing all the main SMA effects was used to describe the mechanical behavior of the working elements. Thanks to the high predictive power of this model, it was possible to obtain a good estimate of the performance of the vibration protection devices under different phase states of the working elements.

However, one of the main problems limiting the predictability of the long-term behavior of SMAs is the instability of their functional properties under cyclic loading. Since martensitic transformations involve a crystal lattice transformation, the growth of a new phase crystal within the austenitic matrix is accompanied by significant interfacial stresses. This leads to the accumulation of irreversible microplastic deformation (MPD) in the boundary regions, caused by the generation and movement of dislocations [43,44]. This phenomenon has a dual influence on performance characteristics:

1. On the one hand, MPD causes irreversible shape changes and the generation of structural defects, which in the long term accelerate fatigue failure. Furthermore, these accumulated changes distort the kinetics of subsequent martensitic transformations, leading to the degradation of functional properties — a shift in characteristic stresses and temperatures, and a reduction in the hysteresis loop and the shape memory effect.
2. On the other hand, since the generation and movement of dislocations require energy, MPD is an additional mechanism of energy dissipation, which theoretically can increase the damping capacity of the material, especially in the initial stages of cyclic loading.

Thus, the influence of MPD on the vibration protection properties of SMAs is complex and ambiguous. However, even in studies [40,41], when describing vibration protection systems, the contribution of microplasticity to the total strain was considered insignificant and was neglected. Nevertheless, it remains unclear how justified this approach is from the perspective of assessing damping properties.

In view of the above, it can be assumed that MPD significantly affects the performance of SMA-based vibration protection devices. Ignoring it in mechanical models may lead to significant errors in predicting damping characteristics and long-term stability. In this regard, the aim of this work is a systematic investigation of the influence of MPD on the effectiveness of vibration protection devices. To achieve this aim, an improved microstructural model that takes this mechanism into account will be used. Based on this model, a parametric study of an oscillatory system will be conducted to quantitatively assess the contribution of microplasticity to energy dissipation and the change in the dynamic response of the structure as a whole.

Materials and Methods

Methodology for modeling of the SMA mechanical behavior

To describe the complex mechanical behavior of SMAs in this work a microstructural model previously developed by the authors [45–50] is used. This approach allows for the correct accounting of the main deformation mechanisms characteristic of SMAs, including MPD. This model and some of its variations have proven themselves to be effective in describing such phenomena in SMA as: fatigue fracture [45], plastic deformation [46], deformation during isothermal holding [47], the effect of martensite stabilization [48], loading under conditions of heat exchange with the environment [49], and the operation of an SMA specimen under conditions of a thermomechanical drive [50]. Therefore, it can be said that the proposed model has great predictive power and can be applied to solving engineering problems, in particular for modeling vibration protection devices based on SMA.

Basic model principles

The model describes the behavior of a representative volume of material, which is considered as a material point. The key principle lies in the multi-level description of the microstructure. The representative volume consists of numerous grains with different crystallographic orientations. Each grain, in turn, can contain austenite and/or several orientational variants of martensite.

According to the Reuss hypothesis, the macroscopic strain of the representative volume ε is calculated as the average over all orientations ω of the strains of individual grains $\varepsilon^{gr}(\omega)$:

$$\varepsilon = \sum_{\omega} f(\omega)\varepsilon^{gr}(\omega), \tag{1}$$

where $f(\omega)$ is the volume fraction of grains with orientation ω.

Kinematics of deformation at the grain level

The strain of an individual grain is represented as the sum of contributions from various physical mechanisms:

$$\varepsilon^{gr} = \varepsilon^{E} + \varepsilon^{T} + \varepsilon^{Ph} + \varepsilon^{MP}, \tag{2}$$

where ε^{E} is elastic strain (according to Hooke's law), ε^{T} is thermal strain (due to thermal expansion), ε^{Ph} is phase strain (associated with the martensitic transformation), ε^{MP} is microplastic strain (associated with plastic accommodation of martensite).

Description of phase transformation

To describe the phase strain, internal variables Φ_n are introduced, where $\frac{\Phi_n}{N}$ represents the volume fraction of the *n*-th orientational variant of martensite (*N* is the total number of variants). The phase strain of a grain is calculated as the averaged contribution of all martensite variants:

$$\varepsilon^{Ph} = \frac{1}{N}\sum_{n=1}^{N} \Phi_n D^n, \tag{3}$$

where D^n is the Bain strain tensor for the *n*-th martensite variant.

The condition determining the onset and course of martensitic transformation is formulated through the balance of thermodynamic forces:

$$F_n = \pm F^{fr}, \tag{4}$$

where F_n is the generalized thermodynamic force causing the growth of the *n*-th variant of martensite, F^{fr} is the dissipative force that prevents the movement of interphase boundaries and causes the presence of temperature-phase hysteresis, the "+" sign corresponds to the forward transformation (austenite → martensite), and the "−" sign to the reverse transformation (martensite → austenite).

The thermodynamic forces F_n and F^{fr} are calculated as follows:

$$F_n = \frac{q_0}{T_0}(T - T_0) + \sigma_{ij}\colon D_{ij}^{n} - \mu \sum_{m=1}^{N} A_{mn}\,(\Phi_m - b_m), \tag{5}$$

$$F^{fr} = q_0 \frac{M_s - T_0}{T_0}, \tag{6}$$

where q_0 is the latent heat of transformation, T_0 is the temperature of thermodynamic phase equilibrium (austenite and martensite), T is the temperature of representative volume, σ is applied stress, b is the density of oriented defects, A is the matrix that determines the interaction of martensite variants described in detail in [51,52], M_s is the start temperature of the forward martensitic transformation.

The coefficient μ and the equilibrium temperature T_0 depend on the material constants and can be calculated as follows:

$$\mu = -\frac{q_0(M_s - M_f)}{T_0(1-2\alpha)}, \tag{7}$$

$$T_0 = \frac{M_s + A_f}{2}, \tag{8}$$

where M_f and A_f are the finish temperatures of the forward and reverse martensitic transformations respectively, α is a material constant characterizing the coherency of martensitic phases.

Accounting for microplastic deformation

The accumulation of MPD is a direct consequence of martensitic transformation. Transformation incompatibility between the growing martensite crystals and the surrounding austenite matrix, arising from differences in crystal lattices, generates significant localized internal stresses. To relax these stresses, accommodative microplastic flow occurs in the boundary regions. Although this flow is initially localized, its contribution can manifest itself at the macroscopic level during the formation of oriented martensite. In this case, the most favorably oriented martensite variants predominate, their volume fraction increasing. Since the MPD associated with the growth of a particular variant is consistent with its Bain strain, this leads to the summation of unidirectional microshears. As a result, the irreversible strain, initially dispersed in microvolumes, accumulates, contributing to the overall macroscopic deformation of the material. A key assumption in describing this deformation mechanism is that the MPD associated with the growth of a particular martensite variant is proportional to its Bain strain deviator:

$$\varepsilon^{MP} = \frac{1}{N}\sum_{n=1}^{N} \kappa \varepsilon_n^{mp} dev(D^n), \tag{9}$$

where ε_n^{mp} is the measure of MPD associated with the growth of the *n*-th martensite variant, κ is the scaling coefficient.

The conditions for the onset of microplastic flow are similar to the condition of plastic flow in the one-dimensional case, taking into account kinematic (translational) and isotropic hardening, where the role of stress is played by the generalized thermodynamic force F_n^p, and the kinematic and isotropic hardening correspond to the thermodynamic forces F^y and F_n^ρ:

$$\left|F_n^p - F_n^\rho\right| = F^y, \quad \left(F_n^p - F_n^\rho\right) dF_n^p > 0. \tag{10}$$

The generalized thermodynamic force causing MPD is calculated as follows:

$$F_n^p = \mu \sum_{m=1}^{N} A_{mn}(\Phi_m - b_m). \tag{11}$$

Evolution of defects and hardening

Microplastic flow is accompanied by the accumulation of two types of defects: *oriented defects* b, that create oriented long-range stress fields, and *scattered defects* f distributed in the volume. The evolution of defect densities is described by the equations:

$$\dot{b_n} = \dot{\varepsilon}_n^{mp} - \frac{1}{\beta^*}|b_n|\dot{\varepsilon}_n^{mp} H\left(b_n \dot{\varepsilon}_n^{mp}\right), \tag{12}$$

$$\dot{f} = \sum_{m=1}^{N} |\dot{\varepsilon}_m^{mp}| + r_1(f - f_0)\Phi^{gr} H(-\Phi^{gr}), \tag{13}$$

where H is the Heaviside function, β^* is the maximum density of oriented defects, r_1 is the recovery coefficient, f_0 is the equilibrium density of scattered defects, Φ^{gr} is volume fraction of all martensite variants in grain.

To obtain a closed system of equations, it is necessary to introduce hardening laws. The model assumes that scattered defects impede dislocation movement, thereby increasing the yield stress. Consequently, their density is related to isotropic hardening. Clusters of oriented defects create internal stress fields, the effect of which is combined with external stress, shifting the center of the yield surface. Consequently, their density is related to kinematic hardening. Linear dependencies are proposed to relate hardening to defect densities:

$$F_n^{\rho} = a_{\rho} b_n, \tag{14}$$

$$F^{y} = a_{y} f, \tag{15}$$

where a_{ρ} and a_y are material constants determining the intensity of the corresponding type of hardening.

Equations (4), (10), (12)–(15) form a closed system that allows for calculating the evolution of all internal variables. Formulas (1)–(3) and (9) are used to calculate material deformations under thermomechanical loading, which is necessary for the subsequent analysis of vibration protection devices.

Model of vibration protection device

This paper presents a numerical study of the effectiveness of a vibration isolation device, the schematic of which is shown in Fig. 1. The device consists of a rigid housing within which a payload is suspended by two helical springs made of TiNi alloy. The springs, which serve as the working elements, are designed to isolate the payload from external vibration.

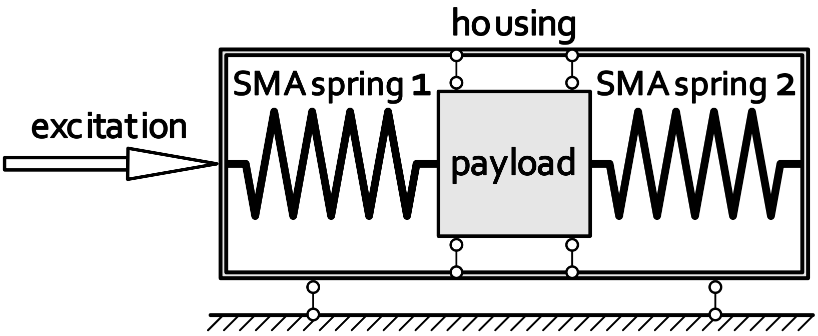

Fig. 1. Schematic diagram of the vibration protection device

The mechanical response of the springs is described by the microstructural model presented in the previous section with a set of material constants listed in Table 1. To analyze the device's behavior under various conditions, the initial phase state of the spring material (austenite or martensite) was determined by selecting a temperature. The modeling assumed that heat exchange between the springs and the surrounding medium occurs sufficiently rapidly, and that temperature changes due to heat generation and absorption during martensitic transformations can be neglected.

Table 1. Material constants for TiNi alloy

Material constant	Symbol	Value
Number of martensite variants	N	12
Latent heat (enthalpy) of the direct martensitic transformation, MJ/m^3	q_0	-180
Characteristic temperatures of martensite transformation, K	M_f M_s A_s A_f	303 323 340 360
Temperature of the thermodynamic equilibrium, K	T_0	341.5
Interaction coefficient of martensite variants	α	0.2
Microplastic strain scaling factor	κ	2.3
Coefficient of isotropic hardening, MPa	a_y	0.2
Coefficients of kinematic hardening, MPa	a_p	5
Maximum value of the oriented defects density	β^*	2.8
Initial value of scattered defects	f_0	20
Scattered defects recovery coefficient	r_1	0
Young's modulus of austenite, GPa	E_A	83
Young's modulus of martensite, GPa	E_M	41

The system is subjected to a harmonic vibration with a specified amplitude and frequency. The payload is assumed to move along one direction only, allowing this oscillatory system to be considered one-dimensional. The main geometric parameters of the springs and the characteristics of the system are given in Table 2.

Table 2. Characteristics of a vibration isolation device

Model Parameter	Symbol	Value
Wire diameter, mm	d_1, d_2	0.5
Coil diameter, mm	D_1, D_2	8.0
Number of coils	-	5
Mass of payload, kg	m	0.22
Drag coefficient	μ	0.5

The movement of the payload is described by the equation:

$$m\ddot{x} = -F_1 + F_2 - \mu\dot{x}, \tag{16}$$

where F_1 and F_2 are the elastic forces arising in the springs; μ is the drag coefficient (viscous friction).

Assuming that the wire experiences only torsion and the stress distribution is linear, we obtain:

$$F_1 = k_1\tau_1, F_2 = k_2\tau_2, \tag{17}$$

$$k_1 = \frac{\pi d_1^3}{8D_1}, k_2 = \frac{\pi d_2^3}{8D_2}, \tag{18}$$

where τ_1, τ_2 are the shear stresses of the material, k_1 and k_2 are the spring stiffnesses, D_1 and D_2 are the diameters of coils, d_1 and d_2 are the wire diameters. Within the framework of the microstructural model, this differential equation is solved numerically using the improved Euler method.

Influence of microplastic deformation

Comparative analysis strategy

A key advantage of the microstructural model used is the ability to selectively account for individual deformation mechanisms. In this work, this allowed us to conduct a series of comparative calculations for two scenarios: one with and one without MPD. This approach allows us to quantitatively estimate the influence of this irreversible process on the damping characteristics and overall performance of the vibration isolation device. The calculations were performed for two initial phase states of the springs material: martensitic (at temperature of 300 K) and austenitic (at temperature of 380 K).

The choice of a temperature of 380 K for the austenitic state (which is 20 degrees higher than the end temperature of the reverse transformation A_f for the selected alloy) guarantees the full realization of the superelastic effect, as well as a temperature reserve necessary to compensate for the possible shift in characteristic temperatures (in particular, A_f) due to the accumulation of MPD. Without this reserve, MPD could lead to incomplete reverse transformation upon unloading and, consequently, to the degradation of the pseudoelastic hysteresis. A further increase in temperature is impractical, as it would shift the hysteresis toward higher stresses. In this case, over a wider stress range, the springs would have a linear-elastic behavior, rather than a pseudo-elastic one, which would lead to a decrease in the damping capacity, since the main contribution to this characteristic is made by the dissipation of energy during the phase transformation.

Determining resonance frequencies

Of greatest practical interest is the system's behavior in the resonant mode, which is the most challenging for any vibration isolation device. However, due to the significant nonlinearity of the SMA deformation properties caused by phase transformations, analytical determination of the resonant frequency is impossible. Therefore, for each of the studied cases (with and without MPD, for each phase state), the resonant frequency was determined numerically. The method involved performing a series of calculations varying the frequency of the external excitation and then identifying the frequency corresponding to the maximum amplitude of the payload mass oscillations.

The results of the numerical resonance identification procedure confirm the significant influence of microplasticity on the system's dynamic response. This is evident from the results presented in Fig. 2, which shows the dependence of the payload oscillation amplitude on the frequency of external excitation with an amplitude of 70 mm for springs in the martensitic state. The resonant frequencies, corresponding to the peak oscillation amplitudes marked by arrows, are distinctly different for the cases with and without accounting for microplasticity. This shift occurs because the accumulation of MPD alters the effective stiffness of the material. Consequently, to ensure a correct comparison of the damping capacity, the subsequent analysis of the system's performance is conducted at their respective resonant frequencies for each excitation amplitude.

The simulation results presented on Fig. 3 confirmed a characteristic feature of materials with nonlinear deformation dependencies: the resonant frequency of a vibration isolation system with SMA springs depends significantly on the amplitude of the external excitation.

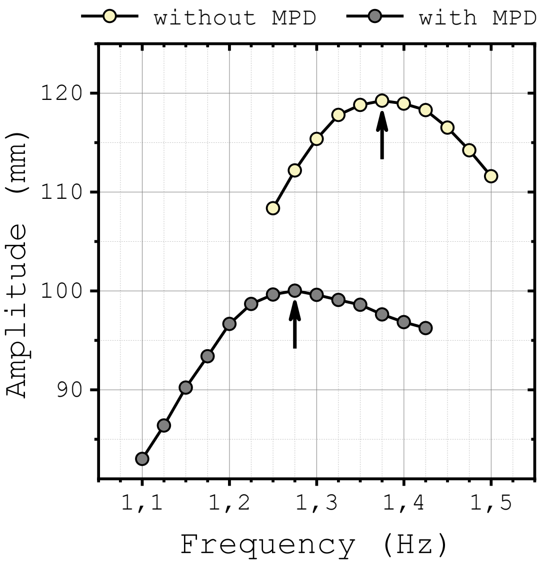

Fig. 2. Dependence of the amplitude of payload oscillation on the frequency of external excitation at a temperature of 300 K (martensite). The amplitude of external influence is 70 mm

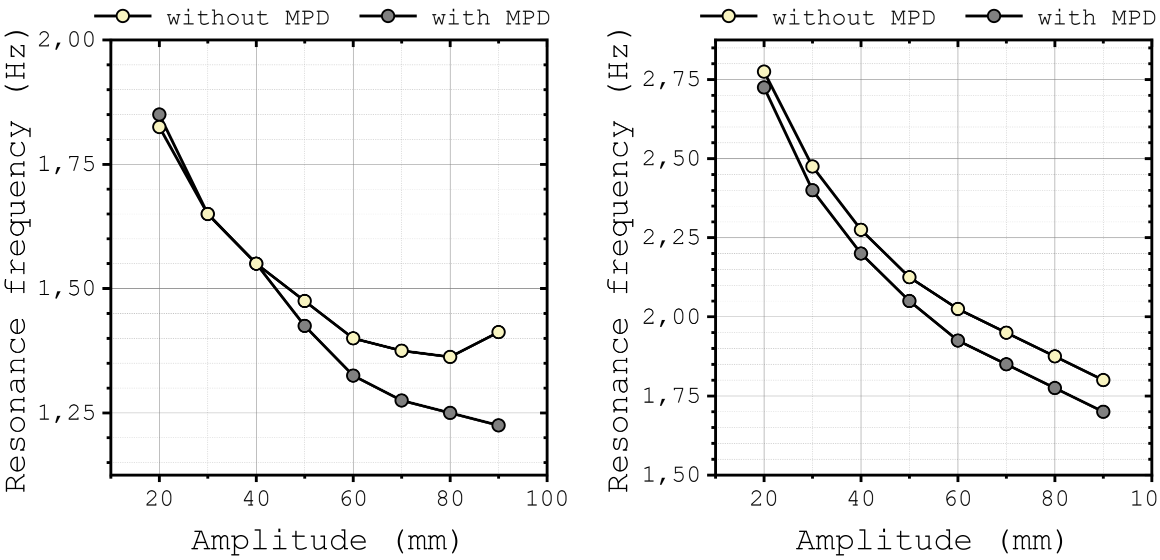

(a) **(b)**

Fig. 3. Dependences of the resonance frequency on the amplitude of the external excitation in the martensitic state, at a temperature of 300 K (a) and in the austenitic state, at a temperature of 380 K (b)

It was found that for both initial phase states (austenitic and martensitic), taking MPD into account leads to a systematic decrease in the resonant frequency compared to the case where microplastic flow is not accounted (Fig. 3). This decrease is explained by the fact that microplasticity is an additional irreversible deformation mechanism that contributes to an increase in the overall deformation of the system and, consequently, a decrease in its effective stiffness.

Importantly, the difference between the resonant frequencies in simulations with and without accounting of microplastic flow increases with increasing excitation amplitude. This fact is consistent with the physics of the process: at high amplitudes and, correspondingly, high stresses, the intensity of microplastic flow increases, enhancing its contribution to the overall mechanical response. In contrast, in the martensitic state, at excitation amplitudes of 40 mm or less, the dependences for both cases are almost identical (Fig. 3(a)). This is explained by the fact that the developed stresses are insufficient to activate MPD, and its influence can be neglected.

The influence of microplasticity on the deformation and force response of SMA springs

Analysis of the data presented in Figs. 4 and 5 reveals a significant influence of microplasticity on the response of the vibration isolation device. Accounting for MPD leads to a reduction in both the spring deformation amplitude and the maximum stresses in the material. This effect demonstrates a clear dependence on the loading level: the difference in deformations and stresses between the two cases increases significantly with increasing external excitation amplitude. For example, with an excitation amplitude of 90 mm, the calculated deformation values in the model accounting for MPD are more than two times lower.

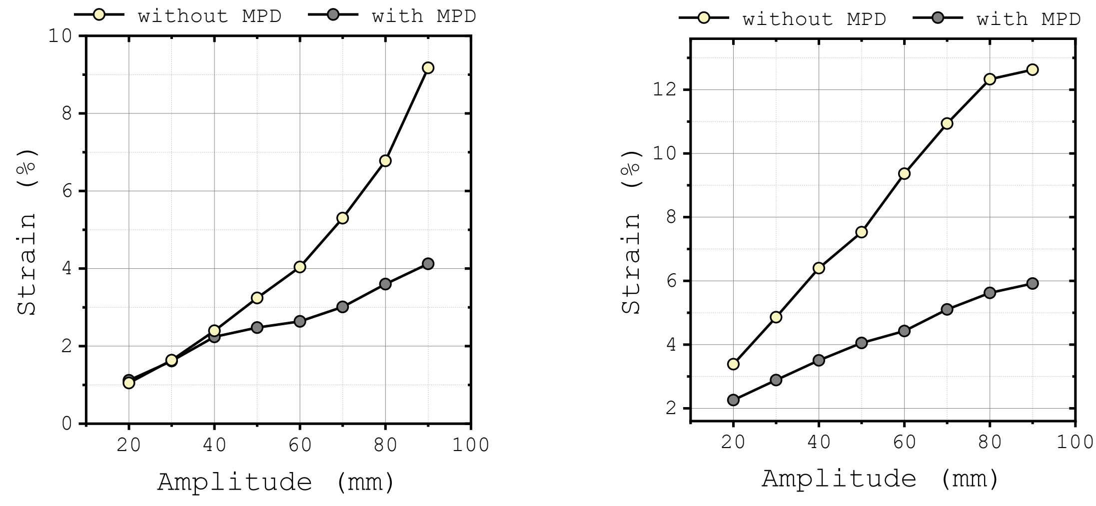

(a) **(b)**

Fig. 4. Dependences of the strain amplitude on the amplitude of external excitation in the martensitic state (temperature of 300 K) (a) and in the austenitic state (temperature of 380 K) (b)

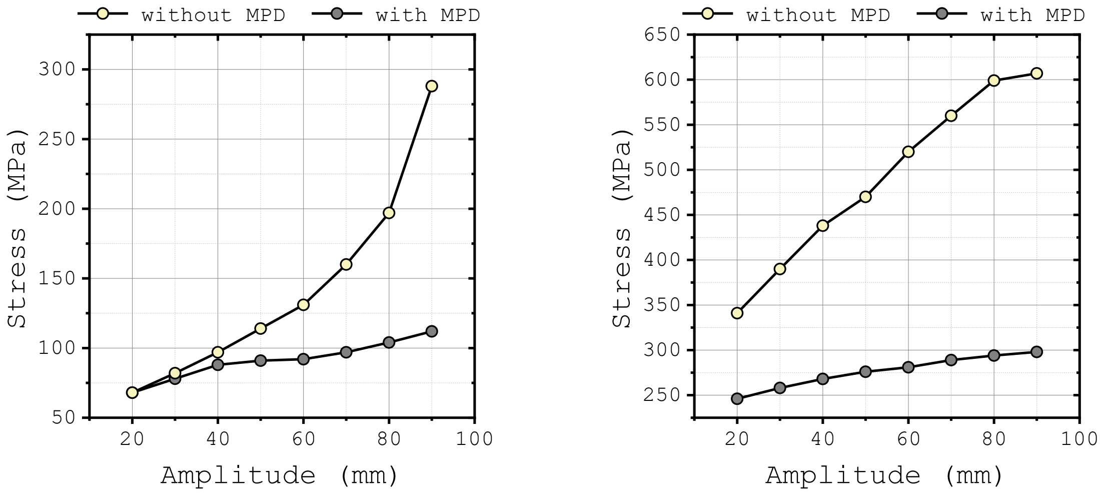

(a) **(b)**

Fig. 5. Dependences of the stress amplitude on the amplitude of external excitation in the martensitic state (temperature of 300 K) (a) and in the austenitic state (temperature of 380 K) (b)

These results are explained by the fact that the energy expended on irreversible microplastic flow is diverted from the processes that determine elastic and phase deformation. As a result, the payload develops a smaller vibration amplitude, and lower stresses occur in the SMA springs. It's also worth noting that at small excitation amplitudes (up to 40 mm) in the martensitic state, the difference in strain and stress between the models becomes negligible (Figs. 4(a), 5(a)). This is consistent with previously obtained results — these amplitudes correspond to strains lying in the region of pure elasticity or elasticity with minor phase reorientation, which do not cause intense microplastic shear.

The obtained results demonstrate that when designing vibration protection devices operating in modes that lead to the occurrence of MPD, taking this mechanism into account is necessary for accurately predicting the dynamic characteristics of the system, in particular, its resonant frequency.

Evaluation of the effectiveness of SMA vibration protection devices

A key advantage of SMA-based vibration isolation devices over systems with conventional elastic elements is their ability to adapt to changing loading conditions, specifically, to avoid resonant modes due to the nonlinearity of their deformation characteristics.

In the austenitic state, nonlinearity is caused by direct martensitic transformation under load (pseudoelasticity). As Fig. 6 shows, with increasing deformation amplitude, the effective stiffness of the device, determined by the slope of the $k_1 - k_3$ lines for amplitudes of 2.5, 5, and 7.5 %, respectively, decreases significantly compared to the stiffness of a linear elastic element k_0 (with Young's modulus of austenite).

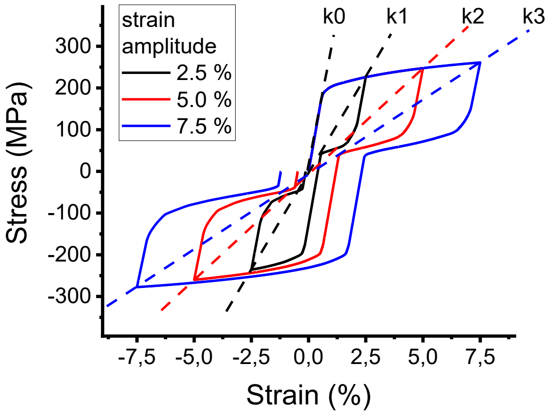

Fig. 6. Two-sided deformation of the TiNi alloy in the austenitic state (temperature of 380 K)

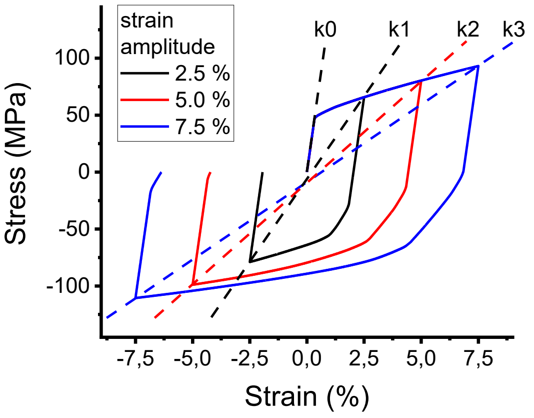

Fig. 7. Two-sided deformation of the TiNi alloy in the martensitic state (temperature of 300 K)

In the martensitic state, the nonlinear response arises from the reorientation of martensite variants. The two-way strain diagrams with amplitudes of 2.5, 5, and 7.5 %, shown in Fig. 7, are qualitatively similar to the strain curves of plastic materials. However, the fundamental difference is that deformation in the SMA is largely reversible. Analysis of the slopes of the secants $k_1 - k_3$ in the Fig. 7 also confirms a decrease in effective stiffness with increasing amplitude of deformation.

The identified nonlinearity forms a positive feedback loop that ensures system adaptation. If the frequency of the external excitation coincides with the natural frequency of the system, determined by the current effective stiffness, this leads to an increase in the oscillation amplitude. In a system with an elastic element, this would cause classical resonance. However, in a system with an SMA, increasing strain leads to a decrease in the effective stiffness, which, in turn, causes a change (decrease) in the system's natural frequency. As a result, the system "moves" away from the resonant frequency of the excitation, limiting the increase in oscillation amplitude.

To quantitatively evaluate the advantages of the SMA for the vibration isolation system under consideration, a comparative simulation of forced vibrations was conducted. Three configurations were studied: with SMA springs in the austenitic and martensitic states, and, for comparison, with conventional linear elastic springs. The stiffness of these reference elastic springs was set equal to the initial stiffness of the austenitic SMA spring (prior to any stress-induced phase transformation), thereby providing a direct baseline for comparison. The excitation was applied with an amplitude of 50 mm in a frequency range of 1 to 6 Hz.

The results, presented in Fig. 8, clearly demonstrate the superiority of SMA-based systems. The configuration with elastic elements exhibits a pronounced resonant peak with a sharp increase in the payload oscillation amplitude. Meanwhile, systems with SMA springs effectively suppress resonant phenomena, preventing a catastrophic increase in amplitude. Moreover, SMA springs in both austenitic and martensitic states, in almost the entire studied frequency range, show a higher efficiency of isolating the payload compared to a linear-elastic analogue.

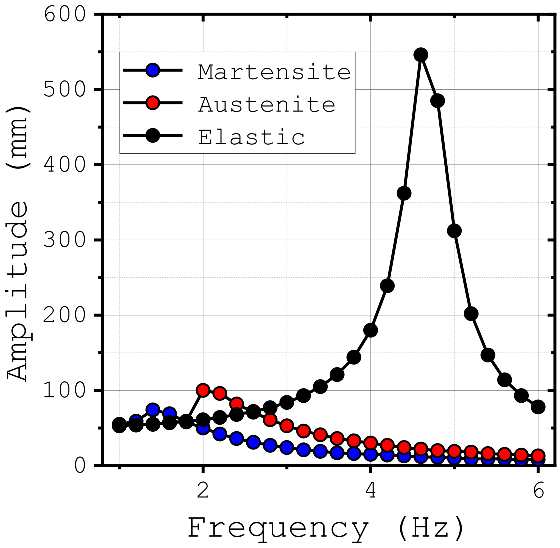

Fig. 8. Dependences of the amplitude of oscillations of the payload on the frequency of the excitation with an amplitude of 50 mm for springs in the martensitic (blue), austenitic (red) states and for the elastic element (black)

The conducted modeling allows for a comparative analysis of the effectiveness of SMA springs in various phase states. As Fig. 8 shows, in the frequency range above 2 Hz, the effective mass oscillation amplitude for springs in the martensitic state is approximately half that of austenitic springs. This effect is explained by the lower effective stiffness and high damping in martensite, caused by the reorientation process.

Therefore, when designing vibration isolation devices, it should be taken into account that the martensitic state is preferable for active vibration damping applications, where the key goal is to minimize vibration amplitude. However, if the priority is maintaining the geometry and self-centering of the structure after strong disturbances, operation in the austenitic state is essential.

Conclusions

This study developed a model of a vibration isolation device based on a TiNi shape memory alloy springs. Using numerical simulation, a comparative analysis of the system's performance was performed with and without MPD. The following key results were obtained:

1. Accounting for microplasticity is critical for accurately predicting the resonant frequencies and damping characteristics of the device at significant loading amplitudes. It was shown that MPD leads to a systematic decrease in the resonant frequency and maximum spring deformations. The magnitude of this effect increases with increasing excitation amplitude.
2. A threshold effect of MPD was established. At low amplitudes (up to ~ 40 mm in the martensitic state), its contribution to the overall system response is negligible, and the device's behavior can be adequately described without taking this mechanism into account.
3. Comparative modeling demonstrated the significant advantage of SMA springs over linear elastic elements. SMA-based devices not only effectively suppress resonance but also reduce vibration amplitudes over a wide frequency range. It was found that the martensitic state provides maximum damping (the amplitudes are reduced by half compared to the austenitic state at frequencies above 2 Hz), while the austenitic state ensures self-centering of device.

Thus, the presented model, which takes MPD into account, enables highly accurate prediction of the behavior of SMA-based vibration protection devices over a wide range of operating conditions and serves as an effective tool for their design.

CRediT authorship contribution statement

Fedor S. Belyaev: conceptualization, investigation, writing – original draft; **Aleksandr E. Volkov**: writing – review & editing, supervision; **Margarita E. Evard**: writing – review & editing, supervision; **Maria S. Starodubova**: investigation.

Conflict of interest

The authors declare that they have no conflict of interest.

References

1. Mohd Jani J, Leary M, Subic A, Gibson MA. A review of shape memory alloy research, applications and opportunities. *Materials & Design (1980-2015).* 2014;56: 1078–1113.

2. Abul H, Safkat TA, Hafiz A. A review of utilizing shape memory alloy in structural safety. *AIUB Journal of Science and Engineering (AJSE).* 2020;19(3): 116–125.
3. Alam MS, Youssef MA, Nehdi M. Utilizing shape memory alloys to enhance the performance and safety of civil infrastructure: a review. *Canadian Journal of Civil Engineering.* 2007;34(9): 1075–1086.
4. Azarbayjani A, Edalat ME, Kheirikhah MM. Earthquake vibration control devices based on shape memory alloys: a review. In: *Proceedings of the 6th International Conference of Seismology and Earthquake Engineering, SEE6-2011, 16–18 May 2011, Tehran, Iran.* Tehran, Iran; 2011.
5. Humbeeck JV, Kustov S. Active and passive damping of noise and vibrations through shape memory alloys: applications and mechanisms. *Smart Materials and Structures.* 2005;14: S171–S185.
6. Kim S. Passive control techniques in earthquake engineering. In: Johnson CD. (Eds.) *Proceedings of the Smart Structures and Materials 1995: Passive Damping, 26 February – 3 March 1995, San Diego, United States.* San Diego, United States; 1995.
7. Buckle IG. Passive control of structures for seismic loads. *Bulletin of the New Zealand Society for Earthquake Engineering.* 2000;33(3): 209–221.
8. Jahangira H, Bagheri M. Evaluation of Seismic Response of Concrete Structures Reinforced by Shape Memory Alloys (Technical Note). *International Journal of Engineering. TRANSACTIONS C: Aspects.* 2020;33(3): 410–418.
9. McCormick J, DesRoches R, Fugazza D, Auricchio F. Seismic Vibration Control Using Superelastic Shape Memory Alloys. *Journal of Engineering Materials and Technology.* 2006;128(3): 294–301.
10. Menna C, Auricchio F, Asprone D. Chapter 13 - Applications of Shape Memory Alloys in Structural Engineering. In: Lecce L, Concilio A. (Eds.) *Shape Memory Alloy Engineering For Aerospace, Structural and Biomedical Applications.* Butterworth-Heinemann; 2015. p.369–403.
11. Somraj D, Surajit D, Purnachandra S. State of art review of shape memory alloy used in civil structures as seismic control device. *IJRET: International Journal of Research in Engineering and Technology.* 2015;04(13): 195–203.
12. Song G, Ma N, Lib HN. Applications of shape memory alloys in civil structures. *Engineering Structures.* 2006;28(9): 1266–1274.
13. Dolce M, Cardone D. Mechanical behaviour of shape memory alloys for seismic applications. Martensite and austenite NiTi bars subjected to torsion. *International Journal of Mechanical Sciences.* 2001;43(11): 2631–2656.
14. Cai W, Lu XL, Zhao LC. Damping behavior of TiNi-based shape memory alloys. *Materials Science and Engineering: A.* 2005;394(1–2): 78–82.
15. Haghdoust P, Conte AL, Cinquemani S, Lecis N. Experimental and Numerical Characterization of High Damping Martensitic CuAlMn Sheets. *Materials.* 2020;13(3): 529.
16. Saedi S, Acar E, Raji H, et al. Energy damping in shape memory alloys: A review. *Journal of Alloys and Compounds.* 2023;956: 170286.
17. Silwal B, Michael RJ, Ozbulut OE. A superelastic viscous damper for enhanced seismic performance of steel moment frames. *Engineering Structures.* 2015;105: 152–164.
18. Shinozuka M, Chaudhuri SR, Mishra SK. Shape-Memory-Alloy supplemented Lead Rubber Bearing (SMA-LRB) for seismic isolation. *Probabilistic Engineering Mechanics.* 2015;41: 34–45.
19. Qiu C, Zhu S. Shake table test and numerical study of self-centering steel frame with SMA braces. *Earthquake Engineering & Structural Dynamics.* 2017;46(1): 117–37.
20. Fang C, Yam MCH, Chan TM, Wang W, Yang X, Lin X. A study of hybrid self-centring connections equipped with shape memory alloy washers and bolts. *Engineering Structures.* 2018;164: 155–168.
21. Wang W, Fang C, Liu J. Self-Centering Beam-to-Column Connections with Combined Superelastic SMA Bolts and Steel Angles. *Journal of Structural Engineering.* 2017;143(2): 04016175.
22. Robertson SW, Pelton AR, Ritchie RO. Mechanical fatigue and fracture of Nitinol. *International Materials Reviews.* 2012;57(1): 1–37.
23. Mahtabi MJ, Shamsaei N, Mitchell MR. Fatigue of Nitinol: The state-of-the-art and ongoing challenges. *Journal of the Mechanical Behavior of Biomedical Materials.* 2015;50: 228–254.
24. Mahtabi MJ, Shamsaei N, Elahinia MH. Fatigue of Shape Memory Alloys. In: Elahinia MH. (Eds.) *Shape Memory Alloy Actuators: Design, Fabrication, and Experimental Evaluation.* John Wiley & Sons; 2015. p.155–190.
25. Tamai H, Kitagawa Y. Pseudoelastic behavior of shape memory alloy wire and its application to seismic resistance member for building. *Computational Materials Science.* 2002;25(1–2): 218–227.
26. Salehi M, Hodgson D, Parnell TK, DesRoches R, Mild E. Experimental evaluation of SMA-based multi-ring damping devices. *Smart Materials and Structures.* 2022;31(11): 115002.
27. Ding C, Wang B, Zhao J, Chen P, Ma K. Seismic resilient reinforced concrete structural wall system with distributed shape memory alloy U-shaped dampers. *Engineering Structures.* 2025;343(D): 121280.

28. Speicher M, Hodgson DE, DesRoches R, Leon RT. Shape Memory Alloy Tension/Compression Device for Seismic Retrofit of Buildings. *Journal of Materials Engineering and Performance.* 2009;18: 746–753.
29. Fang C, Wang W, Zhang A, Sause R, Ricles J, Chen Y. Behavior and Design of Self-Centering Energy Dissipative Devices Equipped with Superelastic SMA Ring Springs. *Journal of Structural Engineering.* 2019;145(10): 04019109.
30. Pappada S, Gren P, Tatar K, Gustafson T, Rametta R, Rossini E, Maffezzoli A. Mechanical and vibration characteristics of laminated composite plates embedding shape memory alloy superplastic wires. *Journal of Materials Engineering and Performance.* 2009;18: 531–564.
31. Zhang RX, Ni QQ, Mauda A, Yamamura T, Iwamoto M. Vibration characteristics of laminated composite plates with embedded shape memory alloys. *Composite Structures.* 2006;74: 389–398.
32. Kothalkar AD, Benitez R, Hu L, Radovic M, Karaman I. Thermo-mechanical response and damping behavior of shape memory alloy—MAX phase composites. *Metallurgical and Materials Transactions A.* 2014;45: 2646–2658.
33. Zhang XX, Hou HW, Wei LS, Chen ZX, Wei WT, Geng L. High damping capacity in porous NiTi alloy with bimodal pore architecture. *Journal of Alloys and Compounds.* 2013;550: 297–301.
34. Huang H, Mosalam KM, Chang W. Adaptive tuned mass damper with shape memory alloy for seismic application. *Engineering Structures.* 2020;223: 111171.
35. Rustighi E, Brennan MJ, Mace BR. A shape memory alloy adaptive tuned vibration absorber: design and implementation. *Smart Materials and Structures.* 2005;14(1): 19.
36. Parlinska M, Balta JA, Michaud V, Bidaux JE, Månson JA, Gotthardt R. Vibrational response of adaptive composites. *Journal de Physique IV.* 2001;11(PR8): 129–134.
37. Parlinska M, Clech H, Balta JA, Michaud V, Bidaux JE, Manson JAE, Gotthardt R. Adaptive composites with embedded shape memory alloys. *Journal de Physique IV.* 2001;11(PR): 197–204.
38. Moradi S, Nia MM. Developing Predictive Equations for the Self-Centering Response of Beam-Column Connections with Steel Angles and Shape Memory Alloy Bolts. In: Gupta R, Sun M, Brzev S, Alam MSh, Ng KTW, Li J, El Damatty A, Lim C. (Eds.) *Proceedings of the Canadian Society of Civil Engineering Annual Conference 2022.* Cham: Springer; 2024. p.1253–1264.
39. Parulekar YM, Reddy GR. Nonlinear Model of Pseudoelastic Shape Memory Alloy Damper Considering Residual Martensite Strain Effect. *Advances in Acoustics and Vibration.* 2012;2012: 261896.
40. Volkov AE, Evard ME, Vikulenkov AV, Uspenskiy ES. Simulation of Vibration Isolation by Shape Memory Alloy Springs Using a Microstructural Model of Shape Memory Alloy. *Materials Science Forum.* 2013;738–739: 150–154.
41. Volkov AE, Evard ME, Red'kina KV, Vikulenkov AV, Makarov VP, Moisheev AA, Markachev NA, Uspenskiy ES. Simulation of Payload Vibration Protection by Shape Memory Alloy Parts. *Journal of Materials Engineering and Performance.* 2014;23: 2719–2726.
42. Evard ME, Volkov AE. Modeling of Martensite Accommodation Effect on Mechanical Behaviour of Shape Memory Alloys. *Journal of Engineering Materials and Technology.* 1999;121(1): 102–104.
43. Simon T, Kröger A, Somsen C, Dlouhy A, Eggeler G. On the multiplication of dislocations during martensitic transformations in NiTi shape memory alloys. *Acta Materialia.* 2010;58(5): 1850–1860.
44. Sidharth R, Mohammed ASK, Sehitoglu H. Functional Fatigue of NiTi Shape Memory Alloy: Effect of Loading Frequency and Source of Residual Strains. *Shape Memory and Superelasticity.* 2022;8: 394–412.
45. Belyaev FS, Volkov AE, Evard ME. Microstructural modeling of fatigue fracture of shape memory alloys at thermomechanical cyclic loading. *AIP Conference Proceedings.* 2018;1959(1): 070003.
46. Belyaev FS, Evard ME, Volkov AE. Simulation of the plastic deformation of shape memory alloys considering shear anisotropy on the slip plane. *Materials Physics and Mechanics.* 2023;51(1): 61–67.
47. Resnina NN, Ivanov AM, Belyaev FS, Volkov AE, Belyaev SP. Simulation of recoverable strain variation during isothermal holding of the Ni51Ti49 alloy under various regimes. *Letters on Materials.* 2023;13(1): 33–38.
48. Volkov AE, Belyaev FS, Volkova NA, Vukolov EA, Evard ME, Rebrov TV. The effect of martensite stabilization in titanium nickelide after various methods of pre-deformation: simulation with a single set of constants. *Materials Physics and Mechanics.* 2024;52(4): 91–99.
49. Belyaev FS, Volkov AE, Vukolov EA, Evard ME, Kudrina KV, Starodubova MS. Influence of latent heat and heat exchange conditions on tension behavior of shape memory alloy specimen. *Materials Physics and Mechanics.* 2024;52(5): 18–28.
50. Belyaev FS, Volkov AE, Gorbachenko DF, Evard ME. Modeling of working cycles of thermomechanical actuators based on shape memory alloys at repeated actuation. *Materials Physics and Mechanics.* 2024;52(6): 81–90.
51. Belyaev FS, Volkov AE, Evard ME, Volkova NA. A Microstructural model of SMA with Microplastic Deformation and Defects Accumulation: Application to Thermocyclic Loading. *Materials Today: Proceedings.* 2015;2(3): S583–S587.
52. Volkov AE, Belyaev FS, Evard ME, Volkova NA. Model of the Evolution of Deformation Defects and Irreversible Strain at Thermal Cycling of Stressed TiNi Alloy Specimen. *MATEC Web of Conferences.* 2015;33: 03013.

MATERIALS PHYSICS AND MECHANICS RESEARCH ARTICLE

Submitted: June 12, 2025 **Revised:** January 20, 2026 **Accepted:** January 28, 2026

Multiple surface crack interaction of non-coplanar cracks

O.M. Al-Moayed [1,2] ✉, **A.E. Ismail** [3], **A.K. Kareem** [4], **S. Jamian** [3]

[1] Department of Scientific Affairs, University of Anbar, Ramadi, Iraq

[2] Renewable Energy Research Centre, University of Anbar, Ramadi, Iraq

[3] Faculty of Mechanical and Manufacturing Engineering, University Tun Hussein Onn Malaysia, Batu Pahat, Malaysia

[4] Biomedical Engineering Department, College of Engineering and Technologies, Al-Mustaqbal University, Babil, Hillah, Iraq

✉ omar.m.f@uoanbar.edu.iq

ABSTRACT

Hollow cylinders represent one of the important elements in the industry. It is widely recognized that fracture characterizes the predominant mode of failure in cylindrical structures, which is precipitated by inherent imperfections or flaws. Over a period, these imperfections (cracks) may propagate and culminate in catastrophic failure, thereby presenting considerable hazards to both the surrounding ecosystem and human safety. Cracks can be single or multiple, and when they are in the multiple form, they can interact to increase pressures that are higher than what the material can withstand. Thus, this paper examines the influence of the interaction between double parallel non-coplanar cracks located on the external surface of a thick hollow cylinder subjected to remote tension and bending loading. Two sorts of separation distances were examined in this study, horizontal (s) and angular (α). The obtained stress intensity factor via finite element analysis was used to quantify the interaction factor along the crack front. The obtained results exhibited that both amplification and shielding interaction impacts could be observed along the crack front for a non-coplanar crack configuration. Additionally, both cracks exhibited the same interaction influence, but in opposite directions. The angular separation distance exhibited a significant influence on the interaction factor, this impact was strongly affected by the shape of the crack.

KEYWORDS

surface cracks • thick cylinder • semi-elliptical crack • crack interaction • non-coplanar cracks

Citation: Al-Moayed OM, Ismail AE, Kareem AK, Jamian S. Multiple surface crack interaction of non-coplanar cracks. *Materials Physics and Mechanics*. 2026;54(1): 57–72.
http://dx.doi.org/10.18149/MPM.5412026_7

Introduction

Hollow cylinders are fundamental components in engineering structures such as aerospace systems, pressure vessels, and pipelines. They are frequently subjected to cyclic loading, internal pressure, and harsh environmental conditions. The development of surface cracks in these structures, due to fatigue, stress corrosion, or manufacturing defects, poses a substantial risk to structural integrity [1]. While single cracks have been broadly studied, the presence of multiple interacting cracks can lead to accelerated crack growth, unexpected stress concentrations, and premature failure. Understanding these interactions is crucial for ensuring the safety and reliability of critical infrastructure. The interaction between multiple surface cracks in hollow cylinders remains a complex and insufficiently understood phenomenon. Closely spaced cracks can influence each other's growth through mechanisms demonstrated by either shielding or amplification [2].

Publisher: Peter the Great St. Petersburg Polytechnic University

This interaction complicates fracture predictions and challenges conventional damage tolerance assessments. Given the potential for catastrophic failures in industrial applications, a deeper investigation into crack interaction effects is essential for improving design standards and maintenance strategies. One of the important criterions in fracture mechanics is the stress intensity factors (SIFs), which can be used efficiently to characterize the crack interaction, particularly in the linear elastic fracture mechanics problems [3].

According to an analysis of cylinder failures that have occurred in service, most of them fall under the fracture sort, meaning that a flaw or crack grows and eventually causes the cylinder to fail [4]. Thus, surface cracks have been widely considered in the literature, either in plates or cylinders (solids and hollow). An efficient numerical method to compute SIFs and simulate coalescence and crack interaction is introduced by [5]. The study integrates principles of fracture mechanics to define fatigue failure to include modelling guidelines for practical implementation. The results revealed that, compared to fracture toughness-based criteria, through-thickness failure provides somewhat more conservative fatigue life predictions. Also, in [6], it was presented a modified strain-based J-integral method using 3D elastic-plastic finite element analysis (FEA). The modified method was utilized to assess circumferential cracks in pipelines subjected to internal pressure and large axial deformation. An analysis of the crack behavior was conducted in [7] by using SIF and J-integral assessment. The failure analysis was performed numerically for a semi-elliptical crack located on a total hip prosthesis. Also, the propagation of a short fatigue crack was predicted in [8] based on a non-local fracture criterion. The study considered non-monotonic crack expansion rate as well as estimating the existence of a single or multiple thresholds of SIF. Besides, in [9], it was experimentally and numerically examined the coalescence and growth of multiple interacting surface cracks. The study displayed that the behavior of crack coalescence was predictable; the study suggests that this method is scalable for multiple-crack structures, maintenance supporting, and safety assessment in engineering structures. In order to predict the crack behavior under dynamic loading [10] examined the stress intensity factors as well as the displacement fields in a rotating hollow cylinder containing an internal crack ring beneath axisymmetric torsion. In another study [11], the plastic stress intensity factor was validated as a more accurate predictor of fatigue life than traditional elastic SIFs. Hence, fatigue crack growth was investigated in a hollow cylinder with a semi-elliptical crack subjected to cyclic tension, torsion, and combined loading. The results indicated that crack growth was accelerated in combined loading compared to pure tension, consequently reducing the fatigue life. In addition, the relationship between SIF and crack velocity was examined numerically by [12]. The finite element methods (FEM) were employed to numerically examine cracks behavior in dual cantilever beam and single notch edge notched samples.

On the other hand, the behavior of cracks caused by explosive loading or blasting was experimentally investigated in [13,14]. A detailed analysis was introduced on the influence of the horizontal and vertical separation distances offsetting the cracks in terms of crack interaction. The stress concentration and distribution along the crack tips were considered. Likewise, the interaction influence between external and internal semi-elliptical cracks located in a pressurized cylinder was investigated via the hybrid boundary element method (HBEM) by [15]. The results showed that both cracks displayed SIFs less than those of isolated (single) cracks. Also, stronger interaction effects were observed for shallow, long cracks. In addition, in [16], it was conducted FEA to evaluate mode I SIFs for single and multiple semi-elliptical cracks positioned in an internally pressurized hollow cylinder for high crack aspect ratios. Based on the results, an empirical formula has been presented to facilitate the prediction of fatigue life as well as integrity assessments in pressurized cylinders. Similarly, the interaction phenomenon in a pressurized cylinder containing two coplanar surface cracks was performed using FEA [17]. This study indicated that there is a direct proportion between the internal pressure and the crack interaction. A 3D FEA was conducted in [18,19] for a hollow cylinder containing an embedded elliptical crack with a semi-elliptical crack, where the Crack Tip Opening Displacement method (CTOD) was applied. The crack orientation, separation distances, and internal pressure levels were examined. The findings displayed that the most severe fracture response was attained under tension loading combined with a high rate of internal pressure. Furthermore, the interaction impact of two similar circumferential cracks on the limit load analysis was investigated in [20]. Therefore, FEA was performed for various crack geometries and interaction criteria. The study proposed new combination rules and indicated that existing codes are conservative, particularly for coplanar cracks, as later supported by [21].

Based on the surveyed literature, it can be concluded that surface crack interaction has been extensively examined. The diversity of these studies lies in one of the following: the cracked body, the crack (orientation, location, and geometry), the number of cracks, separation distances, and loading types. In addition, it has been proven that the SIF criterion is a suitable parameter that could be employed to quantify the interaction phenomenon. Furthermore, several methods can be used to determine the SIFs; however, FEA is more efficient for performing such analyses. Thus, this paper numerically investigates the impact of angular separation distance α (overlapping) on crack interaction. The crack interaction of double parallel non-coplanar cracks is quantified by calculating the interaction factor based on the SIFs. Moreover, different crack geometries and crack separation (horizontal and angular) distances were considered to investigate the influence of the separation distances and crack geometries on crack interaction. The distribution of the normalized SIFs is introduced first, followed by the interaction factor, and finally, the relationship between the angular separation distance and the SIFs is addressed.

Layout of the problem

This study numerically examines a hollow cylinder with double neighboring non-coplanar surface cracks located on the external surface, subjected to separate tension and bending loading as shown in Fig. 1. As described in Fig. 1, this study utilized a straight hollow homogeneous cylinder, with material properties and dimensions explained in Tables 1 and 2, respectively.

It should be noted that both cracks are located on the external surface of the cylinder, and are similar in shape and size, the shape is controlled by a/c, while the depth is controlled by a/t, where a and c represent the depth and length of the crack, respectively. Furthermore, a/c varies from 0.4 to 1.2 to include a variety of slender and transverse crack shapes.

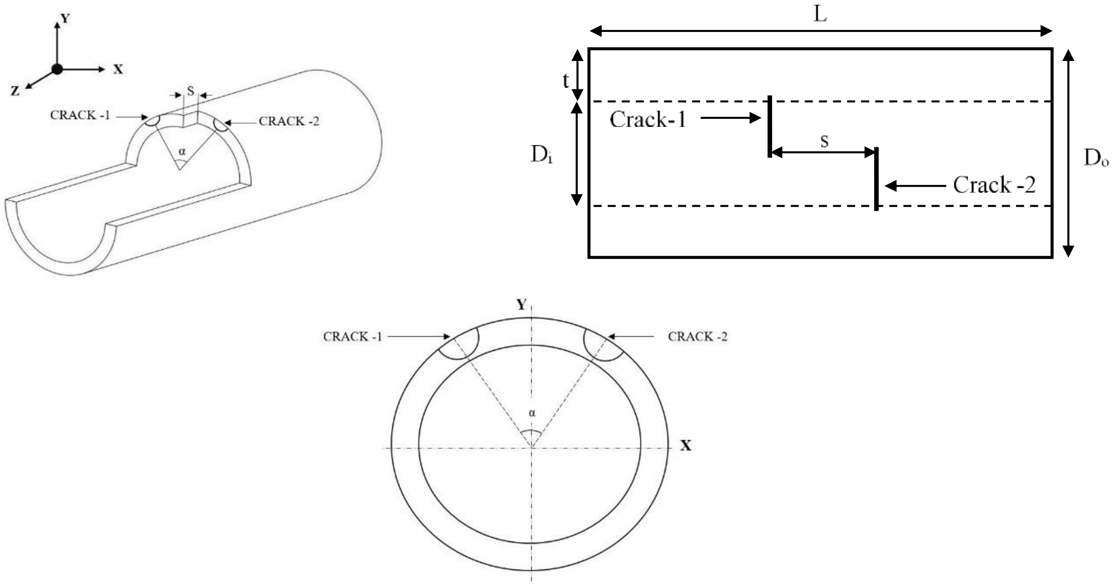

Fig. 1. Problem layout

Table 1. Material properties

Property	Value
Young's modulus, GPa	200
Poisson's ratio	0.3
Tensile yield strength, MPa	250
Tensile ultimate strength, MPa	460

Table 2. Cylinder dimensions

Parameter	Value
Internal diameter D_i, mm	200
Outer diameter D_o, mm	250
Wall-thickness t, mm	25
Length L, mm	750
t/R_i	0.25

Table 3. Crack geometry

a/c	*a/t*	*a*, mm	*c*, mm
0.4	0.2	5	12.5
	0.5	12.5	31.25
	0.8	20	50
0.6	0.2	5	8.3333
	0.5	12.5	20.833
	0.8	20	33.333
0.8	0.2	5	6.25
	0.5	12.5	15.625
	0.8	20	25
1.0	0.2	5	5
	0.5	12.5	12.5
	0.8	20	20
1.2	0.2	5	4.1666
	0.5	12.5	10.416
	0.8	20	16.666

Similarly, *a/t* changes between 0.2, 0.5, and 0.8 to ensure testing shallow and deep cracks throughout the thickness. The examined crack geometries are listed in Table 3.

On the other hand, referring to Fig. 1, the cracks are separated by two separation distances, horizontal (*s*) and angular (α) with respect to the Y-axis. Both horizontal and angular separation distances are recorded in Table 4, where (*s*) is described by the normalized form *s/L*. It should be noted that the *s/L* range was considered as recommended by [22]. It has been reported that 13 mm is the maximum distance at which crack interaction can be detected; otherwise, cracks are considered separate. This means that when the distance between cracks is more than 13 mm, each crack should be considered a single or isolated crack. Therefore, the examined *s/L* reflects the suggested distance and beyond. The purpose of examining beyond stated limits is to verify separation rules.

Table 4. Horizontal and angular separation distances

s/L	*α*, °
0.004	10, 20, 30
0.008	10, 20, 30
0.016	10, 20, 30
0.032	10, 20, 30

Methods

Due to the intricacy of the geometry, finite element methods (FEM) are an effective tool in tackling multiple crack interaction issues [23]. Thus, in this work, the double cracks problem has been modeled and analyzed using Ansys, the finite element (FE) software. Additionally, the stress intensity factor (SIF) is utilized to define the crack interaction phenomenon, where the calculated SIFs are then normalized for each loading type according to the following [24]:

$$F_t = \frac{K_{cal,t}}{\sigma_t \sqrt{\pi a/Q}}, \tag{1}$$

where F_t is the normalized SIFs under remote tension loading, $K_{cal,\,t}$ is the calculated SIFs under tension (extracted from Ansys), σ_t is the axial stress, where $\sigma_t = P/\pi\ (R^2_o - R^2_i)$, *P* is the remote applied force, and R_o and R_i represent the outer and inner radius of the cylinder, individually. Besides, *a* is the crack depth, and *Q* is the shape factor defined by [25]:

$$Q = 1 + 1.464({}^{a}/_{c})^{1.65} \text{ for a/c} \leqslant 1, \tag{2}$$

$$Q = 1 + 1.464({}^{c}/_{a})^{1.65} \text{ for a/c} > 1. \tag{3}$$

On the other hand, for bending loading, the SIFs are normalized according to the following equation [26], where F_{Ben} is the standardized SIFs underneath remote bending, $K_{cal,\,b}$ is the calculated SIFs under bending (which are extracted from Ansys), σ_b is the maximum bending stress:

$$F_{Ben} = \frac{K_{cal,b}}{\sigma_b \sqrt{\pi a/Q}}. \tag{4}$$

After obtaining the normalized SIFs for each type of loading, as previously discussed, the interaction factor has to be identified. In order to calculate the interaction factor Ψ, which is defined as the ratio of the nondimensional SIFs for the case of two cracks to that of a single crack, the following equation is utilized [27]:

$$\Psi = \frac{F_{two\ cracks}}{F_{single\ crack}}. \tag{5}$$

It should be remarked that $F_{two\ cracks}$ and $F_{single\ crack}$ denote standardized SIFs for the case of two and single cracks, respectively. This procedure applies to all examined configurations and loading types. Furthermore, it should be noted that Ψ describes the crack interaction impact, where (Ψ = 1) indicates that there is no crack interaction, while (Ψ < 1) shows that shielding impact, and (Ψ > 1) illustrates the amplification influence between the cracks.

Results

This section introduces the obtained results in this study, where the orientation of the SIFs along the crack front is discussed first, then the interaction factor, and finally, the influence of the inclination angle on the crack interaction is investigated. It ought to be noted that the exploited model for this research was the same as that which has been used by [28].

Distribution of SIFs

The distribution of the normalized SIFs along the crack front is presented in this section, where the normalized SIFs for different crack geometrical parameters are introduced as a function of the normalized crack front position, $2\theta/\pi$. Furthermore, any point on the crack front is described by using θ, where $-90 \leqslant \theta \leqslant 90$, as shown in Fig. 2. Thus, $2\theta/\pi = 1$ at point A, 0 at point B, and -1 at point C.

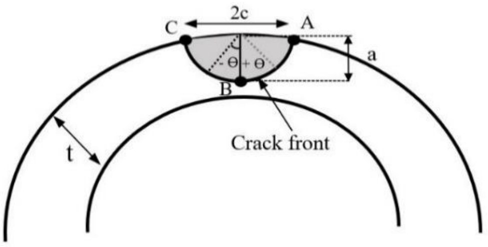

Fig. 2. Crack geometry with points on the crack front

Due to the similar trend revealed by the SIFs with respect to α of the two cracks under each tension and bending loading, the normalized SIFs of one crack for $a/c = 0.4$ and 1.2 are presented in this section for $\alpha = 10°$ only. On the other hand, the remaining values are discussed in terms of the impact of α with respect to a/c. It should be noted that the normalized SIF for the case of a single crack is presented in figures epitomized by F_SINGLE, while SIFs of two cracks are categorized based on the horizontal separation distance, F2 – s/L (0.004, 0.008, 0.016, 0.032).

Figure 3 shows the trend of the normalized SIFs for external noncoplanar parallel cracks under remote tension loading, F_t, for inclination angle $\alpha=10°$, when $a/c = 0.4$ for $a/t = 0.2$, 0.5, and 0.8. Due to cracks overlapping, the interaction between the cracks affected the overall curve shape of the F2 for the double cracks compared to F_SINGLE. In the case of completely parallel cracks [28], the trend of the normalized SIFs for double parallel cracks followed an exactly similar curve to that of F_SINGLE for all the examined s/L, except it was less in value due to the shielding phenomenon. However, in the presence of overlapping between cracks, F2 for all examined s/L ratios exhibited amplification and shielding effects simultaneously.

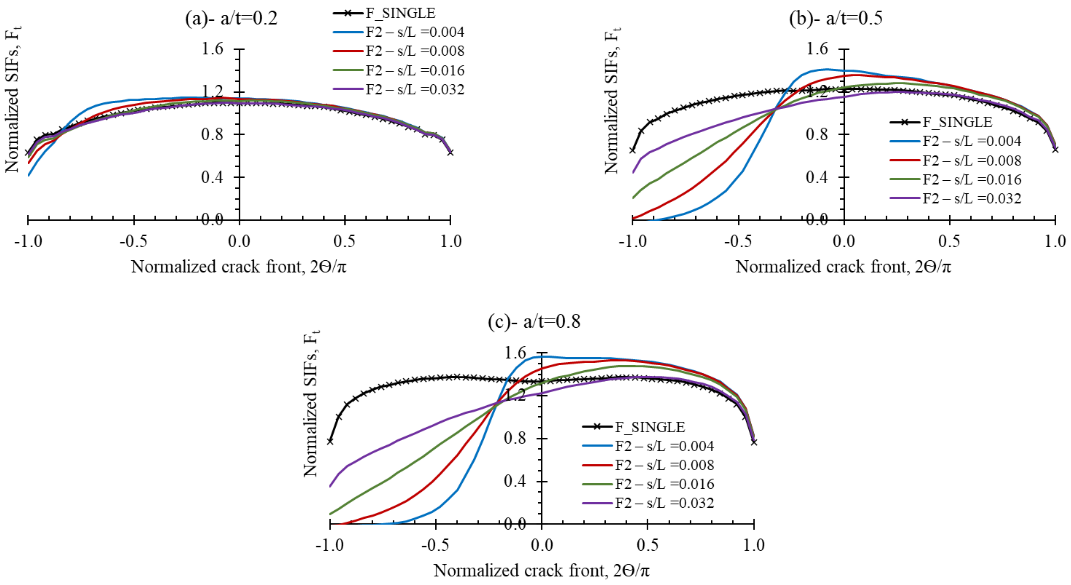

Fig. 3. SIFs under tension for *a/c* = 0.4, *α* = 10°

Additionally, Fig. 3 revealed that for a specific crack shape ratio, *a/c*, the relative depth of the crack, *a/t*, has a strong influence on F_t. Moreover, for *a/t* = 0.2, this impact was found to be tiny for all inspected *s/L*, while for *a/t* ⩾ 0.5, the impact was more pronounced for all observed *s/L* values. On the other hand, the shielding effect occurs within the zone of cracks overlap, while the amplification appears at the point of overlapping, radiates outward, and subsequently decays.

Furthermore, from Fig. 3, it can be inferred that *s/L* displayed insignificant influence on the crack interaction for *a/t* < 0.5, while for *a/t* ⩾ 0.5, the effect was more distinct. The maximum crack interaction influence was attained for F2 – *s/L*= 0.004, which is the smallest horizontal separation distance between the cracks, while the minimum was observed for F2 – *s/L* = 0.032. Despite *s/L* = 0.032 being greater than the limits introduced in [22], it is obvious that F2 – *s/L* = 0.032 did not approach F_SINGLE, due to the presence of a crack interaction, and the two cracks can not be considered isolated. Thus, relying on [22] for structural integrity assessment could lead to underestimation or conservative results, as confirmed by [29]. Moreover, it has been stated that the usage of combination rules presents too much conservatism in the assessment, especially for interacting cracks.

Similarly, Fig. 4 illustrates the normalized SIFs' orientation for non-coplanar cracks exposed to remote tension loading for *a/c* = 1.2 when the inclination angle, *α* = 10°. The increase in the crack aspect ratio displayed that *a/t* behaved in the same manner that was remarked for small *a/c*, except that the interacting cracks were isolated when reaching the maximum separation distance, *s*. This might be interpreted as a high *a/c*; the depth of the crack is greater than the length of the crack, accordingly, the length of the crack has a significant impact on the SIFs.

Alternatively, for shallow cracks, *a/t* = 0.2, the crack interaction was found to be insensitive to the change in horizontal separation distance, while for *a/t* = 0.5, the crack interaction was demonstrated by the amplification effect only. As well, for deep cracks, *a/t* = 0.8, the interaction among the cracks demonstrated by both shielding and magnification, which is the same behaviour that has been noticed for *a/c* = 0.4.

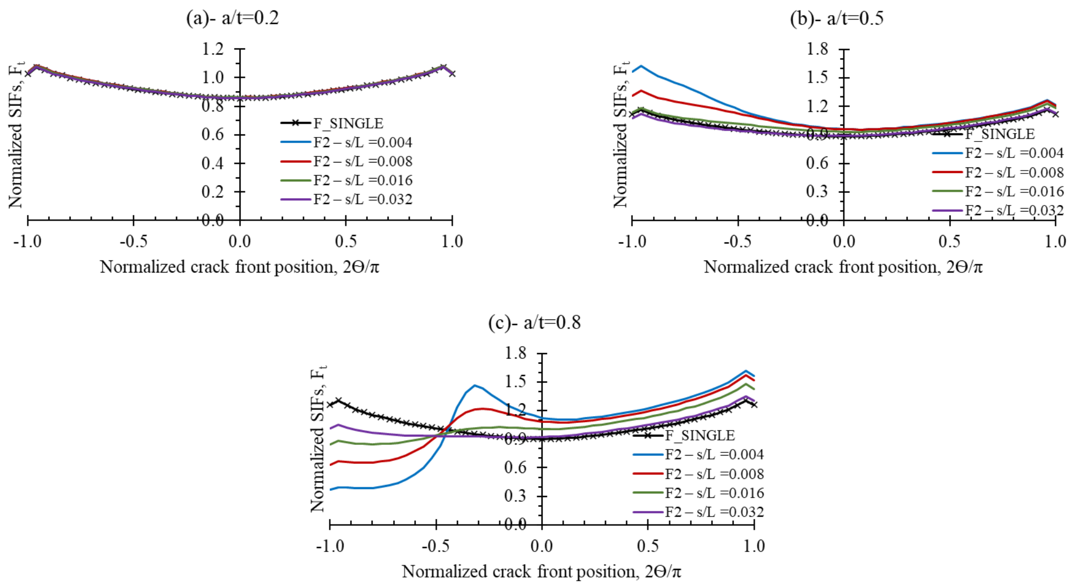

Fig. 4. SIFs under tension for *a/c* = 1.2, *α* = 10°

Figures 5 and 6 display the diffusion of the standardized SIFs for the non-coplanar parallel cracks under remote bending loading, F_{Ben}, for the overlapping ratio defined by *α* = 10°, when *a/c* = 0.4 and 1.2 for *a/t* = 0.2, 0.5, and 0.8. Apparently, the distribution of F_{Ben} for all evaluated *s/L* exhibited a similar trend to that found under tension loading, except that the bending SIFs are slightly less. Additionally, F_{Ben} tendency shown bared that *a/t* has a notable influence on F_{Ben}, however, for *a/t* = 0.2, this effect was found to be negligible for all tested *s/L* ratios, whereas for *a/t* = 0.5 and 0.8, the impact was more evident for all *s/L*. Also, it can be inferred that for low and high crack aspect ratios, shallow cracks (*a/t* ⩽ 0.4), were found to be unresponsive to the change in *s/L*, the impact is extra remarkable for higher values. Nevertheless, the interacting cracks were isolated when *s/L* = 0.032 for a high aspect ratio, while for a low aspect ratio, the influence of each crack on the other still exists.

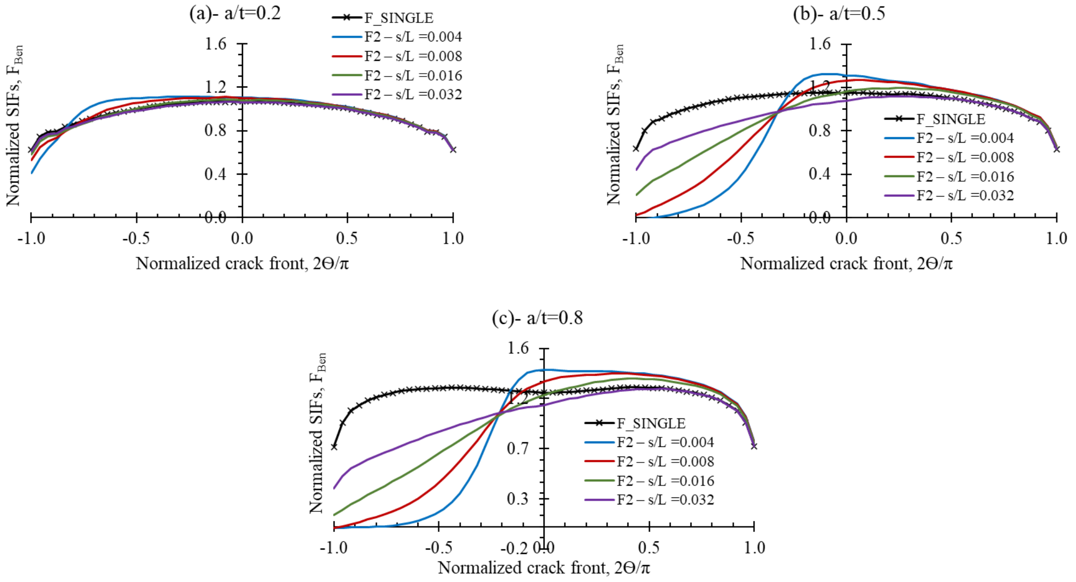

Fig. 5. SIFs under bending for *a/c* = 0.4, *α* = 10°

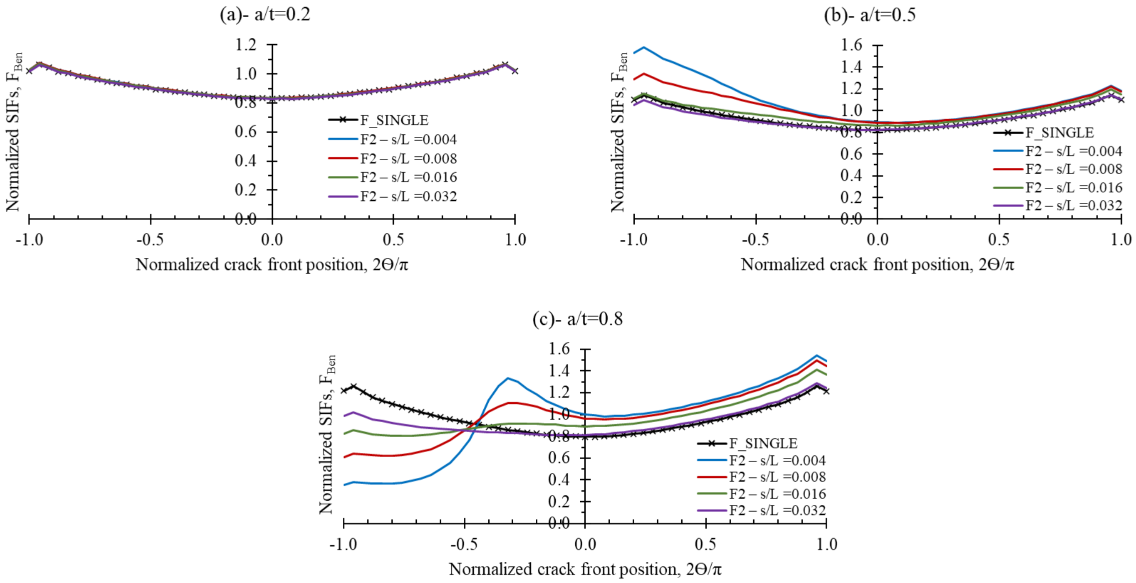

Fig. 6. SIFs under bending for *a/c*=1.2, *α* = 10°

Interaction factor

This section introduces the interaction factor Ψ, which is calculated by Eq. (5), for external non-coplanar parallel cracks subjected to remote tension loading for the examined crack geometry presented in the previous section, *α* = 10°, for *a/c* = 0.4 and 1.2. Moreover, the remaining examined configuration will be discussed in the next section in terms of the effect of the inclination angle. It should be noted that *Ψ* is presented for three points on the crack front A, B, and C, as shown in Fig. 2, A and C are the edge points, and C is the point that lies inside the overlapping zone, while B is the deepest point on the crack front. Furthermore, the influence of crack interaction on SIFs could be demonstrated by three classes. Firstly, enhancement (amplification), which is attained when nondimensional SIFs of two cracks are higher than those of a single crack. The second category is the shielding impact, which is the opposite of amplification; standardized SIFs of a single crack are greater than those of two cracks. Third class is the no interaction situation, when no significant difference in the SIFs of single and double cracks; thus, each crack is treated as an isolated crack. It is worth declaring that this study assumed that, for (Ψ = 1 ± 0.05), there was no interaction, which is the same tolerance ratio considered by [30]. Table 5 elucidates the interaction factor Ψ for external parallel non-coplanar cracks exposed to remote tension when *α* = 10°, *a/c* = 0.4 for different crack depths.

Table 5. Ψ for noncoplanar parallel cracks under tension when *α* = 10°, *a/c* = 0.4

a/t	Point	*s/L* = 0.004	*s/L* = 0.008	*s/L* = 0.016	*s/L* = 0.032
0.2	**A**	1.024	1.017	1.015	1.007
	B	1.040	1.037	1.019	0.998
	C	0.657	0.839	0.930	0.969
0.5	**A**	1.060	1.061	1.053	1.019
	B	1.142	1.101	1.014	0.943
	C	-0.036	0.024	0.318	0.683
0.8	**A**	1.081	1.077	1.065	1.026
	B	1.174	1.090	0.991	0.916
	C	-0.015	-0.023	0.123	0.461

Furthermore, it can be observed that *s/L* exhibited a substantial influence on Ψ. This impact was recognized by magnification and shielding, where the maximum interaction influence was observed for small *s/L*, representing the closest distance between the two cracks. This impact gradually diminished as the two cracks became isolated. In fact, at the maximum examined separation distance *s/L* = 0.032, the cracks with *a/t* = 0.2 have been isolated, and there is no discernible influence between the cracks at A, B, and C. On the other hand, cracks with *a/t* ⩾ 0.5, have no interaction influence at point A, which is the farthest point from the overlapping region, while at points B, and C, the F_t did not approach F_SINGLE, therefore, Ψ value was less than 1.0, which means crack interaction is still affecting. It is worth noting that the negative values of Ψ, which have been seen at point C, for *s/L* = 0.004, denote a change in the crack opening direction, which was changed due to the interaction effect from opening mode to closing mode.

In addition, for the maximum horizontal separation distance *s/L* = 0.032, at point A (the distant point from the region that overlaps), no crack interaction effect is recognized for all examined *a/t*. Equally, an approximately similar trend was recognized at point B (the deepest point at the crack front). However, at point C, the impact of crack interaction still exists when *a/t* = 0.8, where the SIFs value reduction equals 53.9 %.

Table 6 illustrates the quantified interaction factor for non-coplanar interacting cracks subjected to tension loading when *α* = 10°, *a/c* = 1.2. Unlike for shallow cracks (*a/c* = 0.4), Ψ is shown to be insensitive to the change in *s/L* for *a/t* = 0.2, where all Ψ values approach 1 at all crack front points (A, B, and C) for all examined *s/L*, which indicates no interaction. On the other hand, for *a/t* = 0.5, a slight amplification impact has been noticed at points A and B, while at point C, Ψ increased by about 39.6 % due to interaction when *s/L* = 0.004.

Table 6. Ψ for non-coplanar parallel cracks under tension when *α* = 10°, *a/c* = 1.2

a/t	Point	*s/L* = 0.004	*s/L* = 0.008	*s/L* = 0.016	*s/L* = 0.032
0.2	**A**	1.007	1.007	1.007	1.001
	B	1.005	1.006	1.006	0.999
	C	1.011	1.012	1.008	1.001
0.5	**A**	1.085	1.078	1.055	1.011
	B	1.087	1.085	1.055	1.007
	C	1.396	1.175	1.012	0.958
0.8	**A**	1.241	1.205	1.135	1.035
	B	1.249	1.205	1.117	1.022
	C	0.293	0.503	0.673	0.804

Table 7. Interaction factor Ψ, under tension loading for *a/c* = 0.4 and 1.2

a/t	Points	*s/L* = 0.004		*s/L* = 0.032	
		a/c = 0.4	*a/c* = 1.2	*a/c* = 0.4	*a/c* = 1.2
0.2	**A**	1.024	1.007	1.007	1.001
	B	1.040	1.005	0.998	0.999
	C	0.657	1.011	0.969	1.001
0.5	**A**	1.060	1.085	1.019	1.011
	B	1.142	1.087	0.943	1.007
	C	-0.036	1.396	0.683	0.958
0.8	**A**	1.081	1.241	1.026	1.035
	B	1.174	1.249	0.916	1.022
	C	-0.015	0.293	0.461	0.804

Meanwhile, for *a/t* = 0.8, magnification impact was recognized at each A and B, and this influence gradually decreased until reaching the maximum *s/L*. Yet, at C, a reduction in the SIFs resulted due to the crack interaction in terms of shielding impact, the SIFs decreased by 70.7 % when *s/L* = 0.004. It should be noted that when *s/L* = 0.032 exceeds the (13 mm) recommended by [22], Ψ did not approach 1, which means that both cracks still affect each other. This result aligns with the observed impact for *a/c* = 0.4 under tension loading as mentioned earlier.

It should be noted that by examining points A, B, and C in Tables 5 and 6, under tension loading, the increment in *a/c* displayed different impacts on Ψ, as shown in Table 7. The documented behavior for *s/L* = 0.004, points A and B presented similar performance in terms of amplification, shielding, and no interaction, except Ψ for *a/c* = 1.2, slightly higher. However, at point C, for *s/L* = 0.004, a shielding influence was recognized for *a/c* = 0.4, while no interaction was found at the same point for *a/c* = 1.2. In addition, for *a/t* = 0.5, at point C, 39.6 % enhancement resulted due to the change in crack shape, *a/c* = 1.2, while a complete reduction was found for *a/c* = 0.4. It is possible to clarify this discrepancy in terms of the shape of the crack, which strongly influences the interaction phenomenon; deep sharp cracks (*a/c* = 1.2) have more opportunity to show amplification effect than shielding, unlike wide shallow cracks (transverse cracks). On the other hand, despite *s/L* = 0.032 exceeding the limits suggested in [22], crack interaction is still remarkable at point C, especially for *a/t* ⩾ 0.5. Again, the results indicated that the present crack interaction alignment rules might produce underestimation in the stresses or conservative results.

Table 8. Ψ for noncoplanar parallel cracks under bending when $\alpha = 10°$, *a/c* = 0.4

a/t	Point	*s/L* = 0.004	*s/L* = 0.008	*s/L* = 0.016	*s/L* = 0.032
0.2	**A**	1.010	1.004	1.001	0.994
	B	1.037	1.033	1.015	0.994
	C	0.662	0.844	0.937	0.975
0.5	**A**	1.042	1.043	1.036	1.002
	B	1.139	1.097	1.009	0.937
	C	-0.030	0.037	0.334	0.695
0.8	**A**	1.046	1.042	1.031	0.992
	B	1.172	1.085	0.983	0.908
	C	-0.011	-0.011	0.144	0.484

Table 9. Ψ for noncoplanar parallel cracks under bending when $\alpha = 10^{\circ}$, *a/c* = 1.2

a/t	Point	*s/L* = 0.004	*s/L* = 0.008	*s/L* = 0.016	*s/L* = 0.032
0.2	**A**	1.002	1.002	1.002	0.996
	B	1.001	1.003	1.003	0.995
	C	1.008	1.009	1.005	0.998
0.5	**A**	1.074	1.068	1.045	1.002
	B	1.087	1.084	1.053	1.003
	C	1.392	1.172	1.012	0.960
0.8	**A**	1.226	1.190	1.122	1.024
	B	1.259	1.213	1.121	1.020
	C	0.292	0.503	0.676	0.809

Tables 8 and 9 describe Ψ for non-coplanar parallel interacting cracks subjected to bending loading when $\alpha = 10°$ for $a/c = 0.4$ and 1.2. In general, Ψ behavior was similar to that obtained under tension loading for similar *a/c*, where *s/L* exhibited a significant effect on Ψ; as soon as *s/L* declined, the impact of crack interaction decreased. In addition, cracks with $a/t = 0.2$ were isolated for $s/L = 0.032$ at each of A, B, and C, but for cracks with $a/t \geqslant 0.5$, the interaction effect was still pronounced, especially at point C, the nearest point to the second crack.

Influence of angular separation distance

In order to visualize the relationship between the inclination angle and the normalized SIFs in terms of crack interaction, it is necessary to present the SIFs as a function of the inclination angle (or could be used as the overlapping angle). Based on the results presented in the previous section, it was found that the maximum interaction influence was always attained when $s/L = 0.004$ and $a/t = 0.8$. Where $s/L = 0.004$ demonstrates the smallest separation distance between the cracks, while $a/t = 0.8$ represents the deepest relative crack depth ratio. Therefore, the separation distance $s/L = 0.004$ and $a/t = 0.8$ have been selected to present the effect of inclination angle on the distribution of the normalized SIFs since both ratios produced the maximum interaction influence.

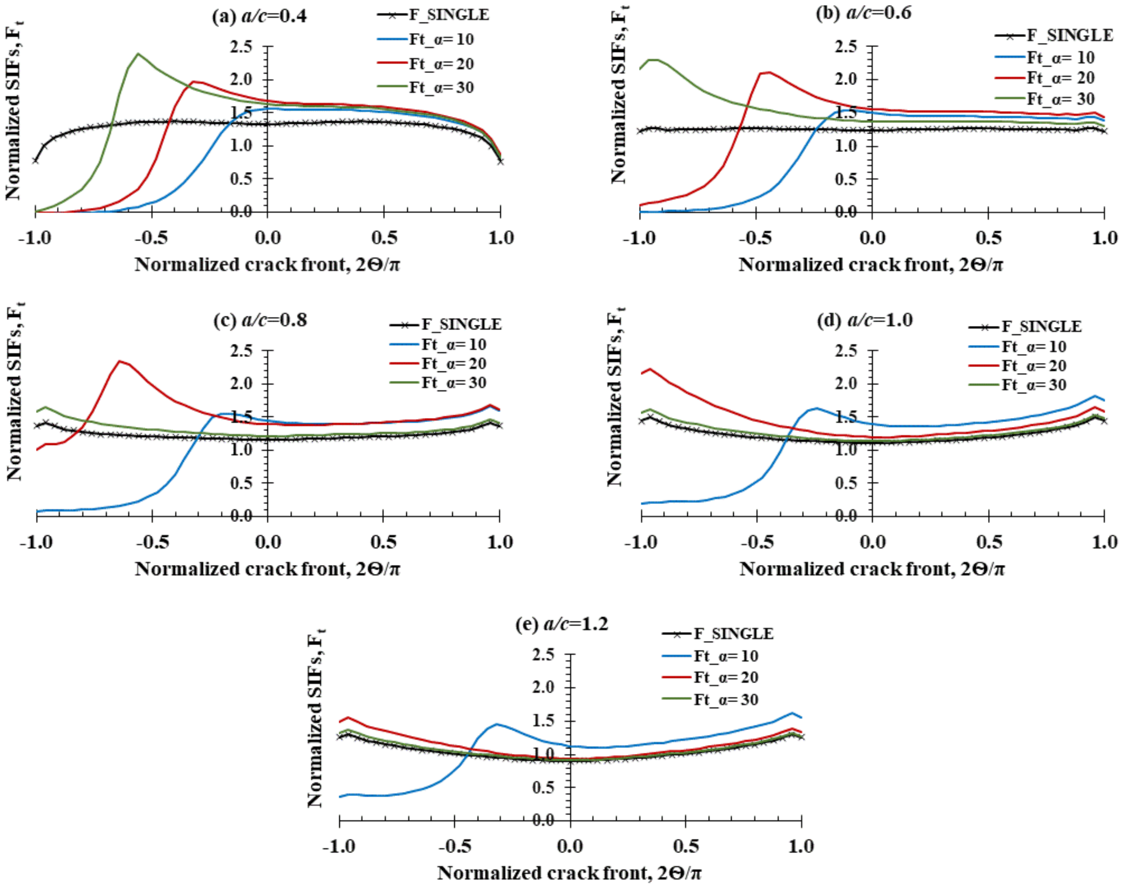

Fig. 7. Relationship between (*α*) and (*a/c*) for $a/t = 0.8$, and $s/L = 0.004$ under tension loading

Figure 7 displays the impact of different inclination angles on the distribution of the normalized SIFs as a function of the crack aspect ratio, *a/c*, under remote tension loading for a non-coplanar parallel cracks configuration when *s/L* = 0.004 and *a/t* = 0.8. Furthermore, to comprise a wide diversity of crack shapes, the crack aspect ratio is considered to be varied from 0.4 to 1.2, which has been presented in Fig. 7(a–e), respectively. Also, the considered inclination angles are α = 10, 20, and 30°.

Obviously, the inclination angle α has a significant influence on crack interaction behavior, and this effect strongly depends on the examined *a/c*, which has produced different impacts. The increase in the *a/c* ratio is accompanied by the decrease in F_t, which indicates that sharp cracks are riskier or more serious than transverse cracks, where for the same α value, the peak F_t is attained when *a/c* = 0.4, while the minimum is when *a/c* = 1.2.

On the other hand, α produced unique behaviors, depending on the examined *a/c*. Moreover, for α = 10°, the F_t distribution followed an approximately similar trend along the crack front with respect to the change in *a/c*, where the amplification effect was noticed in the region from $2\theta/\pi = -0.2$ to 1.0 on the crack front, and the shielding effect was recognized from $2\theta/\pi = -0.2$ to -1, this effect applied to all examined *a/c* ratios, where with the increase of *a/c*, the area that experiences the amplification impact increases also.

Also, for $\alpha = 20°$, the F_t was distributed in two different styles, for $a/c < 1.0$, F_t exhibited both amplification and shielding effects along the crack front, whilst for $a/c \geqslant 1.0$, a severe amplification effect was noticed in the overlapping zone, and a minor amplification impact was observed far away from the overlapping zone. It should be noted that during the change in *a/c* from 0.8 to 1.0 for α = 20°, the F_t behavior switched from the shielding and amplification mixed behavior to the pure amplification impact.

Similarly, for α = 30°, it has been found that for this inclination angle, the influence on the F_t distribution was more pronounced for $a/c \leqslant 0.8$, where it presented both interaction influences amplification and shielding. It should be noted that throughout the change in *a/c* from 0.4 to 0.6 for α = 30°, the F_t behavior exhibited pure amplification impact instead of the combination of shielding and amplification impacts. Moreover, for $a/c \geqslant 1.0$, the inclination angle α = 30° has no significant influence on the distribution of F_t along the crack front.

In the same way, Fig. 8 displays the relationship between α and the normalized SIFs under bending F_B. It is obvious that the impact of α on F_B was found to be similar to that obtained under tension loading, except that F_B was less than F_t. This influence is understandable since SIF for the case of a single crack under tension loading is higher than that under bending loading. However, it was found that the positions where the maximum SIFs are attained along the crack front under each tension and bending are similar, as indicated in Table 10.

Table 10. Maximum normalized SIFs under different types of loading

a/c	**α = 10°**				**α = 20°**				**α = 30°**			
	$2\theta/\pi$	**F_t**	**$2\theta/\pi$**	**F_B**	**$2\theta/\pi$**	**F_t**	**$2\theta/\pi$**	**F_B**	**$2\theta/\pi$**	**F_t**	**$2\theta/\pi$**	**F_B**
0.4	0	1.56	0	1.40	-0.32	1.97	-0.32	1.79	-0.56	2.39	-0.56	2.19
0.6	-0.08	1.54	-0.08	1.38	-0.44	2.11	-0.44	1.93	-0.92	2.29	-0.92	2.16
0.8	0.96	1.66	0.96	1.57	-0.64	2.34	-0.64	2.18	-0.96	1.64	-0.96	1.55
1.0	0.96	1.82	0.96	1.72	-0.96	2.22	-0.96	2.12	-0.96	1.61	-0.96	1.53
1.2	0.96	1.61	0.96	1.54	-0.96	1.55	-0.96	1.48	-0.96	1.36	-0.96	1.29

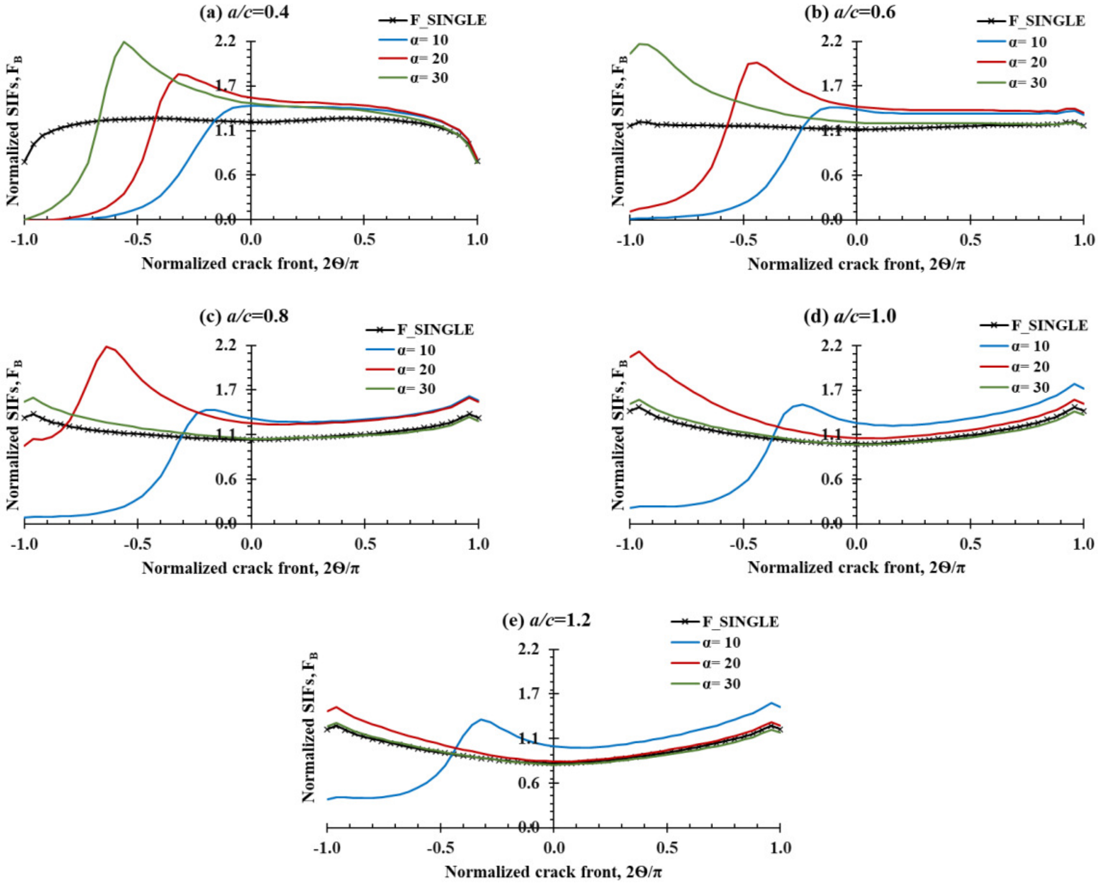

Fig. 8. Relationship between (α) and (a/c) for $a/t = 0.8$, and $s/L = 0.004$ under bending loading

The position on the crack front is defined by the normalized form ($2\Theta/\pi$), where Θ is the parametric angle of the crack, $2\Theta/\pi = 0$ (B, at the deepest point), 1 (A, farthest point with respect to the overlapping zone), and -1 (C, the point within the overlapping zone) Fig. 2. From Table 10, it can be inferred that the maximum F_t and F_B were attained at the same position on the crack front for all examined a/c. Furthermore, for $a/c \leqslant 0.6$, the increase in α was accompanied by an increment in F_t and F_B, while for $0.6 < a/c \leqslant 1.0$, when α advances, F_t and F_B rise until $\alpha = 30°$, where both F_t and F_B exhibited a drop in value. Finally, for $a/c > 1.0$, the increase in the overlap region between the cracks produced a decrease in F_t and F_B. This indicates that the interaction phenomenon reduces as the cracks turn into a transverse shape with respect to the increment in the overlapping angle.

Conclusion

The impact of crack orientation on surface crack interaction has been investigated numerically via finite element analyses. A thick hollow cylinder was considered with double parallel non-coplanar cracks with different crack geometries subjected to tension and bending loading. Based on the results, the interaction influence for the non-coplanar cracks showed amplification and shielding impacts simultaneously along the crack front. The shielding effect is recognized on one side of the crack front (in the overlapping region), while the other side of the crack front shows the amplification effect. This inconsistency in the interaction influence is triggered by the non-coplanar orientation.

Moreover, in the region of overlap, the shielding effect occurs due to the partial parallel orientation, thus the shielding impact appears. But, on the other side of the crack front or the region out of the overlapping zone, the amplification effect occurs. This indicates that for such kinds of crack configurations, the riskiest region is the zone that lies outside the parallel case, or simply, there is no crack in front of this region. This is because the crack will propagate from this region and lead to cylinder failure. It is evident that the presence of the second crack in a completely (or partially) parallel orientation will provide more resistance to the cylinder, where a mutual closing effect is offered by the two cracks towards each other. It should be noted that the inclination angle (or the angular distance), along with a change in *a/c*, provided a unique influence on the SIFs allocation. Furthermore, both α and *a/c* have a significant impact on the crack interaction, since both can convert Ψ from pure shielding to amplification, which may lead to crack extension.

CRediT authorship contribution statement

Omar Mohammed Al-Moayed : writing – original draft, conceptualization, data curation; **Al Emran Ismail** : writing – review & editing, conceptualization, supervision; **Ali Kamil Kareem** : writing – original draft, investigation, data curation; **Saifulnizan Jamian** : writing – review & editing, supervision, investigation.

Conflict of interest

The authors declare that they have no conflict of interest.

References

1. Yang Y, Lam CC, Kou KP. Fatigue life analysis of internal circumferential crack of tubular structures. *International Journal of Damage Mechanics*. 2015;24(5): 711–727.
2. Wang H, Liu Z, Xu D, Zeng Q, Zhuang Z. Extended finite element method analysis for shielding and amplification effect of a main crack interacted with a group of nearby parallel microcracks. *International Journal of Damage Mechanics*. 2016;25(1): 4–25.
3. Anderson TL. *Fracture mechanics: fundamentals and applications*. 4th ed. Boca Raton: CRC press; 2017.
4. Marshall P. *The residual structural properties of cast iron pipes: structural and design criteria for linings for water mains*. UKWIR; 2001.
5. Mishael J, Morato PG, Rigo P. Numerical fatigue modeling and simulation of interacting surface cracks in offshore wind structural connection. *Marine Structures*. 2023;92: 103472.
6. Zhao D, Gao W, Zhao K, Zheng H, Chen J, Yu J, Zheng Z. A strain-based J-integral formulation for an internal circumferential surface crack of pipeline under inner pressure and large axial deformation. *International Journal of Pressure Vessels and Piping*. 2024;212: 105316.
7. Zahaf S, Dahmane M, Belaziz A, Bouri I, Afane N. Failure analysis of semi-elliptical crack behavior in the cement mantle of a total hip prosthesis. *Materials Physics and Mechanics.* 2022;48(2): 242–271.
8. Nosikov AI, Semenov AS, Melnikov BE, Rayimberdiyev TP. Prediction of short fatigue crack propagation on the base of non-local fracture criterion," *Materials Physics and Mechanics*. 2017;31(1–2): 44–47.
9. Kikuchi M. Study on multiple surface crack growth and coalescence behaviors. *AIMS Mater Sci*. 2016;3(4): 1623–1631.
10. Zhuravlova Z, Istenes I, Peck D, Protserov Y, Vaysfeld N. Hidden ring crack in a rotating hollow cylinder under torsion. *Int J Eng Sci*. 2024;194: 103976.
11. Shlyannikov V, Yarullin R, Ishtyryakov I. Surface crack growth in cylindrical hollow specimen subject to tension and torsion. *Fracture and Structural Integrity*. 2015;9(33): 335-344.
12. Kazarinov NA, Petrov YV, Bratov VA, Slesarenko VY. Numerical investigation of stress intensity factor – crack velocity relation for a dynamically propagating crack. *Materials Physics and Mechanics*. 2016;29(1): 39–42.

13. Peng L, Yue Z, Wang X, Zhou J. Experimental study on the interaction mechanism of two dynamic cracks under blasting loading. *International Journal of Rock Mechanics and Mining Sciences*. 2024;184: 105956.
14. Peng L, Yue Z, Wang X, Zhou J. Experimental study on interaction characteristics of explosive cracks under confining pressure and its comparison with free boundary results. *Journal of Materials Research and Technology*. 2024;33: 4637–4653.
15. Guozhong C, Zhimin F, Xianfeng J, Gan L. Analyses on interaction of internal and external surface cracks in a pressurized cylinder by hybrid boundary element method. *International Journal of Pressure Vessels and Piping.* 2004;81(5): 443–449.
16. Kirkhope KJ, Bell R, Kirkhope J. Stress intensity factors for single and multiple semi-elliptical surface cracks in pressurized thick-walled cylinders. *International Journal of Pressure Vessels and Piping.* 1991;47(2): 247–257.
17. Kim D. S, Lo KH. Crack Interaction Criteria in Pressure Vessels and Pipe. *Journal of Offshore Mechanics and Arctic Engineering.* 1995;117(4): 260–264.
18. Zhang YM, Ariffin MZ, Xiao ZM, Zhang WG, Huang ZH. Nonlinear elastic--plastic stress investigation for two interacting 3-D cracks in offshore pipelines. *Fatigue Fract Eng Mater Struct.* 2015;38(5): 540–550.
19. Zhang Y, Fan M, Xiao Z. Nonlinear elastic-plastic stress investigations on two interacting 3-D cracks in offshore pipelines subjected to different loadings. *AIMS Mater Sci*. 2016;3(4): 1321–1339.
20. Kamaya M. A combination rule for circumferential surface cracks on pipe under tension based on limit load analysis. *J Press Vessel Technol.* 2011;133(2): 021205.
21. Coêlho GC, Silva AA, Santos MA, Lima AGB, Santos NC. Stress Intensity Factor of Semielliptical Surface Crack in Internally Pressurized Hollow Cylinder—A Comparison between BS 7910 and API 579/ASME FFS-1 Solutions. *Materials*. 2019;12(7): 1042.
22. American Petroleum Institute (API) and the American Society of Mechanical Engineers (ASME). *Fitness-For-Service API 579-1/ASME FFS-1*. Washinghton, DC: ASME; 2016.
23. Alshoaibi AM, Fageehi YA. Advances in Finite Element Modeling of Fatigue Crack Propagation. *Applied Sciences*. 2024;14(20): 9297.
24. Mohammed O, Kareem AK, Jamian S, Nemah MN. Distribution of mode I stress intensity factors for single circumferential semi-elliptical crack in thick cylinder. *International Journal of Integrated Engineering*. 2019;11(7): 102–111.
25. Newman JC, Raju IS. An empirical stress-intensity factor equation for the surface crack. *Eng Fract Mech*. 1981;15(1): 185–192.
26. Al-moayed OM, Kareem AK, Ismail AE, Jamian S, Nemah MN. Influence Coefficients for a single superficial cracked thick cylinder under torsion and bending moments. *International Journal of Integrated Engineering.* 2020;12(4): 132–144.
27. Jamian SFS, Abed TH, Aldulaymi OH. Interaction Assessment of Stress Intensity Factors of Surface Cracks on Thick Cylinders under Tension Force and Bending Moment. *Journal of Advanced Research in Applied Mechanics*. 2024;118(1): 131–143.
28. Al-Moayed OM, Ismail AE, Kareem AK, Jamian S, de C. Coêlho G. Interaction of double parallel cracks located on a hollow cylinder. *Latin American Journal of Solids and Structures*. 2023;20(10): e514.
29. Coêlho G, Silva A, Santos M. Elastic surface crack interaction and its engineering critical assessment within the framework of fitness-for-service standards. *Frattura Ed Integrità Strutturale*. 2022;16(60): 134–145.
30. Anis SF, Koyama M, Hamada S, Noguchi H. Simplified stress field determination for an inclined crack and interaction between two cracks under tension. *Theoretical and Applied Fracture Mechanics*. 2020;107: 102561.

MATERIALS PHYSICS AND MECHANICS RESEARCH ARTICLE

Submitted: August 12, 2025 **Revised: November 27, 2025** **Accepted: January 21, 2026**

Linear stability analysis of electroconvection in a polarized dielectric porous layer with couple stresses under a sinusoidally time-varying electric potential

C. Rudresha [1] ✉, **C. Balaji** [2], **V. Vidya Shree** [3], **S. Maruthamanikandan** [4]

[1] Sir M Visvesvaraya Institute of Technology, Bangalore, Karnataka, India

[2] CMR Institute of Technology, Bangalore, Karnataka, India

[3] SJB Institute of Technology, Bangalore, Karnataka, India

[4] Sreenidhi University, Hyderabad, Telangana, India

✉ rudresha_maths@sirmvit.edu

ABSTRACT

The linear stability of electroconvection in a horizontally oriented, thermally unstable dielectric fluid layer saturated with a Darcy porous medium and influenced by couple-stress effects are investigated. The system is subjected to a sinusoidally time-varying electric potential applied at the boundaries. The novelty of this work lies in the combined effects of couple stresses, electric field modulation, and Darcy-porous medium, an area not extensively explored in the existing literature. Using the Boussinesq approximation and a regular perturbation technique, we deal with the governing eigenvalue problem and analyze the critical conditions for the onset of convection. The analysis reveals that electric field modulation can exert either a stabilizing or destabilizing influence depending on the modulation frequency and material parameters. At low frequencies, the destabilizing role of the electric Rayleigh number becomes more pronounced, while couple stress effects contribute to system's stabilization. Additionally, the Vadasz number significantly modifies the stability behavior, enhancing the effects of modulation at high frequencies. Our findings highlight the potential of electric field modulation as a viable mechanism for controlling thermal instability in particle-laden dielectric fluids confined within porous structures. The results provide new insights into electrohydrodynamic flow control in engineering systems involving smart fluids and porous media.

KEYWORDS

couple stresses • dielectric fluid • electric field modulation • porous media • linear stability • electroconvection

Citation: Rudresha C, Balaji C, Vidya Shree V, Maruthamanikandan S. Linear stability analysis of electroconvection in a polarized dielectric porous layer with couple stresses under a sinusoidally time-varying electric potential. *Materials Physics and Mechanics*. 2026;54(1): 73–84.
http://dx.doi.org/10.18149/MPM.5412026_8

Introduction

The theory of couple-stress fluids was first introduced by Stokes [1], who generalized Newtonian fluid mechanics to account for microstructural effects such as body couples and particle rotations. These formulations are particularly useful for describing the behavior of complex fluids such as polymers, colloids, and biological suspensions. The study of convection in porous media has received sustained attention due to its broad engineering and geophysical applications, including geothermal energy, filtration, insulation, and chemical processes. Foundational contributions by Ingham and Pop [2],

Publisher: Peter the Great St. Petersburg Polytechnic University

Vafai [3,4], and Nield and Bejan [5] established the theoretical framework for convection in porous layers mainly focusing on Newtonian fluids.

Extensions to non-Newtonian and microstructured fluids have been widely explored. Sharma and collaborators studied couple-stress fluids under magnetic fields and rotation highlighting his stabilizing tendencies in porous layers [6–15]. Maruthamanikandan [16] analyzed instabilities in dielectric and ferrofluids, while Rudraiah et al. [17] investigated electrohydrodynamic (EHD) stability in couple-stress fluid flow through porous channels. These studies demonstrated how porous resistance and microstructural effects alter the onset of convection compared to classical Rayleigh–Bénard systems. Further contributions considered hyperbolic heat transfer [18] and radiative effects in dielectric convection [19] showing how non-Fourier and radiative mechanisms can delay or promote instabilities.

Parametric forcing has also been a subject of interest. Semenov [20] examined instability in liquid dielectrics under variable electric fields, while Smorodin, Velarde, and others [21,22] demonstrated the role of alternating and modulated electric fields in exciting or suppressing instabilities in conducting and dielectric layers. More recent work by Rudresha and his collaborators have systematically studied electroconvection in porous media under electric field modulation considering compact packing and couple-stress effects [23–26]. These studies revealed that porous permeability, modulation frequency, and fluid microstructure strongly affect critical Rayleigh number thresholds.

In parallel, significant progress has been made in porous media convection. Liu et al. [27] and Zhong et al. [28] examined the role of porosity in Rayleigh–Bénard convection demonstrating its influence on flow structure and heat transfer. Other studies focused on instability mechanisms in thermomechanical systems, including thermoacoustic engines [29], swirling vapor flows [30], and nonlinear averaging methods for dynamical systems [31–36]. At the same time, Rudresha et al. [37,38] investigated convection in viscoelastic dielectric fluids under sinusoidal electric fields, while Balaji et al. [39] considered Darcy–Brinkman models under time-dependent magnetic fields, further enriching the theory of EHD and magnetoconvection.

The role of material properties has also been emphasized. Ivukin et al. [40] explored heat transfer optimization in LED (light emitting diode) lamp heat sinks, while Pozdnyakov and Sedakova [41] analyzed wear mechanisms in polymer friction pairs under vacuum and atmospheric conditions. Gupta et al. [42] studied hydromagnetic stability in nanofluid layers with Hall currents showing that nanoscale physics introduces new stabilization pathways.

Although these studies have significantly advanced the understanding of convection in porous and dielectric systems, several limitations still remain. Most analyses focus either on Newtonian fluids or steady external forcing, with limited attention given to couple-stress fluids in porous layers under sinusoidally varying electric fields. In particular, the combined influence of porous resistance, microstructural stresses, and temperature-dependent dielectric permittivity has not been analytically addressed. The present work fills this gap by performing a stability analysis of a dielectric couple-stress fluid in a Darcy porous medium subject to sinusoidal electric field modulation. By employing a regular perturbation approach, corrections to the critical Rayleigh number are obtained, and the influence of parameters such as the electric number, Vadasz number, modulation frequency, porosity, and viscosity ratio are systematically studied. The results provide new insights into electroconvection control and have implications for applications in geothermal systems, MEMS (microelectromechanical systems), electrothermal cooling, and advanced porous heat exchangers.

Mathematical formulation

To investigate the onset of electroconvection under realistic and technologically relevant conditions, we consider a horizontal porous fluid layer of finite thickness d filled with an incompressible, thermally expanding couple-stress fluid. This layer, influenced by gravity, is heated from below and subjected to a time-periodic electric potential across its boundaries. The combined impact of porous resistance, couple-stress viscosity, and sinusoidal electric modulation on the stability of the base state is systematically studied. Unlike classical Rayleigh-Bénard problems, this formulation accounts for a time-dependent electric field, where the modulation acts as a control parameter. It also incorporates non-Newtonian couple-stress effects, which are essential in fluids with microstructure (e.g., suspensions, polymeric fluids), and porous media through a Darcy model. These additions provide a significant departure from the standard formulations.

We establish a Cartesian coordinate system (x, y, z), with the z-axis directed vertically upwards and the origin located at the lower boundary of the porous layer. A temperature difference ΔT is applied across the layer to introduce thermal stratification. The electric potential on the boundaries is sinusoidally modulated in time: $\phi = \pm U(\eta_1 + \eta_2 cos\omega t)$, where U is the potential amplitude, ω is the modulation frequency, and η_1 and η_2 characterize the steady and oscillating components of the imposed electric field. The porous matrix is assumed homogeneous with constant permeability K and porosity δ. The present analysis is based on the following assumptions:

1. Darcy porous medium: the fluid motion obeys Darcy's law with permeability K and porosity δ.
2. Boussinesq approximation: density variations are considered only in the buoyancy term.
3. Incompressible couple-stress fluid: microstructural stresses are included through couple-stress viscosity.
4. Small modulation amplitude: the electric potential modulation parameters η_1 and η_2 satisfy $| \eta_i | \ll 1$.
5. Temperature-dependent permittivity: the dielectric permittivity varies linearly with temperature.
6. Electrostatic approximation: magnetic effects and displacement currents are neglected.
7. Mechanically free and electrically conducting boundaries: stress-free mechanical conditions with prescribed electric potential.
8. Neglect of porous-matrix deformation: the porous skeleton is rigid and stationary.
9. Neglect of Brinkman term: flow resistance follows the Darcy model without viscous shear corrections.

Under these assumptions, the governing equations include:

$$\nabla \cdot \vec{q} = 0, \tag{1}$$

$$\rho = \rho_0[1 - \alpha(T - T_0)], \tag{2}$$

where $\vec{q} = (u, v, w)$ is the Darcy-Brinkman velocity, T is the temperature, α is the thermal expansion coefficient, and ρ_0 is the density at reference temperature T_0.

Accounting for fluid microstructure and electric field influence, the linearized momentum equation (couple-stress fluid in porous medium) becomes:

$$\frac{1}{\delta}\frac{\partial \vec{q}}{\partial t} = -\frac{1}{\rho_0}\nabla p + \frac{\rho}{\rho_0}\vec{g} - \frac{1}{\rho_0 K}[\mu - \mu_c \nabla^2]\vec{q} - \frac{1}{2\rho_0}\left(\vec{E} \cdot \vec{E}\right)\nabla \varepsilon, \tag{3}$$

where μ is the dynamic viscosity, $\mu_c$is the couple-stress viscosity, $\vec{E} = -\nabla\phi$ is the electric field, $\varepsilon$is the temperature-dependent dielectric permittivity, ω denotes the modulation frequency of the applied electric field, and K is the intrinsic permeability of the porous medium. This formulation extends classical Darcy flow by incorporating micro-rotational effects and dielectrophoretic forces, critical for systems with non-uniform electric properties.

Heat transport equation is:

$$A\frac{\partial T}{\partial t} + (\vec{q} \cdot \nabla)T = \kappa \nabla^2 T, \tag{4}$$

where: A is the effective heat capacity ratio of the porous medium and κ is the thermal diffusivity.

Maxwell's electrostatic equations are:

$$\nabla \times \vec{E} = 0 \text{ or } \vec{E} = -\nabla\phi, \tag{5}$$

$$\nabla \cdot \left[\varepsilon \vec{E}\right] = 0. \tag{6}$$

The permittivity ε is assumed to vary linearly with temperature:

$$\varepsilon = \varepsilon_0[1 - e(T - T_0)], \tag{7}$$

with e (> 0)representing the thermal sensitivity of permittivity, a key source of electric buoyancy.

Basic state

In the basic quiescent state, we have $\vec{q}_b = 0$, $T_b = T_0 - \beta z$, $\vec{E}_b = -\nabla\phi_b$ and the background electric potential is:

$$\phi_b = \frac{-2U(\eta_1 + \eta_2 \cos\omega t)}{\log(1 + e\beta d)}\log(1 + e\beta z) + U(\eta_1 + \eta_2 \cos\omega t). \tag{8}$$

With the expression for the electric field:

$$E_b = \frac{2U(\eta_1 + \eta_2 \cos\omega t)}{d}(1 - e\beta z). \tag{9}$$

Perturbation and linearization

We introduce small perturbations: $\vec{q} = \vec{q}\,'$, $p = p_b + p'$, $T = T_b + T'$, $\varepsilon = \varepsilon_b + \varepsilon'$, $\phi = \phi_b + \phi'$, $\rho = \rho_b + \rho'$, $\vec{E} = \vec{E}_b + \vec{E}\,'$.

Non-dimensionalization (dropping *) is carried out using: $(x, y, z) = (dx^*, dy^*, dz^*)$, $T' = \Delta T T^*$, $t = \frac{Ad^2}{\kappa}t^*$, $\vec{q}\,' = \frac{\kappa}{d}\vec{q}^{\,*}\phi = 2U(\eta_1 + \eta_2 \cos\omega t)e\Delta T\phi^*$.

The resulting dimensionless linearized equations are:

1. Vertical momentum equation is:

$$\frac{1}{Va}\frac{\partial}{\partial t}(\nabla^2 w) = R\nabla_1^2 T - \nabla^2 w + C\nabla^4 w + R_e(1 + \eta_3 \cos\omega t)^2 \frac{\partial}{\partial z}(\nabla_1^2 \phi) + \\ + R_e(1 + \eta_3 \cos\omega t)^2 \nabla_1^2 T. \tag{10}$$

2. Poisson equation for potential is:

$$\nabla^2 \phi = -\frac{\partial T}{\partial z}. \tag{11}$$

3. Heat equation is:

$$\frac{\partial T}{\partial t} - w = \nabla^2 T, \tag{12}$$

where $R = \frac{\alpha \rho_0 g \Delta T K d}{\mu \kappa}$ is the Darcy Rayleigh number, $R_e = \frac{4U^2 e^2 \varepsilon_0 \beta^2 \Delta T K \eta_1^2}{\mu \kappa}$ is the electric Darcy Rayleigh number, $Va = \frac{\delta \nu d^2}{K \kappa}$ is the Vadasz number, $C = \frac{\mu_c}{\mu d^2}$ is the couple stress parameter and $\eta_3 = \frac{\eta_2}{\eta_1}$ is modulation amplitude ratio.

4. Boundary conditions are:

$$w = D^2 w = T = \phi = 0 \text{ at } z = 0{,}1. \tag{13}$$

Eliminating T and ϕ from Eqs. (10)–(12), we obtain the governing equation for w:

$$\left(\frac{1}{Va}\frac{\partial}{\partial t} + 1 - C\nabla^2\right)\left(\frac{\partial}{\partial t} - \nabla^2\right)\nabla^4 w = R\nabla^2 \nabla_1^2 w + R_e (1 + \eta_3 \cos \omega t)^2 \nabla_1^2 w. \tag{14}$$

Along with the boundary conditions:

$$w = \frac{\partial^2 w}{\partial z^2} = \frac{\partial^4 w}{\partial z^4} = 0 \text{ at } z = 0{,}1. \tag{15}$$

Method of solution

To investigate the linear stability of the basic state under the influence of a time-dependent sinusoidal electric field, we seek solutions to the governing Eq. (14) using a regular perturbation technique. Our objective is to determine the eigenfunction w and corresponding critical Rayleigh number R that characterize the onset of convection.

We expand the dependent variables in powers of a small perturbation parameter ε, assuming the solution is close to the threshold of instability:

$$\left.\begin{aligned} w &= w_0 + \varepsilon w_1 + \varepsilon^2 w_2 + \ldots\ldots \\ R &= R_0 + \varepsilon R_1 + \varepsilon^2 R_2 + \ldots\ldots \end{aligned}\right\}. \tag{16}$$

Substituting Eq. (16) into the governing Eq. (14) and collecting terms of like powers of ε, we obtain the following hierarchy of linear equations:

Zeroth-order equation: $Lw_0 = 0.$ (17)

First-order equation: $Lw_1 = R_1 \nabla_1^2 \nabla^2 w_0 + 2R_e f \nabla_1^4 w_0.$ (18)

Second-order equation: $Lw_2 = R_1 \nabla_1^2 \nabla^2 w_1 + 2R_e f \nabla_1^4 w_1 + R_2 \nabla^2 \nabla_1^2 w_0.$ (19)

The linear operator L is defined as:

$$L = \left(\frac{1}{Va}\frac{\partial}{\partial t} + 1 - C\nabla^2\right)\left(\frac{\partial}{\partial t} - \nabla^2\right)\nabla^4 - R_0 \nabla_1^2 \nabla^2 - R_e \nabla_1^4. \tag{20}$$

The function $f = \cos \omega t = R_{eal}\{e^{-i\omega t}\}$ arises from the sinusoidal modulation of the electric field, and all perturbation functions w_n are subject to the homogeneous boundary conditions (15). This formulation retains the time-dependent nature of the forcing, which introduces parametric resonance effects into the eigenvalue structure, a key feature of the present analysis.

Solution of the zeroth-order system

The marginally stable mode, corresponding to the onset of convection, is obtained from the general solution of Eq. (17). Considering the most unstable mode (lowest harmonic), we choose the trial solution as:

$$w_0 = \sin \pi z e^{i(lx + my)}, \tag{21}$$

which satisfies the boundary conditions exactly. Here, $a^2 = l^2 + m^2$denotes the square of the horizontal wave number. Substituting Eq. (21) into Eq. (17), the corresponding critical Rayleigh number at zeroth order is obtained as:

$$R_0 = \frac{\left(\pi^2+a^2\right)^2 + C\left(\pi^2+a^2\right)^3}{a^2} - \frac{R_e a^2}{\pi^2+a^2}. \tag{22}$$

The first term represents the classical contribution from buoyancy and couple stress, while the second term arises due to the electric field-induced dielectrophoretic destabilization.

In Fig. 1, the thermal Rayleigh number R_0 is plotted against the wave number α for different values of the electric Rayleigh number R_e. Figure 1 clearly shows the destabilizing influence of the dielectrophoretic force, as increasing R_e shifts the marginal stability curve downward, thereby reducing the critical Rayleigh number.

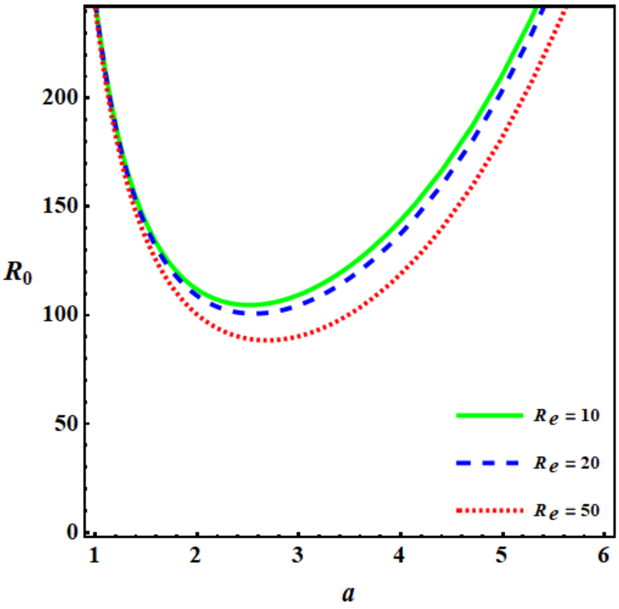

Fig. 1. Darcy Rayleigh number R_0 plotted against the wavenumber a for various electric Darcy Rayleigh numbers number R_e at $C = 0.1$

Solvability condition for second-order correction

To extract R_{2c}, we apply a Fredholm-type solvability condition to Eq. (19), requiring the orthogonality of its right-hand side to the null space of the adjoint operator (i.e., the base mode$sin\,\pi\,z$). After taking a time average over one oscillation period of the imposed electric field, we obtain:

$$R_{2c} = \frac{R_e^2 a^6}{\pi^2+a^2}\left[\sum_{n=1}^{\infty} \frac{A_n}{A_n^2+B_n^2}\right] - \frac{R_e a^2}{\pi^2+a^2}, \tag{23}$$

where the time-periodic modulation introduces a frequency-dependent stabilizing or destabilizing correction to the Rayleigh number. The quantities A_n and B_n encode the temporal interaction between the electric field and fluid inertia and are given by:

$$A_n = -2\left[\frac{\omega^2}{Va}(n^2\pi^2+a^2)^2 - (n^2\pi^2+a^2)^3 - C(n^2\pi^2+a^2)^4 + R_0 a^2(n^2\pi^2+a^2) + R_e a^4\right],$$

$$B_n = \omega\left\{(n^2\pi^2+a^2)^3\left[C + \frac{1}{Va}\right] + (n^2\pi^2+a^2)^2\right\}.$$

This analytical structure demonstrates the nonlinear coupling between modulation frequency ω , couple stress effects, and electrical Darcy Rayleigh forcing, which is central to the novelty of this work.

Results and Discussion

This work presents an analytical investigation into the influence of a sinusoidally time-varying electric field on the onset of thermal convection in a couple-stress fluid contained within a thermally unstable Darcy porous layer. The primary focus is to understand and control the onset of convection by incorporating two key physical mechanisms absent in the classical Rayleigh-Bénard configuration:

1. Suppression of convection due to suspended microstructure, captured by the couple stress parameter C.
2. Time-periodic modulation of the electric field, acting at the boundaries, described by the electric field $\vec{E}(t)$.

A critical observation is that oscillatory convection does not arise in couple-stress fluids under the present configuration, and the electric field modulation is limited to the horizontal boundaries. The analysis assumes a small amplitude of electric field modulation. The results depend sensitively on the modulation frequency ω. At low frequencies ($\omega < 1$), the slow modulation significantly perturbs the system, amplifying disturbances and promoting instability. At high frequencies, the electric forcing tends to average out over time, and the system mimics the unmodulated configuration, thereby restoring stability. Hence, a moderate value of ω is chosen to reveal the competing effects of destabilization and stabilization. Moreover, due to the presence of suspended particles and the consequent enhancement in viscosity (as per Einstein's relation), a higher Vadasz number Va is considered relative to a clean fluid.

To assess the physical relevance of the results, dimensional estimates were obtained using typical dielectric fluid properties. The modulation frequencies required for instability are in the range of 10–100 rad/s. The corresponding temperature differences for onset are approximately 8–20 °C. The electric potential differences required lie in the range of 200–600 V. Representative fluid properties used in the estimates include density $\rho = 950$ kg m^{-3}, kinematic viscosity $\nu = 10^{-5}$–10^{-4} m^{2} s^{-1}, and dielectric permittivity $\varepsilon = (2–5)\cdot 10^{-11}$ F m^{-1}. These values are consistent with common dielectric liquids and validate the physical feasibility of the predicted instability thresholds.

Influence of the electric Rayleigh number R_e

Figure 2 shows the variation of the second-order correction to the Rayleigh number, R_{2c}, with modulation frequency ω, for different values of the electric Darcy Rayleigh number R_e, while keeping the couple stress parameter C and Vadasz number Va fixed. At low frequencies, increasing R_e leads to more negative values of R_{2c}, indicating destabilization due to enhanced electric forcing at the boundaries. As the modulation frequency increases, R_{2c} approaches zero, reflecting reduced influence of the time-varying field. Thus, at lower ω, electric field modulation can effectively trigger instability, whereas at higher ω, it fails to disturb the system significantly, yielding a quasi-steady regime.

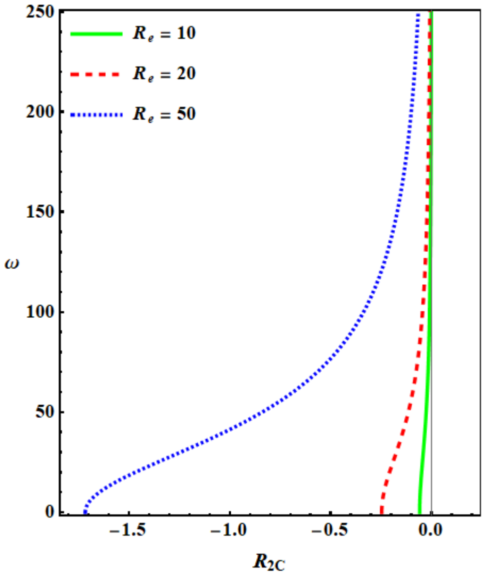

Fig. 2. Variation of correction Rayleigh number R_{2c} with modulation frequency ω for different values of electric Darcy Rayleigh number R_e at $C = 0.1$ and $Va = 10$

Role of couple stress parameter C

Figure 3 displays how R_{2c} varies with ω for different values of the couple stress parameter C. As C increases, R_{2c} increases for all frequencies, implying a stabilizing effect due to the microstructural resistance offered by suspended particles. This behavior is supported by Einstein's viscosity law $\mu_e = \mu_0(1 + 2.5\lambda\varphi)$, where μ_e and μ_0 are the effective and clean fluid viscosities, λ is the shape factor (≥ 1), and φ is the volume fraction of particles. Increased viscosity leads to higher energy dissipation, thereby impeding convective motion. While the Einstein relation is linear and valid for dilute suspensions, for higher concentrations a nonlinear correction is required, which may further enhance this stabilization.

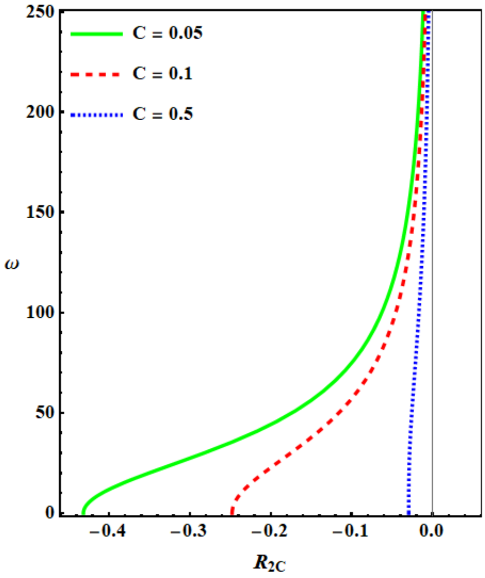

Fig. 3. Variation of R_{2c} with ω for different values of couple stress parameter C at $Va = 10$ and $R_e = 20$

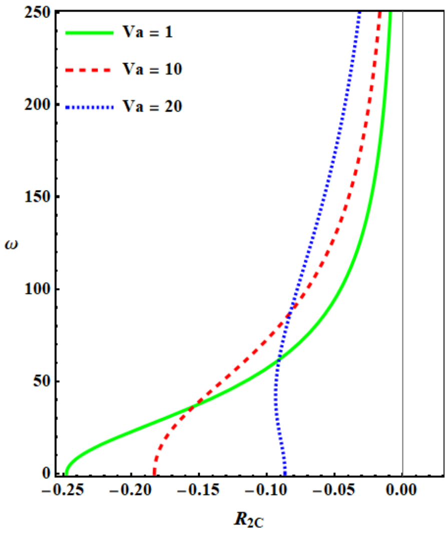

Fig. 4. Variation of R_{2c} with ω for different Vadasz numbers Va at $C = 0.1$ and $R_e = 20$

Impact of the Vadasz number Va

Figure 4 illustrates the impact of the Vadasz number Va on R_{2c} for various modulation frequencies. A larger Va corresponds to an increase in R_{2c}, suggesting delayed convection onset due to stronger momentum diffusion relative to thermal diffusion. This result is particularly important in couple-stress fluids where the microstructure significantly influences viscosity. The combined effect of high C and Va creates a dissipative environment that resists perturbations. Additionally, strong electric fields distort field lines, and such distortions interact with the fluid's microstructure to suppress convective growth.

Electric modulation destabilizes the system at low frequencies but becomes ineffective at high frequencies. Couple stress effects increase the critical threshold, reinforcing system stability. Thermal diffusion (high Va) complements the couple stress damping, especially in particle-laden fluids. These findings highlight that the interplay between electric field forcing, microstructural effects, and porous media transport mechanisms enables fine-tuned control of convective instability. This study therefore offers a framework for designing electrically controlled thermal systems in porous or micro-structured environments, with potential applications in filtration, microfluidics, and enhanced heat transfer technologies.

To validate the present analytical formulation, we compare the results obtained from the model with several known limiting cases that correspond to existing studies:

1. Unmodulated electric field ($\eta_3 = 0$): In this limit, the modulation term disappears and the critical Darcy–Rayleigh number reduces to the steady electric field case. The resulting trend agrees with the unmodulated electroconvection analyses of Smorodin et al. [21] and Rudresha et al. [23–25].
2. Absence of couple-stress effects ($C = 0$): Eliminating microstructural stresses reduces the model to Newtonian dielectric convection in a Darcy porous medium. The behaviour of the critical threshold matches the results reported by Velarde and Smorodin [22] and Rudraiah et al. [17].
3. Large permeability (high Darcy number): when the porous resistance becomes negligible, the system smoothly approaches the classical Rayleigh-Bénard convection limit for dielectric fluids. This limiting behaviour is consistent with standard results in literature. These comparisons confirm that the present model correctly recovers earlier established results in the absence of electric modulation, couple stresses, or porous resistance, thereby validating the analytical solution method used in this work.

Conclusion

This study investigates the onset of electroconvection in a horizontal dielectric fluid layer embedded in a Darcy porous medium, incorporating couple-stress effects under the influence of a time-periodic electric field. A linear stability analysis was employed to explore how electric field modulation, couple stresses, and porous media parameters interact to affect convective behavior. The key conclusions are summarized below:

1. Low-frequency electric field modulation exhibits minimal influence on system stability. However, at moderate and high frequencies, the modulation can significantly alter the stability threshold.

2. Increasing the couple stress parameter enhances system stability. For fluids with suspended particles, this parameter plays a dominant role in suppressing the onset of convection, especially at lower modulation frequencies.
3. While electric field modulation can stabilize the flow, a high electric Rayleigh number counteracts this effect by promoting convection, particularly at intermediate modulation frequencies.
4. The Vadasz number modulates the thermal response due to fluid inertia in porous media. It amplifies the destabilizing effect of modulation at higher frequencies but contributes to stabilization at lower frequencies.

In summary, the results demonstrate that electric field modulation, when combined with Darcy resistance and couple-stress effects, provides a tunable mechanism to delay or promote the onset of electroconvection. These findings have potential applications in engineering systems where convective control in porous or particle-laden fluids is critical, such as electrohydrodynamic cooling, geophysical flows, and materials processing.

CRediT authorship contribution statement

Rudresha Chandrappa conceptualized the problem and supervised the study. **Sokalingam Maruthamanikandan** performed the mathematical analysis and derivations. **Chandrashekar Balaji** and **Venkatesh Vidya Shree** contributed to the interpretation of results and manuscript organization. All authors reviewed and approved the final manuscript.

Conflict of interest

The authors declare that they have no conflict of interest.

References

1. Stokes VK. Couple-stresses in fluids. *Phys. Fluids.* 1966;9(9): 1709–1715.
2. Ingham DB, Pop I, editors. Transport Phenomena in Porous Media. Oxford: Pergamon; 1998.
3. Vafai K. (Ed.) *Handbook of Porous Media.* New York: Marcel Dekker; 2000.
4. Vafai K. (Ed.) *Handbook of Porous Media.* 2nd ed. Boca Raton: Taylor & Francis; 2005.
5. Nield DA, Bejan A. *Convection in Porous Media.* 3rd ed. New York: Springer; 2006.
6. Sharma RC, Thakur KD. On couple-stress fluid heated from below in porous medium in hydromagnetics. *Czech J Phys.* 2000;50(6): 753–760.
7. Sunil, Sharma RC, Pal M. On couple-stress fluid heated from below in porous medium in the presence of magnetic field and rotation. *J Porous Media.* 2002;5(2): 149–157.
8. Sunil, Sharma RC, Chandel RS. Effect of suspended particles on couple-stress fluid heated and soluted from below in porous medium. *J Porous Media.* 2004;7(1): 9–15.
9. Rymkevich PP, Golovina VV, Altukhov AI. Motion equation averaging in potential autonomous systems. *Sci Tech J Inf Technol Mech Opt.* 2020;20(1): 141–146.
10. Hakeem AA, Priya S, Bhose G, Sivanandam S. Magneto-convective hybrid nanofluid slip flow over a moving inclined thin needle in a Darcy–Forchheimer porous medium with viscous dissipation. *Int J Numer Methods Heat Fluid Flow.* 2024;34(1): 334–352.
11. Chandrapushpam T, Bhuvaneswari M, Sivanandam S. Double diffusive MHD squeezing copper–water nanofluid flow between parallel plates filled with porous medium and chemical reaction. *Int J Numer Methods Heat Fluid Flow.* 2024;34(3): 1151–1169.

12. Sivasankaran S, Cheong HT, Aasaithambi T. Effect of localized heater position and length on buoyant convection in an oblique porous cavity using heatlines approach. *Int J Appl Comput Math.* 2025;11: 181.
13. Sivanandam S, Cheong HT, Thangaraj A. Numerical study on free convection in an inclined wavy porous cavity with localized heating. *Modelling.* 2025;6: 30.
14. Janagi K, Sivasankaran S. Impact of tilting angle and density extremum on transient convection in a porous chamber with sinusoidal heating. *Numer Heat Transfer A Appl.* 2023;85(19): 3194–3208.
15. Sivanandam S, Alqurashi TJ, Alshehri HM. Impact of activation energy and cross-diffusion effects on 3D convective rotating nanoliquid flow in a non-Darcy porous medium. *Int J Numer Methods Heat Fluid Flow.* 2024;34(9): 3281–3303.
16. Maruthamanikandan S. *Convective instabilities in Newtonian ferromagnetic, dielectric and other complex liquids [PhD thesis].* Bangalore, India: Bangalore University; 2005.
17. Rudraiah N, Shankar BM, Ng CO. Electrohydrodynamic stability of couple stress fluid flow in a channel occupied by a porous medium. *Spec Top Rev Porous Media.* 2011;2(1): 11–21.
18. Zinoviev EA, Vorotnikov GV, Dovgyallo AI, Nekrasova SO. Boundaries of thermoacoustic instability in the thermoacoustic engine with cryogenic cooling. *J Int Acad Refrig.* 2020;4: 20–26.
19. Seryakov AV, Konkin AV, Alekseev AP. Swirling vapour flow in short linear heat pipes. Part II. *J Int Acad Refrig.* 2024;2: 72–79.
20. Semenov VA. Parametric instability of a nonuniformly heated horizontal layer of liquid dielectric in a variable electric field. *Fluid Dyn*. 1993;28: 734–735.
21. Smorodin BL, Gershuni GZ, Velarde MG. On the parametric excitation of thermoelectric instability in a liquid layer open to air. *Int J Heat Mass Transf.* 1999;42(16): 3159–3168.
22. Velarde MG, Smorodin BL. Convective instability of a plane horizontal layer of weakly conducting fluid in alternating and modulated electric fields. *Fluid Dyn.* 2001;35(3): 339–345.
23. Rudresha C, Balaji C, Vidya Shree V, Maruthamanikandan S. Effect of electric modulation on electroconvection in a dielectric fluid saturated porous medium. *J Mines Met Fuels.* 2022;70(3A): 35–41.
24. Rudresha C, Balaji C, Vidya Shree V, Maruthamanikandan S. Effect of electric field modulation on the onset of electroconvection in an anisotropic porous layer saturated with a dielectric fluid. *J Comput Appl Mech.* 2022;53(4): 10–23.
25. Rudresha C, Balaji C, Vidya Shree V, Maruthamanikandan S. Effect of electric field modulation on the onset of electroconvection in a couple stress fluid. *East Eur J Phys.* 2022;4: 104–111.
26. Rudresha C, Balaji C, Vidya Shree V, Maruthamanikandan S. Onset of electroconvection in a compactly packed dielectric liquid-permeable layer with a modulated electric field. *J Phys Stud.* 2023;27(1): 1401.
27. Liu S, Jiang L, Chong KL, Zhu X, Wan ZH, Verzicco R, Stevens RJAM, Lohse D, Sun C. From Rayleigh-Bénard convection to porous-media convection: how porosity affects heat transfer and flow structure. ArXiv [Preprint] 2020. Available from: doi.org/10.48550/arXiv.2005.09446.
28. Zhong J, Liu S, Sun C. On the thermal effect of porous material in porous media Rayleigh-Bénard convection. ArXiv [Preprint] 2023. Available from: doi.org/10.48550/arXiv.2304.06989.
29. Maruthamanikandan S, Nagouda SS. Convective heat transfer in Maxwell–Cattaneo dielectric fluids. *Int J Comput Eng Res.* 2013;3: 347–351.
30. Nagouda SS, Maruthamanikandan S. Rayleigh–Bénard convection in a horizontal layer of porous medium saturated with a thermally radiating dielectric fluid. *IOSR J Math*. 2015;11(3): 1–6.
31. Balaji C, Maruthamanikandan S, Rudresha C, Vidya Shree V. Anisotropic Darcy–Brinkman magnetic fluid convection under a time-dependent sinusoidal magnetic field. *Ukr J Phys.* 2023;68(11): 730.
32. Sivanandam S, Awan AA, Alshehri HM. Impact of obstacle and Joule heating on magneto-convection of hybrid nanofluid in a channel having heated dimple with entropy generation. To be published in *World J Eng.* [Preprint] 2025. Available from: doi.org/10.1108/WJE-02-2025-0077.
33. Sivanandam S, Alqurashi TJ. Influence of Joule heating and slip on 3D MHD rotating nanoliquid flow with radiation, viscous dissipation, Soret and Dufour effects. To be published in *World J Eng.* [Preprint] 2025. Available from: doi.org/10.1108/WJE-10-2024-0566.
34. Sivanandam S, Thangaraj C, Bhuvaneswari M. MHD double diffusive convective squeezing ternary nanofluid flow between parallel plates with activation energy and viscous dissipation. *Int J Numer Methods Heat Fluid Flow.* 2024;34(12): 4409–4431.
35. Thangaraj C, Sivanandam S, Marimuthu B. Dufour and Soret effects on MHD squeezed nanoliquid flow between parallel plates by differential transform method. *World J Eng.* 2025;22(5): 1127–1137.
36. Geetha SP, Sivasankaran S, Bhuvaneswari M. Partial slip and cross-diffusion effects on magnetohydrodynamic mixed bioconvection flow in a channel with chemical reaction. *J Nanofluids.* 2023;12(7): 1815–1826.

37. Rudresha C, Balaji C, Vidya Shree V, Maruthamanikandan S. Effect of time-dependent sinusoidal electric field on the onset of electroconvection in a viscoelastic fluid layer. *Condens Matter Phys.* 2024;27(4): 43702.
38. Rudresha C, Balaji C, Vidya Shree V, Maruthamanikandan S. Linear stability analysis of a rotating dielectric fluid layer under time-periodic electric field modulation. *Journal of Engineering Mathematics*. 2026;156: 3.
39. Balaji C, Rudresha C, Vidya Shree V, Maruthamanikandan S. Ferrohydrodynamic instability of a couple stress magnetic fluid layer under the influence of time-dependent sinusoidal magnetic field. *Iraqi J Appl Phys.* 2022;18(4): 15–19.
40. Ivukin IN, Bougrov VE, Kovsh AR, Odnoblyudov MA, Shalkovskiy AG, Romanov AE. Heat transfer simulation and retrofit LED lamp plastic heat sink material optimization. *Materials Physics and Mechanics.* 2013;17(2): 178–182. (In Russian)
41. Pozdnyakov AO, Sedakova EB. Thermal analysis of wear of polymer-polymer friction pairs in vacuum and atmosphere conditions. *Materials Physics and Mechanics.* 2024;52(4): 63–80.
42. Gupta U, Ahuja J, Kumar R, Wanchoo RK. On the hydromagnetic stability of a horizontal nanofluid layer with Hall currents. *Materials Physics and Mechanics*. 2016;27(1): 9–21.

MATERIALS PHYSICS AND MECHANICS RESEARCH ARTICLE

Submitted: September 23, 2025 **Revised: January 13, 2026** **Accepted: February 2, 2026**

Influence of rotational speed on performance metrics in friction stir lap welding of aluminium 6061 and stainless steel 304-CFD approach

A. Yadav ✉, A. Jain, R. Verma

NIT Kurukshetra, Kurukshetra, India

✉ amit.insan77@gmail.com

ABSTRACT
The joining of dissimilar materials such as aluminium and steel is of growing importance in modern manufacturing, owing to the demand for lightweight structures with superior mechanical performance. This study investigates the influence of rotational speed on key thermo-mechanical performance measures during dissimilar friction stir lap welding of aluminium alloy-6061 and stainless steel-304. Using finite volume method, numerical simulations were performed to quantify maximum weld interface temperature, maximum weld interface velocity, minimum weld interface viscosity, and tool-workpiece interface torque over a rotational speed range of 200–2200 rpm. Results reveal that maximum weld interface temperature rise steeply up to about 1000 rpm and then plateau due to thermal equilibrium. maximum weld interface velocity increases almost linearly with rotational speed, indicating improved interfacial shear and material mixing. In contrast, minimum weld interface viscosity and tool-workpiece interface torque decrease markedly as rotational speed increases, reflecting enhanced thermal softening and reduced resistance to tool motion. Intermediate rotational speed values (≈ 600–1200 rpm) provide an optimal balance of heat generation, material plasticization and torque, minimising the risk of excessive intermetallic compound growth or welding defects. The findings establish a physics-based framework for selecting process parameters that enhance joint integrity and efficiency in dissimilar friction stir lap welding of AA6061-SS304.

KEYWORDS
friction stir weld • computational fluid-dynamics • finite-volume approach • ANSYS • fluent

Citation: Yadav A, Jain A, Verma R. Influence of rotational speed on performance metrics in friction stir lap welding of aluminium 6061 and stainless steel 304-CFD approach. *Materials Physics and Mechanics*. 2026;54(1): 85–100.
http://dx.doi.org/10.18149/MPM.5412026_9

Introduction

The automotive, aerospace, and marine industries necessitate lightweight structures with superior wear resistance to ensure optimal performance and durability [1]. These specific applications underscore hybrid structures combining lightweight materials such as aluminium (Al) with stainless steel (SS) [2]. Strategically utilising joints made from SS and Al alloys in critical areas provides a practical solution [3]. Various new joining techniques were employed by researchers for joining difficult-to-join and dissimilar materials [4–7]. Friction stir welding (FSW) pioneered and patented by "The Welding Institute UK" in 1991 stands as a promising solution, surpassing traditional fusion welding methods due to its advantages, including reduced heat input, thinner intermetallic compounds (IMCs), and enhanced surface properties [8–10]. FSW has advantages over fusion techniques for welding many metals, such as welding alloys of aluminium, titanium, copper, etc. [11].

Publisher: Peter the Great St. Petersburg Polytechnic University

In FSW, the spinning tool is gradually plunged into the workpiece until the shoulder comes into full contact. This position is maintained until the required temperature is reached, generated by frictional heating and plastic deformation. In order to accomplish the necessary weld, the tool is traversed along the weld line. The side of the rotating tool where the tangential velocity coincides with the traverse speed (TRS) is referred to as the advancing side (AS) [12]. The retreating side (RS) refers to the side of a rotating tool that has a vectorial sense opposite to the tangential velocity and TRS [12]. The workpiece section located ahead of tool is known as leading side, and the section located behind tool is known as trailing side [12]. FSW generates welds without the melting of the base material, hence eliminating the risks of solidification cracking, deformation, porosity, and other related issues. It necessitates no edge preparation and generates transition junctions between dissimilar metals [12].

The primary restriction of FSW is its necessity for distinct tools corresponding to varying workpiece thicknesses, and the resultant exit hole that remains upon the withdrawal of the tool from the workpiece. Large forces on clamp, necessitate robust gripping. It is primarily restricted to linear welding. Furthermore, filler joints are unattainable using FSW [12].

Recent research has largely focused on utilising FSW to repair defects in structural components, whereby friction stir techniques can effectively repair defects such as pores, cracks, grooves, through holes, and the like [13]. Since its inception, extensive research has focused on the influence of various process parameters in FSW [14,15]. These parameters govern heat transfer and material flow, thereby affecting the resulting microstructure and weld quality [16,17]. Achieving optimal welding performance requires careful evaluation of these parameters with respect to key thermo-mechanical measures, namely maximum weld interface temperature (MWIT), maximum weld interface velocity (MWIV), minimum weld interface viscosity (MWIVis), and tool-workpiece interface torque (TWIT) [18]. The present study investigates the effect of tool rotational speed (ROS) on MWIT, MWIV, MWIVis, and TWIT during dissimilar friction stir lap welding (DFSLW) of aluminium alloy 6061 (AA6061) and stainless steel 304 (SS304).

Literature review

In recent years, extensive research has examined the influence of process parameters on the performance of dissimilar friction stir welding (DFSW) of SS304 with various aluminium alloys. Nishida et al. [19] examined development of interfacial microstructures in dissimilar friction stir lap welding (DFSLW) between AA3003-H112 and SS304. Analysis of the bottom surface of the exit-hole showed that there were several mixed layers with ultrafine IMCs. The continuous thin reaction coating that was produced at the interface was also reported to be stronger than the base aluminium alloy. Habibnia et al. [20] researched the concept of microstructural and mechanical properties of dissimilar friction stir butt welds (DFSBW) in AA5050-SS304. Their findings indicated that joint quality increased with a lower tool rotational speed (ROS) and higher TRS.

Ghosh et al. [21] investigated the thermal impact on the microstructure of weld nugget of DFSBW of AA6061 and SS304. Higher heat contribution favored increasing the iron content at the interface, changing IMC composition Fe_2Al_5 to more iron-rich grains in the Fe -Al phase diagram. At intermediate ROS, which was coincident with the formation of Fe_3Al and $FeAl_2$ phases, maximum microhardness and tensile strength were obtained. Balamagendiravarman et al. [22] compared the microstructure and mechanical behaviour of DFSBW of SS304 and commercial pure aluminium. There were minimal changes in microstructure on the steel surface in comparison to aluminium as a result of thermal and mechanical variation. In the interface and stir zone (SZ), Al_3Fe IMCs were observed, and the hardest point was at the SZ. The highest tensile was 78 percent of the aluminium base metal. The same authors in a follow-up study [23] demonstrated that addition of more ROS enhanced IMC layer thickness and facilitated the growth of $FeAl_2$, Fe_4Al_{13}, Fe_2Al_5 and $FeAl_3$. At 400 rpm, it reached the maximum joint efficiency of 90 % and elongation of 4.5 % and the maximum hardness was obtained in the SZ at the high ROS.

In the study by Mahto et al. [24], the practicality of underwater friction stir welding (UFSW) of AA6061 and SS304 was evaluated at different levels of ROS and plunge depth (PD). Less heat input and faster cooling in UFSW inhibited the excessive IMC, fine-tuned the weld microstructure and minimized defects including porosity, voids and kissing bonds leading to greater strength in the joints. They studied interfacial microstructure and corrosion behaviour of the DFSLW in a related study [25]. Reducing grain size was improved by the increasing ROS and the PD because of the rapid cooling and heating speeds. IMCs like Fe_2Al_5 and $AlCrFe_2$ were discovered and the corrosion resistance declined with reducing grain size mainly due to pitting and intergranular corrosion. The researchers of Chitturi et al. [26] investigated how tool tilt angle (TA) and pin depth influence DFSLW of AA5052 and SS304. Low TAs (0° and 1.5°) were found to have tunnel defects and micro-voids whereas defect-free joints were obtained at 2.5° owing to enhanced mixing of the material and formation of IMC. Both sides of the weld have hooks that improved mechanical interlocking and the SZ hardness was almost three times greater than SS304.

Uematsu et al. [27] carried out crack propagation tests on DFSBW joint of AA6061 and SS304. The rates of fatigue crack propagation of the welds were also lower than that of the aluminium base metal and when compared by the effective stress intensity factor range of the fatigue crack propagation, the behavior of the fatigue crack propagation was similar in all the samples. Chitturi et al. [28] also tested the fracture behavior of DFSLW of AA5052 and SS304 at different TAs, ROS, TRS, and PDs. Fractures that were mainly initiated on the aluminium side had mixed brittle-ductile failure modes. X-ray diffraction was used to confirm the formation of AlFe based IMCs, and hardness was found to be between 300−630 HV with different process conditions. Jabraeili et al. [29] examined the effect of the welding parameters on DFSBW of AA2024 and SS304. Tool offset was found to be a vital parameter whereby with positive offsets one will end up with tunnel defects because the heat input was not enough and in the case of negative offsets thick IMC layers were produced. The finest conditions gave a serrated interface of thin IMCs and increased strength and ductility of the joints.

Wang et al. [30] have compared the microstructure and mechanical behavior of AA3003 and SS304 DFSBW joints. Tool offset was more significant compared to ROS on the microstructure of the joints. Reduced ROS enhanced tensile strength and hardness with a constant offset, and the start of a failure was at the weld root and spread through the SZ. The authors of Joshani et al. [31] were researching the DFSBW of AA7075, and SS304 at various ROSs. The increment of ROS enhanced the IMC thickness to 6 μm and diminished joint strength. Optimal tensile strength (about 72 % AA7075) was realized at the lower ROS, whereas fracture moved to the SZ at the higher ROS. Datta et al. [32] made comparisons between DFSBW of DAA1100, and DAA7075 and that of SS304. Joint AA1100 -SS304 was more efficient and ductile. The reduced traverse velocity improved strength and elongation because of the controlled amount of heat.

Kumar et al. [33] examined DFSBW of AA7075 and SS304 and stated that the higher the ROS, the greater was the heat generation leading to thicker IMC layers and less tensile strength. The refinement of the grains was also great, which resulted in equiaxed recrystallized grains and IMCs like $Al_{13}Fe_4$, Al_3Fe_2, and Al_3Mg_2 at the interface. Ou et al. [34] have constructed the model of heat transfer in DFSBW of AA6061 and SS304, to include the welding tool. The model determined peak temperatures with a margin of error of 2.3 % and showed low temperature gradients and IMC thickness at increasing TRSs. DFSBW of SS304 and AA2024-T3 was well investigated by Mir et al. [2,10,35]. Their results pointed to better wear and corrosion resistance, refinement of grains, and hardness in the stir zone with the best heat input and material flow. Zhang et al. [36] were able to obtain defect free DFSBW of SS304 and AA2219 with low ROS at 200 rpm. Substantiation of thin amorphous Al Fe O layer inhibited the Cu rich IMCs yielding high metallurgical bonding and tensile strength of 210 MPa. Nakrani et al. [37] examined fatigue cracking characteristics in DFSBW of SS304 and AA5083, which showed an increased rate of crack propagation at the Al-steel interface, and brittle fractures behavior at the interface. Caetano et al. [38] investigated DFSBW of SS304 and SS410, demonstrating that placing ferritic SS410 on the AS reduced flash formation and voids. Increased axial force eliminated root defects, although it promoted higher flash formation on the AS.

Overall, prior research on DFSW between aluminium alloys and stainless steel has primarily concentrated on interfacial microstructural evolution, IMC formation, and mechanical performance. While studies have highlighted the role of parameters such as ROS, TRS, PD, TA, and welding environment, significant research gaps remain. In particular:

1. The effect of ROS on critical thermo-mechanical performance measures (MWIT, MWIV, MWIVis, and TWIT) has not been systematically quantified.
2. Weld interface viscosity, a key factor governing material flow, mixing, and defect formation, remains underexplored in dissimilar lap welds of AA6061-SS304.
3. Torque variation with ROS and its correlation with weld quality in AA6061-SS304 lap welds have not been addressed.

Most existing studies emphasise butt joints or other aluminium alloys (AA2024, AA5052, AA7075), leaving the practically relevant AA6061-SS304 lap configuration insufficiently studied. To address these gaps, the present work employs a physics-based finite volume method (FVM) simulation using ANSYS® Fluent® to analyse the effect of ROS on MWIT, MWIV, MWIVis, and TWIT in DFSLW of AA6061-SS304. This systematic investigation provides deeper insights into heat generation, material flow, and tool-workpiece interaction, offering a framework to minimise defects and improve joint efficiency.

Simulation design

The simulation model utilises an AA6061 sheet and an SS304 sheet with dimensions of 200 × 75 × 3 mm^3 (each sheet). They are joined in a lap arrangement with an overlap width of 30 mm (Fig. 1). Solidworks® 2017 is used for geometric modelling, while CFD software ANSYS® 19.3 R3 (FLUENT®) is employed for FVM numerical simulation [39]. A flat shoulder tool with a frustum conical pin is employed (Table 1).

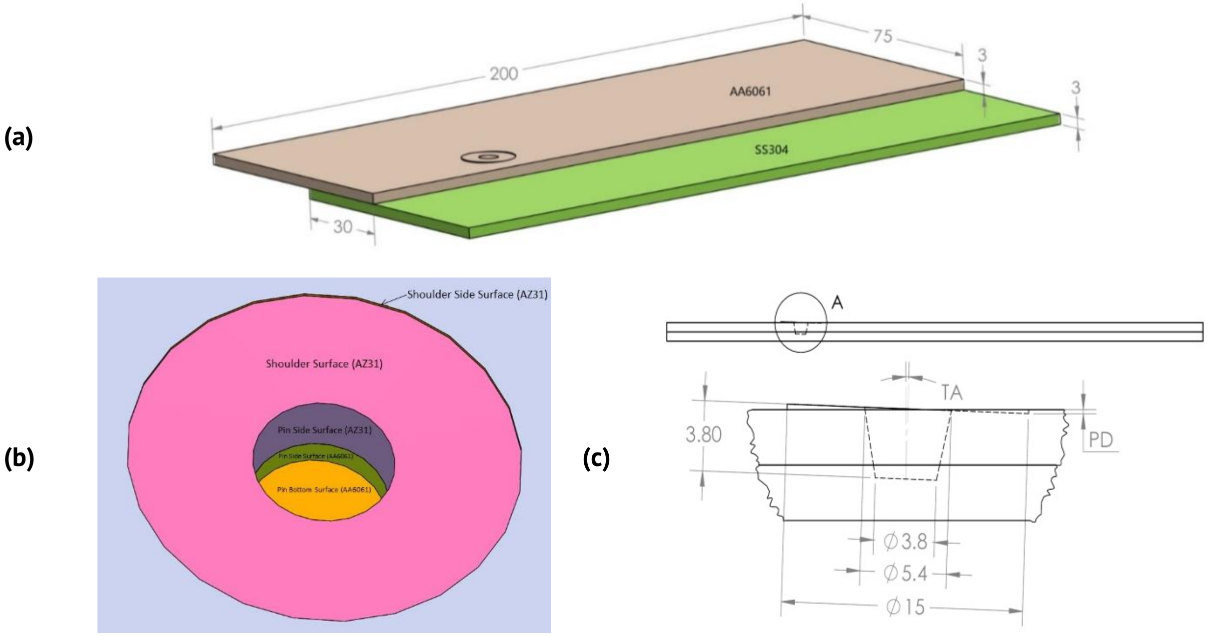

Fig. 1. (a) Arrangement of dissimilar friction stir lap weld of AA6061 with SS304; (b) tool-workpiece interface surfaces; (c) dimensions of tool employed

Table 1. Fixed process parameters

Process parameter	**Value**
Diameter of flat shoulder, mm	15
Pin length, mm	3.8
Pin base diameter, mm	5.4
Pin tip diameter, mm	3.8
PD, mm	0.225
TA	1.5°
Overlap width, mm	30

The Realisable k-epsilon viscous model is employed to simulate the flow of material in a transient state [40]. Mesh with tetrahedral elements (899766 in numbers) and 187342 nodes are utilised, with fine mesh at the interface between the tool and the workpiece, as depicted in Fig. 2 [41]. The present work adheres to the following assumptions:

1. The process is a quasi-steady process, i.e., the rate of heat generation remains constant.
2. Material that has undergone plasticization is classified as non-Newtonian, incompressible, and visco-plastic.
3. The material is presumed to exhibit characteristics of a non-Newtonian fluid, where its viscosity is influenced by both temperature and strain rate.

4. Partial slip condition exists between the tool and the workpiece.
5. Free slip condition exists on the upper, bottom, and side surfaces of the workpiece.
6. The outlet boundary assumes the value of zero pressure.

To make precise predictions about welding, it is crucial to employ realistic boundary conditions [42,43]. Figure 3 displays the parts and boundaries imposed on the model. The inlet boundary condition of flow is defined as follows:

$$u = u_{weld}, v = 0, w = 0, \tag{1}$$

where the TRS is represented by u_weld, whereas the velocity intensities in the X, Y, and Z directions are represented by u, v, and w, respectively.

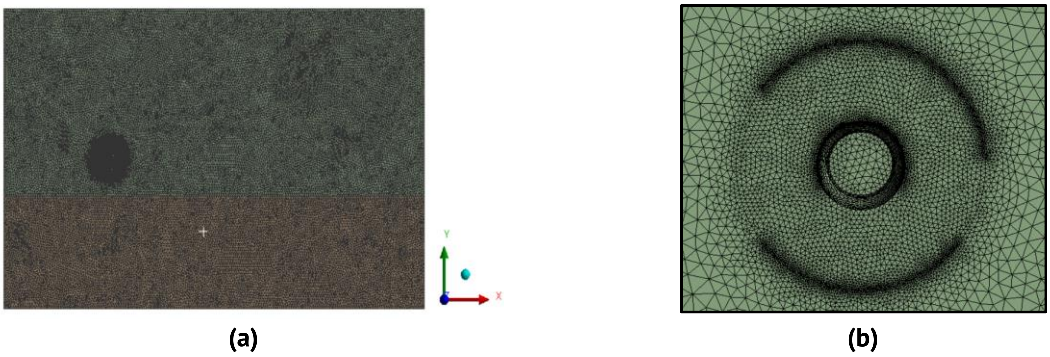

(a) (b)

Fig. 2. (a) Tetrahedron cells' mesh used in the model; (b) close up view (top) of tool-workpiece interface

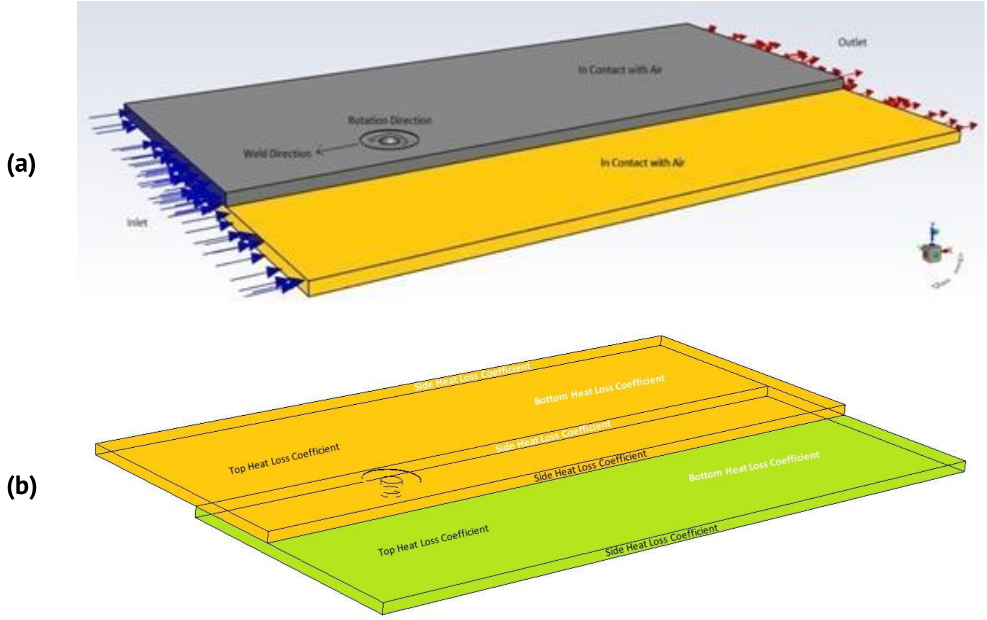

Fig. 3. (a) Flow directions of materials in the model; (b) different heat loss surfaces of the model

The tool periphery velocity, which is the combined effect of tool's ROS and TRS, is provided below:

$$\begin{aligned} u_i &= \omega r sin\theta - u_{weld}, \\ v_i &= \omega r cos\theta, \\ w_i &= 0. \end{aligned} \tag{2}$$

The value of r is such that $r_1 < r < r_3$. The variables u_i, v_i and w_i denote vectors of velocity in the X, Y, and Z directions. The index notation "i" means a specific location on tool's surface where the tool's combined ROS and the TRS are determined. r_1 represents the radius of tool shoulder; r_3 represents the radius of pin bottom; θ is the angle between the horizontal direction vector from the tool axis to any point on the cylindrical surface. In the weld direction, θ is equal to zero.

Tool periphery velocity when tool TA (ξ) and contact state variable (δ) are considered, are represented by equations below [44]. Equations (3)−(5) are used to define the momentum boundary conditions at the tool-workpiece interface, specifically at the shoulder surface (SS), pin side surface (PSS), and pin bottom surface (PBS).

$$u_i = (1-\delta)(\omega r sin\theta)\cos\xi - u_{weld}, \tag{3}$$

$$v_i = (1-\delta)\omega r cos\theta, \tag{4}$$

$$\mathrm{w_i} = (1-\delta)(\omega r \sin\theta)\sin\xi, \tag{5}$$

$\delta_{AA6061} = \left(0.31e^{\omega r/1.87} - 0.026\right)$ (from [45]), $\delta_{SS304} = 0.7$ (from [46]). (6)

The viscosity (η), flow stress (σ), Zener Hollomon parameter (Z) and strain rate ($\bar{\varepsilon}$) are determined using the equations below [47−49]:

$$\eta = \frac{\sigma}{3\bar{\varepsilon}}, \tag{7}$$

$$\sigma = \frac{1}{\beta}\ln\left\{\left(\frac{Z}{A}\right)^{\frac{1}{n}} + \left(1 + \left(\frac{Z}{A}\right)^{\frac{2}{n}}\right)^{\frac{1}{2}}\right\}, \tag{8}$$

$$Z = \bar{\varepsilon}\mathrm{e}^{\left(\frac{Q}{RT}\right)}, \tag{9}$$

$$\bar{\varepsilon} = \left(\frac{2}{3}\varepsilon_{ij}\varepsilon_{ij}\right)^{\frac{1}{2}}, \tag{10}$$

where *T* represents temperature, measured in Kelvin (K), A, β, and n are constants that describe the material properties, *Q* is an activation energy that does not depend on temperature, *R* is the gas constant (8.314 J·K^{-1}·mol^{-1}).

Table 2. Material-constants and properties for AA6061 and SS304 [44,46,51−53]

Parameters		**AA6061**	**SS304**
Material constants	*A*, s^{-1}	2.41 × 10^{8}	1.62 x 10^{16}
	n	3.55	6.1
	Q, J·mol^{-1}	1.45 × 10^{5}	4.46 x 10^{5}
	β, MPa^{-1}	0.0367	0.008
Material density ρ, kg·m^{-3}		2700	7400
Top (h_t) & side (h_s) heat transfer coefficient, W/m^{2}K		80	0.0668T
Bottom (h_b) heat transfer coefficient, W/m^{2}K		150	10*0.0668T
External emissivity of workpiece top surface		0.09	0.17

Table 2 provides the material constants and properties of AA6061 [50]. Equation (7) is used to define the viscosity as a function of temperature and strain rate for the given materials, namely AA6061 and SS304. These equations are implemented through the use of user defined functions.

The heat created during the FSW process is distributed over many regions. The tool's contacting surface with the workpiece is partitioned into three sections: bottom SS, P$_{SS}$, and P$_{BS}$. The SS is subdivided into two sections: shoulder with conical surface

(S_{CS}) and shoulder with flat surface (S_{FS}). All these sections exhibit partial sticking-sliding contact. Heat produced by different sources is provided underneath:

$$Q_{total} = \delta Q_{sticking} - (1-\delta) Q_{sliding}. \tag{11}$$

When the slip coefficient (δ) is equal to zero, heat is only generated through friction. When the value of δ is equal to 1 (indicating a stick), all heat is produced only through the deformation of the plastic material [54].

The assumed maximum yielding shear stress is [55]:

$$\tau_b = \frac{\sigma_s}{\sqrt{3}}, \tag{12}$$

$$(\sigma_s)_{AA6061} = 1160 - 8.88T + 2.97 \times 10^{-2}T^2 - 3.32 \times 10^{-5}T^3 \text{ (from [52])}, \tag{12a}$$

$$(\sigma_s)_{SS304} = 796 - 1.6T + 2.25 \times 10^{-3}T^2 - 1.3 \times 10^{-6}T^3 \text{ (from [46])}, \tag{12b}$$

where σ_s represents the material's yield stress.

The heat-flux (W/m^2) in S_{CS} section is [44,46,51,52]:

$$q_{S_{CS}} = \eta\left(\frac{[(1-\delta_{CSS})\tau_b + (\delta_{CSS})\mu P]2\omega[(r_1^3 - r_2^3)(1+\tan\propto')]}{3(r_1^2 - r_2^2)}\right). \tag{13}$$

The heat-flux (W/m^2) in P_{SS} section is:

$$q_{P_{SS}} = \eta((\omega r - v\sin\theta)((1-\delta_{PSS})\tau_b + (\delta_{PSS})\mu P)). \tag{14}$$

The heat-flux (W/m^2) in P_{BS} section is:

$$q_{P_{BS}} = \eta\left(\frac{2\omega r_3((1-\delta_{PBS})\tau_b + (\delta_{PBS})\mu P)}{3}\right), \tag{15}$$

where μ (0.4 is same for both material) is the coefficient of friction [46,56], P is plunge pressure (Pa), ω is ROS (rad/s), η is fraction of heat transferred to the workpiece (i.e., 0.6 and 0.4 for AA6061 and SS304, respectively [34]), and $\propto'$ is cone angle of shoulder ($\propto' = 0$ for S_{FS})). Plunging pressure of 12 and 109 MPa are taken for AA6061 and SS304, respectively [46,56]. Equations (13)–(15) are used to define the thermal boundary conditions for the SS, P_{SS}, and P_{BS}, respectively.

The specific heat (C_p) equation for AA6061 is shown below [45,46]:

$$(C_p)_{AA6061} = 929 - 0.627T + 1.481 \times 10^{-3}T^2 - 4.33 \times 10^{-8}T^3, \tag{16a}$$

$$(C_p)_{SS304} = 276 + 0.851T - 8.51 \times 10^{-4}T^2 + 3.0 \times 10^{-7}T^3. \tag{16b}$$

The thermal conductivity (k) equation for AA6061 is shown below [45,46]. Equations (16) and (17) are used to define C_p and k, respectively, as material properties for both AA6061 and SS304:

$$k_{AA6061} = 25.22 + 0.3978T + 7.358 \times 10^{-6}T^2 - 2.518 \times 10^{-7}T^3, \tag{17a}$$

$$k_{SS304} = 14.3 - 9.02 \times 10^{-3}T + 4.52 \times 10^{-5}T^2 - 2.49 \times 10^{-8}T^3. \tag{17b}$$

The boundary condition for heat exchange between the top surface of the workpiece and the environment is convective as well as radiative heat transfer [44]. The heat exchange between the bottom and side surfaces of the workpiece is conductive (due to contacts of jigs and fixtures) and convective heat transfer, respectively. All these heat exchanges are converted to convective form as shown below [44]:

$$k\frac{\partial T}{\partial z} = h_t(T - T_0), \tag{18}$$

$$k\frac{\partial T}{\partial z} = h_b(T - T_0), \tag{19}$$

$$k\frac{\partial T}{\partial z} = h_s(T - T_0), \tag{20}$$

where h_t, h_b and h_s are coefficients of heat dissipation at workpiece's top, bottom and side surface, respectively, T_0 is the environmental temperature (300 K) [45]. Equations (18)–(20)

are used to define the thermal boundary conditions for the workpiece's top surface, bottom surface, and side surface, respectively.

Validation of the current model is done with the work by Ou et al. [34]. A 3D CFD model was constructed to study the heat transfer in DFSBW of AA6061 with SS304 with a frustum conical pin tool. In the present study, the above work is replicated, and upon validation of the current methodology and procedure, additional fixed input parameters (TA and PD) are introduced. The temperature distribution data of the model closely corresponds to the experimental data of Ou et al. [34]. Table 3 compares the temperature of the experimental and model. Thus, the numerical modelling method is satisfactory.

Table 3. Comparison results between experimental and modelled temperature

Points (approx.)	Experimental temperature [34], K	Simulation model temperature, K	Error, %
p1 (8.99,0.5,3)	492.3	469.6	4.61
p2 (8.94,1,3)	475.1	455.3	4.16
p3 (-8.06,4,3)	439.4	429.4	2.27

Results and Discussion

This section examines the influence of ROS on the performance measures MWIT, MWIV, MWIVis, and TWIT. The ROS range is selected between 200 and 2200 rpm, based on findings from the literature. To evaluate the effect of ROS on the above performance indicators, all other process parameters: TRS, TA and PD, are maintained constant at 100 mm/min, 1.5°, and 0.225 mm, respectively. Table 4 presents the corresponding performance measures for the investigated ROS range of 200 to 2200 rpm. Simulation experiments were conducted for various values of ROS as process parameters to compute MWIT, MWIV, MWIVis, and TWIT performance measures for each. Columns 4–7 of Table 4 indicate the MWIT, MWIV, MWIVis, and TWIT obtained in each experiment, respectively. The analysis of results is discussed below.

Table 4. Experimental design and its results

S.No.	ROS, rpm	Max. workpiece temperature, K	MWIT, K	MWIV, m/s	MWIVis, kg/(ms)	TWIT, Nm
1	200	533	469	0.0133	3.16E+07	16.14
2	400	691	558	0.0266	1.21E+07	16.06
3	600	809	626	0.0399	4.01E+06	15.99
4	800	890	675	0.0532	2.57E+06	15.82
5	1000	942	722	0.0666	1.45E+06	15.12
6	1200	977	756	0.0799	1.08E+06	14.74
7	1400	1000	785	0.0932	9.83E+05	14.34
8	1600	1017	808	0.1065	9.56E+05	14.04
9	1800	1014	826	0.1199	8.82E+05	13.76
10	2000	1016	829	0.1332	7.50E+05	13.49
11	2200	1018	833	0.1465	6.90E+05	13.26

Effect of ROS on MWIT

From Fig. 4, it is observed that both MWIT and maximum workpiece temperature increase with increasing ROS up to a certain point, after which they tend to stabilise. At lower ROSs (200–600 rpm), a steep rise in both temperatures is noted, indicating that heat generation is highly sensitive to ROS in this range. For instance, MWIT increases from 469 K at 200 rpm to 626 K at 600 rpm, while the maximum workpiece temperature rises from 533 to 809 K over the same range. This behaviour can be attributed to enhanced frictional heat and plastic deformation as the tool speed increases [57].

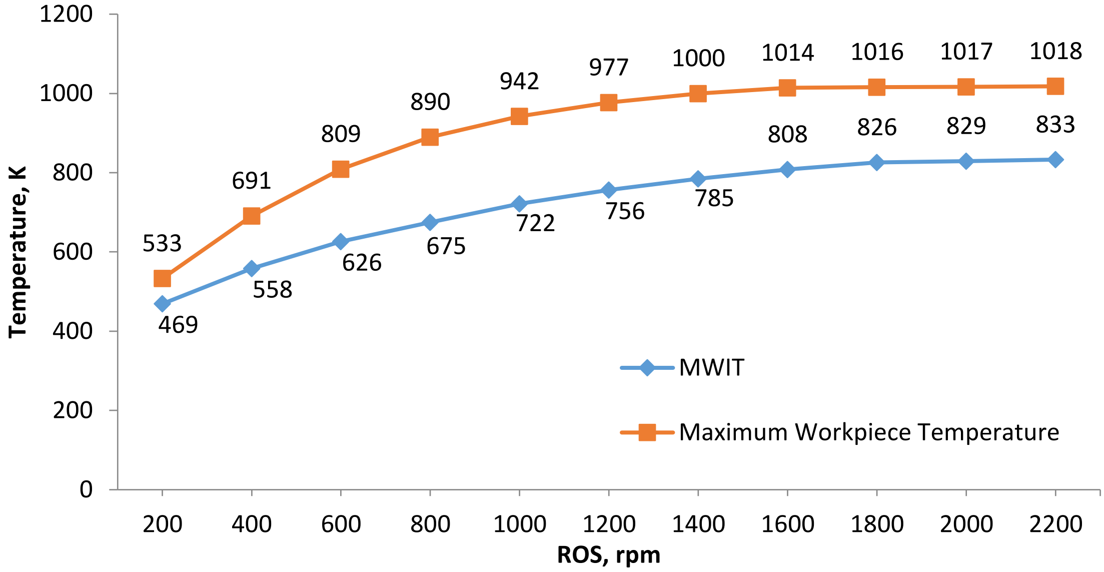

Fig. 4. Effect of ROS process parameter on MWIT performance measure

Beyond ~ 1000 rpm, the temperature curves show a tendency to plateau. The maximum workpiece temperature reaches about 1018 K at 2200 rpm, while MWIT stabilises around 833 K. This saturation effect occurs because, at higher ROSs, the heat dissipation rate through conduction and convection counterbalances the additional heat input, preventing further significant temperature rise [58].

A consistent observation is that the maximum workpiece temperature remains higher than the MWIT across all ROSs. This is expected since the bulk workpiece accumulates heat from both frictional sliding and plastic deformation, whereas the weld interface experiences localised heat generation that is partly dissipated into the adjoining materials [59].

Implications for weld quality: the progressive rise in temperature with increasing ROS enhances diffusion and reaction kinetics at the AA6061-SS304 interface, promoting IMC layer formation. However, excessive IMC growth at higher temperatures may lead to brittle phases, reducing joint toughness [60,61].

Moderate ROS values (600–1200 rpm) provide sufficient thermal softening and material flow without excessive IMC growth, which is favourable for achieving high-strength welds [60,61]. At very low ROS, inadequate heat input results in poor plasticization and insufficient bonding, while excessively high ROS (beyond ~ 1600 rpm) risks overheating, excessive flash formation, or void generation [60,61]. Thus, selecting an optimal ROS range is critical for balancing heat input, material flow, and metallurgical reactions.

Effect of ROS on MWIV

Figure 5 graph presents the variation of MWIV with ROS. It is evident that MWIV increases almost linearly with increasing ROS. At the lowest speed of 200 rpm, MWIV is only 0.0133 m/s, while at the highest speed of 2200 rpm, it reaches 0.1465 m/s, representing more than a tenfold increase. This strong positive correlation reflects the direct dependence of interface velocity on tool rotation, since higher ROS enhances the relative tangential velocity between the tool and the workpiece (from Eqs. (3)–(5)).

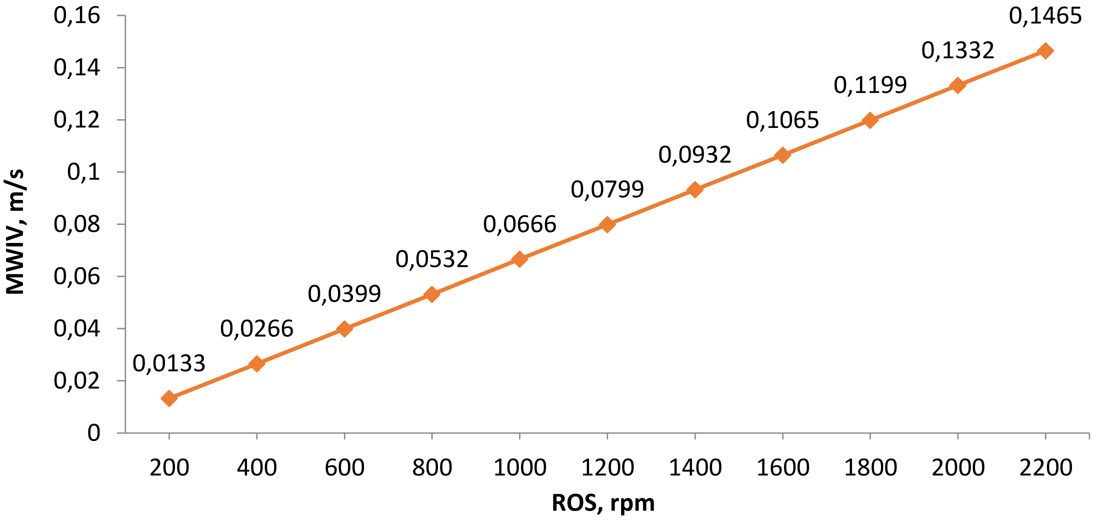

Fig. 5. Effect of ROS process parameter on MWIV performance measure

The nearly linear trend also indicates that material flow at the weld interface scales proportionally with tool speed, without showing saturation or instability within the investigated range. This suggests that ROS is the dominant driver of weld interface shear velocity, which in turn influences plastic deformation, material mixing, and bonding efficiency [62–64]. Therefore, tool speed is sometimes referred to as ROS.

Implications for weld quality: higher MWIV at increased ROS promotes improved plasticization and mixing of AA6061 and SS304 at the interface, which is essential for sound metallurgical bonding [57,63]. Since frictional heating is directly linked to interface velocity, the rising MWIV also complements the increase in weld interface and workpiece temperatures, ensuring sufficient softening for weld formation [62,65]. While low MWIV (at lower ROS) can result in insufficient stirring and weak bonding, excessively high MWIV (at very high ROS) may lead to turbulent flow, uneven mixing, or excessive flash, thereby compromising weld integrity [57,63].

Effect of ROS on MWIVis

A distinct decreasing trend is observed from Fig. 6, where MWIVis reduces rapidly with an increase in ROS up to approximately 1200 rpm, after which the values stabilise with minimal further reduction. At lower rotational speeds (200−600 rpm), extremely high viscosity values are recorded, such as 3.16E+07 kg/ms at 200 rpm and 1.21E+07 kg/ms at 400 rpm. These high viscosities indicate inadequate heat generation, resulting in poor material plasticization and insufficient mixing at the weld interface [63].

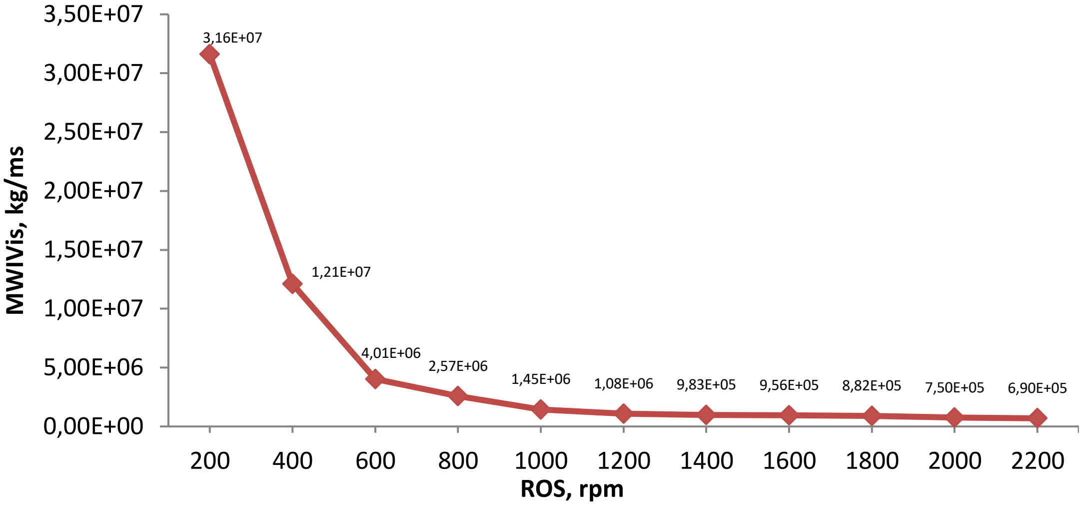

Fig. 6. Effect of ROS process parameter on MWIVis performance measure

As the ROS increases into the intermediate range (600−1200 rpm), MWIVis decreases sharply, reaching values around the order of 106 kg/ms. This reduction highlights the improved thermal softening of the workpiece materials, which enhances plastic flow and promotes effective interfacial bonding [57].

At higher ROSs (1400−2200 rpm), MWIVis values stabilise in the range of 9.83E+05 to 6.90E+05 kg/ms. This plateau suggests that beyond a certain threshold, additional increases in ROS do not significantly improve material plasticization, as the system achieves a thermal equilibrium. Excessively high speeds may therefore lead to diminishing improvements in weld quality while potentially accelerating tool wear and energy consumption [57].

Implications for weld quality: optimal joint formation is likely achieved in the intermediate to moderately high ROS range (1200−1600 rpm), where sufficient heat is generated to ensure effective mixing without excessive thermal input that could cause grain coarsening, intermetallic growth, or tool wear [57,63]. ROS directly governs interface viscosity, which in turn dictates weld strength, microstructural refinement, and overall joint performance [57,63].

Effect of ROS on TWIT

A clear decreasing trend is observed from Fig. 7, where TWIT gradually declines from 16.14 Nm at 200 rpm to 13.26 Nm at 2200 rpm. At lower ROSs (200−800 rpm), TWIT remains relatively high (≈16 Nm), indicating that greater torque is required to overcome the resistance to tool penetration and material flow due to limited heat generation and higher viscosity of the workpiece [57,58]. As the ROS increases, TWIT steadily decreases, dropping to 15.12 Nm at 1000 rpm and further to 14.04 Nm at 1600 rpm.

This reduction corresponds to enhanced softening of the material with increasing ROS, as higher frictional heating lowers viscosity and reduces the mechanical resistance encountered by the tool [57,58].

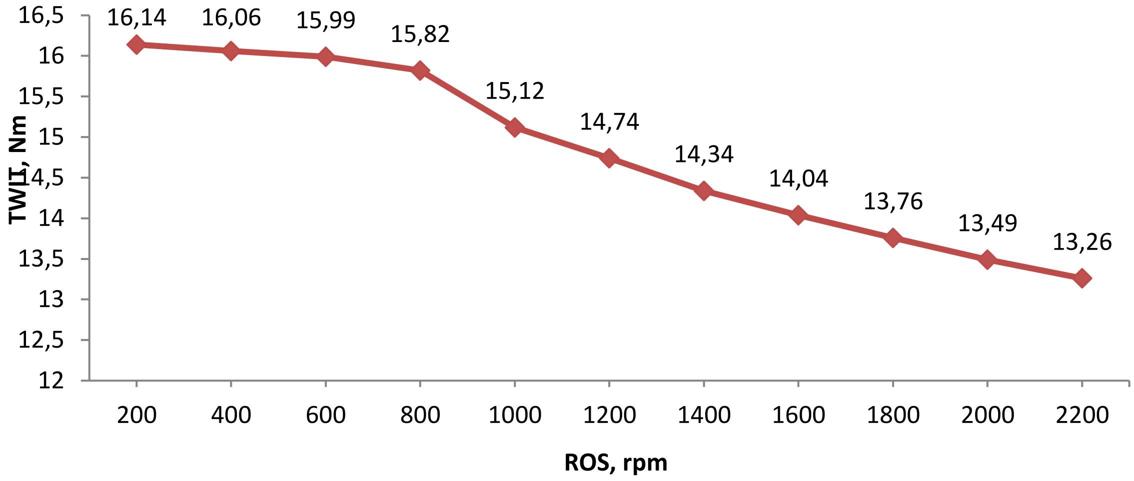

Fig. 7. Effect of ROS process parameter on TWIT performance measure

At higher ROSs (1800–2200 rpm), TWIT stabilises in the lower range of 13.76–13.26 Nm, suggesting that the system approaches thermal equilibrium where additional increases in ROS do not substantially reduce resistance to tool rotation (insufficient forging pressure at the weld interface, potentially leading to reduced consolidation, defect formation, or weaker interfacial bonding may occur) [57,58].

Implications for weld quality: at lower speeds, higher torque values indicate that the tool faces greater resistance due to insufficient heat generation and higher material viscosity. This condition often leads to poor material flow, incomplete mixing, and defect formation at the weld interface [57,58,63].

As the rotational speed increases, the decrease in torque reflects improved thermal softening and reduced flow resistance, which enhances material plasticization and promotes more uniform bonding [57,58,63]. However, excessively low torque values at very high speeds may result in inadequate forging pressure and insufficient compaction of plasticised material, which can compromise interfacial strength [57,58,63].

Conclusions

Numerical simulation of AA6061-SS304 DFSLW has demonstrated that tool ROS strongly governs the weld's thermo-mechanical behaviour:

1. MWIT and overall workpiece temperature initially rise sharply with increasing ROS before stabilising, while MWIV shows a nearly linear increase across the studied range.
2. Conversely, MWIVis and TWIT decrease significantly as ROS increases, highlighting the combined effects of frictional heating and improved material flow.
3. An intermediate ROS window of roughly 600–1200 rpm yields sufficient thermal softening and interfacial mixing without excessive intermetallic compound formation or loss of forging pressure.

These insights provide a quantitative basis for optimising DFSLW process parameters to produce defect-free, high-strength joints and to improve energy efficiency in industrial applications involving aluminium-steel hybrid structures.

CRediT authorship contribution statement

Amit Yadav: writing – original draft, conceptualization, investigation, data curation; **Ajai Jain**: writing – review & editing, supervision, data curation; **Rajiv Verma**: writing – review & editing, conceptualization, supervision, data curation.

Conflict of interest

The authors declare that they have no conflict of interest.

References

1. Tisza M, Czinege I. Comparative study of the application of steels and aluminium in lightweight production of automotive parts. *International Journal of Lightweight Materials and Manufacture*. 2018;1(4): 229–238.
2. Mir FA, Khan NZ, Nisar L, Khan HA, Alrokayan SH. Analyzing microstructural evolution and wear behavior of friction stir welded dissimilar joints of SS304 and 2024-T3 Al alloy. *Materials Letters*. 2024;366: 136493.
3. Kusuda Y. Honda develops robotized FSW technology to weld steel and aluminum and applied it to a mass-production vehicle. *Industrial Robot: An International Journal*. 2013;40(3): 208–212.
4. Lazarević M, Bajić DM, Marinković J, Alil A. Cavitation resistance of explosively welded aluminium/steel joint. *Tribology and Materials*. 2024;3(2): 67–72.
5. Damlacik S, Baydi Z, Küpeli S, Kaplan D, Akan RŞ, Uludağ M. Study on mechanical and microstructural properties of advanced high-strength welded sheet metal. *Tribology and Materials*. 2023;2(2): 68–77.
6. Klobčar D, Pušavec F, Bračun D, Garašić I, Kožuh Z, Vencl A, Trdan U. Influence of Friction Riveting Parameters on the Dissimilar Joint Formation and Strength. *Materials*. 2022;15(19): 6812.
7. Milašinović V, Alil A, Milašinović M, Vencl A, Hatala M, Dikić S, Gligorijević B. Continuous Drive Friction Welded Al/Cu Joints Produced Using Short Welding Time, Elevated Rotational Speed, and High Welding Pressures. *Materials*. 2024;17(13): 3284.
8. Tsang S. Friction welding. In: Olson DL, Siewert TA, Liu S, Edwards GR. (eds.) *ASM Handbook. Volume 6: Welding, Brazing and Soldering*. Materials Park (OH): ASM International; 1993. p.315–317.
9. Heidarzadeh A, Mironov S, Kaibyshev R, Çam G, Simar A, Gerlich A, Khodabakhshi F, Mostafaei A, Field DP, Robson JD, Deschamps A, Withers PJ. Friction stir welding/processing of metals and alloys: A comprehensive review on microstructural evolution. *Progress in Materials Science*. 2021;117: 100752.
10. Mir FA, Khan NZ, Parvez S, Siddiquee AN. Investigations on surface properties of friction stir welded dissimilar AA2024-T3 and 304 stainless steel joints. *Tribology International*. 2024;193: 109312.
11. Elmetwally HT, Abdelhafiz MA, Mahmoud E, El-Sheikh SA, Abdullah AA. Effect of Friction Stir-Welding Tool Pin Geometry on the Characteristics of Al-Cu Joints. *Applied Engineering Letters*. 2023;8(2): 60–69.
12. Nandan R, DebRoy T, Bhadeshia HKDH. Recent advances in friction-stir welding: Process, weldment structure and properties. *Progress in Materials Science*. 2008;53(6): 980–1023.
13. Lakli B, Berrahou M, Serier M. Temperature and Plastic Strain Evaluation during Friction Stir Repair of Corrosion Defects in Al2024. *Applied Engineering Letters*. 2025;10(1): 25–34.
14. Sun Z, Wu CS, Kumar S. Determination of heat generation by correlating the interfacial friction stress with temperature in friction stir welding. *Journal of Manufacturing Processes*. 2018;31: 801–811.
15. Zhai M, Wu CS, Su H. Influence of tool tilt angle on heat transfer and material flow in friction stir welding. *Journal of Manufacturing Processes*. 2020;59: 98–112.
16. Jain R, Pal SK, Singh SB. A study on the variation of forces and temperature in a friction stir welding process: A finite element approach. *Journal of Manufacturing Processes*. 2016;23: 278–286.
17. Shi L, Wu CS. Transient model of heat transfer and material flow at different stages of friction stir welding process. *Journal of Manufacturing Processes*. 2017;25: 323–339.

18. Kamalvand E, Jabbari A, Reza SM, Mazdak S, Beygi R, Mohammadi S. Effect of friction stir welding parameters on the deep drawing of tailor-welded blanks (TWBs). *CIRP Journal of Manufacturing Science and Technology*. 2021;33: 91–99.
19. Nishida T, Ogura T, Nishida H, Fujimoto M, Takahashi M, Hirose A. Formation of interfacial microstructure in a friction stir welded lap joint between aluminium alloy and stainless steel. *Science and Technology of Welding and Joining*. 2014;19(7): 609–616.
20. Habibnia M, Shakeri M, Nourouzi S, Givi MKB. Microstructural and mechanical properties of friction stir welded 5050 Al alloy and 304 stainless steel plates. *The International Journal of Advanced Manufacturing Technology*. 2015;76: 819–829.
21. Ghosh M, Gupta RK, Husain MM. Friction stir welding of stainless steel to Al alloy: Effect of thermal condition on weld nugget microstructure. *Metallurgical and Materials Transactions A*. 2014;45: 854–863.
22. Balamagendiravarman M, Kundu S, Chatterjee S. An analysis of microstructure and mechanical properties on friction stir welded joint of dissimilar 304 stainless steel and commercially pure aluminium. *Archives of Metallurgy and Materials*. 2017;62(3): 1813–1817.
23. Murugan B, Thirunavukarasu G, Kundu S, Kailas SV, Chatterjee S. Interfacial Microstructure and Mechanical Properties of Friction Stir Welded Joints of Commercially Pure Aluminum and 304 Stainless Steel. *Journal of Materials Engineering and Performance*. 2018;27: 2921–2931.
24. Mahto RP, Gupta C, Kinjawadekar M, Meena A, Pal SK. Weldability of AA6061-T6 and AISI 304 by underwater friction stir welding. *Journal of Manufacturing Processes*. 2019;38: 370–386.
25. Mahto RP, Anishetty S, Sarkar A, Mypati O, Pal SK, Majumdar JD. Interfacial Microstructural and Corrosion Characterizations of Friction Stir Welded AA6061-T6 and AISI304 Materials. *Metals and Materials International*. 2019;25: 752–767.
26. Chitturi V, Pedapati SR, Awang M. Effect of tilt angle and pin depth on dissimilar friction stir lap welded joints of aluminum and steel alloys. *Materials*. 2019;12(23): 3901.
27. Uematsu Y, Kakiuchi T, Ogawa D, Hashiba K. Fatigue crack propagation near the interface between Al and steel in dissimilar Al/steel friction stir welds. *International Journal of Fatigue*. 2020;138: 105706.
28. Chitturi V, Pedapati SR, Awang M. Investigation of weld zone and fracture surface of friction stir lap welded 5052 aluminum alloy and 304 stainless steel joints. *Coatings*. 2020;10(11): 1062.
29. Jabraeili R, Jafarian HR, Khajeh R, Park N, Kim Y, Heidarzadeh A, Eivani AR. Effect of FSW process parameters on microstructure and mechanical properties of the dissimilar AA2024 Al alloy and 304 stainless steel joints. *Materials Science and Engineering A*. 2021;814: 140981.
30. Wang J, Ling X, Zhang W, Lu X, Chen C. Microstructures and mechanical properties of friction stir welded butt joints of 3003-H112 aluminum alloy to 304 stainless steel used in plate-fin heat exchanger. *Journal of Materials Research and Technology*. 2022;21: 3086–3097.
31. Joshani E, Beidokhti B, Davodi A, Amelzadeh M. Evaluation of dissimilar 7075 aluminum/AISI 304 stainless steel joints using friction stir welding. *Journal of Alloys and Metallurgical Systems*. 2023;3: 100017.
32. Datta A, Shrivastava A, Mandal N, Roy H, Chakraborty SS. A comparative investigation of butt friction stir welding of aluminium alloys, AA 1100 and AA 7075, with AISI 304 stainless steel. *Welding in the World*. 2023;67: 1449–1465.
33. Kumar R, Manjaiah M, Davidson MJ. The effect of friction stir welding on the microstructure and mechanical properties of the dissimilar SS304 and Al7075-T6 alloy joints. *Welding International*. 2023;37(11): 643–654.
34. Ou W, Guo G, Cui C, Zhang Y, Qian L. Heat transfer in aluminum-steel joint and weld tool during the friction stir welding: Simulation and experimental validation. *The International Journal of Advanced Manufacturing Technology*. 2023;125: 2211–2224.
35. Mir FA, Khan NZ, Mukhtar Z, Badruddin IA, Kamangar S, Nisar L. Friction stir welding of AA2024-T3 and SS304 alloys: microstructural analysis, microhardness evaluation, and tensile performance. *Physica Scripta*. 2024;99(10): 105970.
36. Zhang M, Liu JM, Xue P, Liu FC, Wu LH, Ni DR, Xiao BL, Wang KS, Ma ZY. Eliminating Cu-rich intermetallic compound layer in dissimilar friction stir welding of 304 stainless steel and 2219 Al alloy via ultralow rotation speed. *Journal of Materials Processing Technology*. 2024;329: 118444.
37. Nakrani J, Yan W, Shrivastava A. Fatigue crack growth behavior in SS304-Al5083 dissimilar friction stir welded joints. *Procedia Structural Integrity*. 2024;61: 188–194.
38. Caetano GDQ, Andrade TC, Motta MF, Miranda HC, Farias JP, Bergmann LA, Dos Santos JF, Silva CC. Assessment of the joint configuration and welding parameters for the dissimilar joining of AISI 304L and AISI 410S stainless steels by friction stir welding. *The International Journal of Advanced Manufacturing Technology*. 2024;133: 5691–5703.

39. Kumar A, Bansal SN, Chandraker R. Computational modeling of blast furnace cooling stave based on heat transfer analysis. *Materials Physics and Mechanics*. 2012;15(1): 46–65.
40. Yadav A, Jain A, Verma R. Effect of tilt angle for conical pin tool with a conical shoulder on heat transfer and material flow using numerical simulation in friction stir welding. *Materials Physics and Mechanics*. 2023;51(3): 126–145.
41. Yadav A, Jain A, Verma R. Numerical Simulation of Friction Stir Welding Process to Investigate the Effect of a Conical Pin Tool with a Flat and Conical Shoulder on Heat Transfer. *NanoWorld Journal*. 2023;9(S1): S239–S242.
42. Hasan AF. CFD modelling of friction stir welding (FSW) process of AZ31 magnesium alloy using volume of fluid method. *Journal of Materials Research and Technology*. 2019;8(2): 1819–1827.
43. Yadav A, Jain A, Verma R. Rotational Speed Influence on Weld Temperature in Friction Stir Lap Joint of Aluminium Alloy 6061 Using Numerical Simulation. *Journal of Polymer and Composites*. 2024;12(S02): 235–245.
44. Nandan R, Roy GG, DebRoy T. Numerical simulation of three dimensional heat transfer and plastic flow during friction stir welding. *Metallurgical and Materials Transactions A*. 2006;37(4): 1247–1259.
45. Yang CL, Wu CS, Lv XQ. Numerical analysis of mass transfer and material mixing in friction stir welding of aluminum/magnesium alloys. *Journal of Manufacturing Processes*. 2018;32: 380–394.
46. Nandan R, Roy GG, Lienert TJ, DebRoy T. Numerical modelling of 3D plastic flow and heat transfer during friction stir welding of stainless steel. *Science and Technology of Welding and Joining*. 2006;11(5): 526–537.
47. Thomas WM, Johnson KI, Wiesner CS. Friction stir welding—recent developments in tool and process technologies. *Advanced Engineering Materials*. 2003;5(7): 485–490.
48. Sheppard T, Wright DS. Determination of flow stress: Part 1 constitutive equation for aluminium alloys at elevated temperatures. *Metallurgical Technology*. 1979;6(1): 215–223.
49. Sheppard T, Jackson A. Constitutive equations for use in prediction of flow stress during extrusion of aluminium alloys. *Materials Science and Technology*. 1997;13(3): 203–209.
50. Tello KE, Gerlich AP, Mendez PF. Constants for hot deformation constitutive models for recent experimental data. *Science and Technology of Welding and Joining*. 2010;15(3): 260–266.
51. Hasan AF, Bennett CJ, Shipway PH, Cater S, Martin J. A numerical methodology for predicting tool wear in friction stir welding. *Journal of Materials Processing Technology*. 2017;241: 129–140.
52. Darvazi AR. A semi-analytical solution for temperature distribution in friction stir welding. Research Square [Preprint] 2021. Available from: doi.org/10.21203/rs.3.rs-521499/v1
53. Sadeghian B, Taherizadeh A, Atapour M. Simulation of weld morphology during friction stir welding of aluminum–stainless steel joint. *Journal of Materials Processing Technology*. 2018;259: 96–108.
54. Hamilton C, Dymek S, Sommers A. A thermal model of friction stir welding in aluminum alloys. *International Journal of Machine Tools and Manufacture*. 2008;48(10): 1120–1130.
55. Neto DM, Neto P. Numerical modeling of friction stir welding process: A literature review. *The International Journal of Advanced Manufacturing Technology*. 2013;65: 115–126.
56. Zhang J, Shen Y, Li B, Xu H, Yao X, Kuang B, Gao J. Numerical simulation and experimental investigation on friction stir welding of 6061-T6 aluminum alloy. *Materials & Design*. 2014;60: 94–101.
57. Mishra RS, Ma ZY. Friction stir welding and processing. *Materials Science and Engineering R: Reports*. 2005;50(1–2): 1–78.
58. Mishra RS, Mahoney MW. (Eds.) *Friction Stir Welding and Processing*. Materials Park (OH): ASM International; 2007.
59. Mishra RS, De PS, Kumar N. *Friction Stir Welding and Processing: Science and Engineering*. Berlin: Springer; 2014.
60. Khalafe WH, Sheng EL, Bin Isa MR, Omran AB, Shamsudin SB. The Effect of Friction Stir Welding Parameters on the Weldability of Aluminum Alloys with Similar and Dissimilar Metals: Review. *Metals*. 2022;12(12): 2099.
61. Safeen MW, Russo Spena P. Main Issues in Quality of Friction Stir Welding Joints of Aluminum Alloy and Steel Sheets. *Metals*. 2019;9(5): 610.
62. Schmidt H, Hattel J, Wert J. An analytical model for the heat generation in friction stir welding. *Modelling and Simulation in Materials Science and Engineering*. 2004;12(1): 143–157.
63. Yadav A, Jain A, Verma R. Effect of pin shapes on temperature distribution in friction stir lap joint of AA6061 with AZ31 using numerical simulation. *International Journal of Simulation and Process Modelling*. 2024, 21(4): 251-263.
64. Arora A, Nandan R, Reynolds AP, DebRoy T. Torque, power requirement and stir zone geometry in friction stir welding through modeling and experiments. *Scripta Materialia*. 2009;60(1): 13–16.
65. Ulysse P. Three-dimensional modeling of the friction stir-welding process. *International Journal of Machine Tools and Manufacture*. 2002;42(14): 1549–1557.

MATERIALS PHYSICS AND MECHANICS RESEARCH ARTICLE

Submitted: September 19, 2025 **Revised: December 17, 2025** **Accepted: January 15, 2026**

Tool wear and surface roughness analysis in hard turning of AISI 4340 steel with coated carbide inserts

M. Zulfiqar [1], A.S. Jamali [1], S. Hussain [2]

[1] Quaid-e-Awam University of Engineering, Science and Technology, Nawabshah, Sindh, Pakistan

[2] Indus University, Karachi, Pakistan

✉ muradzulfiqar@gmail.com

ABSTRACT

The performance of CVD-coated carbide inserts ($TiCN/Al_2O_3$) in hard turning AISI 4340 steel at cutting speeds of 60, 95, 180, and 250 m/min, under both dry and wet conditions are investigated. The goals were to evaluate tool wear, surface roughness, and wear mechanisms over different machining conditions. Surface roughness Ra value was noticed, and it dropped to Ra = 0.30 μm at 180 m/min but increased at 250 m/min due to vibration, edge instability, and wear. Flank wear rose with cutting speed: 186 μm at 60 m/min, 265 μm at 180 m/min, 542 μm at 250 m/min (dry), and 692 μm (wet), exceeding ISO tool life (VB = 300 μm) due to edge breakage, flaking, and adhesion. The examination of the tool surface by SEM and EDS revealed abrasion and slight coating delamination at low speeds, adhesion and oxidation at intermediate speeds, and catastrophic tool failure at high speeds.

KEYWORDS

AISI 4340 steel • CVD coated insert • hard turning • surface roughness

Citation: Zulfiqar M, Jamali AS, Hussain S. Tool wear and surface roughness analysis in hard turning of AISI 4340 steel with coated carbide inserts. *Materials Physics and Mechanics.* 2026;54(1): 101–117. http://dx.doi.org/10.18149/MPM.5412026_10

Introduction

AISI 4340 is a medium carbon low alloy steel, widely known for its good tensile strength. It is commonly used in making shafts, gears, screws and heavy-duty studs. Because of its properties, especially after hardening, it is applied in aerospace, automotive and defense industries for critical components where toughness and reliability are very important [1] The alloying elements like chromium, nickel and molybdenum improve their hardenability and strength. But the same factors that give high performance also make machining very difficult, especially when hardness is above 45 HRC (hardness Rockwell C). Under dry or severe cutting conditions this problem gets even worse. In machining, the main difficulties are fast tool wear, high cutting temperature, and heavy friction at the chip–tool interface. These lead to thermal instability, dimensional inaccuracy, and poor surface quality, which eventually affect productivity and cost [2,3]. Even with conventional coolant, the wear cannot be fully eliminated because cutting fluid does not always reach the chip–tool zone effectively at high speed and hardness [4]. Hardened AISI 4340 has a tempered martensitic microstructure that strongly resists plastic deformation. This makes it fall under difficult-to-machine materials since machining produces high forces and high wear, as reported by Boztepe et al. [5]. The presence of hard carbides in tempered martensite accelerates abrasive wear and reduces tool life.

Publisher: Peter the Great St. Petersburg Polytechnic University

Selvaraj [6] showed the adhesive and abrasive wear on the cutting tool at higher cutting speeds negatively affect the surface finish of the workpiece. Darwish [7] mentioned that tool wear is a key reason for poor surface finish, inaccuracies and shorter tool life. Minouiz et al. [8] noted adhesion, abrasion and edge rounding as main wear mechanisms for PVD-coated tools, while for CVD (chemical vapor deposition) coated tools built-up edge (BUE) and chipping were dominant during continuous cutting at high speed. Calaph et al. [9] observed that speed, feed and depth of cut have significant influence on flank wear in CNC (computer numerical control) turning of EN8 steel. Šramhauser et al. [10] also showed that coating thickness and structure matter a lot, thinner Al_2O_3 (aluminium oxide) improved chip flow and heat transfer while TiN-coated tools gave surface roughness of 0.76 μm.

Furthermore, Bag et al. [11] studied hardened AISI 4340 and found cutting speed as the most dominant factor (66.06 %) influencing flank wear. They reported that increasing speed from 80 to 260 m/min caused rubbing due to high temperature and pressure, leading to thermal softening of the cutting edge. Butt et al. [12] observed similar wear trends for turning of 45 HRC AISI 4340 using TiCN (titanium carbonitride)/Al_2O_3/TiN carbide tools at speeds 50–200 m/min and feeds 0.051–0.101 mm/rev. Kishore et al. [13] further showed that the temperature resulting from the tool-workpiece rubbing causes larger surface wear and defects. The tool flank rubs against the surface of material and adhesive wear, abrasion combined with heat is produced from contact. Hurtasenko et al. [14] associated very high shear zone temperatures with adhesive, diffusion, and brittle fracture type wear. Hassan et al. [15] reported crater wear as the main form in machining DC53 steel hardened to 40 HRC. Likewise, Santos et al. [16] observed adhesion–abrasion wear during dry micro-milling of AISI D2. With development of coatings and improved tool geometry, wear has been reduced. Ahmed et al. [17] showed that TiAlN coating increased tool life, while Jouini et al. [18] found that Al_2O_3/TiCN coating improved surface quality at high speeds on AISI 4340. Silva et al. [19] reported that coated tools had better thermal stability, while Çakan et al. [20] noted TiSiN+Al_2O_3+TiN multilayers gave better results when turning AISI D2. Rashid et al. [21] studied hard turning of AISI 4340 with a CBN insert and obtained very low surface roughness (0.45 μm). They also concluded that lower feed improves finish but increases wear, showing the trade-off between tool life and surface quality. More improvement was also noted with multilayer coatings. Kumar et al. [22] reported over 15 times higher tool life in dry drilling of AISI D2, and Hamadi et al. [23] confirmed better tool life for coated inserts while machining AISI 4140. Dry high-speed machining is considered cost-effective and environmentally friendly [24]. But at very high speeds, cutting force, plastic deformation and surface damage increase, which accelerates tool wear and reduces quality [25,26].

Although many studies are done on tool wear and surface roughness separately, only few looked at their direct relationship under dry and wet machining with coated carbide tools at high speeds. Also, the exact wear mechanisms that affect surface finish are still not clear. From the literature, it can be seen that little work is reported on Al_2O_3/TiCN multilayer CVD-coated carbide tools in high-speed hard turning of hardened AISI 4340 steel. Since high-speed machining is important for achieving good surface finish, this gap is critical. Therefore, the present study investigates tool wear and surface roughness of hardened AISI 4340 steel at different cutting speeds. SEM (scanning electron microscopy) and EDS (energy dispersive spectroscopy) analysis are used to identify the dominant wear mechanisms. This work contributes to better understanding of machinability of AISI 4340 steel and offers practical guidance for optimizing cutting conditions, monitoring tool wear, and improving surface finish in hard turning.

Materials and Methods

Material and heat treatment

Commercial AISI 4340 steel rods, sourced from Peoples Steel Mills in Pakistan, were used in this study. The material, in its as-received state, had a hardness of nearly 30 HRC. In order to bring the hardness level suitable for hard turning, the rods were heat treated. The treatment involved austenitizing at 850 °C for 120 min in an RJX-45 box furnace, then quenching in HJ-20 oil to near room temperature. and subsequently tempered at 480 °C for 120 min. The purpose of this tempering step was to relieve internal stresses, lower brittleness, and at the same time enhance toughness while still keeping the hardness at a high level. The final hardness, checked with an Insize Rockwell tester (ASTM E18) (Fig. 1(b)), was found to be around 55 ± 1 HRC. The chemical composition was determined using a Spectrolab M9 spectrometer shown in Fig. 1(a), while the microstructure was observed with a Versamet 2 metallurgical microscope. Prior to machining tests, the outer layer of the heat-treated rods was lightly cut to remove any surface inconsistencies. For each experimental run, a cutting length of 120 mm was used. Every set of machining parameters was repeated three times, giving a total cutting distance of 360 mm for each condition. The average values from the three repetitions were taken for further analysis.

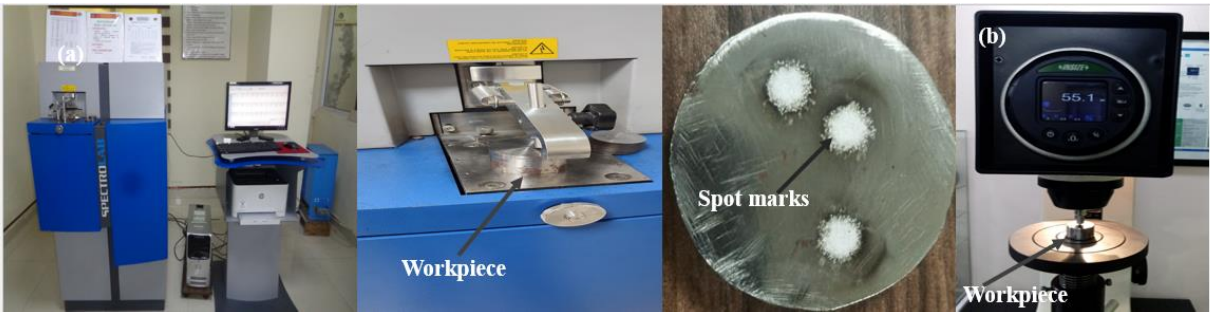

Fig. 1. Spectrometric analyses (a), hardness tester (b)

Experimental setup

Turning experiments were conducted utilizing a Goodway CGL-2 CNC lathe equipped with a FANUC Oi-TF control system shown in Fig. 2(a). The tool-workpiece configuration is depicted in Fig. 2(b), illustrating the hard turning of the heat-treated AISI 4340 steel. For wet machining trials at 250 m/min, a commercial mineral based cutting oil (Arab Lube, diluted at 1:20 with water) was applied as a conventional flood coolant, and was used exclusively at a cutting speed of 250 m/min as depicted in Fig. 2(c) The coolant was directed at the tool–chip interface through an external nozzle to evaluate its effectiveness at high-speed cutting conditions. Cutting experiments were carried out at four cutting speeds of 60, 95, 180, and 250 m/min, while the feed rate and depth of cut were kept constant throughout the study at 0.1 mm/rev and 0.5 mm, respectively. This selective use was intended to compare dry and wet machining under maximum thermal load conditions, while all other trials were conducted dry. The experimental design is comprehensively detailed in Table 1.

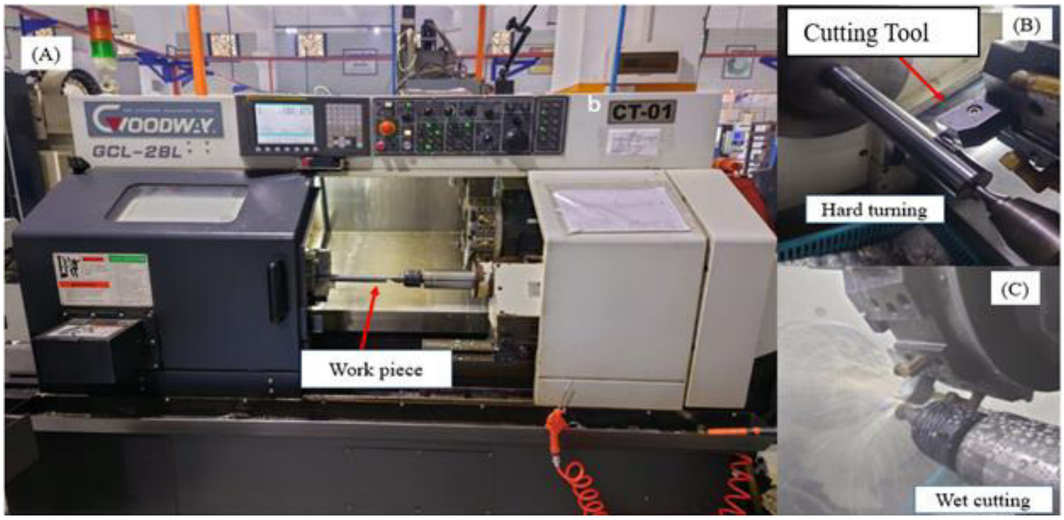

Fig. 2. Experimental setup showing (a) CNC lathe, (b) tool and workpiece, hard turning, (c) wet cutting with coolant

Table 1. Workpiece and setup specifications

Parameters	Details / Specifications
Material	AISI 4340 Steel
Workpiece length, mm	200
Machining length, mm	120
Workpiece diameter, mm	30
Workpiece hardness, HRC	55 ± 1
Tooling	Mitsubishi CVD-coated carbide inserts (CNMG 120404)
Insert coating	CVD multi-layer coating of TiCN and Al_2O_3
Tool nose radius, mm	0.4
Tool holder	PCLNR 2020K12
Machine	Goodway CGL-2 CNC Lathe with FANUC Oi-TF control
Cutting speeds, m/min	60, 95, 180, and 250
Machining environment	Dry conditions (low to high-speed machining); Cutting fluid for high-speed machining
Feed rate, mm/rev constant	0.1
Depth of cut, mm constant	0.5

Cutting tools

For the experimental machining trials, the cutting tool selected was a commercially available CVD coated carbide insert from Mitsubishi Materials [27]. This particular insert is characterized by a sophisticated multilayer coating system, primarily consisting of $TiCN/Al_2O_3$ layers, which is engineered to provide enhanced wear resistance and thermal stability during cutting. The geometry of the insert includes a defined tool nose radius of 0.4 mm, a feature critical for influencing surface finish and tool strength. A schematic representation detailing the insert's geometry can be found in Fig. 3. For mounting, the insert was securely assembled onto a standard PCLNR 2020K12 style tool holder. Photographic evidence of the actual physical insert, along with its complete assembly onto the tool holder to show the final cutting geometry, is clearly provided in Fig. 4(a,b) respectively.

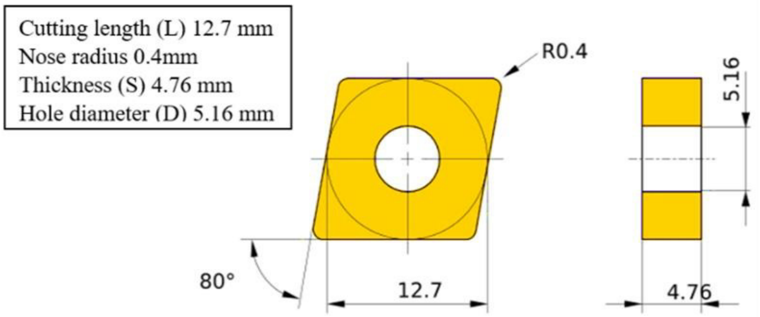

Fig. 3. Schematic of the selected CVD-coated carbide insert (CNMG 120404). Based on [27]

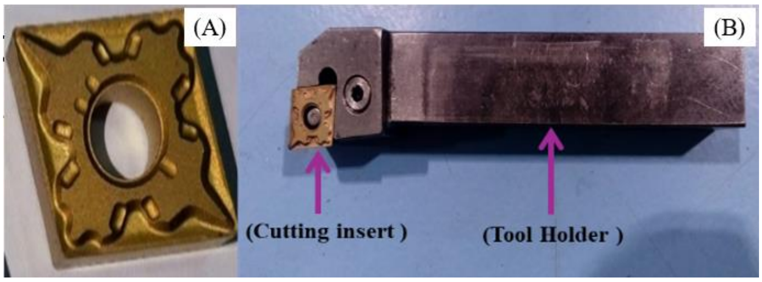

Fig. 4. (a) CVD-coated cutting insert; (b) insert mounted on PCLNR 2020K12 tool holder

Tool wear measurement

Flank wear (VB) was measured after each 120 mm cutting pass using a Dino-Lite Premier AM7013MT digital microscope, and the final values reported correspond to the tool condition after the third pass (total cutting length = 360 mm). An average flank wear criterion of VB ⩾ 300 μm was adopted in accordance with ISO 3685 as the reference limit and measurement accuracy was ensured by calibrating the system with a certified stage micrometer before and during testing. For a more in-depth investigation into the fundamental mechanisms responsible for the wear, advanced characterization techniques

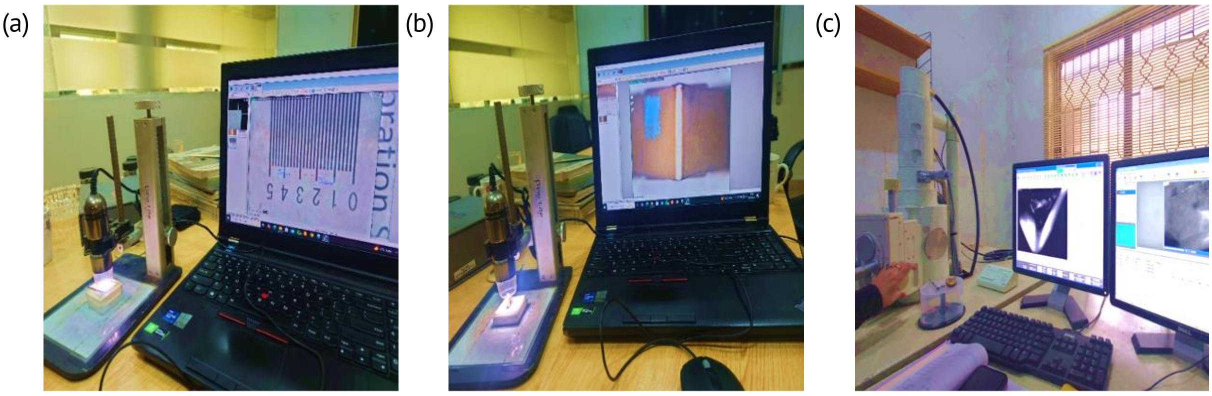

Fig. 5. Tool wear measurement and analysis setup: (a) calibration of Dino-Lite microscope; (b) flank wear measurement on tool edge; (c) SEM/EDS analysis of worn tools

were employed. This involved using SEM on a Jeol JSM 6380 unit, which provided high-magnification imagery of the wear scars and crater formation. Furthermore, energy dispersive X-ray spectroscopy (EDS) was performed with a JED-2300 detector attached to the SEM; this allowed for elemental analysis of the worn surfaces to identify diffusion and adhesion processes. The complete experimental arrangement used for these tool wear measurement and subsequent analysis procedures is visually detailed in Fig. 5.

Surface roughness measurement

Arithmetic average surface roughness R_a was measured in accordance with ISO 4287/4288 standards using a calibrated Mitutoyo SJ-310 tester, with a cutoff length of 0.8 mm, evaluation length of 4.0 mm, and probe speed of 0.5 mm/s. For each experimental condition, three roughness measurements were taken at distinct locations on the workpiece after each cut, and the mean value was used for analysis. The measurement setup is shown in Fig. 6. This integrated approach allowed direct correlation between tool wear progression and surface quality, while SEM/EDS analyses validated the underlying wear mechanisms.

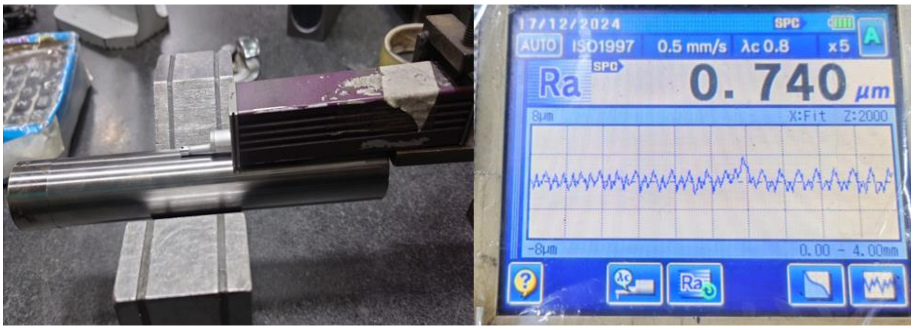

Fig. 6. Surface roughness measurement setup using Mitutoyo SJ-310 tester

Results and Discussion

Material characterization

The chemical composition of the heat-treated AISI 4340 steel is provided in Table 2. The measured values are consistent with the ASTM A29 standard range for AISI 4340. Chromium (Cr), nickel (Ni), and molybdenum (Mo) add hardness, strength, and ductility, while carbon (C) gives wear resistance by forming a carbide. The heat treatment applied provided a hardness level of 55 ± 1 HRC (ASTM E18), confirming suitability for hard turning.

The microstructure, given in Fig. 7, was prepared according to ASTM E3 and etched using 2 % Nital as per ASTM E407. A tempered martensitic matrix characteristic of quenched and tempered AISI 4340 steel was seen at a 400 ×magnification. This structure provides high wear resistance by means of martensite and carbides, and toughness that causes high cutting forces and thermal stresses during cutting [15]. Understanding this microstructure is crucial for interpreting the machining behavior observed in the experiments, as it directly influences tool wear mechanisms and surface roughness outcomes.

Table 2. Chemical composition of heat-treated AISI 4340 steel (measured using Spectrolab M9)

Elements	C	Mn	Cr	Si	Ni	Mo	Fe
Wt. %	0.38	0.63	0.99	0.3	2.01	0.3	Balance

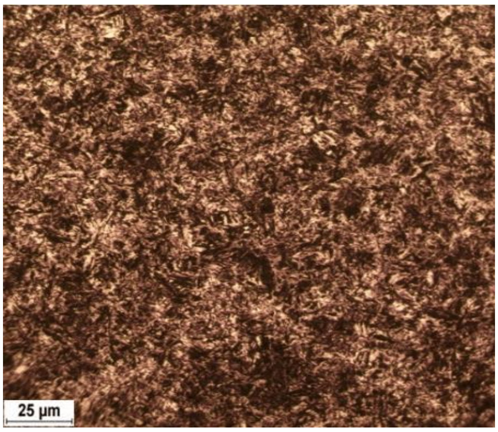

Fig. 7. Tempered martensitic microstructure of heat treated AISI 4340 steel

Surface roughness

The surface roughness (R_a) 0.931–1.069 µm with the cutting speed *V* of 60 m/min that corresponded to the three subsequent cuts (Fig. 8) was also characterized by a relatively high roughness. From 95 m/min, increasing the cutting velocity the surface roughness decreased to 0.657–0.877 µm (Fig. 9). At 180 m/min, even better results were achieved, showing R_a values of 0.303–0.612 µm (Fig. 10). Such a gradual decrease in R_a at higher speeds is considered to result from the shorter tool workpiece contact time and thermal

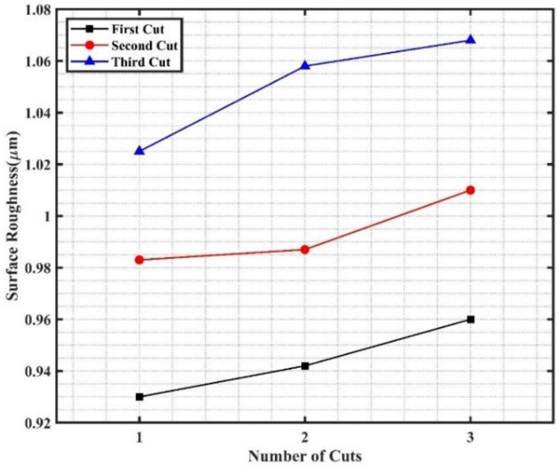

Fig. 8. Surface roughness at *V* = 60 m/min

\

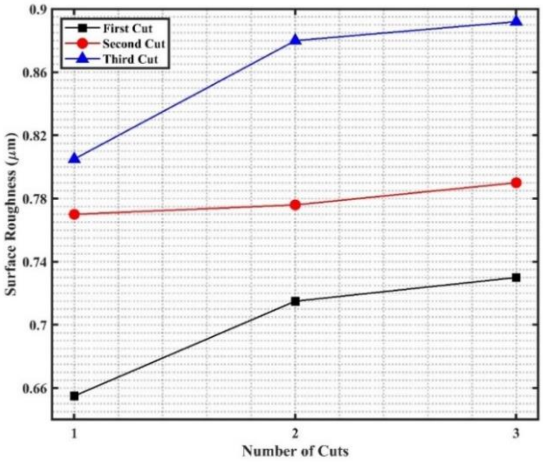

Fig. 9. Surface roughness at *V* = 95 m/min

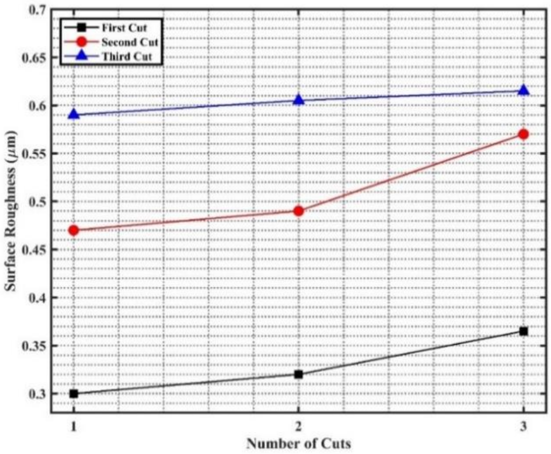

Fig. 10. Surface roughness at *V* = 180 m/min

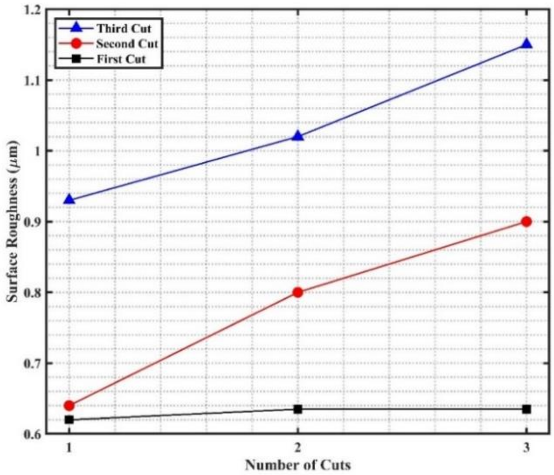

Fig. 11. Surface roughness at V = 250 m/min

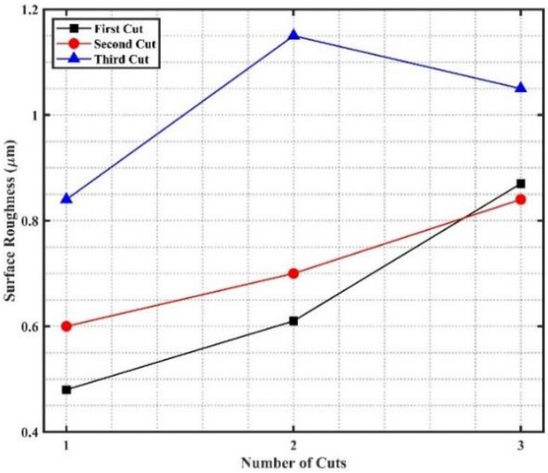

Fig. 12. Surface roughness at V = 50 m/min (wet)

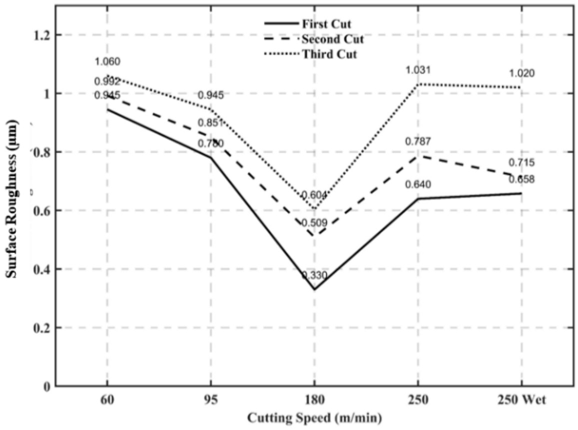

Fig. 13. Variation of surface roughness (R_a) with cutting speed for different numbers of cuts

softening of the workpiece material that enables smoother cutting. Similar trends have been reported in previous studies [28]. Surface roughness R_a was increased at 250 m/min (the maximum cutting speed) than at 180 m/min as depicted in Fig. 11. At higher cutting speeds, the cutting tool may suffer from extreme edge damage, such as flaking, notching or even catastrophic wear, which results in a blunt edge [18]. This can result in uneven cuts and differences in the texture of the surface. In addition, chatter and vibrations introduce oscillations at the tool edge, which cause the formation of an irregular surface pattern, and consequently an increase in the roughness [29].

Furthermore, for the highest speed of 250 m/min, surface roughness values became slightly better when wet cutting was performed (from 0.490 to 1.069 μm) than those for dry cutting, as presented in Fig. 12. It is noted that, despite the coolant application, R_a increased on the third cut, and the trend was different in comparison with the first cut at this speed. The uneven roughness pattern at high speeds, even during wet machining might be caused by vibration, instability, or sudden tool breakage and notching in the tool's cutting edge [30]. The general behavior is highlighted in Fig. 13, which collects R_a variation at all cutting speeds and conditions. The results show a U-shape, i.e., roughness decreases with increasing speed up to 180 m/min where the lowest surface roughness ($R_a \approx 0.30–0.61$ μm) was achieved, and increases again at 250 m/min. In wet cutting at

250 m/min, R_a values became better than for dry cutting but increased with respect to moderate cutting speeds (95–180 m/min). These findings confirm that moderate to high cutting speeds (95–180 m/min) provide the optimum balance between surface finish and machining stability, whereas excessively high speeds lead to deterioration despite the use of coolant, due to high cutting temperature and excessive tool wear [15].

Tool wear

Figure 14 depicts the flank wear (VB) evolution through several cuts at different cutting speeds. The wear measured from 186 μm at 60 m/min to 229 μm at 95 m/min, and 265 μm at 180 m/min. At 250 m/min, wear sharply increased to 542 μm under dry conditions, exceeding the ISO 3685 tool life standard (V_b = 300 μm). Under wet conditions at 250 m/min, wear reached 692 μm as depicted in Table 3 after final cut. Elevated temperatures in hard turning led to coolant evaporation, which failed to cool the tool, causing thermal softening and reduced wear resistance [31]. These results indicate that tool wear remains moderate up to 180 m/min but becomes significant beyond that, with catastrophic wear at 250 m/min.

Figure 15 illustrates the final flank wear value after the last cut, highlighting the sharp increase in wear, especially under wet conditions. Figure 16 digital microscopic pictures further illustrate wear progression at different cutting speeds, showing mild wear at 60 and 95 m/min, moderate wear at 180 m/min, and severe adhesion and localized chipping and indicating accelerated coating delamination with significant wear observed at 250 m/min. Under wet cutting conditions at the same cutting speed of250 m/min, severe edge chipping, Flaking, coating delamination and were evident, this is due to high-speed machining of hardened steel generates high temperatures which result in failure of a tool [32].

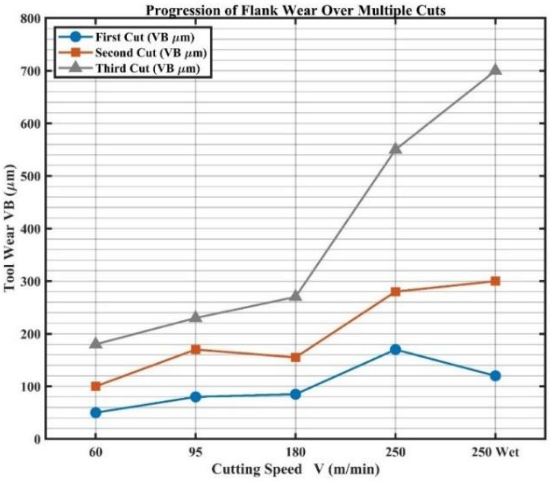

Fig. 14. Flank wear progression (μm) across first, second, and third cuts at different cutting speeds, including wet conditions

Table 3. Flank wear of CVD-coated tool at different cutting speeds after final cut

Speed, m/min	Flank wear, μm
60	186
95	229
180	265
250	542
250 (wet)	692

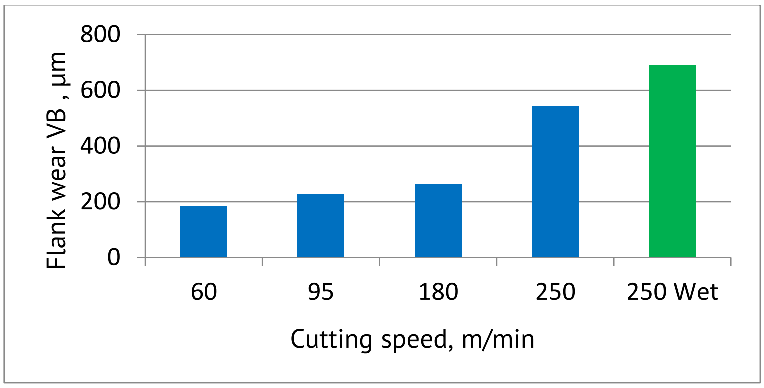

Fig. 15. Flank wear (VB) after final cut at different cutting speeds under dry and wet conditions

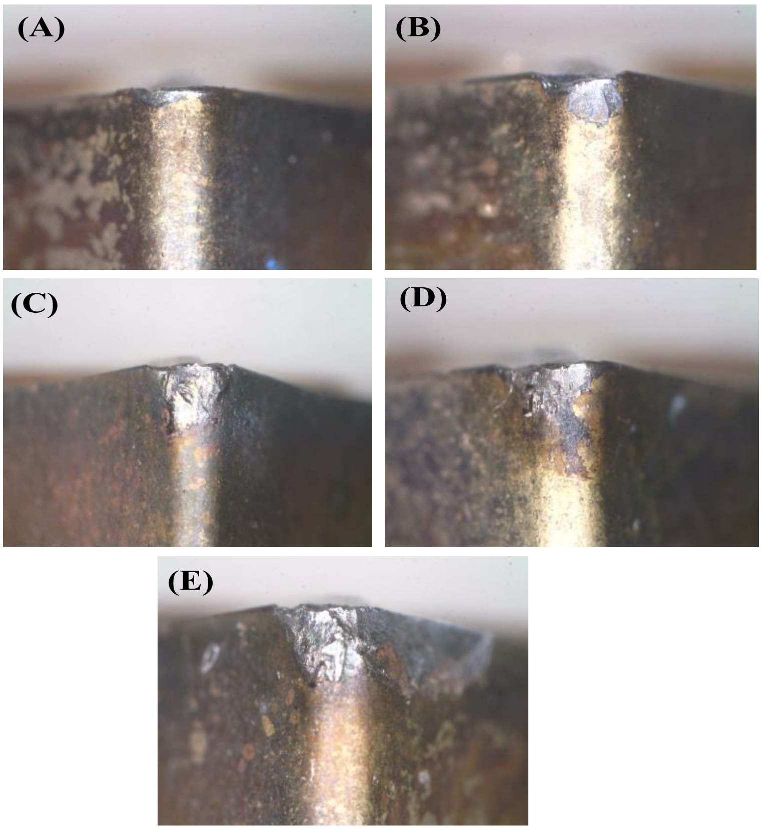

Fig. 16. Optical images of tool wear progression at cutting speeds: (a) 60 m/min; (b) 95 m/min; (c) 180 m/min; (d) 250 m/min (dry); (e) 250 m/min (wet)

SEM and EDS analysis of cutting tool

The EDS analysis of the fresh CVD-coated carbide insert, shown in Fig. 17 reveals the presence of carbon (C), oxygen (O), aluminum (Al), and titanium (Ti) supporting the multi-layer coating structure (TiCN/ Al_2O_3) on the tool. Notably no tungsten (W) was noticed on the fresh tool surface, as the underlying substrate is fully covered by the CVD coating. This baseline composition provides a clear reference for interpreting element redistribution during machining.

The substantial tungsten content observed in the EDS analyses of worn tool surfaces (10-59 wt. % in Figs. 18–22) is attributed to the substrate material (W). As seen in the EDS analysis of the fresh insert (Fig. 17), no tungsten is detected on the unused tool due to complete coverage by the multi-layer CVD coating. The presence of tungsten after cutting, particularly at higher cutting speeds, indicates local delamination of the coating, exposing the tungsten-rich substrate. Variations in tungsten content result from differences in coating loss severity, which increases with cutting speed, and the adhesion of workpiece material layers. At lower cutting speeds (60 m/min), the coating remains largely intact, while higher cutting speeds cause more significant coating damage and greater exposure of the substrate.

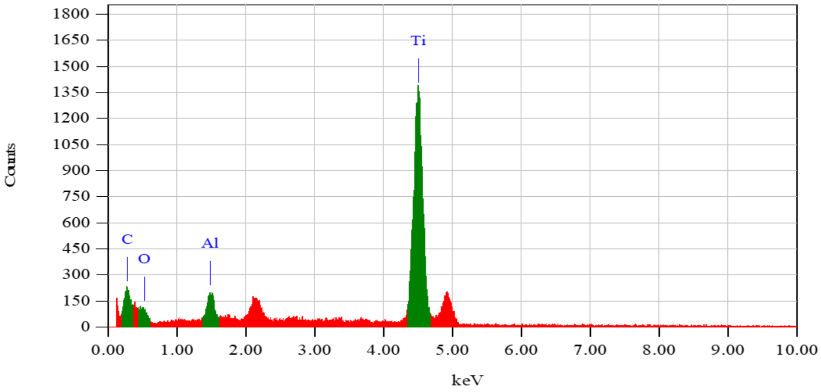

Elements	(Wt. %)
C	6.95
O	6.05
Al	2.65
Ti	84.35

Fig. 17. EDS analysis of the fresh CVD-coated carbide insert before cutting

The wear mechanisms of the CVD-coated carbide inserts were examined by SEM after the experiments, and EDS spot analysis on the worn areas revealed that the dominant wear mechanisms evolved with increasing cutting speed, consistent with previous research on hard turning [33].

At cutting speed 60 m/min SEM images Fig. 18(a)revealed coating delamination and parallel abrasion marks on the flank, indicative of abrasive wear and formation of grooves caused by hard metallic carbides in the steels [15]. EDS analysis (Fig. 18(b)) confirmed strong Al and Ti peaks from the tool coating, suggesting the protective layer remained largely intact. Minor Fe traces indicated slight workpiece material adhesion, and low Oxygen content ruled out significant oxidation. Consequently, small scale abrasion with coating delamination dominated at low cutting speeds in hard turning, aligning with prior research [34].

At a cutting speed of 95 m/min, Fig. 19, SEM analysis revealed the formation of a built-up edge on the rake face, characteristic of adhesive wear during the hard turning [35]. EDS confirmed elevated Fe, Cr, and Ni transferred from the AISI 4340 workpiece. The progression of flank wear and repeated BUE, detachment indicates cyclic adhesion and tearing, corroborating existing research [36,37]. Although coating elements were still detected, at lower levels than at 60 m/min, indicating that the coating was not completely removed. Their reduced intensity indicated partial loss of the protective layer. adhesion and abrasion occur concurrently at this intermediate speed, with elevated temperatures accelerating material transfer.

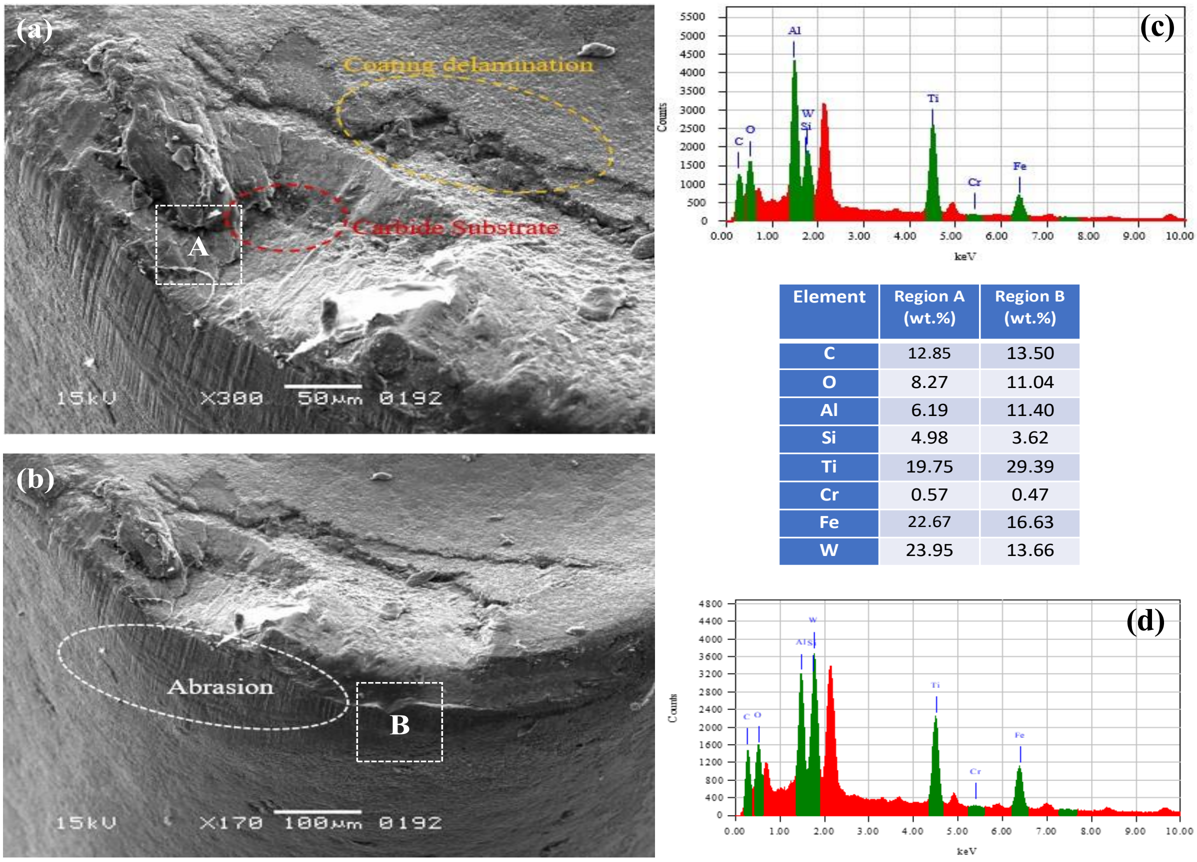

Element	Region A (wt.%)	Region B (wt.%)
C	12.85	13.50
O	8.27	11.04
Al	6.19	11.40
Si	4.98	3.62
Ti	19.75	29.39
Cr	0.57	0.47
Fe	22.67	16.63
W	23.95	13.66

Fig. 18. SEM (a,b) and EDS (c,d) analysis on the worn tool at V = 60 m/min

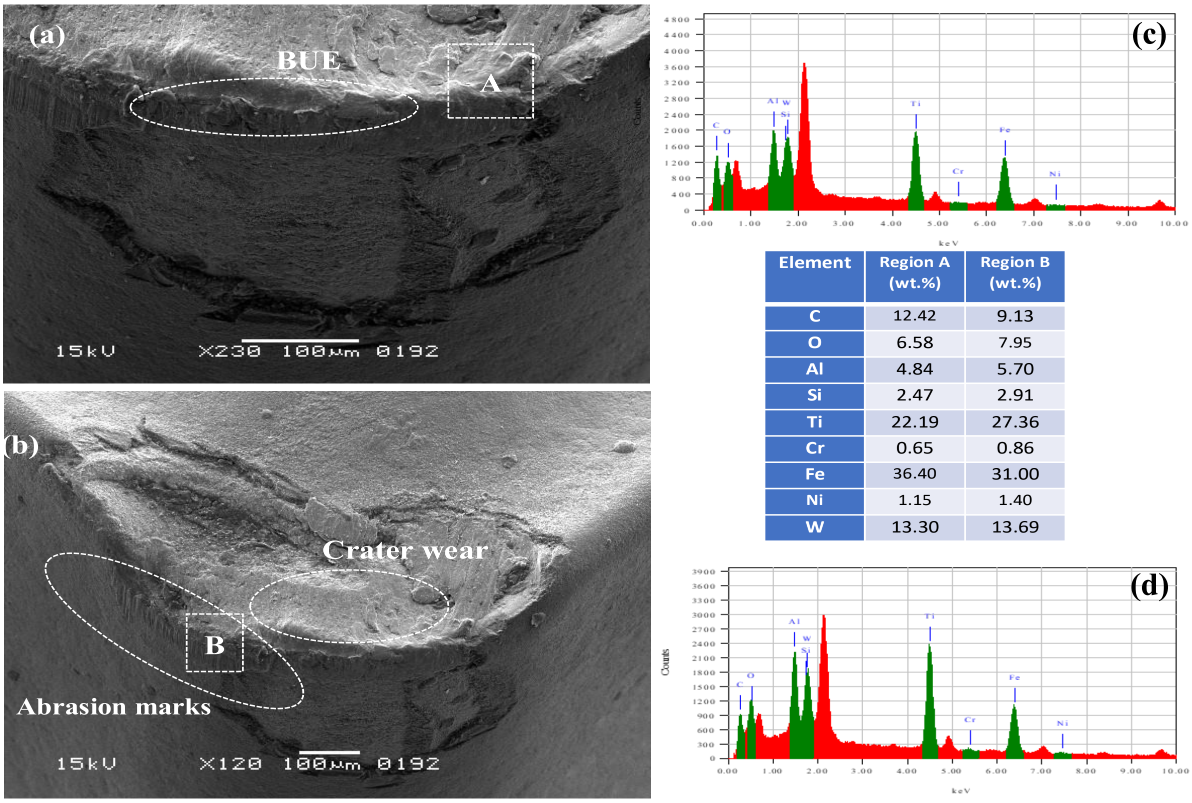

Element	Region A (wt.%)	Region B (wt.%)
C	12.42	9.13
O	6.58	7.95
Al	4.84	5.70
Si	2.47	2.91
Ti	22.19	27.36
Cr	0.65	0.86
Fe	36.40	31.00
Ni	1.15	1.40
W	13.30	13.69

Fig. 19. SEM (a,b) and EDS analysis (c,d) on the worn tool at V = 95 m/min

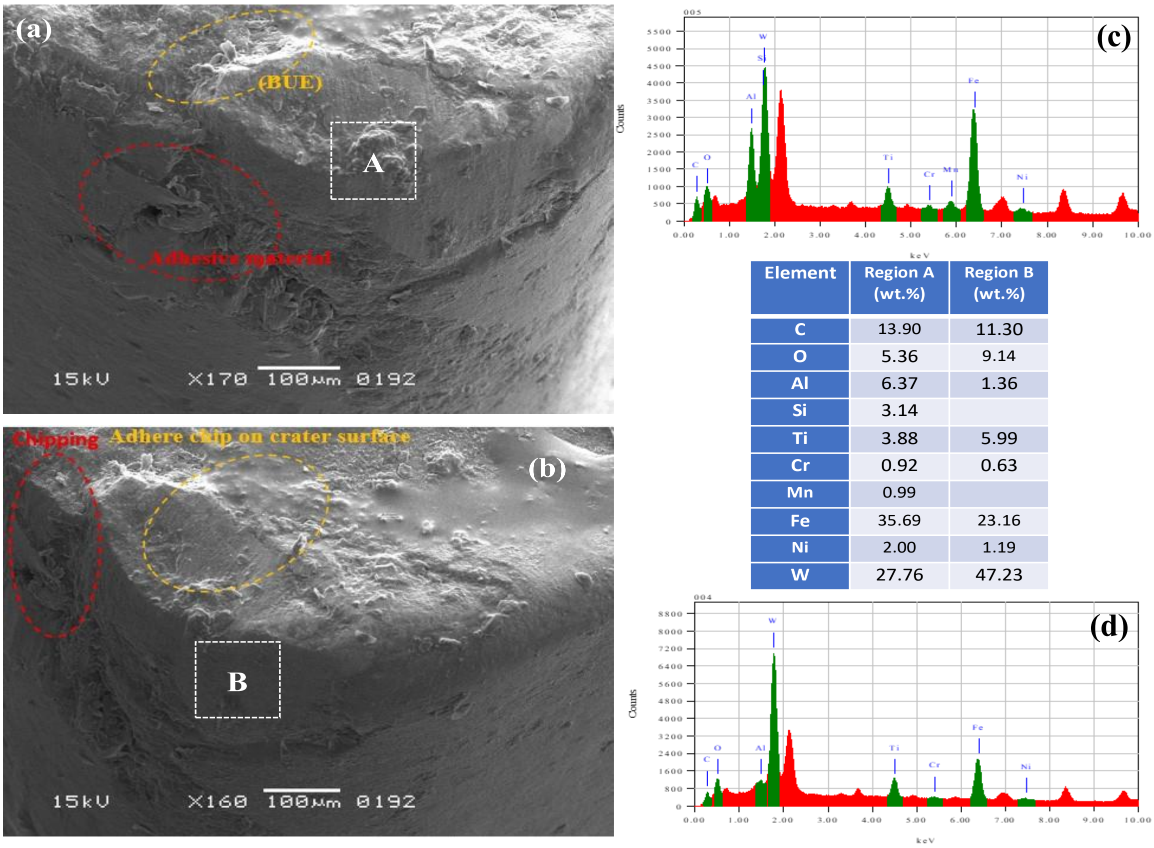

Element	Region A (wt.%)	Region B (wt.%)
C	13.90	11.30
O	5.36	9.14
Al	6.37	1.36
Si	3.14	
Ti	3.88	5.99
Cr	0.92	0.63
Mn	0.99	
Fe	35.69	23.16
Ni	2.00	1.19
W	27.76	47.23

Fig. 20. SEM (a,b) and EDS analysis (c,d) on the worn tool at V = 180 m/min

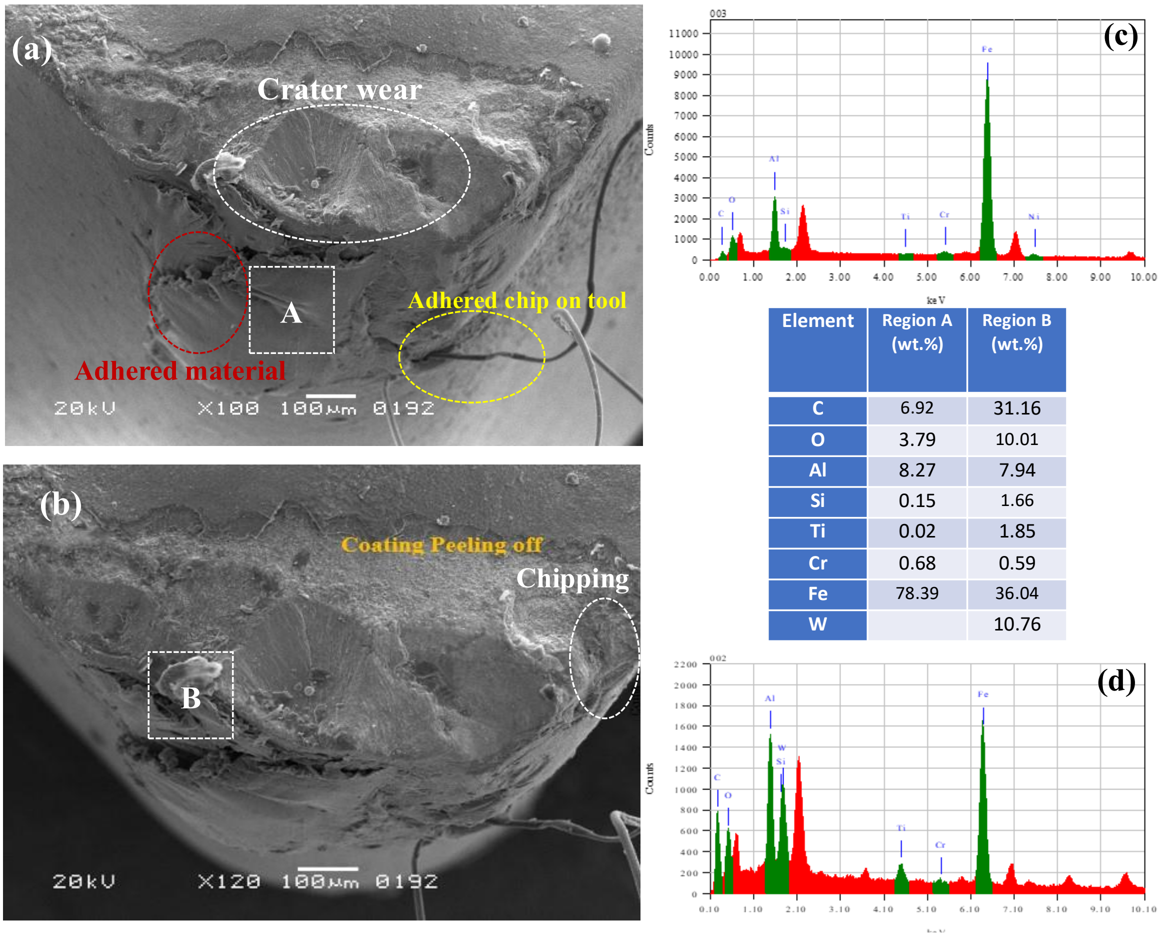

Element	Region A (wt.%)	Region B (wt.%)
C	6.92	31.16
O	3.79	10.01
Al	8.27	7.94
Si	0.15	1.66
Ti	0.02	1.85
Cr	0.68	0.59
Fe	78.39	36.04
W		10.76

Fig. 21. SEM (a,b) and EDS analysis (c,d) on the worn tool at V = 250 m/min

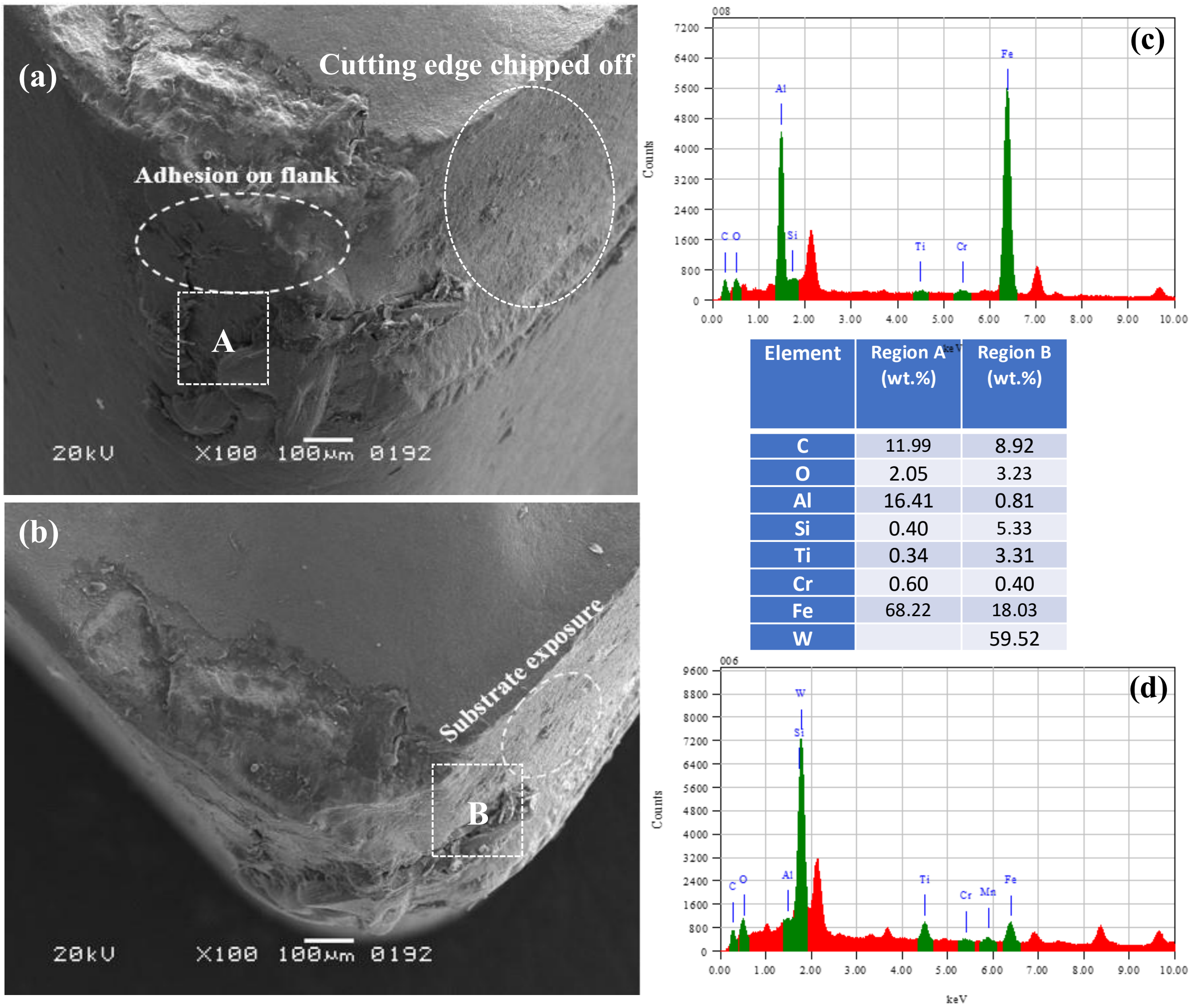

Element	Region A (wt.%)	Region B (wt.%)
C	11.99	8.92
O	2.05	3.23
Al	16.41	0.81
Si	0.40	5.33
Ti	0.34	3.31
Cr	0.60	0.40
Fe	68.22	18.03
W		59.52

Fig. 22. SEM (a,b) and EDS analysis (c,d) on the worn tool at V = 250 m/min (wet)

Furthermore at 180 m/min, SEM images (Fig. 20) revealed crater formation on the rake face, pitting, and a pronounced flank wear land. EDS spectra showed a strong Fe peak and a distinct oxygen signal, suggesting adhesive oxidative wear. Reduced Al and Ti peaks, along with the appearance of W, indicated coating removal and exposure of the carbide substrate. These findings are consistent with reports of crater wear in hard turning, where adhesion, abrasion, and oxidation dominate at higher cutting speeds [18,38].

At a cutting speed of 250 m/min, SEM examination revealed significant tool degradation, characterized by deep cratering, edge fragmentation, and considerable plastic deformation at the tool-chip contact zone. EDS analysis presented in Fig. 21 indicated substantial adhesion and oxidation, as evidenced by elevated Fe and O signals, also deep crater formation on rake face of tool is evident. EDS indicates reduced coating elements and increased Fe and O consistent with coating loss and oxidation signify the failure of the protective coating and exposure of the underlying substrate shows flaking. Furthermore, SEM imaging Fig. 21 captured adhered chip fragments fused to the rake face, which are prone to dislodgment, leading to the removal of both coating and substrate material. This mode of wear is a recognized phenomenon in the high-speed hard turning of steels [36,39].

Interestingly, at 250 m/min (with coolant), tool wear was surprisingly more severe. Although oxidation appeared slightly reduced, SEM images (Fig. 22) revealed catastrophic coating spallation, edge chipping, and substrate exposure. EDS spectra confirmed strong Fe peaks (workpiece adhesion) and W signs the exposure of substrate. These results reveals that conventional cutting fluids were ineffective at controlling the extremely high temperatures in high speed hard turning, leading instead to accelerated flaking and rapid tool failure [32,40].

Conclusions

In this work, CVD-coated carbide inserts $TiCN/Al_2O_3$ were used for high-speed hard turning of AISI 4340 steel. Tool wear, surface roughness, and the main wear mechanisms were examined under different cutting speeds and machining environments. From the study, the following points can be concluded:

1. Flank wear (VB) increased with cutting speed in a consistent manner. It went from about 186 μm at 60 m/min to 265 μm at 180 m/min, and then jumped sharply to 542 μm under dry cutting at 250 m/min. Under wet cutting at 250 m/min, tool wear reached 692 μm because of heavy flaking and fast coating delamination, which is well beyond the ISO 3685 tool life criterion (VB = 300 μm).
2. SEM and EDS analysis confirmed that at lower cutting speeds (60–95 m/min), light abrasive wear with mild coating delamination and small-scale abrasion were the main modes. At medium speed (around 180 m/min), adhesion and oxidation effects became more visible, and crater wear also appeared. At the highest tested speed (250 m/min), catastrophic tool failure occurred with severe coating spallation, edge chipping, strong adhesion, oxidation and exposure of the substrate at the tool edge.
3. Under flood-cooling condition, higher wear was observed at 250 m/min compared to dry cutting. SEM/EDS revealed increased spallation and adhered workpiece material, suggesting that coolant boiling and ineffective interface cooling may contribute to coating failure in this condition. Further testing with alternative cooling/lubrication strategies is required to confirm the generality of this observation.
4. The range 95 and 180 m/min is suitable cutting speed range for the machining of AISI 4340 steel under the present conditions. At this range, machining performance was found to be more consistent, with improved surface finishing and long tool life compared to both at very low and at very high speeds.
5. For future work, advanced cooling and lubrication methods such as minimum quantity lubrication (MQL) or cryogenic cooling will be investigated, as they could help reduce severe wear at higher speeds and increase tool life during hard turning.

CRediT authorship contribution statement

Murad Zulfiqar: conceptualization, methodology, investigation, formal analysis, data curation, writing – original draft, writing – review & editing; **Abdul Sattar Jamali**: conceptualization, supervision, writing – review & editing; **Saddam Hussain**: data curation.

Conflict of interest

The authors declare that they have no conflict of interest.

References

1. Barros RA, Abdalla AJ, Rodrigues HL, Pereira MDS. Caracterização de um aço AISI/SAE 4340 com diferentes microestruturas através da técnica de tríplice ataque. *Revista brasileira de aplicações de vácuo.* 2015;34(2): 71–74.

2. Sujitno T, Mulyani E, Suprapto, Andriyanti W, Suharlan D, Malau V. Effect of Diamond-Like Carbon Thin Film on the Fatigue Strength of AISI 4340 Steel. *Advances in Materials.* 2019;8(1): 21–26.

3. Wang L, Zhang Y, Liu H. Study on Experimental Method of Fracture Toughness for AISI 4340 Steel Using Circumferentially Cracked Round Bar. *SSRN*. [Preprint] 2025. Available from: https://doi.org/10.2139/ssrn.5079339

4. Kamruzzaman M, Dhar N. Effect of High-Pressure Coolant on Temperature, Chip, Force, Tool Wear, Tool Life and Surface Roughness in Turning AISI 1060 Steel. *Gazi University Journal of Science.* 2010;22(4): 359–370.

5. Boztepe A, Gecu R. Influence of Cryogenic Treatment and Tempering Temperature on Microstructural Evolution and Dry Sliding Wear Behavior of AISI D3 Cold-Work Tool Steel. *Journal of Tribology.* 2025;147(6): 064201.

6. Selvaraj DP. Optimization of surface roughness of duplex stainless steel in dry turning operation using Taguchi technique. *Materials Physics and Mechanics.* 2018;40(1): 63–70.

7. Darwish A. A Novel Deep Learning Model for Tool Wear Estimation of Cutting Tools. *Sustainable Machine Intelligence Journal.* 2024;9(1): 2.

8. Minquiz GM, González-Sierra NE, Méndez JF, Reyes ACP, Moreno MM, Morales-Sánchez A, López JAL, Hernandez-Simon ZJ, Carral CD. Analysis of Wear Mechanisms Under Cutting Parameters: Influence of Double Layer TiAlN/TiN PVD and TiCN/Al_2O_3 Chemical Vapor Deposition-Coated Tools on Milling of AISI D2 Steel. *Coatings.* 2024;14(12): 1491.

9. Calaph YC, Ganesh PSPS, Shanawaz AM, Kavitha S, Muthusamy C, Arunprasath K. Analysing the impact of cutting parameters of CNC machining on EN8 steel with high strength carbide tool tip insert. *Interactions.* 2024;245: 74.

10. Šramhauser K, Kraus P, Špalek F, Černý P, Ufitikirezi JDDM, Zoubek T, Strob M, Kononets Y, Kříž P, Vochozka V. Intercomparison of Indexable Cutting Inserts' Wear Progress and Chip Formation During Machining Hardened Steel AISI 4337 and Austenitic Stainless Steel AISI 316 L. *Materials.* 2024;17(22): 5418.

11. Bag R, Panda A, Sahoo AK, Kumar R. Sustainable High-Speed Hard Machining of AISI 4340 Steel Under Dry Environment. *Arabian Journal for Science and Engineering.* 2023;48: 3073–3096.

12. Najar K, Mursaleen M, Dar T. Experimental evaluation of multilayered CVD- and PVD-coated carbide turning inserts in severe machining of AISI-4340 steel alloy. *Jurnal Tribologi.* 2021;29: 117–143.

13. Kishore G, Parthiban A, Mohana Krishnan A, Radha Krishnan B. Investigation of the surface roughness of aluminium composite in the drilling process. *Materials Physics and Mechanics.* 2021;47(5): 739–746.

14. Khurtasenko AV, Cherednikov II, Mamchenkova AA, Chauev KV, Bondarenko AA. Assessment of wear and destruction of solid carbide cutters during milling of hardened steel 4X5MF1C with a hardness of 52 HRC. *Bulletin of BSTU named after V.G. Shukhov.* 2024;6: 81–92.

15. Hassan S, Khan SA, Naveed R, Saleem MQ, Mufti NA, Farooq MU. Investigation on tool wear mechanisms and machining tribology of hardened DC53 steel through modified CBN tooling geometry in hard turning. *The International Journal of Advanced Manufacturing Technology.* 2023;127(1–2): 547–564.

16. Santos AJD, Reis BCM, Pereira NFS, De Oliveira DA, Rubio JCC, Abrão AM, Câmara MA. Tribological effects of micromilling of hardened AISI D2 steel on tool wear and top burr formation. *The International Journal of Advanced Manufacturing Technology.* 2023;127: 5327–5341.

17. Ahmed F, Kumaran ST, Ahmad F. Analysis of Wear Mechanisms and Chip Morphology During Machining of Tool Steel Using TiAlSiCrN-Coated WC-Co Ball end Mills. To be published in Research Square. [Preprint] Available from: doi.org/10.21203/rs.3.rs-1144076/v1

18. Jouini N, Yaqoob S, Ghani JA. Investigations on the machinability performance of Al2O3/TiCN CVD coated carbide tools in sustainable high-speed hard-turning of AISI 4340 alloy steel. *Materials Research Express.* 2024;11(9): 096509.

19. Silva RYOAD, Silva MLD, Conti PHDMC, Costa AFD. Application of CVD Coated Turning Inserts in the Machining of ABNT 8620 Steel at Different Cutting Speeds. *Revista De Gestão Social E Ambiental – RGSA.* 2024;18(12): e010133.

20. Cakan A, Albayrak O, Gozmen Sanli B, Guven O, Ugurlu M, Atmaca H. Cutting performance of coated carbide inserts in hard turning of hardened AISI D2 cold work tool steels. *Proceedings of the Institution of Mechanical Engineers, Part C: Journal of Mechanical Engineering Science.* 2024;238(19): 9504–9513.

21. Rashid WB, Goel S, Davim JP, Joshi SN. Parametric design optimization of hard turning of AISI 4340 steel (69 HRC). *The International Journal of Advanced Manufacturing Technology.* 2016;82: 451–462.

22. Kumar R, Sahoo AK, Mishra PC, Das RK. Comparative study on machinability improvement in hard turning using coated and uncoated carbide inserts: part II modeling, multi-response optimization, tool life, and economic aspects. *Advances in Manufacturing.* 2018;6: 155–175.

23. Hamadi B, Yallese MA, Boulanouar L, Khellaf A, Haddad A. A Comparative Study of the Performance of Uncoated, PVD, CVD and MTCVD Coated Carbide Inserts in Dry Turning of AISI4140 Steel. *Periodica Polytechnica Mechanical Engineering.* 2022;66(4): 314–324.
24. Pawanr S, Gupta K. Dry Machining Techniques for Sustainability in Metal Cutting: A Review. *Processes.* 2024;12(2): 417.
25. Panda A, Sahoo AK, Panigrahi I, Kumar R. Tool condition monitoring during hard turning of AISI 52100 Steel: A case study. *Materials Today: Proceedings.* 2018;5(9): 18585–18592.
26. Bushlya V, Gutnichenko O, Zhou J, Avdovic P, Ståhl J-E. Effects of cutting speed when turning age hardened Inconel 718 with PCBN tools of binderless and low-CBN grades. *Machining Science and Technology.* 2013;17(4): 497–523.
27. Mitsubishi Materials Corporation. *Turning inserts: CNMG120404-MA.* Available from: *https://www.mitsubishicarbide.net/mht/enuk/turning_inserts/no_srs/20041777* [Accessed 22th September 2025]
28. Novakova J, Petrkovska L, Brychta J, Cep R, Ocenasova L. Influence of high speed parameters on the quality of machined surface. *World Academy of Science, Engineering and Technology.* 2009;56: 274–277.
29. Miko E, Nowakowski Ł. Analysis and Verification of Surface Roughness Constitution Model After Machining Process. *Procedia Engineering.* 2012;39: 395–404.
30. Nouari M, List G, Girot F, Coupard D. Experimental analysis and optimisation of tool wear in dry machining of aluminium alloys. *Wear.* 2003;255(7–12): 1359–1368.
31. Sharma VS, Dogra M, Suri NM. Cooling techniques for improved productivity in turning. *International Journal of Machine Tools and Manufacture.* 2009;49(6): 435–453.
32. Dhar N, Kamruzzaman M. Cutting temperature, tool wear, surface roughness and dimensional deviation in turning AISI-4037 steel under cryogenic condition. *International Journal of Machine Tools and Manufacture.* 2007;47(5): 754–759.
33. Mallick R, Kumar R, Panda A, Sahoo AK. Current Status of Hard Turning in Manufacturing: Aspects of Cooling Strategy and Sustainability. *Lubricants.* 2023;11(3): 108.
34. Cakan A. Wear behavior of multilayer coated carbide tools in finish dry hard turning. *Materials Testing.* 2016;58(9): 772–777.
35. Szablewski P, Legutko S, Ungureanu N, Petru J, Smak K, Krawczyk B. Comparative Assessment of Tool Wear and Surface Topography After Superfinish Turning of Inconel 718 with Carbide and Ceramic Inserts. *Applied Sciences.* 2025;15(8): 4265.
36. Ranjan Das S, Panda A, Dhupal D. Hard turning of AISI 4340 steel using coated carbide insert: Surface roughness, tool wear, chip morphology and cost estimation. *Materials Today: Proceedings.* 2018;5(2): 6560–6569.
37. Wagri NK, Jain NK, Petare A, Das SR, Tharwan MY, Alansari A, Alqahtani B, Fattouh M, Elsheikh A. Investigation on the Performance of Coated Carbide Tool during Dry Turning of AISI 4340 Alloy Steel. *Materials.* 2023;16(2): 668.
38. Yaqoob S, Ghani JA, Jouini N, Juri AZ. Performance evaluation of PVD and CVD multilayer-coated tools in machining high-strength steel. *Coatings.* 2024;14(7): 865.
39. Chinchanikar S, Choudhury SK. Wear behaviors of single-layer and multi-layer coated carbide inserts in high speed machining of hardened AISI 4340 steel. *Journal of Mechanical Science and Technology.* 2013;27: 1451–1459.
40. Jasni NAH, Lajis MA, Kamdani K. Tool Wear Performance of TiAlN/AlCrN Multilayer Coated Carbide Tool in Machining of AISI D2 Hardened Steel. *Advanced Materials Research*. 2012;488–489: 462–467.

MATERIALS PHYSICS AND MECHANICS RESEARCH ARTICLE

Submitted: November 23, 2025 **Revised: February 3, 2026** **Accepted: February 16, 2026**

Parameter identification of the Norton-Bailey creep model using isochronous curves

R.V. Fedorenko ✉, **A.V. Lukin**

Peter the Great State Polytechnical University, St. Petersburg, Russia

✉ fedorenko_rv@spbstu.ru

ABSTRACT

Structural integrity assessment of metal components in advanced reactor systems operating at elevated temperatures requires calculations that account for the sequence and duration of loading throughout their service life. Numerical simulation of such processes is performed using nonlinear inelastic material models, whose parameters are determined based on experimental data. The development and verification of an automated numerical algorithm for identifying the parameters of the Norton-Bailey creep law are considered. The algorithm utilizes initial data in the form of a set of material isochronous curves at a specific temperature. It implements an optimization procedure aimed at minimizing the discrepancy between the normative and the computed isochronous curves. The generation of the computed isochronous curves is performed using the Abaqus software package. It is demonstrated that the developed algorithm enables the highly accurate identification of the constants for the Norton-Bailey law.

KEYWORDS

creep • parameter identification • isochronous curves • optimization • closed nuclear fuel cycle

***Funding**. The research is partially funded by the Ministry of Science and Higher Education of the Russian Federation as part of the World-class Research Center program: Advanced Digital Technologies (contract No. 075-15-2022-311 dated 20.04.2022).*

Citation: Fedorenko RV, Lukin AV. Parameter identification of the Norton-Bailey creep model using isochronous curves. *Materials Physics and Mechanics*. 2026;54(1): 118–129.
http://dx.doi.org/10.18149/MPM.5412026_11

Introduction

Currently, nuclear power plants are one of the primary sources of energy generation. A major challenge associated with nuclear power is the depletion of natural resources for fuel production. Consequently, extensive global efforts are underway to reduce their consumption and seek alternative energy sources. Within the framework of the concept for achieving technological leadership of the Russian Federation, the necessity of developing highly efficient energy systems has been outlined. This includes the development of closed nuclear fuel cycle technology and the creation of a thermonuclear reactor capable of producing more energy than it consumes to initiate the fusion reaction [1]. To achieve these goals, development is currently ongoing on fast-neutron reactors with liquid metal coolant and the domestic TRT thermonuclear reactor [2–4]. A key operational feature of such facilities is high temperatures, for instance, exceeding 450 °C during normal operation and up to 900 °C in accident scenarios for the fast-neutron reactors. Designing structures for such temperatures is complicated by the occurrence of significant thermal deformations in the system and the necessity to account for the long-term properties of materials.

Publisher: Peter the Great St. Petersburg Polytechnic University

"The theory of plasticity was brought to life primarily by the needs of turbine construction; subsequently, it found application in nuclear power, chemical engineering, aviation, and rocket technology" is a quote from the fundamental work of Yu.N. Rabotnov, "Creep of Structural Elements" [5]. Indeed, 60 years after the publication of this work, the relevance of creep issues as applied to critical structural components remains undiminished.

Material creep under high temperatures and significant load durations can pose challenges in strength substantiation. In addition to the reduction in the general strength characteristics of the material, issues such as long-term cyclic strength [6] and structural stability under creep conditions arise [7,8].

Regulatory approaches to the strength substantiation of reactor installations [9,10] prescribe simplified procedures within elastic formulations. For instance, accounting for long-term material characteristics at elevated temperatures involves reducing allowable stresses according to the material's isochronous curves; however, this approach possesses significant conservatism. In practice, it is quite difficult to meet the criteria for long-term static and long-term cyclic strength for structural components operating at elevated temperatures within elastic formulations.

Nuclear industry standards [9,10] allow for the possibility of performing strength calculations that consider nonlinear material properties (hardening, creep, microstructure, etc.). In the realm of creep theory, a wide variety of different models exists, each with certain advantages and disadvantages.

Deformation of a material by the creep mechanism is traditionally divided into 3 stages [5]. The first stage is interesting from the perspective of material behavior and the mechanisms of creep initiation, where strain increases non-uniformly over time, eventually reaching a constant rate, which marks the beginning of the second creep stage. During the second (steady-state) stage creep strains accumulate linearly with time. The third stage shows a rapid increase in strain, typically associated with the onset of material failure (hence, engineers often do not consider this zone).

Two basic models are commonly used to describe secondary creep:

1. Power law (the Norton model [11]): $\dot{\varepsilon} = A\sigma^n$, where A and n are material parameters. The advantage of this law is its simplicity, but this is also its drawback: integrating the relation shows that ε depends linearly on time, which hinders the description of a family of isochronous curves with a single set of parameters.
2. Modified power law (the Norton-Bailey model [12]): $\dot{\varepsilon} = A\sigma^n t^m$, where m is a material parameter. This model is the most widespread in engineering practice due to its simplicity from the standpoint of parameter identification [13]. It is free from the drawback of the basic Norton model regarding linear time dependence.

To additionally account for the primary creep stage, one can use, for example, the Darveaux model [14]. In this model, the secondary stage is described by a relation that does not include a time component and can be used independently to describe secondary creep using the hyperbolic sine law $\dot{\varepsilon}_s^{cr} = C_{ss}[\sinh(\alpha\tilde{q})]^n e^{\left(-\frac{Q}{R(\theta-\theta^Z)}\right)}$, where C_{ss} and α are material constants, Q is the activation energy, R is the universal gas constant, θ is the temperature, θ^Z is the absolute zero temperature in the adopted system of units.

Accounting for the non-steady-state component allows for describing the progression of primary creep: $\dot{\varepsilon}^{cr} = \dot{\varepsilon}_s^{cr}\left[1 + \epsilon_T B e^{(-B\dot{\varepsilon}_s^{cr} t)}\right]$, where ϵ_T and B are material parameters.

For describing tertiary creep, models enhanced with material damage parameters can be used, for example, according to the Kachanov-Rabotnov model [15–19]. Based on it, various models considering material damage can be formulated [20,21]. For instance, the Othman model [22]: $\dot{\varepsilon} = \frac{A}{(1-\omega_1)(1-\omega_2)^n}\sinh(B\sigma)$, $\dot{\omega_1} = C(1-\omega_1)^2\dot{\varepsilon}$, $\omega_1 = 1 - \frac{\rho_1}{\rho}$, $\dot{\omega_2} = \frac{\dot{\varepsilon}}{3\varepsilon_u}\left(\frac{\sigma_1}{\sigma_e}\right)^v$, where ω_1 and ω_2 are two damage parameters. ω_1 accounts for the role of increasing dislocation density ρ during creep, ω_2 represents damage due to void formation in the material (cavitation), ρ_1 is the initial dislocation density, σ_1 is the first principal stress, σ_e is the effective stress, and $A,\ B,\ C,\ n,\ v,\ \varepsilon_u$ are material constants.

Due to the lack of a unified model, it is often challenging in practice to identify parameters for a specific material model that is most suitable for a given problem. Necessary data for commonly used materials can often be found, but in most cases, difficulties may arise in searching for parameters. For example, standard [23] presents isochronous curves for most structural steels, and standard [9] provides parameters for a specific creep model for some of them. For certain classes of materials, work has been done to identify parameters for various creep models. In [13], parameter identification for the Norton-Bailey model is performed using a regression approach. The procedure for identifying parameters for modeling tertiary creep using the Nelder-Mead method for VZhM4 and VZhM5U alloys is described in [24]. In [25], the selection of creep and plasticity parameters for ZhS32 alloy at elevated temperatures is carried out. In [26], based on an experiment with multi-step loading of a specimen under creep conditions, parameters for the Liu-Murakami [27] damage-based model (for describing all creep stages) are fitted. The results of identification procedure using Levenberg-Marquardt algorithm for unified models describing steady-state and transient creep in [28]. In [29], a two-layer algorithm is proposed for the rapid identification of parameters in a fractional-order creep model of piezoelectric actuator.

The aim of the present research is to develop an automated algorithm for identifying creep parameters, using a family of isochronous curves at a specific temperature as the initial data. At the first stage of development, parameter identification for the modified Norton-Bailey model [12] is performed, as this model is widely used in engineering practice.

Method

The parameter identification procedure is conducted in two stages. The first stage involves the direct identification of the model parameters based on a set of isochronous curves. The second stage entails the numerical solution of a verification problem: uniaxial tension of a specimen, considering the implemented creep model and the identified parameters, using the Abaqus software [30]. The results are then compared with the original isochronous curves. The choice of Abaqus for verification is justified by its convenience for implementing user-defined creep models, its accuracy in solving nonlinear problems, and its recognition by the scientific community as a research tool.

The simplest model from the parameter identification standpoint is the time-hardening form of the Norton-Bailey law [12]:

$$\dot{\varepsilon}_{cr} = \varepsilon_0 \left(\frac{\tilde{q}}{\sigma_0}\right)^n (\varepsilon_0 t)^m, \tag{1}$$

where $\varepsilon_0, \sigma_0, n, m$ are the identifiable model parameters, $\dot{\varepsilon}_{cr}$ is the creep strain rate, t is the time, and $\tilde{q}$ is the equivalent stress.

It is worth noting that the Russian standard GOST [9] recommends a truncated form of this model (without the time component) for accounting for creep in nonlinear strength calculations. A universal reference with parameters for this model for an arbitrary material, across various durations and temperatures, does not exist. In Abaqus [30], it is possible to specify separate parameter values for different temperatures; therefore, identification is performed separately for each temperature, therefore, the identifiable parameters become temperature-dependent, although in the classical approach, only parameters ε_0 and σ_0 exhibit temperature dependence according to the Arrhenius equation. The procedure's workflow is conveniently demonstrated using a real material example. We consider structural steel 12Kh18N12T/12Kh18N10T (AISI 321), used for some critical components of reactor installations. GOST [9] provides isochronous curves for this material; for demonstration, the curves at a temperature of 550°C are considered (Fig. 1).

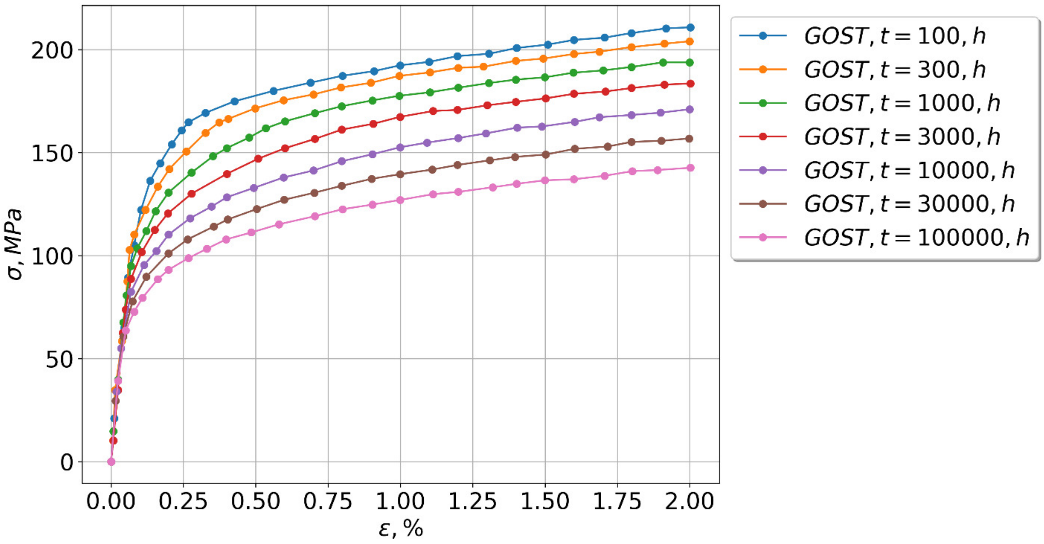

Fig. 1. Isochronous curves for 12Kh18N12T/12Kh18N10T (AISI 321) steel, T = 550 °C

During parameter identification, it is assumed that the loading rate in the experimental studies was constant, with the time for the corresponding isochronous curve taken at 2 % strain ($\varepsilon = 0.02$). Then, taking the experimental time denoted on the standard curves as τ, the following holds:

$$\dot{\varepsilon}_{cr} = \frac{0.02}{\tau}. \tag{2}$$

Consequently,

$$\varepsilon_0^{m+1} \left(\frac{\tilde{q}}{\sigma_0}\right)^n t^m = \frac{0.02}{\tau}. \tag{3}$$

To facilitate algorithm development, a transition is made to a direct dependence of stress on strain:

$$\tilde{q} = \sigma_0 \left[\frac{0.02}{\tau} \, \varepsilon_0^{-m-1} \cdot t^{-m} \right]^{1/n}. \tag{4}$$

The goal of the procedure is to find parameters in the last relation that ensure coincidence with the original isochronous curves for all considered times. The parameter search uses a global minimum search procedure based on the simplicial homology global optimization (SHGO) method [31]. Briefly, the algorithm uses concepts from combinatorial integral homology theory to find subdomains that are approximately locally convex and characterizes the objective function as it runs. It solves a derivative-free optimization problem with constraints (CDFO) [32,33] of the form:

$$\begin{aligned} &\min f(x), \quad x \in \mathbb{R}^n. \\ &g_i(x) \geq 0, \ \forall i = 1, \dots, m, \\ &h_j(x) = 0, \ \forall j = 1, \dots, p, \end{aligned} \tag{5}$$

where x is the vector of variables/parameters, $f(x)$ is the objective function ($f\colon \mathbb{R}^n \to \mathbb{R}$), $g_i(x)$ are inequality constraints, $h_j(x)$ are equality constraints, and $x_l \leq x \leq x_u$ are the lower and upper bounds for the parameters.

The functional is constructed individually for each problem. Since the research aim is to find a single set of parameters describing the family of isochronous curves, a functional combining several sub-functionals of the same order is adopted:

$$F = \sum_{i=1}^{nfs} f_i \to min, \tag{6}$$

where index $nfs = 5$ indicates the number of sub-functionals to be described below. This allows for the simultaneous control of several criterion values reflecting different characteristics of the compared isochronous curves.

Sub-functional f_1 is the classical Frobenius norm [34]:

$$f_1 = \frac{||Y - X||}{||X||}, \tag{7}$$

where X is the matrix of values for the approximating curves, and Y is the matrix of values for the approximated curves.

In the procedure, all curves (approximating and approximated) are interpolated onto the same grid of abscissa values (strains of the isochronous curves). Thus, matrices X and Y essentially represent sets of stress value vectors for each curve.

Sub-functional f_2 is the relative sum of local Frobenius norms, computed for each isochronous curve separately, after which the average norm value for the set of curves is calculated:

$$f_2 = \frac{1}{N_\tau} \sum_{j=1}^{N_\tau} \frac{\left\| \overline{y}_j - \overline{x}_j \right\|}{\left\| \overline{x}_j \right\|}, \tag{8}$$

where N_τ is the number of isochronous curves, $X = \sum_{j=1}^{N_\tau} \overline{x}_j$, $Y = \sum_{j=1}^{N_\tau} \overline{y}_j$.

Sub-functional f_3 is the maximum relative deviation between the approximated and approximating curves across the entire family of curves:

$$f_3 = \max\left(\max\left(\frac{\overline{y}_j - \overline{x}_j}{\overline{x}_j} \right) \right), \ j \in [1, N_\tau]. \tag{9}$$

Sub-functional f_4 is the relative Euclidean norm of the maximum relative deviations of each curve:

$$f_4 = \frac{1}{N_\tau} \sqrt{\sum_{j=1}^{N_\tau} err_j^2}, \ err_j = \max\left(\frac{\overline{y}_j - \overline{x}_j}{\overline{x}_j} \right), \tag{10}$$

where err_j is the relative deviation between the approximated and approximating curves.

Sub-functional f_5 is an integral criterion that evaluates the local relative deviation of the integrals of the two curves, which are then assessed using the relative Euclidean norm:

$$f_5 = \frac{1}{N_\tau}\sqrt{\sum_{j=1}^{N_\tau} int_j^2}\,, \; int_j = \frac{\left|\int_0^t \overline{y}dt - \int_0^t \overline{x}dt\right|}{\max\left(\int_0^t \overline{x}dt, \int_0^t \overline{y}dt\right)}, \tag{11}$$

where t is the calculation time.

The form of each sub-functional shows that their values range from 0 to 1, allowing for a combined functional comprising quantities of similar orders of magnitude. The procedure iteration concludes after a specified number of iterations is reached, upon which the parameter values yielding the minimal functional value are output. The sufficiency of iterations is checked by analyzing the convergence of the iterative process results.

After obtaining the optimal set of parameters, a numerical solution for the problem of uniaxial tension of a specimen is performed using the finite element method. A kinematic loading condition is applied, inducing a total strain of 2 % by the end of the calculation.

The material is considered viscoelastic: density, elastic modulus, Poisson's ratio, and the creep model parameters (according to the identification stage results) are specified. An arbitrary creep model can be implemented in Abaqus using the user subroutine CREEP [30]. For implementing simple creep models in metals, it is sufficient to define two quantities in this subroutine: the increment of creep strain over one integration time step and the derivative of the creep strain increment with respect to stress (the solution Jacobian). For the considered Norton-Bailey model, these relations are:

$$\Delta\varepsilon_{cr} = \varepsilon_0^{m+1}\left(\frac{\tilde{q}}{\sigma_0}\right)^n \cdot \left[\frac{1}{1+m}\left(t^{m+1} - (t-\Delta t)^{m+1}\right)\right], \frac{\partial \Delta\varepsilon_{cr}}{\partial \tilde{q}} = \Delta\varepsilon_{cr}\cdot(n/\tilde{q}\,). \tag{12}$$

The numerical simulation in Abaqus [30] employs an implicit time integration scheme for the equations of geometrically and physically nonlinear viscoelasticity within a quasi-static formulation (neglecting inertial forces).

Results and Discussion

The outcome of the identification procedure is an optimal set of parameters for the selected creep model. Table 1 presents the parameter values identified by the procedure for steel 12Kh18N12T/12Kh18N10T (AISI 321) at temperatures of 500, 550, and 600 °C. For convenience in further use of the parameters, all values are given in the SI system.

Table 1. Parameters of the Norton-Bailey model for steel 12Kh18N12T/12Kh18N10T (AISI 321)

T, °C	ε_0	σ_0, MPa	m	n
500	2.7013e-07	604.78	-0.7995	3.8593
550	2.4694e-09	338.76	-0.7076	4.3129
600	1.0412e-08	344.63	-0.6607	3.6015

The convergence of the procedure and the optimal functional value are demonstrated in Fig. 2 for each temperature and its corresponding parameter set. The number of iterations of the procedure is plotted on the abscissa axis, and the value of the inverse functional, which is being minimized, is plotted on the ordinate axis. The inverse value is used because initial perturbing values that inflate the functional value arise during the procedure, complicating the visualization of results.

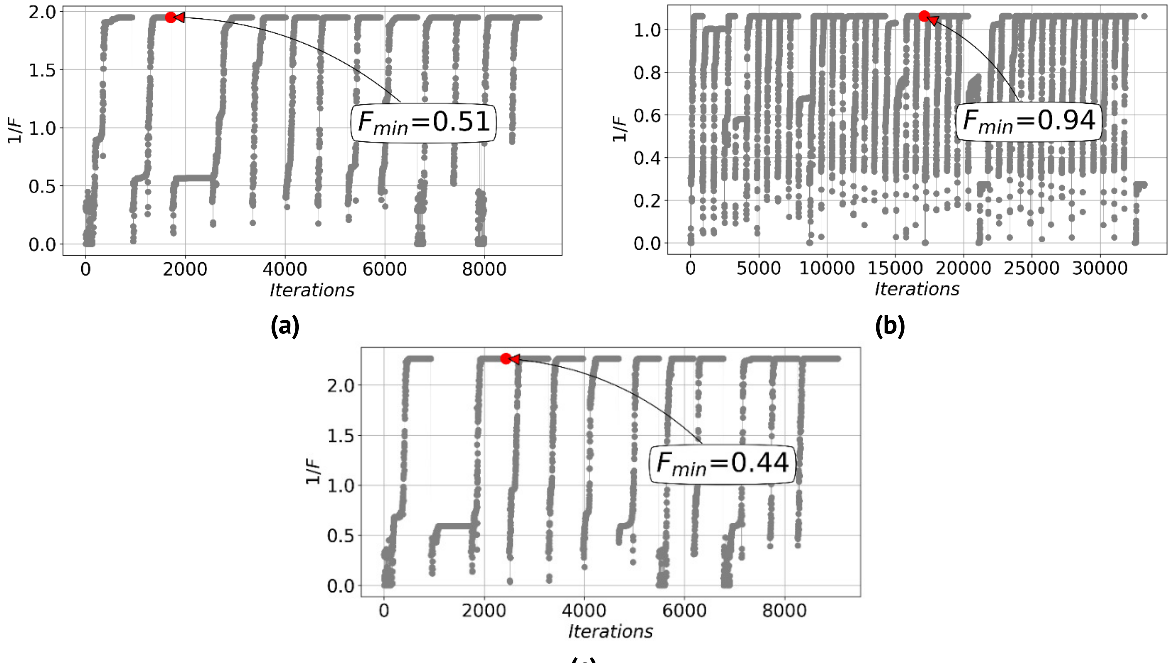

(a) **(b)**

(c)

Fig. 2. Identification procedure results at (a) 500 °C, (b) 550 °C, and (c) 600 °C

Each "vertical" set of points represents one iteration of the optimization procedure. It is evident that in each iteration, the procedure finds a final parameter value close to the optimal one, indicating its stability and convergence (no need for additional refinement iterations). Moreover, this optimal value is achieved within the first few iterations of the procedure.

The identified parameters are assigned to the user-defined creep model in Abaqus, after which the calculation of uniaxial tension of a viscoelastic specimen is performed. The simulation results for different loading rates yield material stress-strain diagrams, which are subsequently compared with the standard isochronous curves. Figures 3–5 demonstrate the standard and numerical curves.

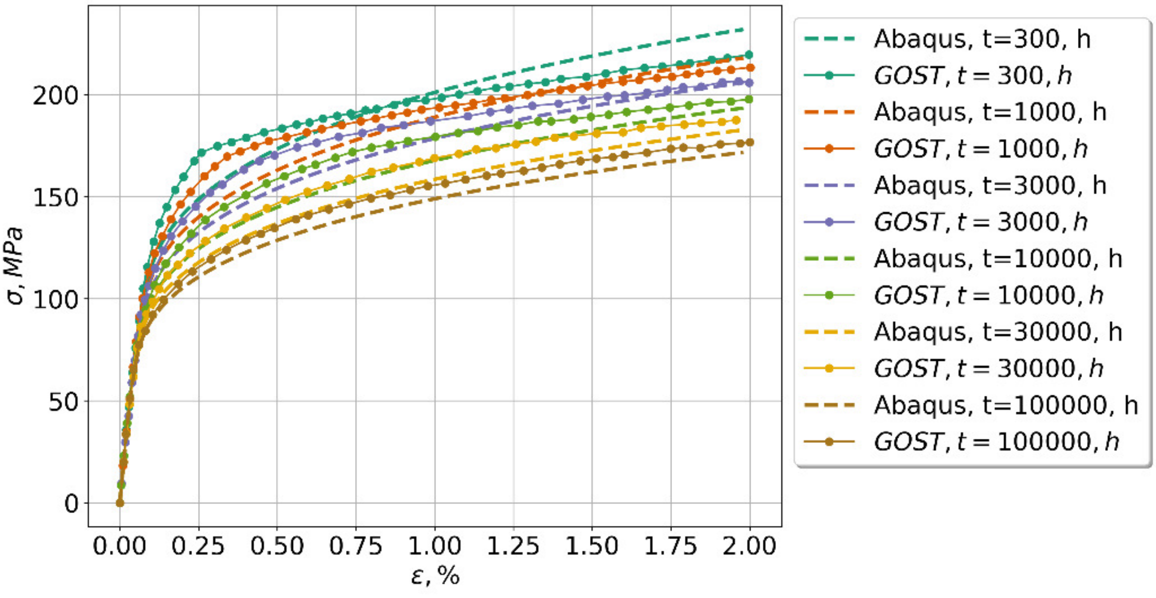

Fig. 3. Isochronous curves for AISI321 steel, T = 500 °C

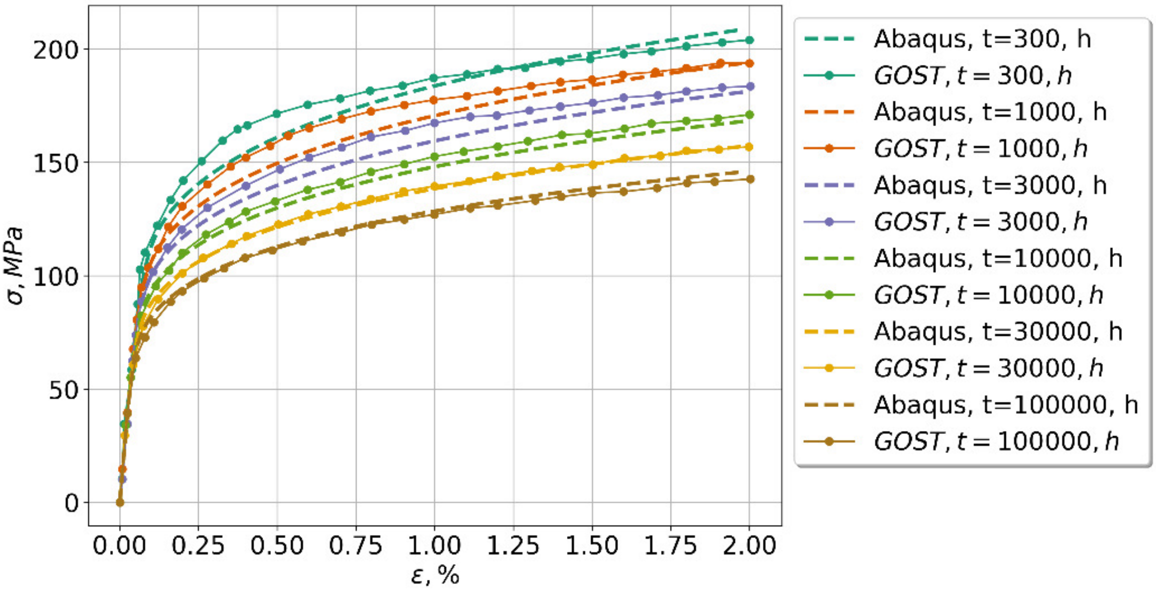

Fig.4. Isochronous curves for AISI321 steel, T = 550 °C

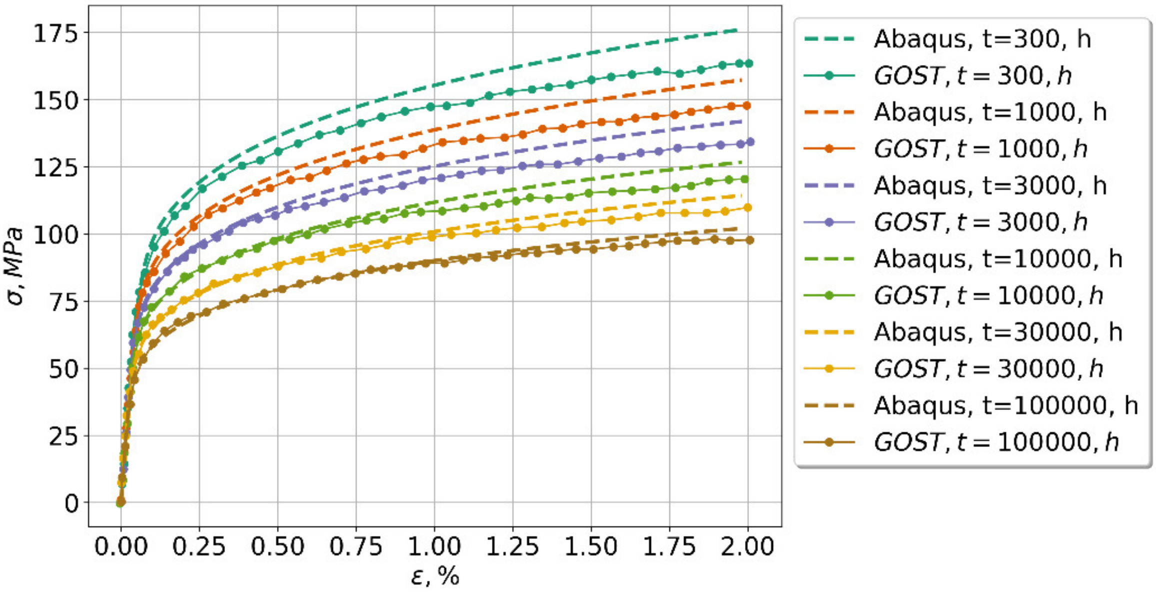

Fig. 5. Isochronous curves for AISI321 steel, T = 600 °C

Good agreement between the curves is observed for all temperatures at times exceeding 10,000 h. For shorter times, a larger discrepancy in the results is noted. For a quantitative assessment of the adequacy of the identified parameters, an analysis of the maximum and average deviation of the curves at different times for the three temperatures was performed (Fig. 6). The time corresponding to the isochronous curve required to reach 2 % strain, normalized to the maximum time value among the entire set of curves, is plotted on the abscissa axis. The quantities are determined pointwise, forming an array of local deviations, after which the maximum and average error values for the entire curve are determined:

$$err_{max} = \max\left(\left|\frac{\sigma_{norm}-\sigma_{abq}}{\sigma_{norm}}\right|\right),\ err_{mean} = \overline{\left|\frac{\sigma_{norm}-\sigma_{abq}}{\sigma_{norm}}\right|}, \tag{13}$$

where err_{max} and err_{mean} are the maximum and average errors, respectively, σ_{norm} and σ_{abq} are the stresses according to the standard and numerical (Abaqus) isochronous curves, respectively.

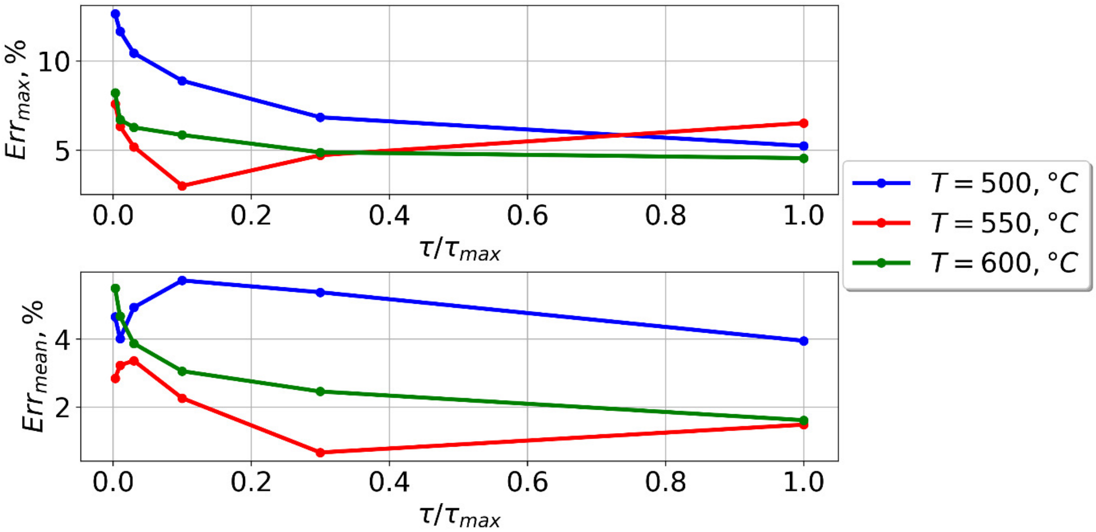

Fig. 6. Maximum and average deviations between standard and numerical curves for all analyzed cases

The maximum deviation between the curves does not exceed 13 %, and it is observed for fast loading rates. For slow loading rates, a decrease in both the maximum and average error is observed. The average error for all analysed cases does not exceed 5 %.

Discrepancies in results at short loading durations are associated with the limitations of the Norton-Bailey model. Its modification can be implemented, for example, by considering approaches mentioned in [27]0 or by introducing a separate set of creep model parameters for times less than 3000 h. Table 2 presents the model parameters for such short-term exposure. Figures 7–9 show normative and numerical isochronous curves obtained using the identified parameters.

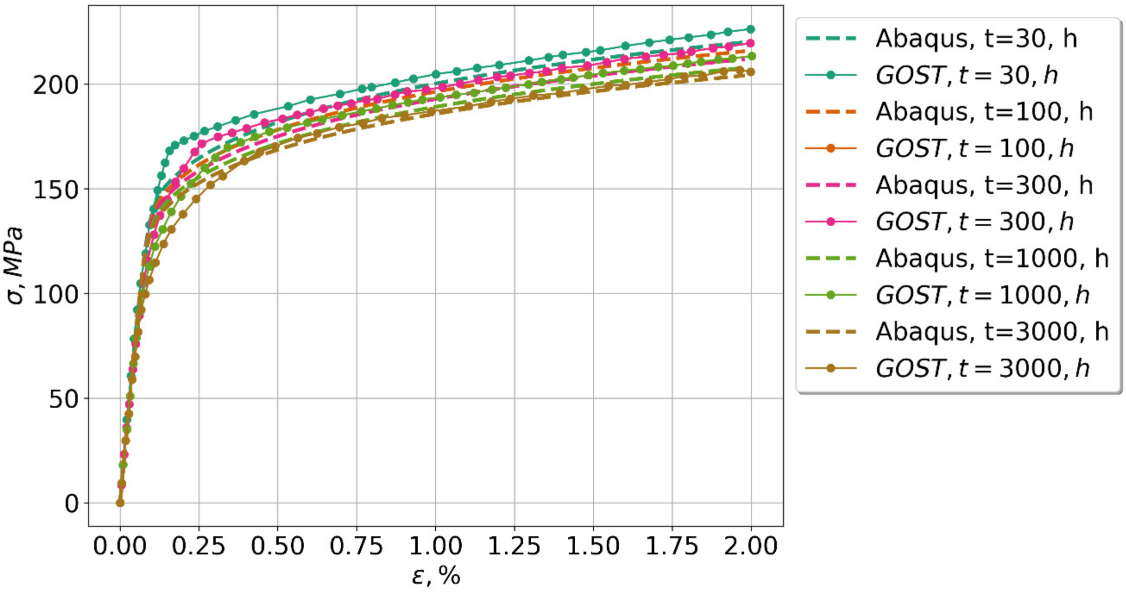

Fig. 7. Isochronous curves for AISI321 steel for $t < 3000$ h, $T = 500$ °C

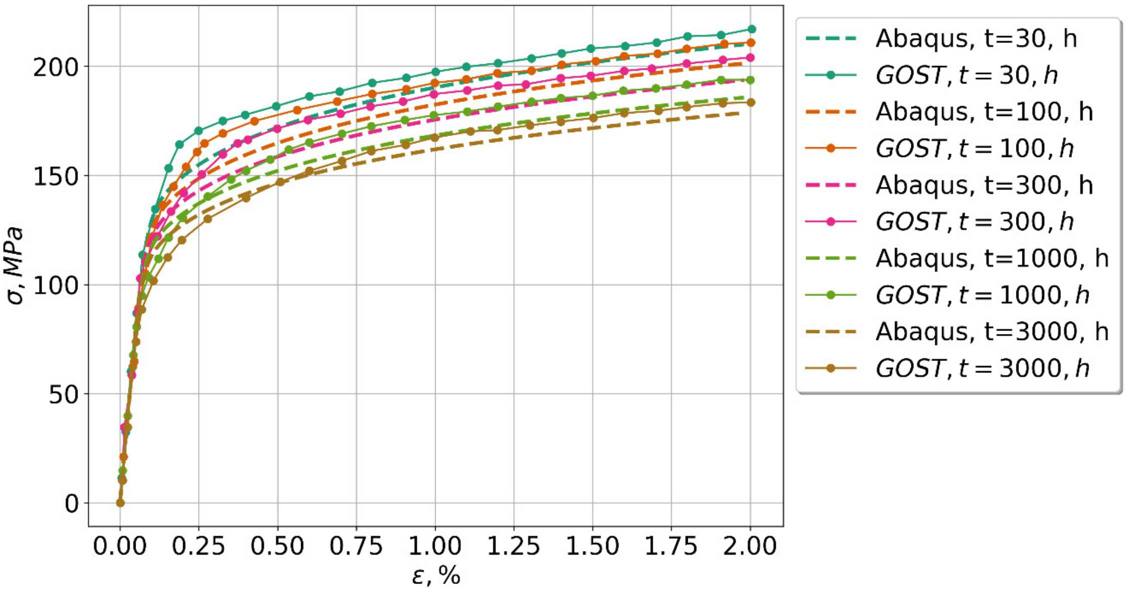

Fig. 8. Isochronous curves for AISI321 steel for $t < 3000$ h, $T = 550$ °C

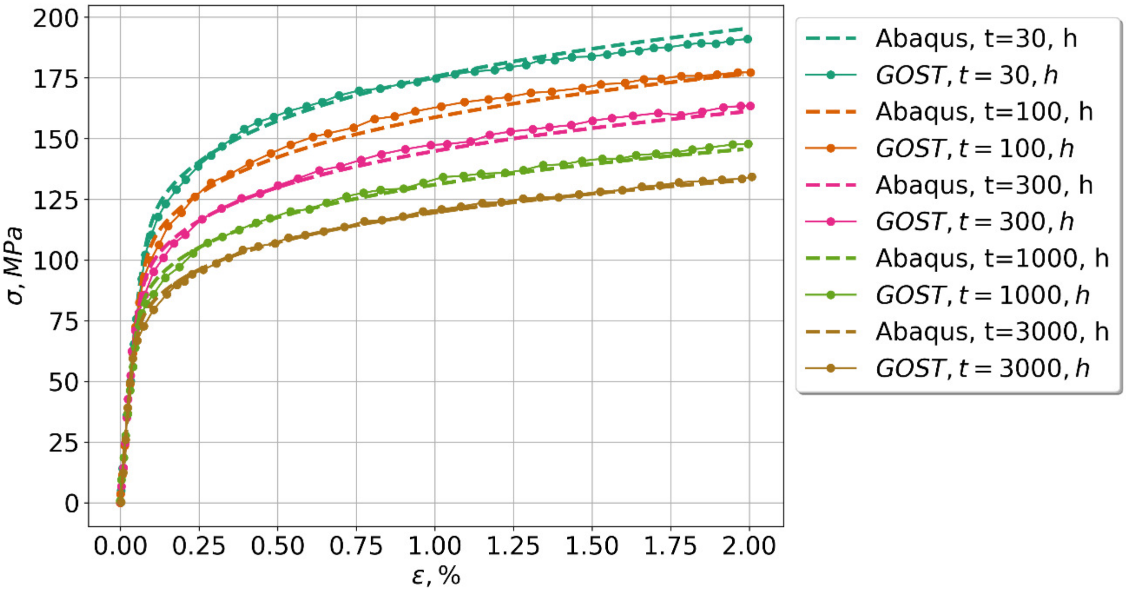

Fig. 9. Isochronous curves for AISI321 steel for $t < 3000$ h, $T = 600$ °C

Table 2. Parameters of the Norton-Bailey model for steel 12Kh18N12T/12Kh18N10T (AISI 321) for $t < 3000$ h

T, °C	ε_0	σ_0, MPa	m	n
500	2.4856e-09	352.28	-0.8937	6.5109
550	1.6635e-08	340.11	-0.8034	5.5911
600	3.5435e-08	313.22	-0.6487	4.1957

Conclusions

This paper presents the results of developing an automated procedure for identifying the parameters of an arbitrary creep model, demonstrated using the Norton-Bailey model based on a set of isochronous curves at a constant temperature. The results are presented for steel grade 12Kh18N12T/12Kh18N10T (AISI 321) at temperatures of 500, 550, and 600 °C.

Good agreement is demonstrated between the standard creep curves and the numerical curves obtained in Abaqus using the developed model with the identified parameters. The maximum deviation between the calculated and standard curves does not exceed 13 % for fast loading rates and 8 % for slow loading rates. On average, the deviation between the curves does not exceed 5 % for all analyzed cases and decreases with slower loading rates.

CRediT authorship contribution statement

Roman V. Fedorenko: investigation, conceptualization, writing – original draft; **Aleksei V. Lukin**: supervision, writing – review & editing.

Conflict of interest

The authors declare that they have no conflict of interest.

References

1. *Decree of the President of the Russian Federation No. 529, dated 18 June 2024. On the Approval of the Priority Areas for Scientific and Technological Development and the List of Critical Science-Intensive Technologies*. Available from: http://www.kremlin.ru/acts/bank/50755 [Accessed 17th February 2026]. (In Russian)
2. Adamov EO, Kaplienko AV, Orlov VV, Smirnov VS, Lopatkin AV, Lemekov VV, Moiseev AV. Fast neutron reactor with lead coolant BREST: from concept to technology implementation. *Atomic Energy*. 2020;129(4): 185–194. (In Russian)
3. Shamarin IV, Gavrilov PM. High-temperature nuclear power technologies. *Izvestiya Tomskogo Politekhnicheskogo Universiteta*. 2010;316(4): 5–9. (In Russian)
4. Krasilnikov AV, Konovalov SV, Bondarchuk EN, Masul IV, Rodin IY, Mineyev AB, Kuzmin EG, Kavin AA, Karpov DA, Leonov VM, Hayrutdinov RR, Kukushkin AS, Pornov DV, Ivanov AA, Belchenko YI, Denisov GG. Tokamak with reactor technologies (TRT): concept, missions, main features and expected characteristics. *Plasma Physics*. 2021;47(11): 970–985. (In Russian)
5. Rabotnov YV. *Creep of structural elements*. Moscow: Nauka; 1966. (In Russian)
6. Le X, Takaki K, Takamoto I. Creep-fatigue life evaluation of type 304 stainless steel under non-proportional loading. *International Journal of Pressure Vessels and Piping*. 2021;194: 104467.
7. Lokoshchenko AM. *Creep and long-term strength of metals*. Moscow: Fizmatlit; 2016. (In Russian)
8. Lokoshchenko AM, Teraud VV. Creep of a long narrow membrane under constrained conditions until failure. *Journal of Applied Mechanics and Technical Physics*. 2013;54(3): 126–133 (In Russian)
9. National Standard of the Russian Federation. GOST R 59115.10-2021. *Rules for strength assessment of equipment and pipelines of nuclear power installations. Confirmatory analysis on stage of design*. Moscow: Standartinform; 2021. (In Russian)
10. American Society of Mechanical Engineers. ASME BPVC.III.5-2015. *Division 5 – High Temperature Reactors*. New York: ASME; 2015.
11. Norton FH. *The Creep of Steels at High Temperatures*. New York: McGraw-Hill; 1929.
12. Betten J. *Creep Mechanics*. 2nd ed. Berlin: Springer; 2005.
13. May D, Gordon A, Segletes D. The Application of the Norton-Bailey Law for Creep Prediction Through Power Law Regression. In: *Proceedings of the ASME Turbo Expo*. 2013. p.GT2013-96008.
14. Darveaux R, Banerji K. Constitutive relations for Tin-based Solder Joints. *IEEE Transactions on Components, Hybrids, and Manufacturing Technology*. 1992;15(6): 1013–1024.
15. Kachanov LM. On the time to failure under creep conditions. *Izvestiya Akademii Nauk SSSR, Otdelenie Tekhnicheskikh Nauk*. 1958;(8): 26–31. (In Russian)
16. Rabotnov YN. On the mechanism of long-term fracture. In: *Problems of strength of materials and structures*. Moscow: USSR Academy of Sciences Publishing House; 1959. p.5–7. (In Russian)
17. Rabotnov YN. On creep rupture. *Journal of Applied Mechanics and Technical Physics*. 1963;(2): 113–123. (In Russian)

18. Hong J, Wang T, Zhu B, Li D, Dong H, Zuo D, Huang J, Man Z, Zhang G. Enhancing creep life prediction under large-shear deformation based on a modified Kachanov–Rabotnov model. *Nuclear Engineering and Design.* 2026;448: 114694.
19. Kachanov LM. *Fundamentals of fracture mechanics*. Moscow: Nauka; 1974. (In Russian)
20. Sandström R. Tertiary Creep. In: *Basic Modeling and Theory of Creep of Metallic Materials.* Cham: Springer; 2024. p.233–256.
21. Saitova RR, Arutyunyan AR. Creep and long-term strength of high-entropy alloys. *Materials Physics and Mechanics.* 2025;53(3): 116–121.
22. Othman AM, Hayhurst DR, Dyson BF. Skeletal point stresses in circumferentially notched tension bars undergoing tertiary creep modelled with physically based constitutive equations. *Proceedings of the Royal Society of London. Series A, Mathematical and Physical Sciences.* 1993;441(1912): 343–358.
23. National Standard of the Russian Federation. GOST R 59115.4-2021. *Rules for strength assessment of equipment and pipelines of nuclear power installations. Long-term mechanical properties of structural materials.* Moscow: Standartinform; 2021. (In Russian)
24. Grishchenko AI, Semenov AS. Effective methods of parameter identification for creep models with account of III stage. *MATEC Web of Conferences.* 2016;53: 01041.
25. Grishchenko AI, Semenov AS, Getsov LB. Modeling inelastic deformation of single crystal superalloys with account of γ/γ' phases evolution. *Material Physics and Mechanics.* 2015;24(4): 325–330.
26. Shirmer RW, Selent M, Abendroth M, Kiefer B. Identification of creep parameters from multi-step relaxation tests on miniaturised specimen. *Proceedings in Applied Mathematics and Mechanics.* 2023;23(4): e202200144.
27. Liu Y, Murakami S. Damage localization of conventional creep damage models and proposition of a new model for creep damage analysis. *JSME International Journal, Series A: Solid Mechanics and Material Engineering.* 1998;41(1): 57–65.
28. Katanakha NA, Semenov AS, Getsov LB. Unified model of steady-state and transient creep and identification of its parameters. *Strength of Materials.* 2013;45(4): 495–505.
29. Tashakori S, San-Millan A, Vaziri V, Aphale SS. Fast Parameter Identification of the Fractional-Order Creep Model. *Actuators.* 2024;13(12): 534.
30. *Abaqus 2017 Theory Guide*. Providence, RI: Dassault Systèmes; 2017.
31. Endres SC, Sandrock C, Focke WW. A simplicial homology algorithm for lipschitz optimization. *Journal of Global Optimization.* 2018;72(1): 181–217.
32. Conn AR, Scheinberg K, Vicente LN. *Introduction to Derivative-Free Optimization.* Philadelphia: Society for Industrial and Applied Mathematics; 2009
33. Kelley CT. *Iterative Methods for Optimization.* Philadelphia: Society for Industrial and Applied Mathematics (SIAM); 1999
34. Gantmakher FR. *Theory of matrices.* 5th ed. Moscow: Fizmatlit; 2004. (In Russian)

MATERIALS PHYSICS AND MECHANICS RESEARCH ARTICLE

Submitted: September 11, 2025 **Revised: October 29, 2025** **Accepted: December 4, 2025**

The elastic properties of natural fibre reinforced composite materials using homogenisation modeling

R.E. Guzman-Lopez [1], S. Gomez Suarez [1], R.A. Gonzalez-Lezcano [2]✉

[1] Universidad Pontificia Bolivariana, Bucaramanga, Colombia

[2] Universidad San Pablo-CEU, Madrid, Spain

✉ rgonzalezcano@ceu.es

ABSTRACT

The numerical simulation of composite materials brings in a challenge in the resolution of problems with a high nonlinearity of both, material, and geometry (geometrically complex structures), with different size scales. Some common examples such as additive manufacturing 3D, metal alloys, porous media, polycrystalline materials and composites, a significant computing challenge is shown where all length scales are resolved by a single finite element model. This would require many elements, and computing the solution would be unfeasible, even using modern and near-future computing resources. The standard way to solve this situation of scale in finite element analysis is numerical homogenization technique. Material properties for a composite material are average, instead of simulating the full microstructure. With homogenized material data, it only required a macroscopic simulation using significantly less computational sources. The mechanical behavior of composites materials reinforced with natural fibers, is studied by means of a short fiber composite numerical model. The influence that the spatial distribution and the volumetric fraction of the cylindrical fibers have on the effective elastic properties of the numerical model was established (Young´s modulus *E*, Shear modulus *G*, Poisson´s ratio) - curves are presented corresponding to tension test applied on fique fibers and polylactic acid-biopolymer.

KEYWORDS

representative volume element • multiparticle cell • fiber-reinforced composites • composite materials natural fibre composites

***Funding**. The authors would like to express their gratitude to Engineering Department of Universidad Pontificia Bolivariana-Bucaramanga, project code: BIC-008-0822-F4M.*

Citation: Guzman-Lopez RE, Gomez Suarez S, Gonzalez-Lezcano RA. The elastic properties of natural fibre reinforced composite materials using homogenisation modeling. *Materials Physics and Mechanics*. 2026;54(1): 130–138. http://dx.doi.org/10.18149/MPM.5412026_12

Introduction

The usage of methods and models to evaluate thermo-elastic properties of composite materials has been widely investigated in the past years. Different models have been proposed and are currently used in many engineering applications, including analytical models [1–6], semi-empirical models [7–9], homogenization models [8,10,11] and cell methods [12–15]. The cell models are generally constructed from a discretization by the finite element method (FEM) of a representative volume element (RVE) of a composite material. Obtaining RVE can generally be done using numerical algorithms [9,10] and it must be a volume small enough from a macroscopic point of view to be treated as a continuous point of matter and, at the same time, large enough to be considered representative of the meso/micro-structure of the material.

Publisher: Peter the Great St. Petersburg Polytechnic University

The analytical models are based on the fact that the effective mechanical properties of the composite can be obtained by relations between the volumetric measure of the meso/micro stress and strain fields. In the elastic regime, the analytical models represent the stress and strain fields present in the composite material through their average values in matrix and reinforcement. The individual contributions are quantified considering that the average stresses and strain in each phase are related through their respective stiffness tensors, C_m and C_i. The objective of the analytical models (meanfield) in elasticity is centered by finding the stiffness tensor [C] of the elastic constitutive matrix $\bar{\sigma} = C{:}\,\bar{\varepsilon}$. Mori-Tanaka [10] developed a well-known model which is widely used for modeling different kinds of composite materials, based on the studies of Eshelby [4] and Benveniste [11] of tensional fields inside a particle embedded in an elastic matrix of infinite length, based on an Equivalent inclusion method. In [16], it was suggested self-consistent formulation in which the material is represented in such a way that all phases are embedded in an equivalent material whose properties are the properties to be determined. Christensen et al. [17] also proposed their generalized self-consistent formulation, in which the particle is embedded in a matrix, and this particle−matrix composite, in turn, is embedded in a material whose elastic constants are the unknowns of the problem. Whitney and Riley [18] proposed analytical expressions using strain-energy balances to obtain elastic constants in composite materials reinforced with unidirectional fibers.

FEM has been extensively used in the literature to analyze a periodic unit cell, to determine the thermo-mechanical properties and damage mechanisms of composites [14,18]. Böhm H. [19] studied unit cell models for describing the elastoplastic behavior of short fiber reinforced metal matrix composites (MMCs) reinforced by randomly oriented short fibers, providing a foundational approach for micro-scale modeling.

Zihui Xia et al. [20] presented a FEM micromechanical analysis method applied to unidirectional and angleply laminates subject to multiaxial loading conditions, demonstrating the application of FEM in varied reinforcement configurations. Younes R. [21] presented a comparative study of analytical micromechanical models and numerical models (FEM) evaluating the elastic properties of unidirectional composite materials (glass/epoxy, carbon/epoxy, polyethylene/epoxy composite), offering critical insight into the validity of numerical models. Srivastava V.K. [22] used numerical homogenization tools for the evaluation of the effective material properties of the short fiber composites, using modified random sequential adsorption algorithm (RSA) [22,23], which is a relevant approach for generating realistic microstructures.

The homogenization method based on the finite element method (FEM) allows the replacement of a heterogeneous medium with an equivalent homogeneous one using information from the meso/micro scale, through the local response, on the microscopic scale depending on the state of charge on the macro scale. In cell models, the macroscopic stress and strain tensors associated with a particular mechanical stress imposed on the multiparticle cell can be obtained in two ways: They may be calculated either from the external forces acting on the faces of the cell or from the volumetric average of the stress and strain microfields within the calculation domain [13,24−27].

The homogenization method establishes mathematical relationships between the meso/micro fields and the macroscopic stress−strain fields by using cell-based formulations derived from perturbation theory. In homogenization models for short-fiber composite materials, it is generally recommended to employ representative volume elements (RVEs) that contain a sufficiently large number of fibers to capture the statistical characteristics of their spatial distribution.

One common approach to determine an appropriate RVE size consists of selecting an initial RVE and performing macroscopic simulations to assess the influence of fiber spatial arrangement on stress and strain fields. The size of RVE is then progressively increased to verify whether the microscopic results change significantly. If notable variations occur, the initial RVE size is insufficient; if results remain stable, the initial RVE can be considered representative.

In this work, the geometries and meshes of RVEs were generated using Ansys Material Designer 2024R1, whose algorithms compute the homogenized properties of a composite from the known properties of its constituent materials. The developed Short Fiber Composite Model (RVE) was used to analyze the influence of model parameters—such as fiber volume fraction (*f*) and fiber orientation—on the resulting homogenized elastic properties (Young's modulus *E*, shear modulus *G*, and Poisson's ratio *v*).

Furthermore, as requested, a more detailed analysis of the key publications cited in this section has been incorporated, highlighting their methodological contributions and relevance to the present homogenization framework.

Methods

Characteristics of the RVE model

The micromechanical model for the composite material reinforced with fique fibers is configured using the RVE technique. The model is characterized by several parameters that define the geometry and distribution of fibers within the RVE. These parameters include the fiber volume fraction, which represents the portion of the RVE occupied by the fiber material, and the seed number used to generate random fiber orientations in the case of randomized RVEs. The model also incorporates the orientation tensor, the aspect ratio (defined as the ratio of fiber length to diameter), and the total number of cylindrical fibers contained in the RVE.

As shown in Fig. 1, the RVE model of the composite material consists of short fique fibers randomly arranged in a polylactic acid (PLA) biopolymer matrix. The cylindrical reinforcement fibers are generated without spatial interference, and if a fiber intersects one of the planes that defines the boundaries of the cell, it is duplicated on the opposite face of the cell. This procedure results in a multiparticle cell with periodic geometry (Fig. 1). The generated RVE was used to analyze the influence of the fiber volume fraction and fiber orientation (*f*) on the engineering constants E_x, E_y, E_z, G_{xy}, G_{yz}, G_{xz}, ν_{xy}, ν_{yz}, and ν_{xz}.

The orientation is randomly assigned by tracing a symmetric orientation tensor. The tensor A and its components Aij are now expressed consistently using italic mathematical notation to ensure uniformity throughout the manuscript. The three diagonal entries are: A_{11}, A_{22}, and A_{33}. These values indicate how closely the fibers are aligned with the corresponding coordinate direction. In this case, multiparticle models were generated in which the fibers are oriented parallel to the XZ plane:

$$A_{i,j} = \sum_{k=1}^{N} d_i{}^{(k)} d_j{}^{(k)}. \quad (1)$$

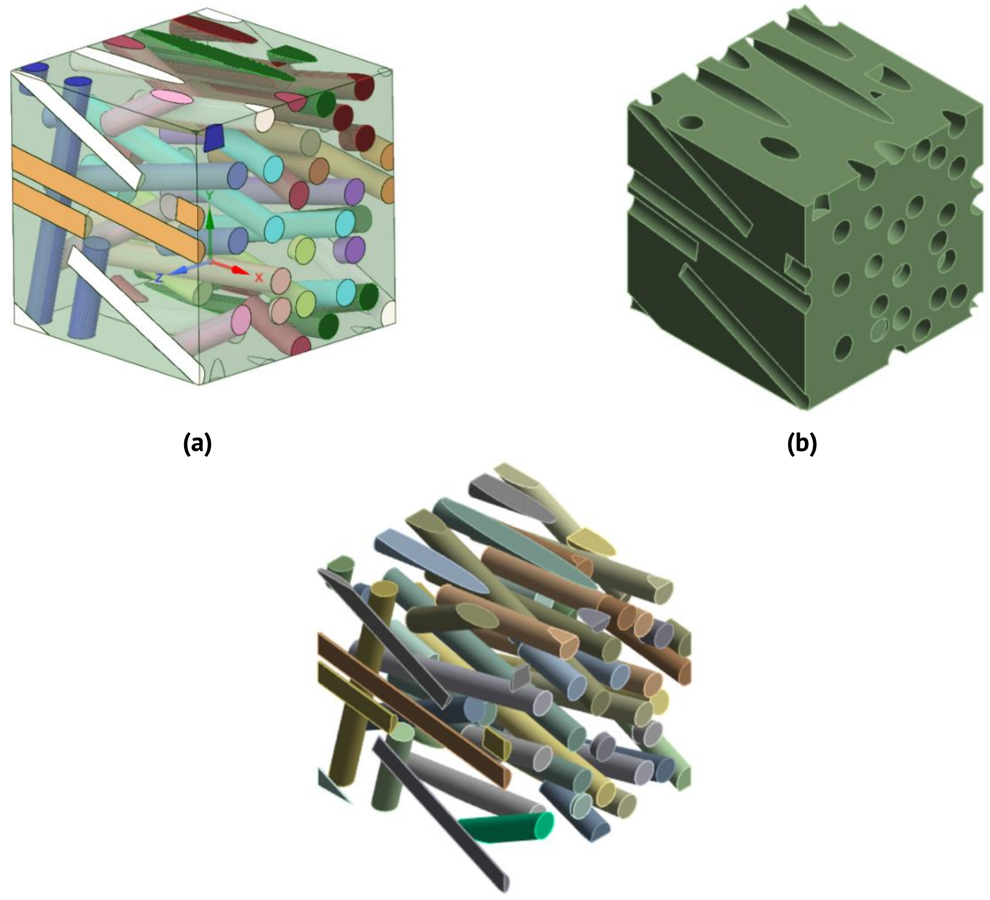

(a) **(b)** **(c)**

Fig. 1. Parts of the RVE: (a) composite NFCs, (b) matrix, (c) short fibers

Numerical FE modeling

The geometries and periodic meshes of the RVE were generated using Ansys Material Designer 2024 R1. Figure 2 shows the distributed mesh-quality metric for the model, which was discretized using 4-node tetrahedral elements. This metric is based on the ratio between the element volume and the square root of the cube of the sum of the squared edge lengths for 3D elements. As a general rule, the minimum acceptable value for this mesh metric should be greater than 0.2.

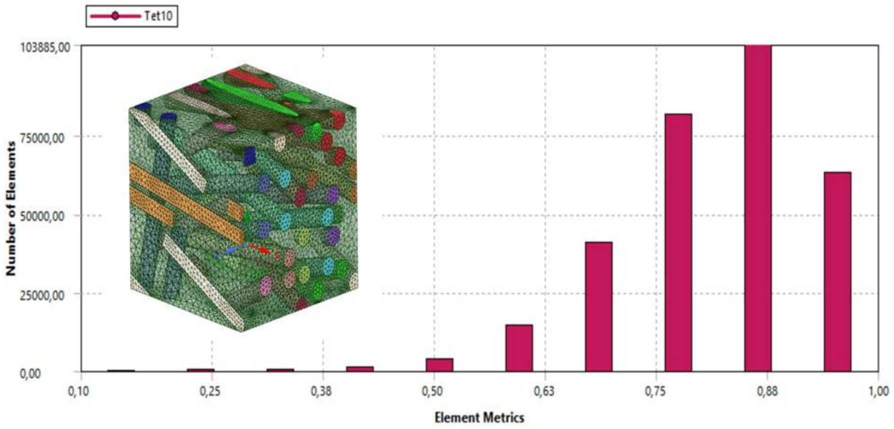

Fig. 2. The mesh-quality metric for the model RVE

For the model shown in Fig. 2, the mesh consists of 309,319 elements and 434,508 nodes. The generation parameters used were: fiber volume fraction $f = 0.1$, number of fibers $N = 24$, aspect ratio = 15, and orientation tensor components $A_{11} = 0$, $A_{22} = 0.8$ and $A_{33} = 0.2$ indicating that the fibers are oriented parallel to the XZ plane.

Results

The mechanical properties of the constituent materials used in the numerical multiparticle-cell models were obtained from tensile tests performed on the fique fibers and the PLA matrix (Ingeo biopolymer 2003D). Figure 3 shows the stress–strain (σ–ε) curves corresponding to the tensile tests conducted on both the fique fibers and the polylactide (PLA) matrix. The σ–ε curves are plotted up to the respective tensile ultimate strenghts.

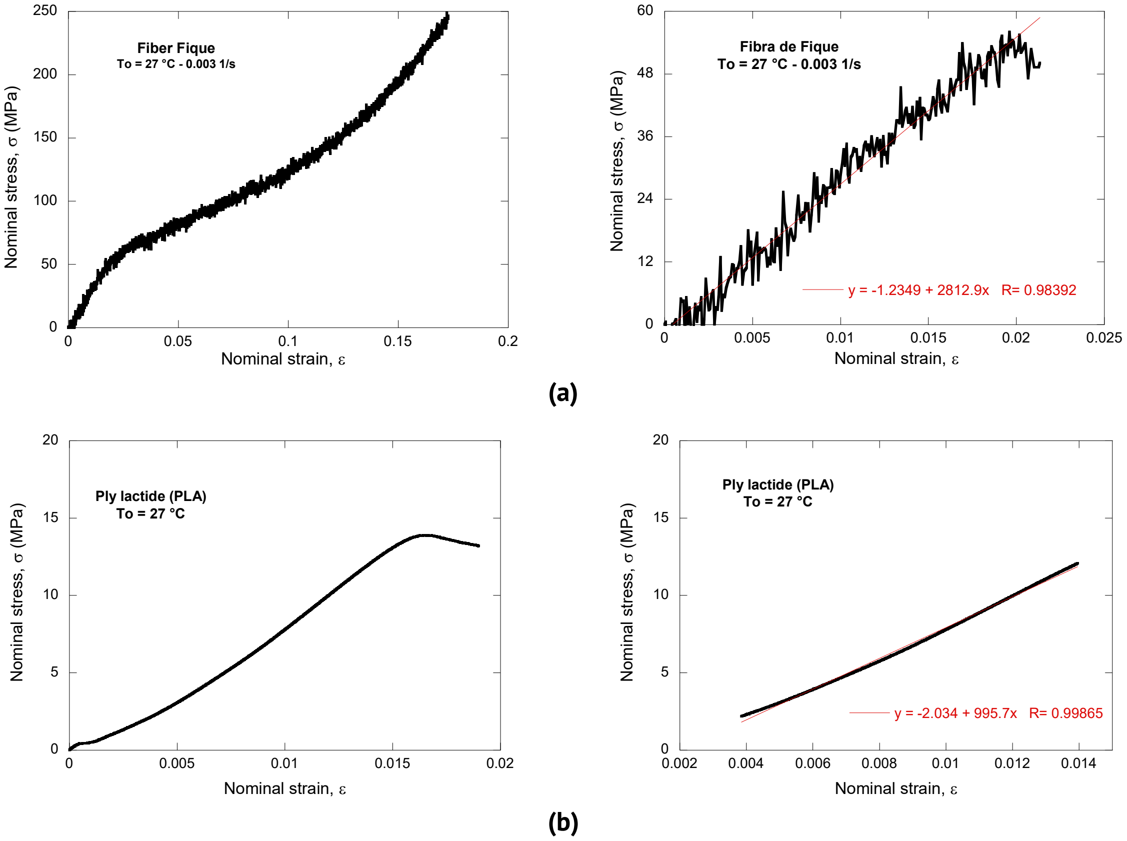

Fig. 3. (a) Stress–strain (σ–ε) curves obtained experimentally for the polylactide (PLA) matrix at 27 °C, including the complete response up to the ultimate tensile strength and the linear fit in the elastic region. (b) Stress–strain (σ–ε) curves for the fique fibers tested at 27 °C and a strain rate of 0.003 s^{-1}, showing the full mechanical response and the corresponding linear fit in the elastic region. The equations of the fitted lines and the correlation coefficient R are included in each graph

Table 1 displays elastic modulus, the poisson´s ratio and the tensile ultimate strength of the materials that are used in the RVE model. The geometric parameters of diameter D, and aspect ratio (L/D) of the short fibers of the RVE model are presented in Fig. 4. The normal distribution curves are shown, being able to set a mean value and its standard deviation for 198 measured values. Figure 5 shows the cross section of a fiber and the lengths of some short fibers can be observed.

Table 1. Material properties for the constituents of the composite

Materials	Elastic modulus, GPa	Poisson's ratio	Tensile ultimate strength, MPa
Fique	0.943–2.800	0.300	30.000–240.000
PLA	0.995	0.360	13.900

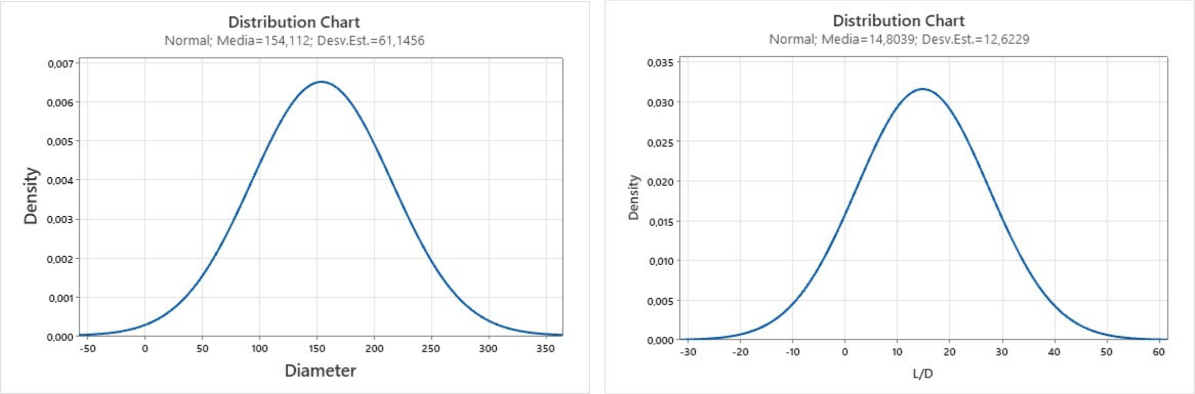

(a) **(b)**

Fig. 4. (a) Chart distribution normal of values the fiber diameter and (b) aspect ratio

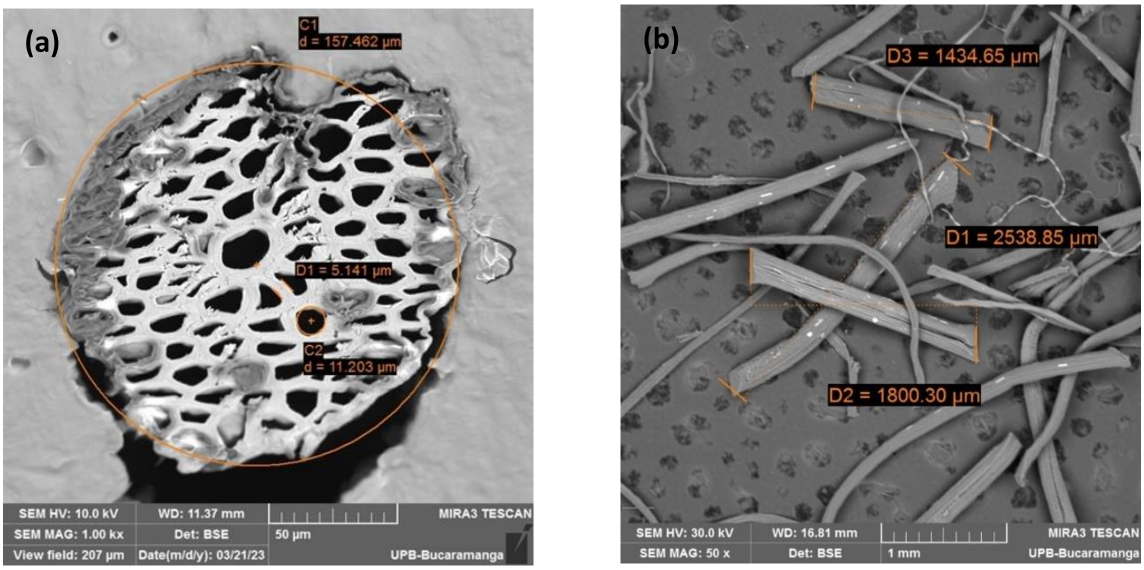

Fig. 5. (a) Cross section of raw fique fibers, SEM image: 1000 x magnification. (b) Longitudinal image of raw fique fibers magnified at 50

Table 2 shows the results of the FEM analysis of the elastic engineering constants for several RVE models. The dependence of the results with respect to the fiber volume fraction and the tensor orientation is observed, keeping the aspect ratio ($L/D \approx 15$) constant. Figure 6 shows the results of the elastic modulus in the directions E_x, E_y, E_z, and the shear moduli G_{xy}, G_{yz}, G_{zx}, as expected, they increase with the volumetric fraction, while ν is decreasing, it is also observed that the variation of the orientation of the fibers given by the orientation tensor ($A_{i,j}$) are not significant (Table 2). According to the fact that the random distribution of the fibers is parallel to the XZ plane, the results present an isotropic behavior in the plane, while the perpendicular components present significant differences.

Table 2. Numerical results for elastic engineering constants

Parameters	**Value #1**	**Value #2**	**Value #3**	**Value #4**	**Value #5**	**Value #6**	**Value #7**
Fiber volume fraction	0.05145846	0.051468	0.102659	0.102723	0.193572	0.205736071	0.244535
Orientation tensor A_{11}	0.2000062	0.299994	0.22155	0.3627	0.223056	0.332688133	0.269775
Orientation tensor A_{22}	0.7999938	0.700006	0.77845	0.6373	0.776944	0.667311867	0.730225
Number of fiber	34	34	24	24	16	17	11
Engineering constants							
E_1, MPa	1048.04669	1050.762	1103.798	1109.172	1224.381	1230.306896	1281.017
E_2, MPa	1069.42596	1065.035	1140.699	1127.192	1288.706	1274.770353	1349.442
E_3, MPa	1047.52113	1047.6	1102.763	1103.917	1208.46	1223.474354	1274.172
G_{12}, MPa	38.112641	388.3994	412.3265	413.9153	451.792	465.2257714	481.4119
G_{23}, MPa	385.002686	384.913	404.9138	404.6695	442.8969	448.8552857	467.5487
G_{31}, MPa	383.727959	383.9225	402.775	403.0845	438.1448	445.3709344	461.6207
n^{12}	0.35082724	0.352427	0.344875	0.350177	0,328909	0.339509741	0.330379
n^{13}	0.36139787	0.360252	0.360531	0,356824	0.361243	0.354052931	0.355162
n^{23}	0.35626227	0.356909	0.352371	0.353002	0.349525	0.345615269	0.343473
Density							
$r^{(\text{t mm}\hat{}\text{-3})}$	3.13E-09	3.13E-09	3.13E-09	2.86E-09	2.86E-09	2.86E-09	2.79E-09

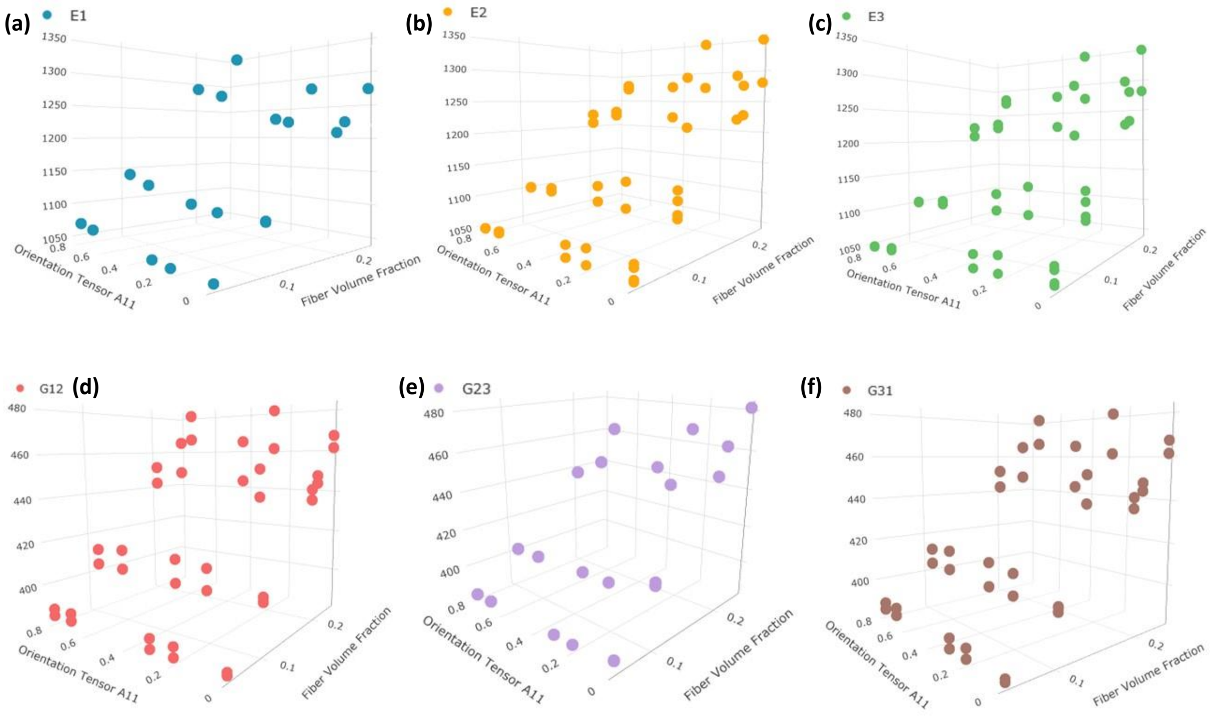

Fig. 6. (a–c) Elastic moduli E_x, E_y, E_z and (d–f) shear moduli G_{12}, G_{23}, G_{31}

Conclusions

1. Influence of fiber volume fraction: the elastic properties of the natural fiber composites (NFCs) increase consistently with higher fiber volume fractions. This confirms that the reinforcing effect of fique fibers is directly proportional to their concentration within the PLA matrix.
2. Effect of fiber orientation: for the RVEs generated in this study—where fibers were intentionally aligned parallel to the XZ plane—significant directional dependence was observed in the elastic moduli (E_x, E_y, E_z), shear moduli (G_{xy}, G_{yz}, G_{xz}), and Poisson ratios (ν_{xy}, ν_{yz}, ν_{xz}). Mechanical anisotropy arises predominantly from this controlled orientation.
3. Spatial distribution of fibers: although extrusion processes typically lead to non-uniform particle distribution due to flow-induced alignment or clustering, the numerical results obtained here indicate low sensitivity of effective elastic properties to the particular fiber distributions examined. This outcome may be related to the restricted set of configurations analyzed.
4. Agreement between transverse and longitudinal moduli: for a given fiber volume fraction, the elastic modulus showed a tendency toward similar values along the transverse and longitudinal directions, except in the direction perpendicular to the XZ plane, where fiber alignment dominates mechanical behavior.
5. General mechanical response of the composite: the combined effects of fiber volume fraction, spatial distribution, and orientation determine the global stiffness of NFCs. Among these factors, fiber orientation is shown to be the most decisive in governing anisotropy, while fiber distribution plays a comparatively minor role within the analyzed parameter space.

CRediT authorship contribution statement

Rolando Enrique Guzman-Lopez: conceptualization, methodology, investigation, writing—original draft preparation, writing—review and editing, supervision, project administration; **Sergio Gomez Suarez**: conceptualization, methodology, investigation, writing—original draft preparation, writing—review and editing; **Roberto Alonso Gonzalez-Lezcano**: methodology, investigation, writing—review and editing, supervision.

Conflict of interest

The authors declare that they have no conflict of interest.

References

1. Voigt W. On the relationship between the two elastic constants of an isotropic body. *Ann. Phys.* 1889;274(12): 573–587.
2. Reuss A. Berechnung der Fließgrenze von Mischkristallen auf Grund der Plastizitätsbedingung für Einkristalle. *ZAMM - J. Appl. Math. Mech.* 1929;9(1): 49–58.
3. Hashin Z, Rosen BW. The Elastic Moduli of Fiber-Reinforced Materials. *J. Appl. Mech.* 1964;63: 223–232.
4. Eshelby JD. The determination of the elastic field of an ellipsoidal inclusion, and related problems. *Proc. Roy. Soc. A.* 1957;241(1226): 376–396.

5. Theocaris PS, Spathis G, Sideridis E. Elastic and viscoelastic properties of fibre-reinforced composite materials. *Fibre Sci. Technol.* 1982;17(3): 169–181.
6. Whitney JM, Riley MB. Elastic properties of fiber reinforced composite materials. *AIAA J.* 1966;4(9): 1537–1542.
7. Affdl JCH, Kardos JL. The Halpin-Tsai equations: A review. *Polym. Eng. Sci.* 1976;16(5): 344–352.
8. Hill R. Theory of mechanical properties of fibre-strengthened materials: I. Elastic Behaviour. *J. Mech. Phys. Solids*. 1965;13(4): 189–198.
9. Chamis CC. Mechanics of composite materials: Past, present, and future. *J. Compos. Technol. Res.* 1989;11(1): 3–14.
10. Mori T, Tanaka K. Average stress in matrix and average elastic energy of materials with misfitting inclusions. *Acta Metall.* 1973;21(5): 571–574.
11. Benveniste Y. A new approach to the application of Mori-Tanaka's theory in composite materials. *Mech. Mater.* 1987;6(2): 147–157.
12. Millithaler P., Sadoulet-Reboul E., Ouisse M., Dupont J. B., Bouhaddi N. Equivalent orthotropic material properties for stators of electric cars. *Civil-Comp Proc.* 2015;106: 1–12.
13. Rodríguez FJ, Dardati PM, Godoy LA, Celentano DJ. Derivation of nodular cast iron elastic properties via computational micromechanics. *Rev. Int. Metod. Numer. Para Calc. y Disen. En Ing.* 2015;31(2): 91–105.
14. Viñuela JZ, Torres M, Silva RG. Cohesive zone modeling in load – unload situations. *Int. J. Mech. Sci.* 2022;222: 107205.
15. Rodriguez FJ, Dardati PM, Godoy LA, Celentano DJ. A computational micromechanics approach to evaluate effective properties of ductile cast iron. In: *Proc. 10th Int. Symp. Sci. Process. Cast Iron – SPCI10 A, 2014*. 2014.
16. Den Eindmck V. *Berechnung der elastischen Konstanten des Vielkristalls aus den Konstanten des Einkristalls.* 1958.
17. Christensen RM, Lo KN. Solutions for effective shear properties in three phase sphere and cylinder models. *Journal of the Mechanics and Physics of Solids*. 1979;27(4): 315–330.
18. Hyer MW, Waas AM. Micromechanics of Linear Elastic Continuous Fiber Composites. In: *Compr. Compos. Mater.* 2000. p.345–375.
19. Böhm HJ, Eckschlager A, Han W. Multi-inclusion unit cell models for metal matrix composites with randomly oriented discontinuous reinforcements. *Comput. Mater. Sci.* 2002;25(1–2): 42–53.
20. Xia Z, Zhang Y, Ellyin F. A unified periodical boundary conditions for representative volume elements of composites and applications. *Int. J. Solids Struct.* 2003;40(8): 1907–1921.
21. Younes R, Hallal A, Fardoun F, Hajj F. Comparative Review Study on Elastic Properties Modeling for Unidirectional Composite Materials. In: Hu N. (Ed.) *Compos. Their Prop.* 2012. p.1–18.
22. Srivastava VK, Gabbert U, Berger H. Representative volume element analysis for the evaluation of effective material properties of fiber and particle loaded composites with different shaped inclusions. In: Proulx T. (Ed.) *Mechanics of Time-Dependent Materials and Processes in Conventional and Multifunctional Materials, Volume 3. Conference Proceedings of the Society for Experimental Mechanics Series.* New York: Springer; 2011. p.185–192.
23. Kari S. *Micromechanical modelling and numerical homogenization of fibre and particle reinforced composites*. Germany; 2007.
24. Zahr-Viñuela J. *Comportamiento mecánico de materiales compuestos de matriz metálica y refuerzo de partículas : un enfoque basado en celdas multipartícula.* 2010.
25. García Sánchez GF, Guzmán López RE, Gonzalez-Lezcano RA. Fique as a sustainable material and thermal insulation for buildings: study of its decomposition and thermal conductivity. *Sustainability.* 2021;13(13): 7484.
26. Pavan R, Prashant A, Ameen T, Yashwant M, Avinash S, Irulappasamy S. Numerical simulation of low-velocity impact test on biocomposite laminates. *Materials Physics and Mechanics*. 2022;50(4): 355–364.
27. Suardana NPG, Lokantara IP, Lim JK. Influence of water absorption on mechanical properties of coconut coir fiber/poly-lactic acid biocomposites. *Materials Physics and Mechanics*. 2011;12(1): 45–53.

MATERIALS PHYSICS AND MECHANICS

54 (1) 2026

УЧРЕДИТЕЛИ

Санкт-Петербургский политехнический
университет Петра Великого
Адрес: 195251, Санкт-Петербург,
Политехническая ул., д. 29

Институт проблем Машиноведения
Российской академии наук
Адрес: 199178, Санкт-Петербург,
Большой пр-кт В.О., д. 61

ИЗДАТЕЛЬ

Санкт-Петербургский политехнический университет Петра Великого
Адрес: 195251, Санкт-Петербург, Политехническая ул., д. 29

Журнал зарегистрирован в Федеральной службе по надзору в сфере связи, информационных технологий и массовых коммуникаций (РОСКОМНАДЗОР), свидетельство ПИ №ФС77-69287 от 6 апреля 2017 года.

АДРЕС И ТЕЛЕФОН РЕДАКЦИИ

199178, Санкт-Петербург, Большой пр-кт В.О., д. 61

Тел. редакции: +7(812)552 77 78, доб. 224

E-mail редакции: mpmjournal@spbstu.ru

Компьютерная верстка Л.И. Гузилова

Подписано в печать 07.04.2026 г. Выход в издания в свет: 27.04.2026 г.
Формат 60х84/8. Печать цифровая
Усл. печ. л. 10,0. Тираж 100. Заказ____.
Цена: Бесплатно

Отпечатано в **Издательско-полиграфическом центре Политехнического университета Петра Великого**
Адрес: 195251, Санкт-Петербург, Политехническая ул., 29
Тел.: +7(812)552 77 17

MPM, Vol. 54, No. 1, 2026

MPM
SCIENTIFIC
JOURNAL